Durham E-Theses

Performance studies for the Cherenkov Telescope Array (CTA) with prospects for detecting pulsed gamma-ray emission.

RULTEN, CAMERON,BOYD

How to cite:

RULTEN, CAMERON,BOYD (2012) *Performance studies for the Cherenkov Telescope Array (CTA) with prospects for detecting pulsed gamma-ray emission.*, Durham theses, Durham University. Available at Durham E-Theses Online: http://etheses.dur.ac.uk/3632/

Use policy

Performance studies for the Cherenkov Telescope Array (CTA) with prospects for detecting pulsed gamma-ray emission.

by

Cameron Boyd Rulten

Durham
University

Submitted in conformity with the requirements

for the degree of Doctor of Philosophy

Department of Physics

University of Durham

United Kingdom

Performance studies for the Cherenkov Telescope Array (CTA) with prospects for detecting pulsed gamma-ray emission.

Cameron Boyd Rulten

Abstract

Currently in the design stage, the Cherenkov Telescope Array (CTA) is an advanced facility for ground-based high-energy gamma-ray astronomy. This research presents the projected system performance of CTA calculated as part of a large Monte Carlo simulation effort including air shower and telescope response simulations. The integral sensitivity of CTA's baseline Subarray-E is found to be nearly an order of magnitude more sensitive between 100 GeV and 10 TeV compared to existing ground-based Cherenkov telescope systems. This research finds that this particular subarray achieves CTA's goal of milli-Crab sensitivity at 1 TeV. In addition, this work uses a multi-layer perceptron neural network to separate the cosmic-ray background from the gamma-ray signal. This includes employing 5 different methods for estimating the neural network response cut, with the energy-scaled significance method being found to provide the best and most stable performance. Performance measures calculated include: energy resolution, angular resolution, effective collecting area as well as flux sensitivity. In addition, the results of three small studies are also presented. The first includes the performance results of a high-altitude (3700 m) subarray. This research confirms a gain in sensitivity at the lowest detectable energies under $\sim$100 GeV. The second and third are small technical studies on CTA's dynamic range performance. Finally, to assess CTA's prospects for detecting pulsed gamma-ray emission data for the Crab and Vela pulsars taken from Fermi Gamma-Ray Space Telescope observations are analysed and compared with the CTA sensitivity performance derived in this research. Results for CTA Subarray-E and Subarray-B suggest these arrays will both have sufficient sensitivity performance for detecting the Vela pulsar if it behaves as expected on the basis of the published spectra.

Declaration

The material contained within this thesis has not previously been submitted for a degree at Durham University or any other university. The research reported within this thesis has been conducted by the author unless indicated otherwise.

Copyright Notice

Acknowledgements

I would like to thank everyone who has supported me in writing this thesis. Particular thanks should go to my supervisors Dr. Paula Chadwick, Dr. Sam Nolan and Dr. Steve Rayner for their much appreciated encouragement, patience and feedback. They have contributed a great deal of their time to reading through this thesis as well as providing useful and informative feedback. I would also like to thank past and present members of the Very High-Energy Gamma-Ray Group at Durham University including Dr. Hugh Dickinson and Dr. Michael Daniel for their patience and willingness to answer numerous questions regarding ROOT, C++ and Linux. Thanks should also go to Dr. Sam Nolan who helped to guide me through the minefield of simulation software and tools. His help and support for the past three and a half years has been invaluable. Thanks are also extended to my colleague and friend Dr. Daniel Parsons who has worked with me in the CTA Monte Carlo group for the past three and a half years. A general thanks to all the other group members who I have not named here, but thank you for your encouragement and friendship. Outside of the work environment, I would like to thank my family who have always believed in me and never deterred me from following my dreams. Its been a long road since those first few days when Gladys used to get me ready for my school days at Glenashley Junior Primary. Being able to do a PhD requires an incredible amount of support and my family have always provided this for me. Last but not least a special thanks should go to Rhianne Jones who has had to put up with me and my research over this past three and a half years. It must be so tough living with a physicist, we are stubborn, always right and just assume everyone else understands our language. This thesis has become as much a part of her life as it has mine. Thanks Rhianne for all the support, encouragement and understanding over the past few years.

Without all your support this thesis would not have been completed.
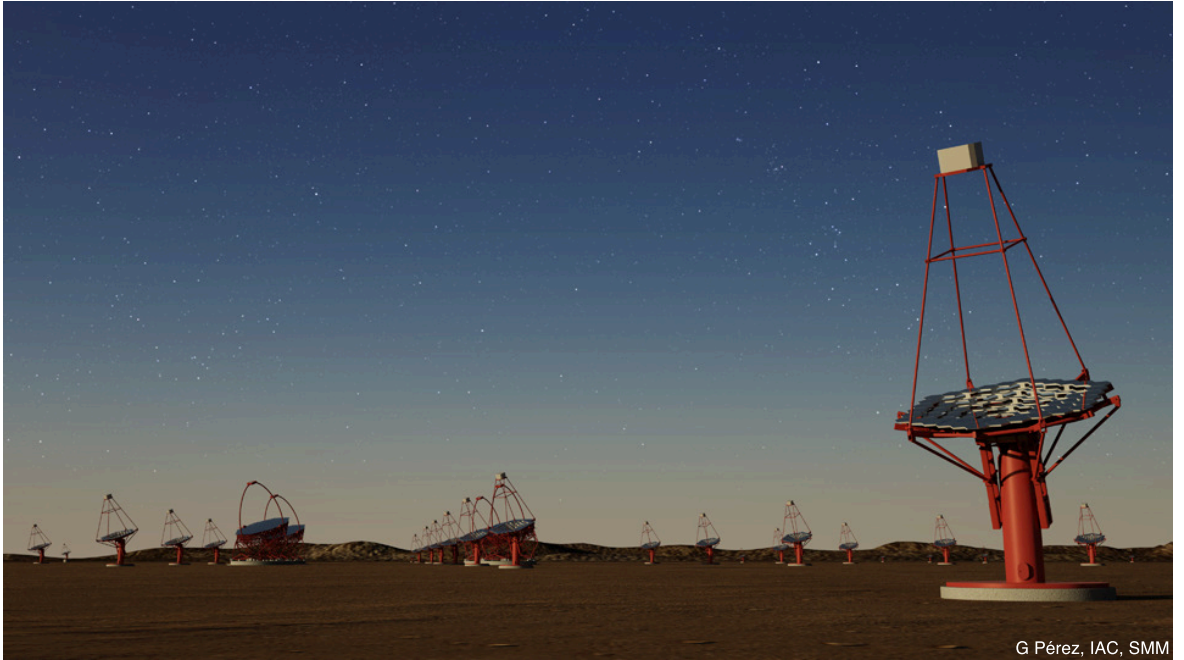
G Pérez, IAC, SMM

Artist's impression of CTA.

"Let the sky fall

Let the sea sink

Let the Earth shake

Let the Sun break

Let the Universe, go spinning free

If my darling ever leaves me."

Alvin Lee, Ten Years After (1971)

Table of Contents

List of Figures

List of Tables

Introduction

Currently in the design stage, the Cherenkov Telescope Array (CTA) is an advanced facility for ground-based high-energy gamma-ray astronomy. It is an international initiative that aims to build a next-generation Cherenkov telescope system with up to an order of magnitude better sensitivity, compared to existing ground-based Cherenkov systems, in the 100 GeV - 10 TeV energy range. This thesis presents the findings of Monte Carlo simulations conducted in order to derive the energy resolution, angular resolution and sensitivity performance of CTA.

Chapter 1 provides a brief introduction to gamma-rays and their astrophysical origin within the known Universe. This includes discussion of cosmic-rays, gamma-rays and the different interactions that lead to the production of gamma-rays. Models and physical concepts that describe gamma-ray production mechanisms are highlighted. Attention will be given toward pulsars, how they might produce gamma-rays and why they are interesting astrophysical objects. Furthermore, some of the principal interactions that lead to gamma-ray absorption and attenuation are also discussed, as these interactions provide us with an opportunity for observing gamma-rays. Chapter 2 provides a brief introduction to gamma-ray astronomy, using space-based and ground-based telescopes. This includes discussion of Extensive Air Showers (EAS), both electromagnetic and hadronic, which are capable of producing Cherenkov light within the Earth's atmosphere. How Cherenkov light is detected using the imaging Atmospheric Cherenkov technique is highlighted including stereoscopic techniques, the Hillas parameters and background rejection. Some observational techniques as well as some detector calibration terms, relevant to the Monte Carlo simulation work, are also

highlighted.

Chapter 3 provides an introduction to the Cherenkov Telescope Array (CTA). This includes discussion of the motivations, the specifications and the possible telescope array layouts. The results of extensive Monte Carlo simulation work are presented in order to assess the expected performance of CTA. This includes air shower and telescope simulations through to image reconstruction and background rejection. Energy resolution, angular resolution, array effective collecting area and sensitivity curves have been generated to provide a measure of array performance which allows for different array layouts and analysis methods to be compared. The procedure for producing the sensitivity curves is discussed, which includes various optimisation cuts that have been made. Particular attention is given to the background rejection method including the post-cut signal and background efficiency.

Chapter 4 presents the results of three short focused studies undertaken for the CTA Monte Carlo working group (MCWG). The first study addresses the effect of site altitude on the overall array sensitivity. The second and third studies address two specific questions relating to the dynamic range of the pixels to be used in the cameras. Concentrating on the upper dynamic range, the second study examines the amplitude at which the camera pixels can be saturated before adversely affecting subarray performance. The third study investigates what effect changing the photo-electron to digital counts ratio has on subarray performance, within the context of the current analysis framework.

Chapter 5 presents the analysis results of observational data for the Crab and Vela pulsars recorded with the *Fermi* Large Area Telescope (LAT). A discussion of the data reduction and timing analysis is presented. This includes discussion of using the recommended binned likelihood method to derive the differential energy spectra for the Crab and Vela pulsars. These are compared with *Fermi's* published results as well as the latest results from both MAGIC and VERITAS. Finally, using the sensitivity performances derived in this research, the prospects for detecting pulsed gamma-ray emission with the CTA telescope system is also discussed. Finally, a summary of the research findings as well as future research work to be conducted is also given.

Chapter 1

The Gamma-ray Universe

The following chapter provides a brief introduction to the field of very high-energy gamma-ray astronomy. This includes discussion of cosmic-rays, gamma-rays and the different interactions that lead to the production of gamma-rays. Where applicable, theoretical models explaining the production mechanisms will be highlighted and examples provided, illustrating various objects within our known universe that are believed to produce gamma-rays. Attention will be given toward pulsars, how they might produce gamma-rays and why they are interesting astrophysical objects. Furthermore, some of the principal interactions that lead to gamma-ray absorption and attenuation are also discussed, as these interactions provide us with an opportunity for observing gamma-rays.

1.1 Cosmic-rays

Ionized nuclei incident upon the Earth are referred to as 'cosmic-rays'. The story of how these cosmic-rays were discovered, one hundred years ago, by Victor Hess in 1912 is well known [106]. His discovery of cosmic radiation later earned him a Nobel prize in physics [99].

It is believed that cosmic-rays (at GeV energies) are comprised of approximately 90% protons and 9% helium nuclei (α-particles) with the remaining 1% being electrons (e^-) [65].

Measurements of these cosmic-rays produce an energy spectrum that follows a broken power law distribution over an energy range spanning thirteen orders of magnitude. Figure 1.1 shows this cosmic-ray spectrum which suggests that from Earth we measure a flux of approximately 1 particle per metre squared per second at energies of approximately 10^{11} eV ($\sim$100 GeV) compared to a flux of less that 1 particle per kilometre squared per century at energies around 10^{20} eV (10^{11} GeV). Two distinctive features are illustrated called the 'knee' and the 'ankle'. It is widely believed that the likely progenitors of cosmic-rays are Supernova Remnants (SNRs) and other Galactic sources below the knee, Galactic and extra-galactic components between the knee and ankle, and an extra-galactic component such as Active Galactic Nuclei (AGN) above the ankle [106].

Cosmic-rays are extremely energetic charged particles that are affected by the magnetic field of the Sun [48] and indeed our host Galaxy the Milky Way. One interpretation of the knee feature in the cosmic-ray spectrum is that it represents the energy at which a particle's gyro-radius becomes too large for confinement within the Galactic magnetic field. Thus these particles are allowed to leak out of the Milky Way and explains why a falloff is observed in the cosmic-ray spectrum shown in Figure 1.1 [45]. Furthermore, the influence of these magnetic fields means that (with the exception of the highest energy cosmic-rays) they cannot be traced back to their origin.

The latest findings from the Pierre Auger Observatory [111] suggest that there may be a correlation between cosmic-ray events above 55 EeV within an angular separation of less than 3.1 degrees from AGN [104]. Attempts to confirm this with a larger set of data are currently underway.

Like all electromagnetic radiation, gamma-rays travel in straight lines and thus can be traced back to their origins. Given that gamma-rays are a by-product of particle acceleration, the observation of gamma-rays helps us to identify acceleration sites of cosmic-rays and gamma-ray astronomy plays a leading role in trying to better understand the acceleration mechanisms.
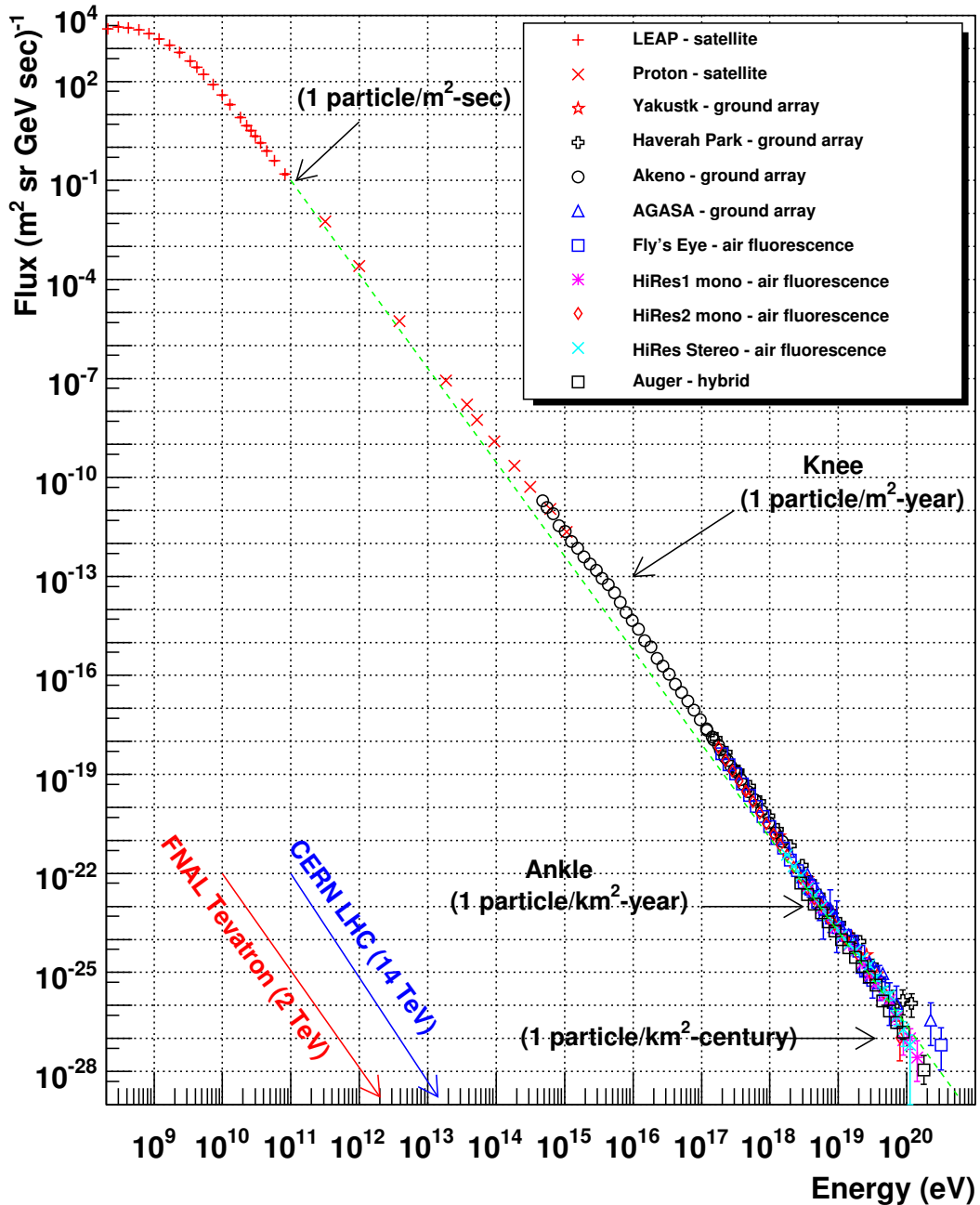
Figure 1.1: Shown here is the observed cosmic ray spectrum from 10^8 eV to 10^{20} eV [70]. This is an updated version of the famous Swordy.S [110] plot which shows a spectrum that follows a broken power law, the index of which changes at the two highlighted features called the "knee" and the "ankle". It is believed that supernova remnants can account for most of the very high-energy cosmic-rays below the knee. Cosmic-rays with energies between the knee and the ankle are assumed to originate from both Galactic and extra-galactic sources. Beyond the ankle it is thought that some extragalactic component (for example AGN) is involved. One interpretation of the knee feature in the cosmic-ray spectrum is that it represents the energy at which a particle's gyro-radius becomes too large for confinement within the Galactic magnetic field.

1.2 Gamma-rays

Gamma-rays are the most energetic form of electromagnetic radiation and the γ-ray waveband, in practice, includes photons whose energies are ≥ 100 keV [89]. At these energies gamma radiation has very small wavelengths ($\lambda \leq 0.01$ nm) and extremely high frequencies ($\nu \geq 3 \times 10^{19}$ Hz). Figure 1.2 illustrates the Fermi Gamma-Ray Space Telescope (*Fermi*) [11] all-sky survey after two years of operation. Here we see the gamma-ray sky at energies above 1 GeV and below 300 GeV where the colour intensity corresponds to the brightness of the gamma-ray source. This all-sky image clearly illustrates the diffuse glow prevalent along the Milky Way plane, but it also highlights the many discrete gamma-ray sources both close to and and away from the Galactic plane. Many of these sources are objects such as pulsars and supernova remnants, and how these objects produce gamma-rays is of great interest, particularly as strong magnetic fields and/or violent shock waves are required in order to accelerate relativistic particles to such high energies. Thus one of the key motivations for pursuing gamma-ray astronomy is that it enables us to study these extreme environments and hence enable us to better understand the particle acceleration mechanisms. Some of the mechanisms for producing gamma-rays are discussed in Section 1.3.

1.3 Gamma-ray production

Gamma-rays are produced in electromagnetic and hadronic interactions. During electromagnetic interactions, gamma-rays can be produced when electrons (and/or positrons) interact with either matter or radiation fields like in the strong magnetic fields of pulsars for example. In addition, gamma-rays can also be produced when hadrons interact with matter or when particles decay, for example the acceleration of protons in the shock fronts of supernova remnants.

Gamma-rays cannot be focused and it is only by the physical processes that attenuate gamma-rays which allow us to observe them, for example when a gamma-ray interacts with
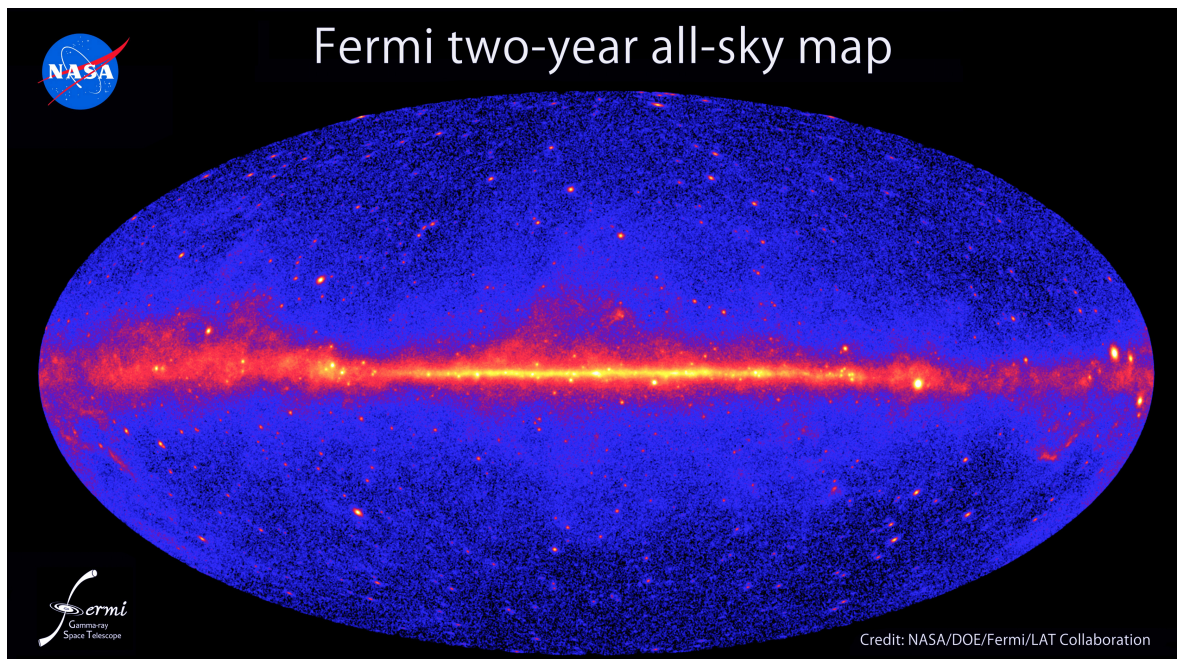
Figure 1.2: The all -sky image of gamma-rays above 1 GeV and below 300 GeV captured by the *Fermi* Gamma-Ray Space Telescope after 2 years of operation. The diffuse glow of gamma-rays emitted from the plane of our galaxy is clearly visible as is the many discrete gamma-ray sources close to and away from the galactic plane. Many of these gamma-ray sources are believed to be violent objects such as pulsars and supernova remnants.

matter or with other photons.

1.3.1 Electromagnetic interactions

1.3.1.1 Bremsstrahlung

Bremsstrahlung or 'braking radiation' was first noted, although in a different context, by Nicolas Tesla during the 1880s [89]. The process is identical to free-free emission and occurs when a particle is decelerated or deflected in the strong electric field of an atomic nucleus. In astrophysics this might occur when a relativistic electron passes through a gas or plasma and is decelerated suddenly over a small distance, resulting in an energy loss. Energy is conserved through the emission of radiation whose energy spectrum depends on the energy levels of the atomic electrons as well as the velocity with which the incident electron is travelling. Thus very high-energy gamma-rays can be emitted when an incident electron is travelling at relativistic speeds, where its kinetic energy (E) is much greater

than the rest mass energy of the electron. The Bremsstrahlung interaction process can produce photons with frequencies up to $\nu = \frac{E}{h}$ (where h is Plank's constant) and results in an intensity spectrum of gamma-rays following a power-law $N_\gamma(E) \propto E^{-\alpha}$ [89] where α is the 'spectral index'. Figure 1.3 illustrates the Bremsstrahlung interaction process.
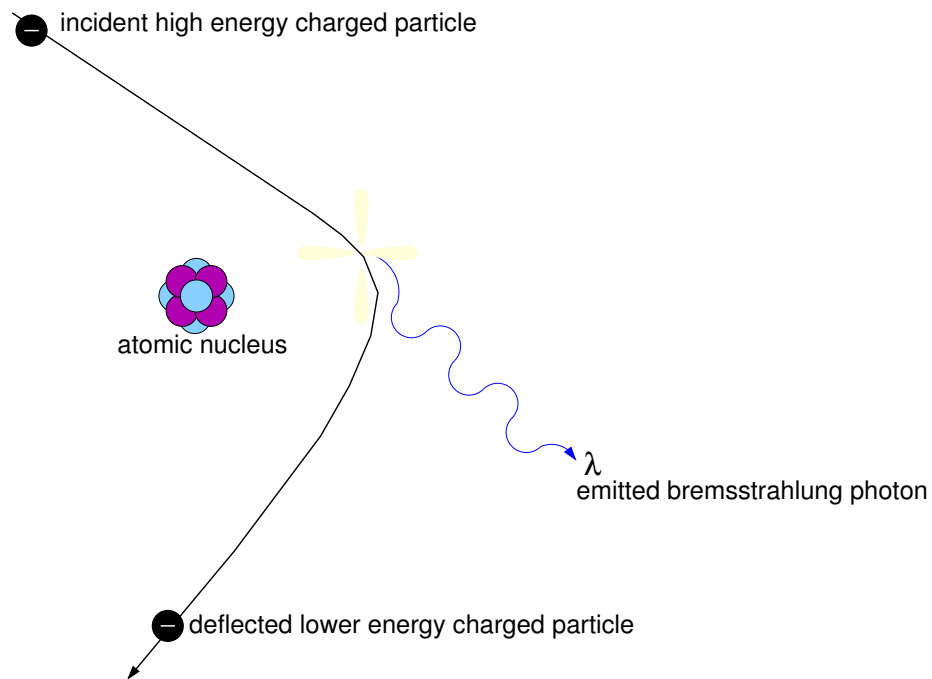
Figure 1.3: Bremsstrahlung Radiation [69] illustrated here occurs when a relativistic electron is decelerated over a very short distance in the strong electric field of an atomic nuclei. The electron loses energy and is deflected during the interaction which also results in the emission of a photon.

In addition to being an interaction process responsible for electron accelerated gamma-ray sources, for ground-based gamma-ray astronomy, Bremsstrahlung is also the process that produces secondary photons in electromagnetic air showers. Air showers and the importance of Bremsstrahlung stopping power will be discussed in Section 2.2.1.

1.3.1.2 Inverse Compton scattering

When a photon interacts with an electron or any other charged particle, as illustrated in Figure 1.4, the photon transfers some of its energy to the electron and the result is a scattered photon with lower energy and longer wavelength. Also known as the Compton effect; the transfer of energy is often expressed as a change in frequency or wavelength [89].

For the case of a photon scattering off a stationary electron we can estimate the change in energy as shown in Equation 1.1

$$\Delta E = \frac{E_{primary}E_{scattered}}{m_e c^2}\left(1 - \cos\theta\right) \tag{1.1}$$

where ΔE is the resulting change in energy, $E_{primary}$ is the energy of the incident photon with wavelength λ_i, $E_{scattered}$ the energy of the scattered photon with wavelength λ_f, m_e the mass of the electron, c the speed of light and θ the scattering angle.
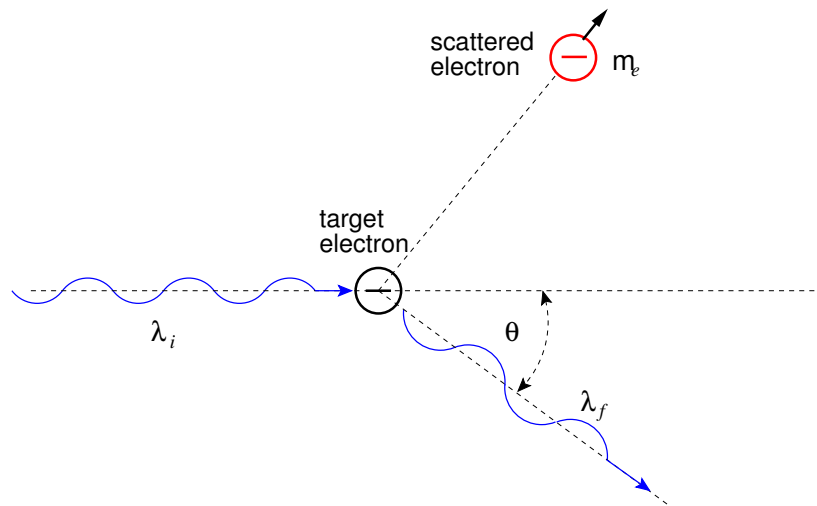
Figure 1.4: When a high-energy photon scatters off an electron, the photon transfers some of its energy to the electron. Called Compton scattering, this interaction process results a scattered photon with increased wavelength and hence lower energy. The incident photon has a wavelength λ_i and the scattered photon a wavelength λ_f. The electron mass is m_e and the scattering angle θ. Adapted from [114].

In the case where a relativistic electron collides with a low-energy photon, from an ambient field for example, the photon is up-scattered to higher energies. This is the exact opposite of the Compton scattering interaction highlighted above. This is an important gamma-ray production mechanism and it is widely believed that this is the primary process giving rise to the high-energy part of the double-hump spectral energy distribution commonly found for the blazar class of AGNs. Figure 1.5 illustrates this interaction process. It is also believed that this is an important gamma-ray production mechanism for pulsars.

During the inverse Compton interaction (see Figure 1.5), the head-on collisions suggest the

Rest Frame:

$E \approx \gamma E_0$

$E \approx \gamma E_0$

Laboratory Frame:

$E = E_0$

$E \approx \gamma^2 E_0$
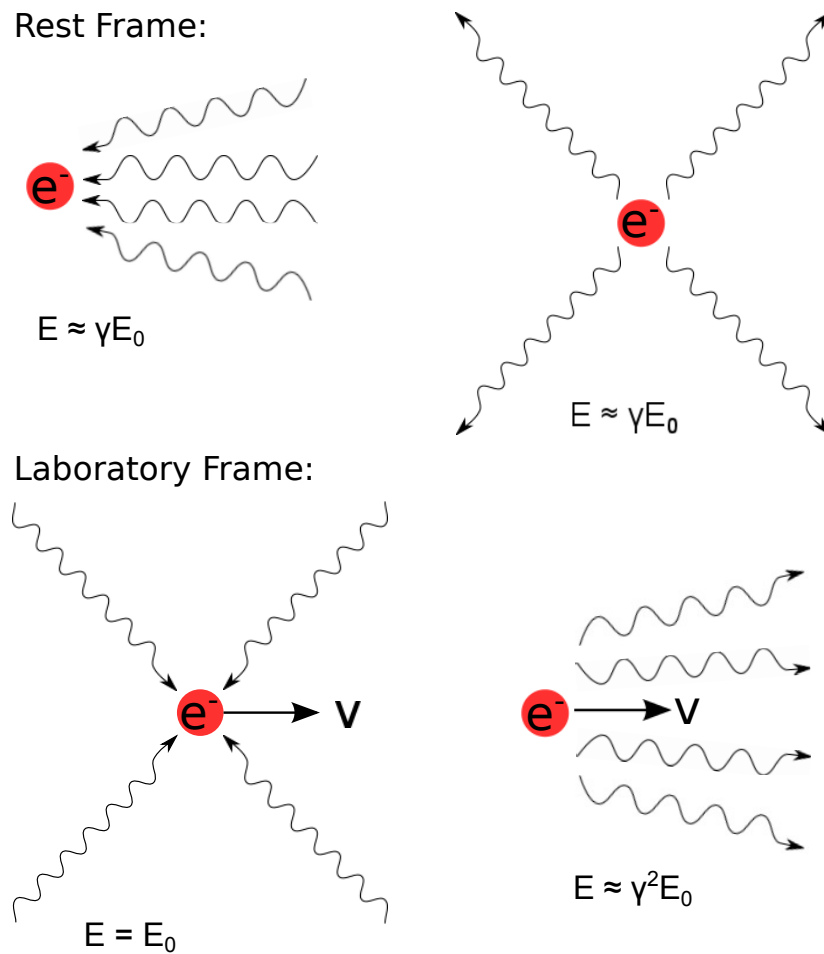
Figure 1.5: When a relativistic electron collides with a low-energy photon, the photon is up-scattered to higher energies. Known as inverse Compton Scattering, this process is the exact opposite of the Compton Scattering effect where the photon transfers some of its energy to the electron. This is an important gamma-ray production mechanism and it is widely believed that this is the primary process giving rise to the high-energy part of the double-hump spectral energy distribution commonly found for blazars.

photon energy is given by the centre-of-momentum frame and hence the scattered energy is now shown in Equation 1.2.

$$E_{\text{scattered}} \approx \gamma E_{\text{primary}} \left(1 + \beta \cos\theta \right) \tag{1.2}$$

where $\beta = \frac{v}{c}$, v is the velocity and c the speed of light. Thus when we change back to the observer's frame of reference the result is very high-energy photons with an energy gain proportional to γ^2 [89].

1.3.1.3   Synchrotron & curvature radiation

Synchrotron radiation is emitted when relativistic electrons are deflected by magnetic fields. In astrophysics, this is the most common interaction for producing non-thermal radiation, particularly x-rays. As the relativistic electrons follow the curved field lines, they radiate an electromagnetic field forwards in a beamed cone i.e. in the direction of the electron's velocity.
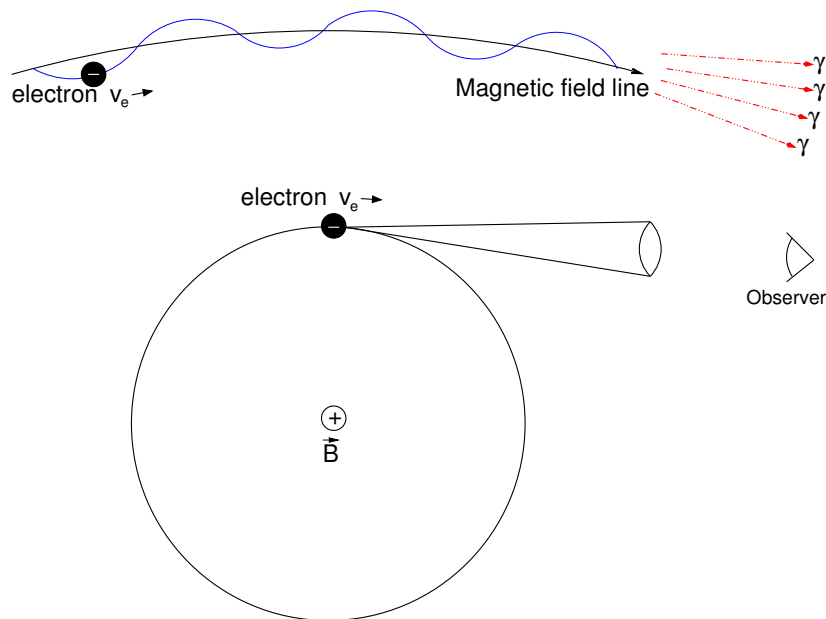
Figure 1.6: Synchrotron radiation occurs when a relativistic electron with velocity v_e is confined to travel along the magnetic field lines $\vec{B}$ of an object. The electron emits synchrotron radiation which is beamed forward in a cone.

Synchrotron radiation is linearly polarised in the plane of the circular motion and the beaming effect which results enables astronomers to detect many x-ray sources. Indeed this beaming effect makes synchrotron sources the brightest known x-ray sources in astronomy. Some of the sources seen emitting synchrotron radiation include AGNs, SNRs and pulsar wind nebulae (PWNs). Neutron stars with unusually strong magnetic dipole fields $10^{14} - 10^{15}$ G, sometimes called Magnetars [57], are also synchrotron emitters. Synchrotron radiation can be observed over a wide range of energies i.e. from radio through to x-rays. Figure 1.7 shows a composite image of the synchrotron emission emitted by the supernova remnant G21.5-0.9 in the radio (blue) and x-ray (pink) wavelengths.

Pulsars, too, are seen to produce both synchrotron and curvature radiation [114]. Curvature radiation occurs when the electron's motion is confined along the very strong magnetic field lines and is linearly polarised in the plane of the curved field lines [48]. The non-relativistic case is called cyclotron radiation.
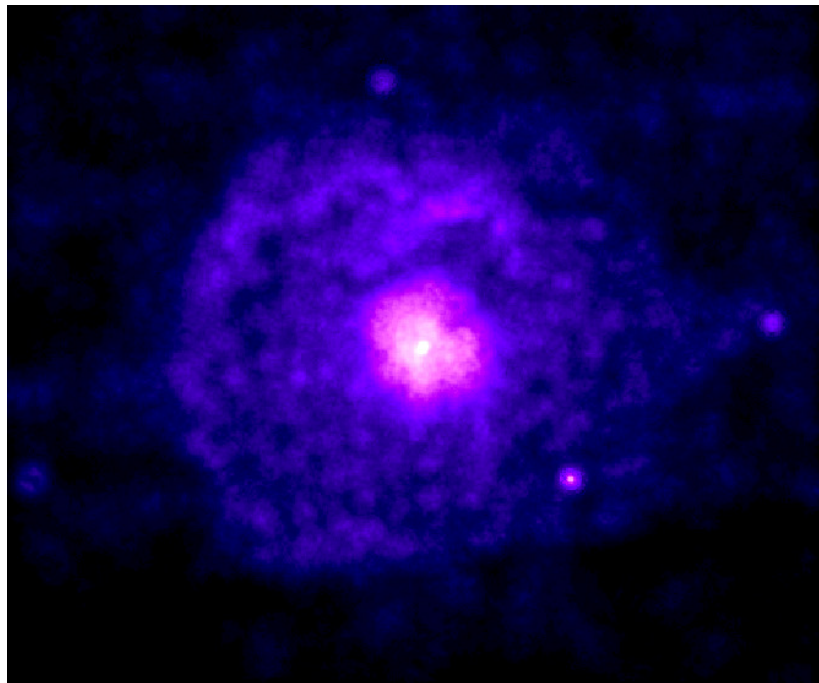
Figure 1.7: This is a composite image of the supernova remnant G21.5-0.9 which is believed to have once been a massive star that exploded $\sim$ 40,000 years ago. This image was created from observations taken in the radio (blue) and x-ray (pink) wavelengths and illustrates the synchrotron emission generated by high-energy electrons spiralling around the magnetic field lines. It is believed that the high-energy electrons are produced by a rapidly rotating neutron star. Credit NASA/CXC/SAO

Synchrotron sources are expected to follow a power law energy spectrum shown in Equation 1.3 where A is a constant and α is the 'spectral index' [49].

$$I\left(E\right) = AE^{-\alpha} \tag{1.3}$$

1.3.1.4 Synchrotron Self Compton model

Within gamma-ray astronomy synchrotron sources often provide an indication for the potential of very high gamma-ray emission. These sources are believed to provide the lower energy radiation which can be up-scattered by inverse Compton processes. This gamma-ray production mechanism is described by the synchrotron self Compton model (SSC). Figure 1.8 illustrates the spectral energy distributions (SEDs) for seven different blazars including Markarian 421 (Mkn 421) which is an active galaxy $\sim$ 400 million light years from Earth within the constellation of Ursa Major. The SEDs for these sources demonstrate the double-hump feature of the SSC model, synchrotron emission (first peak) and inverse Compton emission (second peak) [66]. It is believed that sources like Mkn 421 produce gamma-rays via the SSC process.

1.3.2 Hadronic interactions

As well as the electromagnetic interactions highlighted in 1.3.1, gamma-rays can be produced from hadronic interactions. For example, when high-energy protons collide with matter, for example interstellar gas, this physical interaction produces both charged and neutral pions as shown in Equation 1.4.

$$p + nucleus_{gas} \rightarrow nucleus_{anything} + \Pi(\pi^{+}; \pi^{-}; \pi^{0}) \tag{1.4}$$
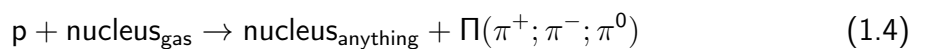
Pions of all charges are produced in almost equal number, except at lower energies where the π^{+} is favoured [88]. In astrophysical sources like supernova remnants that produce
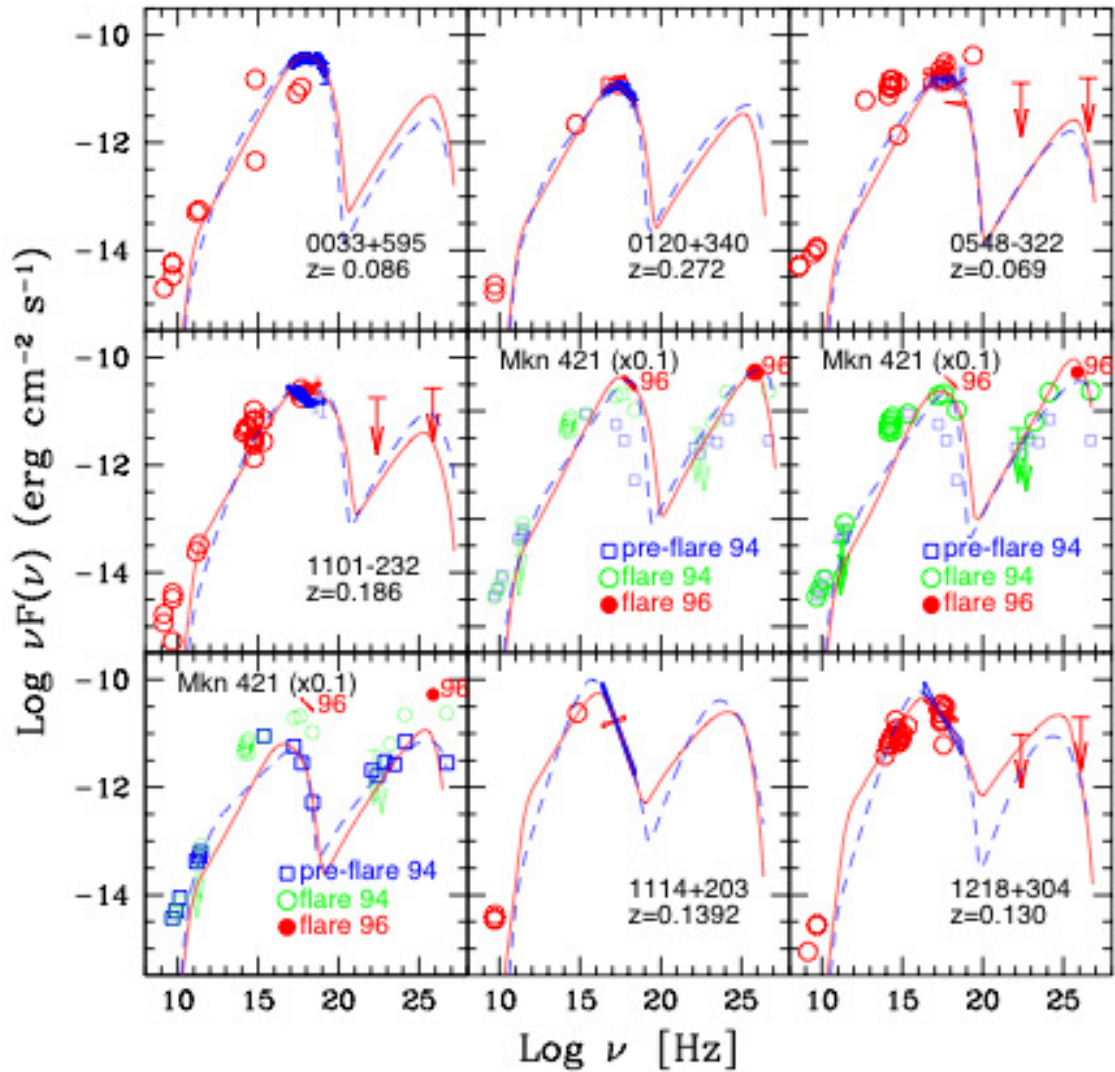
Figure 1.8: Illustrated here are the spectral energy distributions for a number of blazar AGNs. The SEDs for these sources demonstrate the double-hump feature of the SSC model where the first peak is believed to be as a result of synchrotron emission and the second peak due to inverse Compton scattering. It is believed that sources like Mkn421, shown here, produce gamma-rays via the SSC process. [66]

energetic shock fronts, it is believed that protons are accelerated to high energies and then interact with the nuclei of the interstellar medium producing pions of all charges. The neutral pions produced in such interactions then decay into very high-energy gamma-rays as shown in Equations 1.5 and 1.6. However these decay processes are not equally likely.

$$\pi^0 \rightarrow \gamma\gamma \tag{1.5}$$

$$\pi^0 \rightarrow \gamma + e^+ + e^- \tag{1.6}$$

It is suggested that much of the diffuse gamma-ray emission illustrated in Figure 1.2 results from the neutral pion decay process.

1.4 Gamma-ray absorption & attenuation

Section 1.3 presented some of the key astrophysical gamma-ray production mechanisms. This section will now focus on how gamma-rays are absorbed or attenuated.

1.4.1 Pair production $\gamma\gamma$ interactions

When gamma-ray photons collide with other photons they can be attenuated. When these interactions occur, matter is produced in the form of electron positron pairs as shown in Equation 1.7.

$$\gamma + \gamma \rightarrow e^- + e^+ \tag{1.7}$$

The required energy threshold for pair production by $\gamma\gamma$ interactions is shown in Equation 1.8:

$$E_{\text{threshold}} \geq 2m_e c^2 \tag{1.8}$$

where m_e is the rest mass energy of an electron and c is the speed of light. Given that the rest mass energy of an electron is 511 keV, the threshold energy for pair production must be greater than or equal to 1.022 MeV. Thus provided energy and momentum are conserved, gamma-ray photons are ideal candidates for pair production.

1.4.2 Pair production γ + matter interactions

When gamma-rays collide with matter they can interact in the field of atomic nuclei to produce electron positron pairs. Pair production from such $\gamma+$ matter interactions is shown in Equation 1.9 and Figure 1.9 provides a simple sketch of the pair production process.

$$\gamma + \text{nucleus} \rightarrow e^- + e^+ + \text{nucleus} \tag{1.9}$$
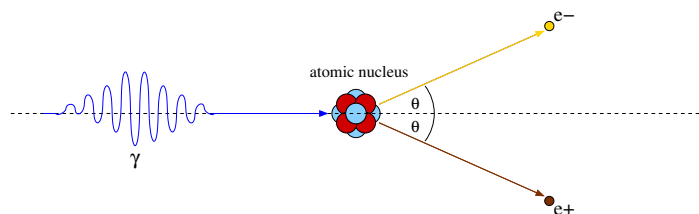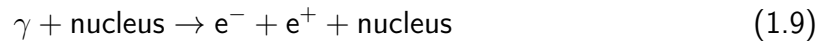
Figure 1.9: Pair Production: When a high-energy photon collides with the nucleus of an atom electron positron pairs are created. These physical processes are responsible for attenuating much of the gamma radiation incident on the Earth. Such interactions occur with atmospheric nuclei making it very unlikely for gamma radiation to reach the ground.

Gamma-rays are able to propagate from their source to the Earth because there is a relatively small amount of matter along their path. However, when a gamma-ray enters the Earth's atmosphere the density of matter increases substantially and gamma-rays are attenuated. It is via these physical processes that gamma-rays incident on the Earth interact with atmospheric nuclei to produce electron positron pairs and hence electromagnetic air showers. It is these secondary products of the $\gamma+$ matter interactions that we are able to

detect and which are used to infer the energy of the primary photon. The observational techniques that take advantage of this natural phenomenon are discussed in Chapter 2.

Before discussing how very high gamma-rays can be detected, the sections which follow will focus on pulsars. This includes highlighting some of their key characteristics as well as how they might produce gamma-rays.

1.5   Gamma-rays from pulsars

Pulsars were discovered by Jocelyn Bell & Anthony Hewish in 1967 using 2048 radio dipole antennae tuned to a frequency of 81.5 MHz [48]. Bell discovered a periodic signal that passed overhead at intervals of exactly 1 sidereal day and this convinced her that the source was not from within the solar system. The periodic signal, or radio pulses, occurred with an extremely regular rate of one pulse every 1.33730113 seconds[116]. Bell confessed that both she and her supervisor Anthony Hewish considered the possibility that the signal originated from 'little green men'. However the discovery of a second periodic signal of a different rate and from a completely different location on the sky convinced both Bell and Hewish that the source of the signal was indeed astrophysical and not alien. Since these humble beginnings much work has been conducted in detecting pulsed radio signals from stars and to date there are >1800 known pulsars. Pulsars are well-studied objects with certain characteristics that have enabled astronomers to build a coherent model of the stars responsible for emitting pulsed radiation. Figure 1.10 illustrates the averaged pulsed radio signal recorded for a set of known pulsars. The average pulse period for this distribution is approximately 0.38 seconds. However, with the majority of pulsars having a period between 0.2 and 5 seconds >100 objects have millisecond periods. This distribution of pulsar periods suggests that two different classes of pulsar exist: the millisecond pulsars and the normal pulsars. Using only the period information it is not exactly clear where the two pulsar classes are defined, and the millisecond name is somewhat misleading because it is possible for a young normal pulsar, like the Vela pulsar, to have a millisecond period.

This is discussed further in Chapter 5.

The distribution of known radio-loud pulsar periods
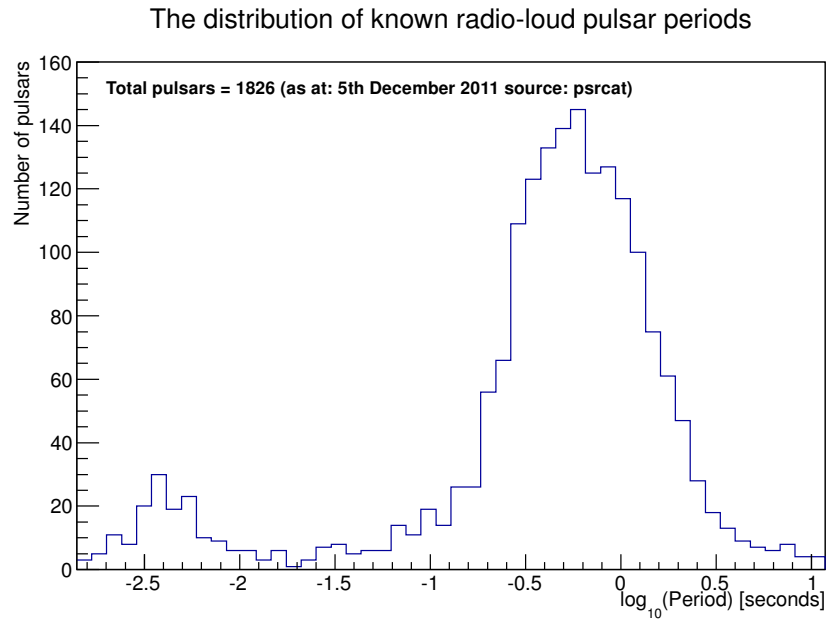
Figure 1.10: The distribution of known radio-loud pulsar periods as at 5th December 2011 [91].

For any given pulsar the period between pulses occurs with extremely high accuracy, better than one part in 10^8 [116]. The amount of energy in a pulse can vary hugely and the intensity and shape of the pulses vary from pulse to pulse. However, the averaged pulse recorded over many pulses for a single pulsar defines the pulsar's pulse shape and is very stable [109]. Thus the pulse shape may consist of a single peak, a double peak or possibly even more peaks. Another characteristic of radio-loud pulsars is that all their periods are increasing i.e. the frequency of their pulses is gradually slowing down. This slow-down rate is called the period derivative, $\dot{P} = dP/dt$. The ratio of the pulsar's period and its period derivative provides an estimate of the pulsar's characteristic lifetime i.e. the length of time until the pulsar stops assuming the period derivative remains constant. The final characteristic of known radio-loud pulsars, is the measurement precision to which their pulses occur. For example, the period of pulsar B1937+21 has been determined to be 1.557806468819794 milliseconds [81]. Such precise measurements require the best atomic clocks.

Pulsars emit a broadband energy spectrum from radio wavelengths to gamma-rays. Figure

1.11 illustrates a pulsar sky map in Galactic coordinates from the *Fermi* 1 year pulsar catalogue [17]. Shown are the many radio loud-pulsars (black and grey dots), gamma-ray detected millisecond pulsars (red triangles) and normal gamma-ray pulsars (blue squares and green dots). It appears that the density distribution of pulsars is highest close to the Galactic plane except for the gamma-ray detected millisecond pulsars.
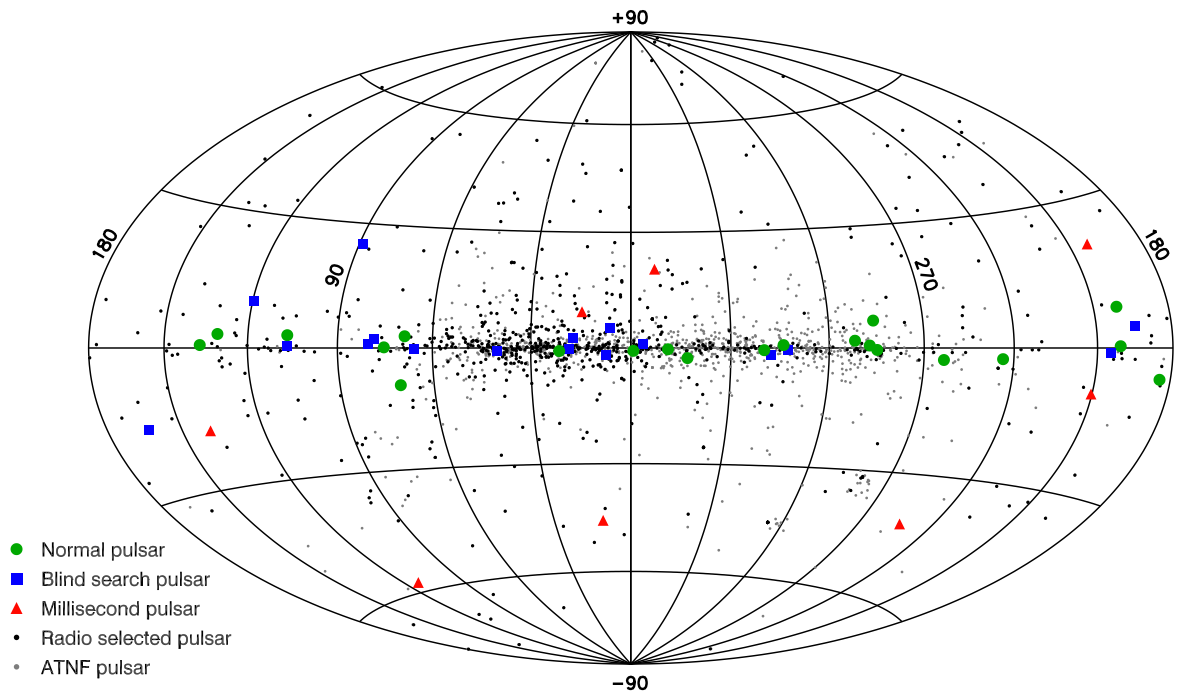
Figure 1.11: Sky map of known radio-loud and gamma-ray detected pulsars in Galactic coordinates. Shown are the many radio-loud pulsars (black and grey dots), *Fermi* detected gamma-ray millisecond pulsars (red triangles), *Fermi* detected normal gamma-ray pulsars (green dots) and *Fermi* blind-search detected gamma-ray pulsars (blue squares). It appears that the density distribution of pulsars is highest close to the Galactic plane except for the gamma-ray detected millisecond pulsars. [17].

1.5.1   Pulsar spin-down luminosity

The known pulsars highlighted in the previous section are *radio pulsars*, and strictly speaking these objects should be called *rotation-powered neutron stars* as it is widely accepted these objects are rapidly rotating neutron stars as first suggested by Gold [67]. For convenience the generic term *pulsar* is used. The power generated by this rapid rotation can be seen either as the pulsed radiation highlighted above or as nebular emission. The nebular emission

results from a relativistic wind of particles which are emitted from the neutron star. Not all pulsars exhibit nebular emission, but consideration of these different components must be taken into account when studying such objects. This is discussed further in Chapter 5.

Over the course of its characteristic lifetime, a pulsar loses rotational kinetic energy. When considering the total power (energy budget) generated by a pulsar, the radio emission seen from these objects is energetically insignificant ($\sim 10^{-6}$) when compared to the high-energy emission ($\sim 10^{-3}$) [82]. Often this rate of energy loss ($\dot{E}$) is also called spin-down energy, spin-down power or spin-down luminosity (L_{sd}) and is show in Equation 1.10

$$\dot{E} \equiv L_{sd} \equiv I_{ns}\omega\dot{\omega} \equiv -\frac{4\pi^2 I_{ns}\dot{P}}{P^3} \tag{1.10}$$

where I_{ns} is the neutron star's moment of inertia typically assumed to be $I_{ns} \approx 10^{45}$ [g cm^2] [92]., P the measured period, $\dot{P}$ the measured period derivative and ω the angular frequency where $\omega \equiv 2\pi/P$. Thus by recording a pulsar's period and period derivative it is possible to estimate the total available spin-down luminosity independently of any models. For example, using the values listed in Table 1.1, the spin-down luminosity for the Crab and Vela pulsars are found to be $\dot{E}_{Crab} = 4.3 \times 10^{38}$ erg s^{-1} and $\dot{E}_{Vela} = 6.6 \times 10^{36}$ erg s^{-1} respectively.

Table 1.1: Pulsar values.

Pulsar	I_{ns}	P	$\dot{P}$
Crab	1.0×10^{45} g cm^2	33.6 ms	4.2×10^{-13} s s^{-1}
Vela	1.0×10^{45} g cm^2	89.3 ms	1.2×10^{-13} s s^{-1}

1.5.2 Pulsar particle acceleration

It is widely accepted that spin-down luminosity is carried away by magnetic dipole radiation which is emitted at a given frequency Ω shown in Equation 1.11

$$\dot{E}_{dipole} = -\frac{B_p^2 R^6 \Omega^4 \sin^2 \alpha}{6c^3} \tag{1.11}$$

where B_p is the pure magnetic dipole field at the neutron star pole, R is the neutron star radius and α is the angle offset between the magnetic dipole moment and the neutron star spin axis. Equating $\dot{E}$ with $\dot{E}_{dipole}$ the magnetic field is then inferred from Equation 1.12 to be [92]

$$B = 1.3 \times 10^{19} (P\,\dot{P})^{1/2}\ [\mathrm{G}] \qquad (1.12)$$

where P is the measured period and $\dot{P}$ the measured period derivative. It is believed that particle acceleration inside the pulsar magnetosphere gives rise to pulsed non-thermal radiation [82] and thus astronomical observations of the pulsed gamma-rays originating from pulsars provide a direct probe into the particle acceleration mechanisms. Various models exist that propose to explain the high-energy emission from pulsars such as the polar-cap model [71], the slot-gap model [31], the outer-gap model [103] and the two-pole caustic model [58]. These models are generally categorised as either polar-cap models or outer-gap models. The main difference being that for polar-cap models, particle acceleration occurs close to the star surface near the poles; whereas for outer-gap models the acceleration region is close to the pulsar's light cylinder defined in Equation 1.13 [92]

$$R_{LC} = \frac{c}{P/2\pi} \qquad (1.13)$$

where c is the speed of light and P is the measured period. The geometry illustrating these acceleration regions is shown in the next section.

1.5.3   Pulsar high-energy emission geometry

Figure 1.12 shows a sketch of the pulsar high-energy emission geometry which includes a rapidly rotating neutron star that has a very strong dipole magnetic field. A key feature of this basic model is the angular offset α between the star's rotation axis Ω and its magnetic field axis B. It is believed that charged particles are accelerated within the

star's co-rotating magnetosphere and high-energy radiation is emitted via the curvature, synchrotron and inverse Compton scattering processes. The last closed magnetic field line defines the light-cylinder radius R_{LC}.
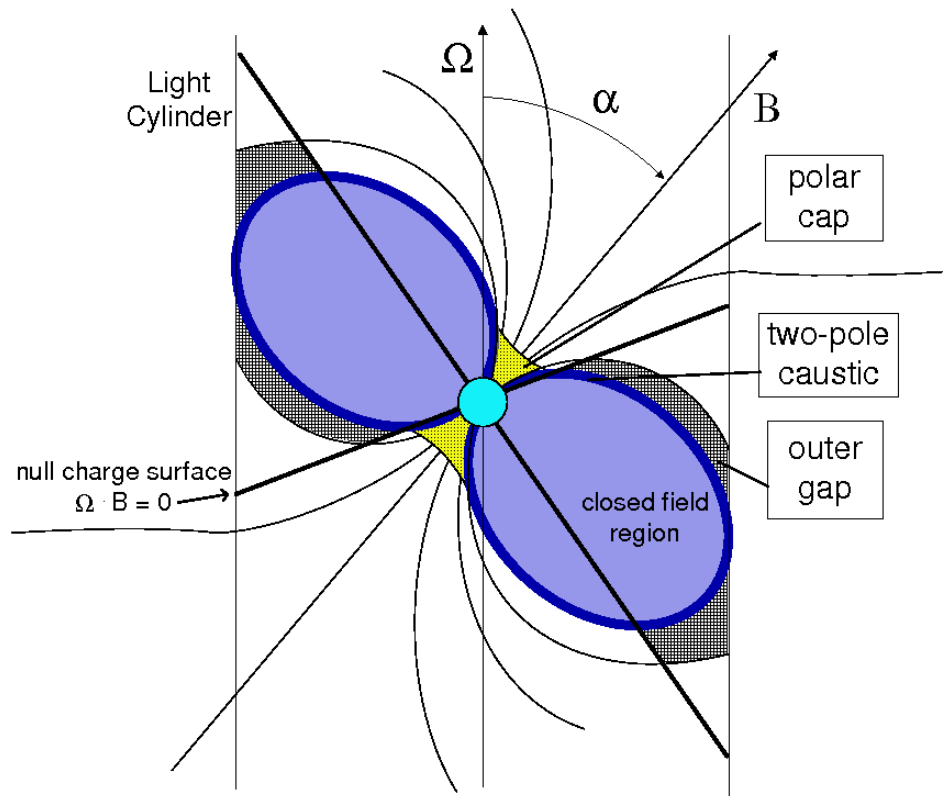
Figure 1.12: Simple sketch of the pulsar high-energy emission geometry illustrating a magnetic pole axis B misaligned by angle α with respect to the pulsar's rotational axis Ω. Also highlighted is the polar-cap, the outer-gap and the two-pole caustic acceleration regions. Image adapted from [82]

All the models struggle to produce the non-thermal off-pulse emission detected over the full pulse phase for gamma-ray emitters like the Crab and Vela [82]. Despite this, the latest findings from *Fermi* suggest that many of their pulsar detections seem to favour the outer-gap models which propose the high-energy emission mainly originates from curvature radiation of electrons [17]. However, there is still a large degree of uncertainty in the specifics of the physical processes that produce broadband non-thermal radiation in a pulsar's magnetosphere. For example it is suggested by Kaspi et al. [82] that differences between the models occur in the assumed geometry of the pulsars and only better ob-

servations with more sensitive instruments will help to better understand the acceleration mechanisms of pulsars.

Chapter 2

Gamma-ray Astronomy

The following chapter will discuss how very high-energy gamma-rays can be detected both from the surface of the Earth and from satellites. Gamma-rays can be detected only indirectly using the products of the interactions discussed in Section 1.4. Consideration of extensive air showers and the generation of Cherenkov radiation will be made. The imaging atmospheric Cherenkov technique will be highlighted including the Hillas parameterisation method and other relevant stereoscopic and shower reconstruction techniques.

2.1   Space-based observations

The Earth's atmosphere is opaque to electromagnetic radiation with energies above ~ 1 eV. As a consequence, high-energy astronomy has to be conducted above the Earth's atmosphere. Unfortunately conducting experiments above the atmosphere imposes restrictions and is costly; for example the *Fermi* gamma-ray space telescope cost a total of $ 690 million (USD) [44]. Space-based gamma-ray detectors use similar technologies to those found in traditional particle physics experiments, but there are greater restrictions on the size of the detectors. For example, the *Fermi* satellite is approximately 2.8 metres high and with a diameter of 2.5 metres has a maximum effective area of ~ 0.8 m^2 at 100 GeV. Figure 2.1 shows the *Fermi* LAT effective area as a function of energy for photons of normal incidence

onto the detector.

Fermi - Effective Area at normal incidence cos(θ)>0.975 (P7SOURCE_V6 18/10/2011)
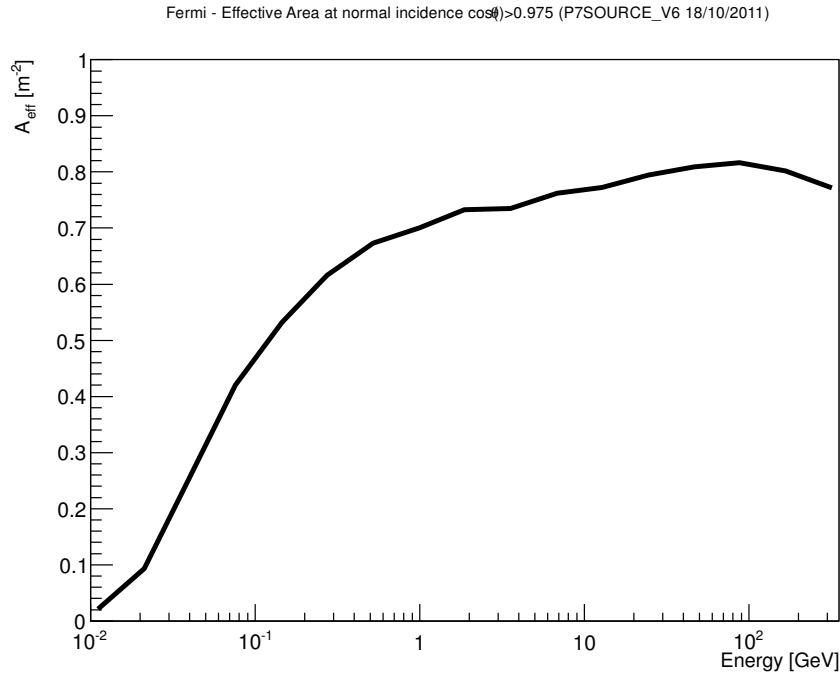
Figure 2.1: The total effective area (black line) of the *Fermi* LAT as a function of energy for photons of normal incidence onto the detector i.e. $\mathrm{Cos}(\theta) > 0.975$. [101]

Relative to ground-based detectors, this is very small and limits the instrumental sensitivity and hence detectable gamma-ray fluxes. However a major benefit of placing a detector like *Fermi* in orbit around the Earth, is that the instrument has a very large field of view ($>$ 2 steradians) allowing astronomers to see nearly the whole visible sky as the instrument is not constrained to a static point with respect to the Earth. The *Fermi* satellite has two primary detectors, the gamma-ray burst monitor (GBM) and the large area telescope (LAT). The GBM is sensitive to x-rays and gamma-rays in the approximate energy band 8 keV to 40 MeV and its primary purpose is for detecting transient sources. This instrument will not be discussed any further in this thesis, but further information can be obtained in Lichti et al. [87]. The LAT is sensitive to gamma-ray photons in the approximate energy range 20 MeV $\lesssim$ E $\lesssim$ 300 GeV and its primary scientific goals are to better understand the astrophysics mechanisms that accelerate charged particles in sources like AGNs, SNRs and pulsars as well as study the diffuse Galactic gamma-ray emission, gamma-ray bursts and other transient gamma-ray sources. In addition, *Fermi* is trying to determine the nature

of the many still-unidentified sources discovered by the EGRET detector [93]. The LAT detector comprises three main systems; a silicon-strip tracker [32], a calorimeter [79] and an anti-coincidence detector (ACD) [93]. Figure 2.2 shows a cross-section sketch of the *Fermi* LAT detector illustrating the basic concept of gamma-ray detection based on the physical processes outlined in Section 1.4.2.
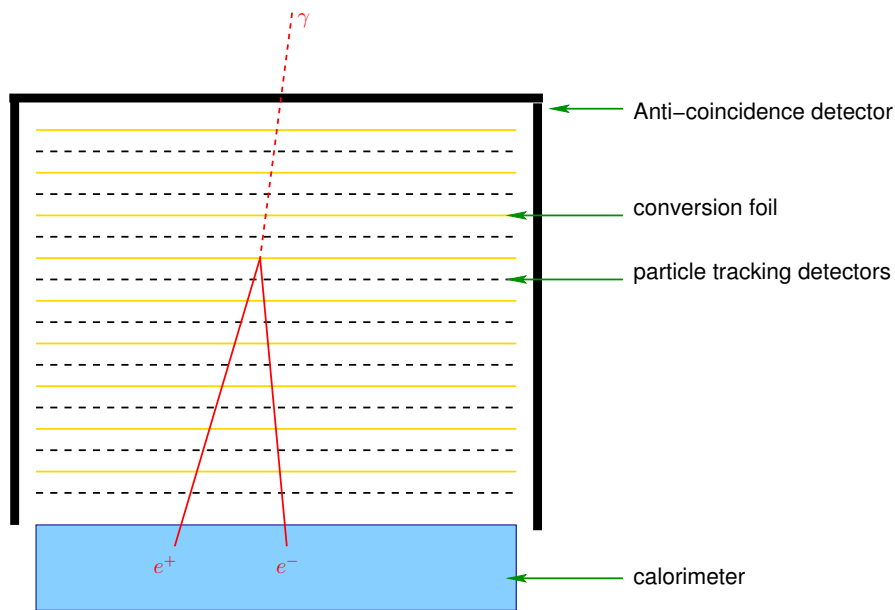
Figure 2.2: Sketch illustrating the basic detector systems of the *Fermi* LAT [79]

2.1.0.1   *Fermi* background rejection

The *Fermi* LAT performs background rejection by means of an anti-coincidence detector (ACD). The ACD acts as a shield which helps to block out the cosmic-ray background encountered in space-based detectors. The ACD covers the top and all four sides of the *Fermi* LAT detector and the goal of the ACD is to restrict any residual background cosmic-rays to $\lesssim 10$ % of the diffuse gamma-ray background intensity [93]. Having a physical shield that actively rejects the charged cosmic-ray background is another major benefit of conducting high-energy astronomy experiments above the atmosphere as no additional event reconstruction techniques are needed to separate the signal from background which could introduce a larger systematic uncertainty.

2.1.0.2 *Fermi* angular resolution

The *Fermi* LAT angular resolution performance is shown in Figure 2.3. Here angular resolution is defined as the angular distance containing 68% of the reconstructed photon directions which is the same definition used for ground-based Cherenkov telescopes discussed further in Section 3.4. It is clear that there is a very strong energy dependence on the reconstructed gamma-ray direction for photons detected with this instrument. The work presented in Chapter 5 discusses how this energy dependent angular resolution effects the gamma-ray photon selection procedure implemented for analysing *Fermi* pulsar data. Furthermore, it appears that the best spatial resolution achievable with *Fermi* is approximately 0.2 degrees ($\sim$12 arc-minutes) at 100 GeV. This is nearly a factor 2.5 larger than can be achieved with a next-generation ground-based Cherenkov telescope as shown in Chapter 3.
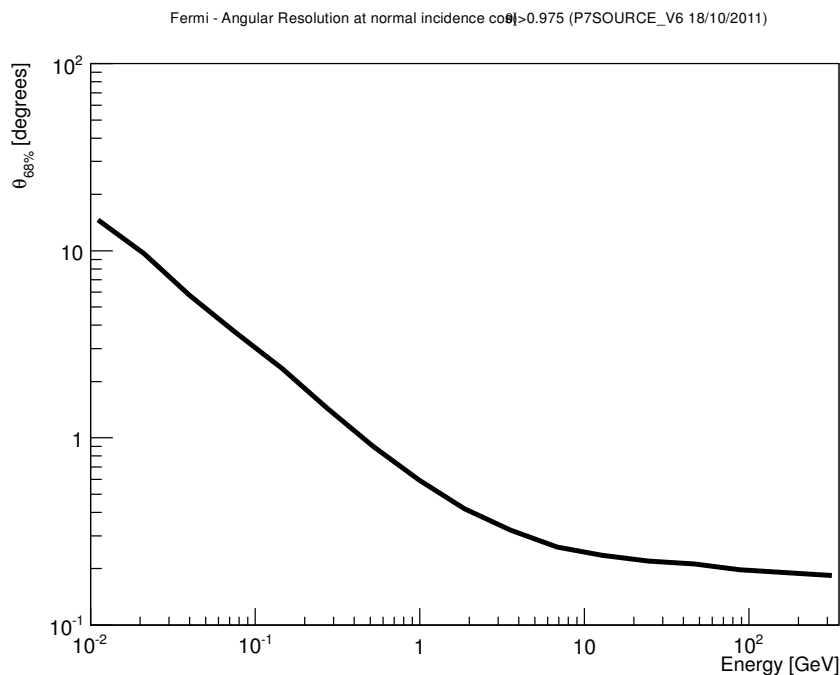
Figure 2.3: Angular resolution of the *Fermi* LAT as a function of energy (black line) for photons of normal incidence onto the detector i.e. Cos(θ) > 0.975. [101]. Here angular resolution is defined as the angular distance containing 68% of the reconstructed photon directions which is the same definition used for ground-based Cherenkov telescopes discussed further in Section 3.4. There appears to be a strong energy dependence that needs to be considered when analysing *Fermi* data.

2.1.0.3 *Fermi* energy resolution

The energy resolution of the *Fermi* LAT is shown in Figure 2.4 and Equation 2.1 shows how this is defined.

$$\frac{\Delta E}{E} = \frac{E_{reconstructed} - E_{true}}{E_{true}} \tag{2.1}$$

It appears as though *Fermi* can reconstruct the photon energy to within 10% of the true photon energy between energies of a few hundred MeV to ~ 100 GeV. This is better than the energy resolution achievable ($\sim 16.5\%$ at 100 GeV) with a next-generation ground-based Cherenkov telescope as shown in Chapter 3.
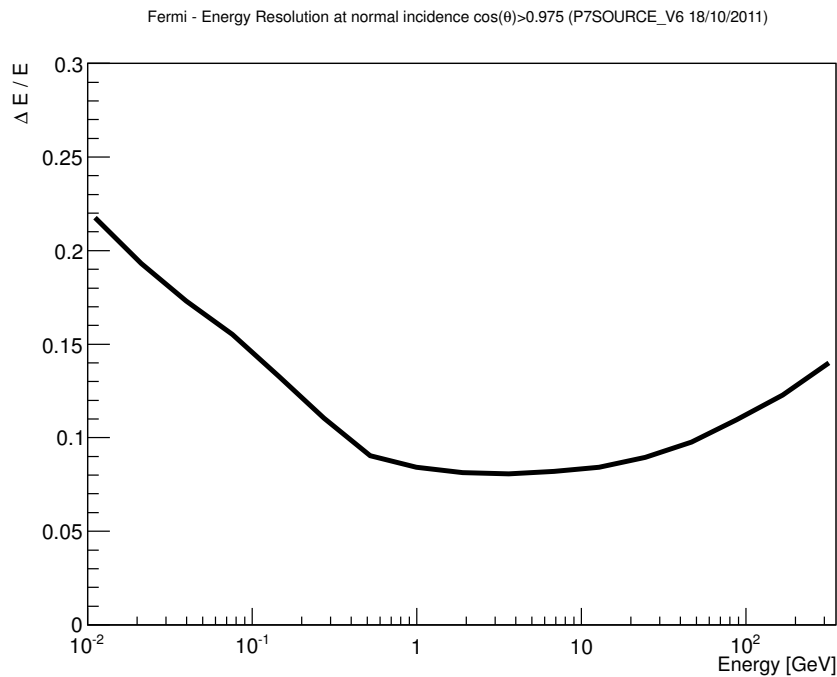
Figure 2.4: Energy resolution of the *Fermi* LAT as a function of energy (black line) for photons of normal incidence onto the detector i.e. $\text{Cos}(\theta) > 0.975$. [101].

2.2 Ground-based observations

As mentioned above, at the highest photon energies it is possible to observe gamma-rays from the ground. As with space-based detectors, gamma-rays can only be observed by

ground-based detectors through the secondary products of their attenuation when they interact with matter (Section 1.4.2). However, unlike space-based detectors, ground-based detectors do not need to construct the interacting media; instead, the atmosphere becomes the medium within which the gamma-ray interacts and attenuates.

When a gamma-ray enters the Earth's atmosphere it interacts within the Coulomb field of the atmospheric nuclei and, via the physical processes highlighted in Chapter 1, the gamma-ray produces an electron positron pair which also interacts with the atmosphere, causing a cascade effect and resulting in an electromagnetic air shower. It is the Cherenkov light produced by these secondary electromagnetic air showers that can be observed from the ground using the imaging atmospheric Cherenkov technique (IACT). A few notable experiments that implement the IACT, the High-Energy Stereoscopic System (H.E.S.S.) [9], the Major Atmospheric Gamma-ray Imaging Cherenkov (MAGIC) [12] and the Very Energetic Radiation Imaging Telescope Array System (VERITAS) [13] have helped to establish this field of ground-based astronomy. The discoveries made by these ground-based gamma-ray experiments have furthered our understanding of the technique itself as well as the violent objects in our universe that produce very high-energy gamma-rays.

2.2.1 Extensive air showers

Extensive air showers (EAS) form within the Earth's atmosphere when cosmic-rays enter the atmosphere and interact with the nuclei of atmospheric atoms. Cascades of charged secondary particles are produced via the physical processes highlighted in Chapter 1 and these secondary particles also interact with atmospheric nuclei. Two primary interactions that initiate EAS are presented in the following sections.

2.2.1.1 Gamma-ray air showers

Very high-energy gamma-rays entering the Earth's atmosphere can initiate an air shower by pair production. For the cascade to continue, the resulting electron positron pairs need an

energy > 20 MeV which is the critical energy for pair production. EAS initiated by gamma-rays occur at altitudes of between 8 km to 12 km depending on the initial photon energy. The greater the energy of the primary gamma-ray photon, the closer to the ground the air showers can propagate and the greater the intensity of the Cherenkov light produced. Figure 2.5 illustrates a simplified air shower model.
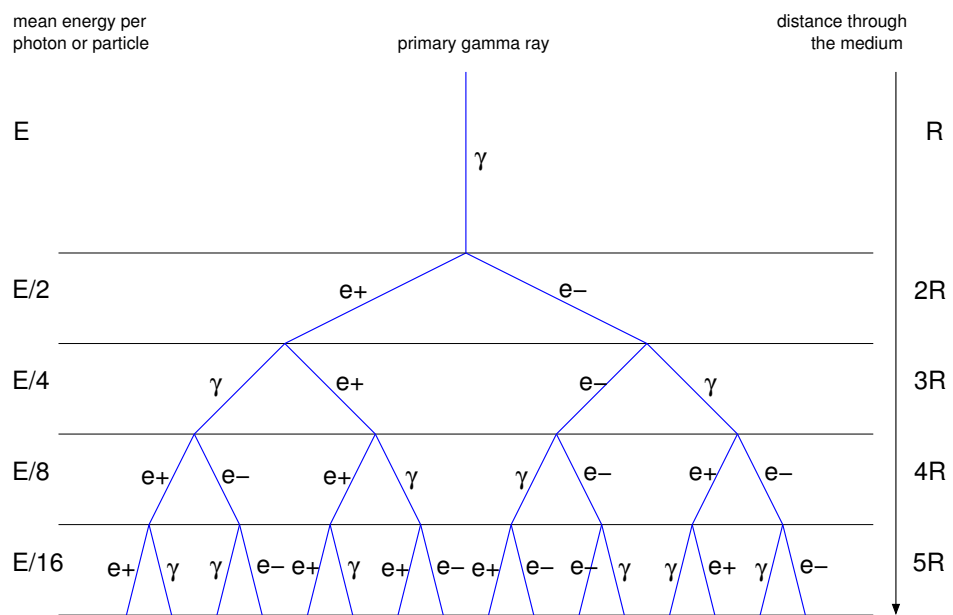
Figure 2.5: A gamma-ray-induced electromagnetic air shower illustrating the energy loss process by pair production. This is a simple model adapted from Longair[88]

For gamma-rays to be produced via Bremsstrahlung the electron positron pairs need an energy $\gtrsim$ 84 MeV [68].

2.2.1.2 Hadronic air showers

When high-energy charged particles (hadrons) enter the Earth's atmosphere they interact with the nuclei of atmospheric atoms initiating a particle cascade as the primary particle decays into secondary particles and photons. These air showers occur $\sim 10^3$ times more often than the gamma-ray-induced airshowers and produce many more types of secondary particles, primarily due to the initial production of pions in the air shower. If the products of neutral pion decay (shown earlier in Equations 1.5 and 1.6) possess enough energy they can pair produce and also initiate electromagnetic air showers. Figure 2.6 illustrates the

complexity of cosmic-ray initiated air showers including the large background electromagnetic air showers that result from the decay of secondary particles. Fortunately it is possible to distinguish between an electromagnetic air shower initiated by a cosmic-ray and one by a gamma-ray, and the techniques for doing this will be discussed in Section 2.2.3.2.
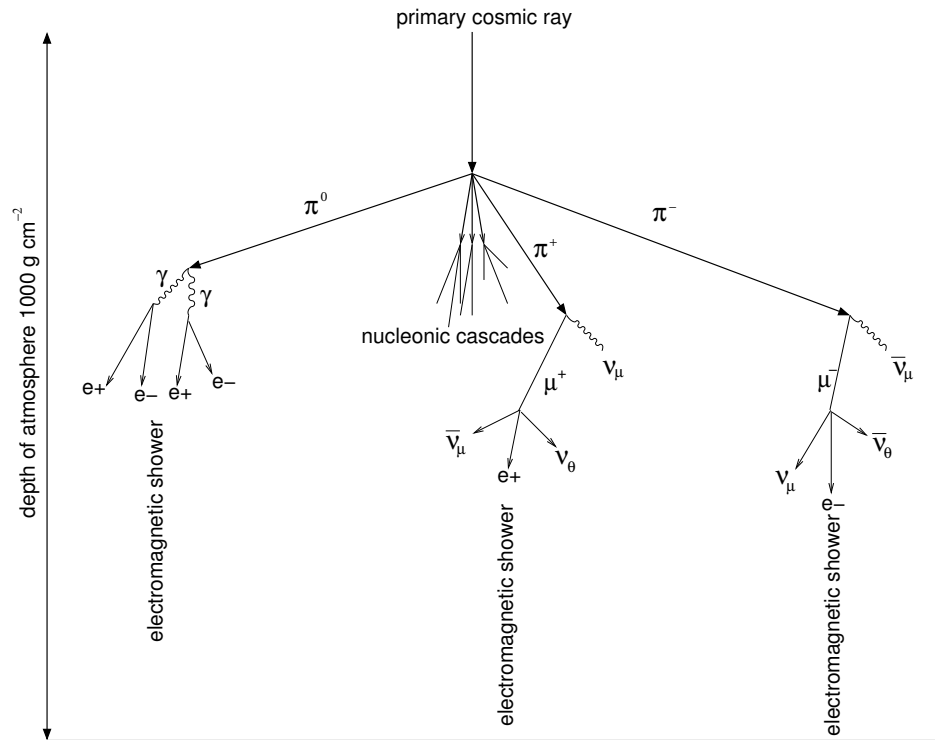
Figure 2.6: Illustration of a cosmic-ray initiated air shower in which many types of secondary particle are produced [88]. This includes neutral and charged pions which decay and produce secondary particles capable of initiating electromagnetic air showers. Due to the high frequency of cosmic-ray initiated air showers compared to that of gamma-ray initiated air showers, this results in a significant background for ground-based gamma-ray telescopes.

2.2.2 Cherenkov light

When a particle travels through a medium like the Earth's atmosphere at a velocity which exceeds the phase velocity of light in that medium, a shock-wave forms behind the relativistic particle resulting in an energy loss and the production of Cherenkov light. Cherenkov light propagates outward at a fixed angle relative to the velocity vector of the moving particle and Huygens simple geometric construction of its formation is shown in Figure 2.7. The Huygens construction is useful for working out the direction of the Cherenkov light

wavefront determined by the Cherenkov opening angle $\theta_{\check{c}}$ defined in Equation 2.2.

$$\theta_{\check{c}} = \arccos\left(\frac{1}{\mathsf{n}\beta}\right) \tag{2.2}$$

where n is the refractive index of air, $\beta = \frac{v}{c}$, v the particle velocity and c the speed of light.
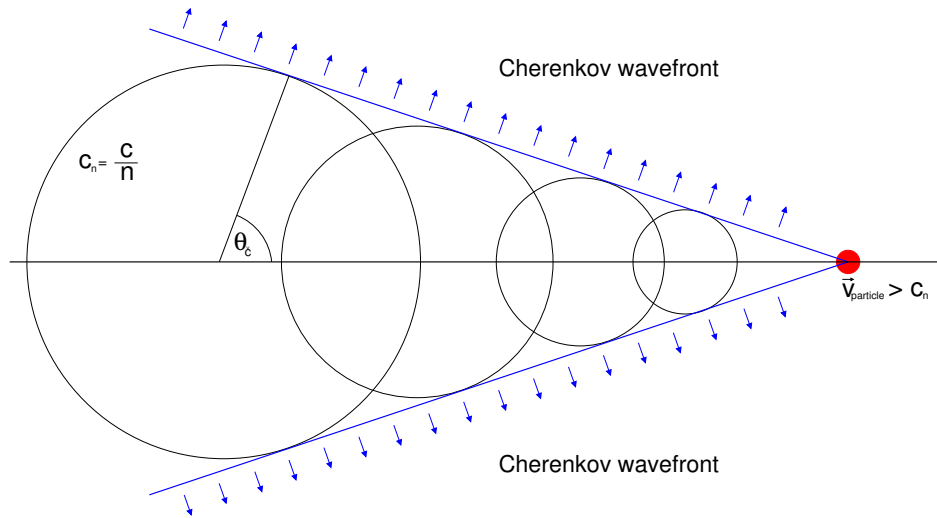
Figure 2.7: Illustrated here is the simple Huygens construction, adapted from Weekes [88], for working out the direction of the Cherenkov wavefront produced when a particle travels within a medium at a velocity v which exceeds the phase velocity c_n of light in that medium. A shockwave forms behind the relativistic particle resulting in energy-loss and the production of Cherenkov light at a fixed angle $\theta_{\check{c}}$ relative to the velocity vector of the particle.

Relativistic particles within the Earth's atmosphere typically emit Cherenkov light at opening angles between 1 and 2 degrees. For a gamma-ray-induced air shower occurring at an altitude of approximately 9 km with a Cherenkov opening angle of $\theta_{\check{c}} = 0.8°$, the Cherenkov light produced in the shower propagates towards the ground, resulting in a light pool of radius ± 125 m. The Cherenkov opening angle gets smaller with increasing altitude of Cherenkov light photon emission. This results in a focusing effect on the ground and hence the number of Cherenkov photons from a given air shower arriving at the ground can be shown as a lateral intensity profile. This is a slowly rising plateau from the shower axis outward to a distance of about 120 m where a bump or 'shoulder' occurs before the photon density reduces at a rate proportional to $\frac{1}{r^2}$ (Figure 2.8). The bump comes from high-energy electrons that travel in non-deviated parallel paths which are related to the opening angle

and altitude of emission [96].

The Cherenkov radiation emission formula derived by Frank and Tamm [63] is shown in Equation 2.3.

$$\frac{dE}{dt} = \frac{e^2}{c^2} \int \sin^2\theta d\theta \ \omega d\omega \tag{2.3}$$

By analogy, this can be understood as the medium radiating as a dipole i.e. it is the medium which produces Cherenkov radiation not the particle itself. This is evident from the charge-squared dependency (i.e. e^2 term) of the intensity and the $\sin^2\theta$ angular distribution of the power. The spectral distribution of the Cherenkov radiation is given by the Fourier transform of Equation 2.3 and is proportional to the $\omega d\omega$ term. The spectrum of Cherenkov radiation is then given by the Frank and Tamm [63] relation in Equation 2.4.

$$\frac{d^2N}{dxd\lambda} = \frac{2\pi\alpha}{\lambda^2} \sin^2\theta \tag{2.4}$$

where α is the fine structure constant, λ the wavelength of the emitted radiation and dx the unit path length. This λ^{-2} dependency implies that the intensity of Cherenkov radiation is strongly peaked at short wavelengths i.e. blue/ultra-violet. For a given air shower the number of Cherenkov photons per unit path length dx, between two wavelengths λ_1 and λ_2, can then be estimated using Equation 2.5 [43].

$$\frac{dN}{dx} = 2\pi\alpha z^2 \int_{\lambda_1}^{\lambda_2} \left(1 - \left(\frac{c}{vn(\lambda)}\right)^2 \frac{1}{\lambda^2}\right) d\lambda \tag{2.5}$$

where $\alpha \approx \frac{1}{137}$ is the fine structure constant, z the charge of the particle, v the particle velocity, $n(\lambda)$ the refractive index as a function of wavelength and c the speed of light. This implies that the number of Cherenkov photons per unit path length produced in the atmosphere is proportional to the refractive index of air, which is a function of density and altitude. For detailed information on how atmospheric parameters effect ground-based gamma-ray astronomy further reading of [43], [95], [97] and [106] is highly recommended.
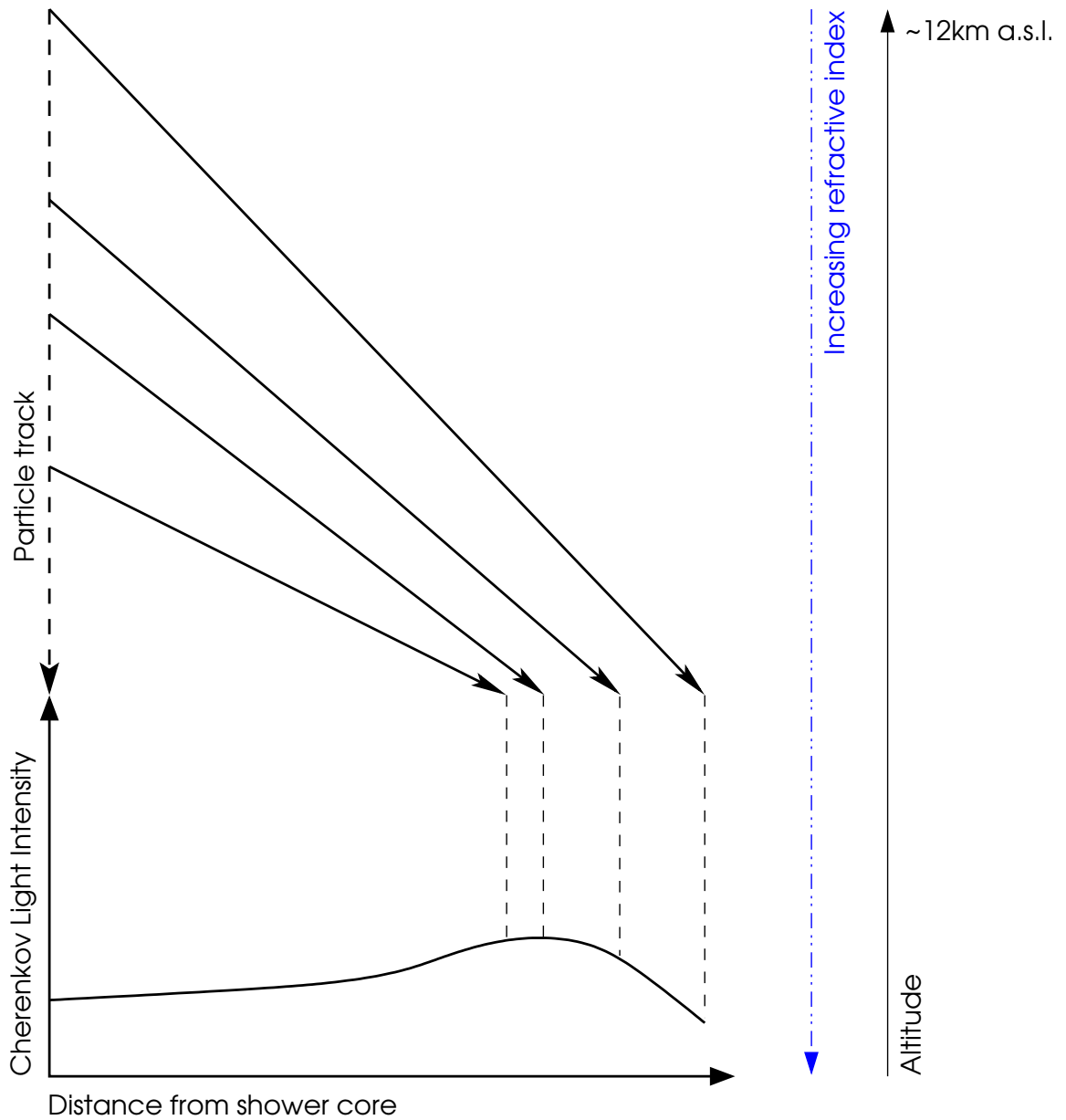
Figure 2.8: The deeper into the Earth's atmosphere a gamma-ray penetrates, the greater the refractive index of air and hence the Cherenkov light produced in extensive airshowers is focused on the ground as shown here. Also shown here is the increasing Cherenkov opening angle the greater the refractive index and hence the closer to the ground the Cherenkov light is produced. The bump in Cherenkov photon intensity comes from high-energy electrons that travel in non-deviated parallel paths which are related to the opening angle and altitude of emission [96] Image adapted from [55].

Figure 2.9 illustrates the vertical cross section (upper panels) and top-down view of the Cherenkov lightpool (lower panels) for a 50 GeV simulated gamma-ray air shower, a 300 GeV simulated gamma-ray air shower and a 1 TeV simulated hadronic air shower. From this illustration we can see a critical difference between the gamma-ray-induced air showers and the hadronic air shower. The vertical cross-section shows the Cherenkov photons produced in the air shower tend to be confined very tightly around the primary axis of the shower-initiating gamma-ray. In comparison, the spread out distribution of secondary particles produced in hadronic showers results in Cherenkov photons that are also distributed broadly from the primary axis. In addition, the top-down view of the Cherenkov lightpool on the ground clearly shows a symmetrical circle on the ground for the gamma-ray air showers, whereas the hadronic shower lightpool is less well defined. This provides us with a method of distinguishing hadronic from gamma-ray initiated Cherenkov radiation based on the distribution of light within the focal plane of the telescope.

2.2.3   The imaging atmospheric Cherenkov technique

Sections 2.2.1 and 2.2.2 highlighted how gamma-rays and hadrons are able to produce a shower of secondary particles when they enter the Earth's atmosphere and interact within the field of atmospheric nuclei. Due to the high-energy of the primary particle, the secondary particles are also relativistic and are able to produce Cherenkov light which creates a well defined lightpool on the ground (see Figure 2.9). The imaging atmospheric Cherenkov technique is the method employed to observe the short-lived Cherenkov pulses of light produced in these air showers. In principle the method is straight forward. A telescope with a large collection area that focuses the Cherenkov light from the air showers onto a camera is placed on the ground. The Cherenkov light pulses produced in air showers only last for a few nanoseconds meaning the cameras need to perform extremely fast image capture. Traditionally the camera pixels have been comprised of photo-multiplier tubes (PMTs) optimised for wavelengths of approximately 320 nm. To date PMTs have performed well at capturing the exceptionally faint Cherenkov light against a very bright night sky background.
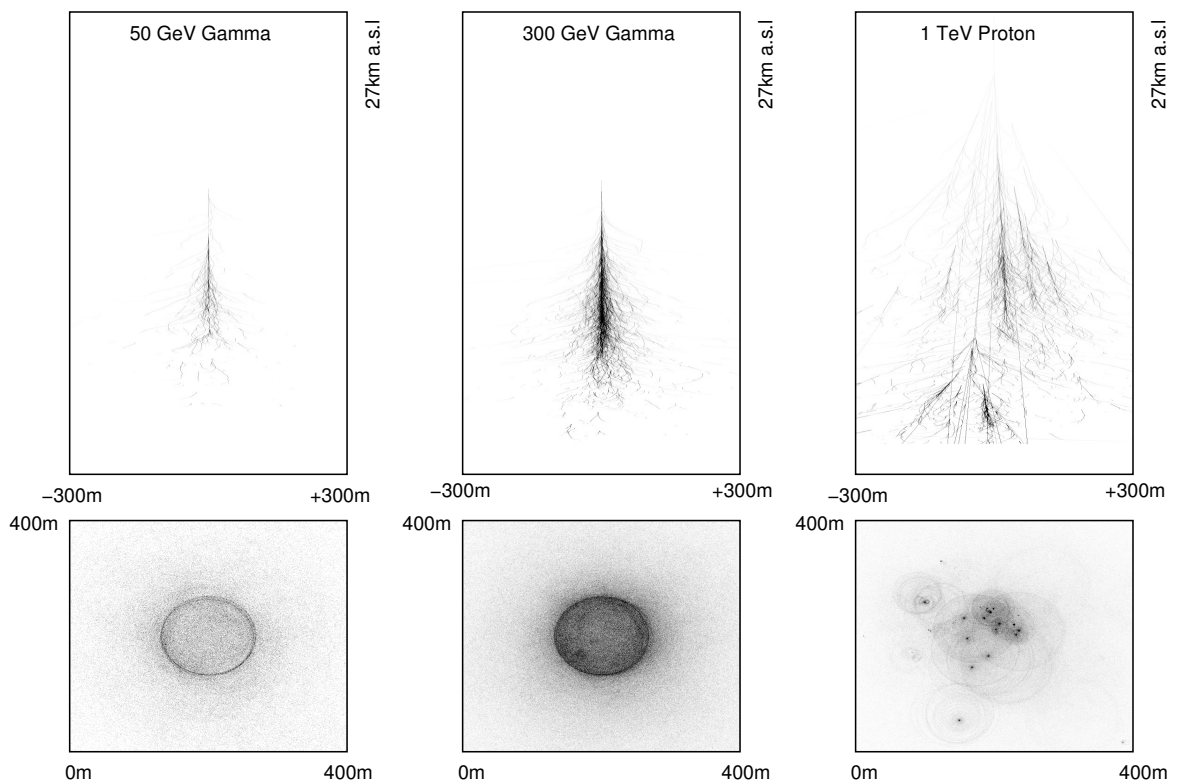
Figure 2.9: The vertical cross section (upper panels) and top-down view of the Cherenkov lightpool (lower panels) for a 50 GeV simulated gamma-ray air shower, a 300 GeV simulated gamma-ray air shower and a 1 TeV simulated hadronic air shower. The vertical cross-section shows the Cherenkov photons produced in gamma-ray-induced air showers tend to be confined very tightly around the primary axis of the incident gamma-ray. In comparison the hadronic air shower tends to scatter Cherenkov photons more broadly around the primary axis. The top-down view of the Cherenkov lightpool on the ground clearly shows a symmetrical circle on the ground for the gamma-ray air showers which become elongated and elliptical when viewing at an increasing angle away from the primary axis. In contrast, the hadronic shower lightpool is less well defined. Images courtesy of Dr. Konrad Bernlöhr [37]

However new technologies have emerged such as multi-anode photomultipliers (MAPMTs) [10] and silicon photomultipliers (SiPMs) [47] that may provide improved performance for ground-based gamma-ray telescopes.

Figure 2.10 illustrates the basic concept of the ground-based imaging atmospheric Cherenkov technique compared to the silicon strip detectors used in space-based gamma-ray telescopes such as *Fermi*.

2.2.3.1   Night sky background

Against the night sky background (NSB), Cherenkov light is extremely faint and to maximise the signal to noise ratio (SNR) ground-based gamma-ray telescopes should ideally operate under dark sky conditions i.e. a dark site and preferably not during moonlight hours. The signal to noise ratio for a Cherenkov telescope is expressed in Equation 2.6 [27].

$$\frac{S}{N} \propto \left(\frac{\epsilon A_{mirror}}{\tau \Omega_{pixel}}\right)^{\frac{1}{2}} \tag{2.6}$$

where ϵ is the optical efficiency i.e. efficiency of the optical system including the quantum efficiency of the camera PMTs, A_{mirror} the mirror collecting area, Ω_{pixel} the pixel solid angle acceptance and τ the exposure time. For the duration of the camera exposures or integration windows, the flux intensity of Cherenkov light is relatively bright against the NSB. In current generation ground-based gamma-ray telescope cameras, typically each pixel has an integration window that is much smaller than the Cherenkov light pulse width i.e. a few nanoseconds. The energy threshold is inversely proportional to the signal to noise ratio. Equation 2.6 therefore also makes clear that maximising collecting area as well as increasing optical efficiency results in the energy threshold decreasing. Lowering the energy threshold below what is achievable with the current generation of ground-based gamma-ray astronomy instruments is very important for observations of pulsars. This will be discussed further in Chapter 5.

Current generation Cherenkov telescopes like H.E.S.S. include a pixel-level trigger, that

γ

Fermi gamma ray telescope
$30\ \mathrm{MeV} \lesssim \mathrm{E} \lesssim 300\ \mathrm{GeV}$
Collection area $\approx 3.2\ \mathrm{m}^2$

Space

Atmosphere

γ

$E_\gamma \approx 300\ \mathrm{GeV}$

Height $\approx 8\ \mathrm{km\ a.s.l}$

$\theta_{\check{c}} \approx 0.8°$

Cherenkov light cone

Imaging atmospheric Cherenkov telescope
Diameter $\approx 12\ \mathrm{m}$
Collection area $\approx 100\ \mathrm{m}^2$

Ground

Cherenkov lightpool area $\approx 4 \times 10^4\ \mathrm{m}^2$
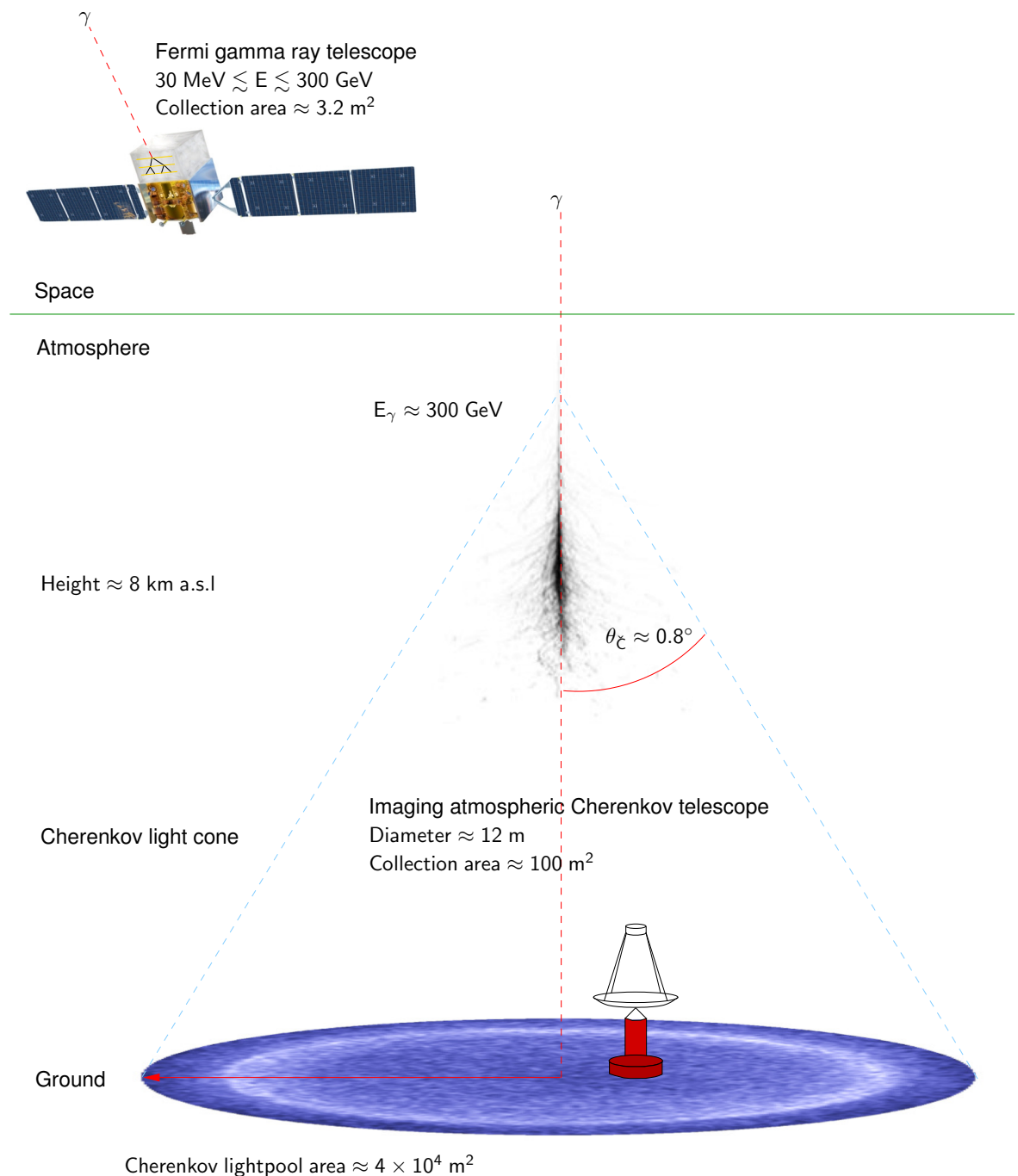
Figure 2.10: Sketch illustrating two gamma-ray detection techniques; from the ground using the imaging atmospheric Cherenkov technique and from space using silicon strip detectors. This sketch shows an example of a gamma-ray-induced air shower occurring at an altitude of $\approx 8\ \mathrm{km\ a.s.l.}$ The pulsed Cherenkov light from the shower propagates towards the ground at an opening angle of $\approx 0.8°$. The Cherenkov light arrives in a well defined lightpool of radius $\approx 120\ \mathrm{m}$. Adapted from [33].

is the recorded pixel photo-electron count needs to satisfy a minimum number of photo-electrons before triggering the telescope. Pixel-level triggers help to distinguish between Cherenkov signal and Poisson fluctuation NSB. A benefit of the new pixel technologies highlighted earlier is a reduction in pixel size diameter to about 0.1 degrees which is expected to improve both telescope triggering, shower reconstruction and hence sensitivity performance [21].

2.2.3.2 Background rejection

Section 2.2.1.2 highlighted that hadronic-induced air showers produce secondary electrons and positrons capable of initiating electromagnetic air showers. This results in a significant background that needs to be taken into account by ground-based gamma-ray telescope systems. Unlike space-based telescopes, it is not possible to construct active anti-coincidence shields for ground-based instruments. Instead analysis methods utilising the image parameters are required in order to reject the background Cherenkov light produced in hadronic air showers.

In Section 2.2.1.2 it was noted that cosmic-rays are responsible for most of the electromagnetic pair-production air showers in the atmosphere, and thus being able to distinguish between gamma-ray-induced air showers and cosmic-ray-induced air showers is critical to the success of very high-energy gamma-ray astronomy from the ground. Fortunately within hadronic air showers, pions are produced with a large transverse momenta and hence their particle distribution is much more spread out compared to that of gamma-rays, whose secondary air shower particles are confined relatively closely to the original gamma-ray path. As a result, the Cherenkov light from gamma-ray-induced air showers arrives in a well-defined lightpool compared to that from hadronic air showers (as shown in Figure 2.9). Camera images of the gamma-ray-induced air shower are therefore also well defined and can best be described by an ellipse whereas images of hadronic air showers are not.

The elliptical shape seen by the cameras is dependent on the energy of the primary gamma-ray as well as the distance of the shower's core-axis from the camera. The width of the

elliptical image is related to the lateral development of the air shower and the length is an indicator of distance from the camera. In addition, for a given primary energy the Cherenkov light intensity captured by the PMTs will be greater for gamma-ray-induced air showers compared to that from hadronic air showers. These key differences make it relatively easy to distinguish between a gamma-ray-induced air shower and the hadronic air showers. Figure 2.11 shows simulated camera images of a 1 TeV gamma-ray air shower and a 1 TeV hadronic (proton) air shower. When comparing images of the different air showers like this, distinguishing between the two is obvious to the eye.

Primary: gamma of 1.000 TeV energy at 87 m distance   **Primary: proton of 1.000 TeV energy at 83 m distance**
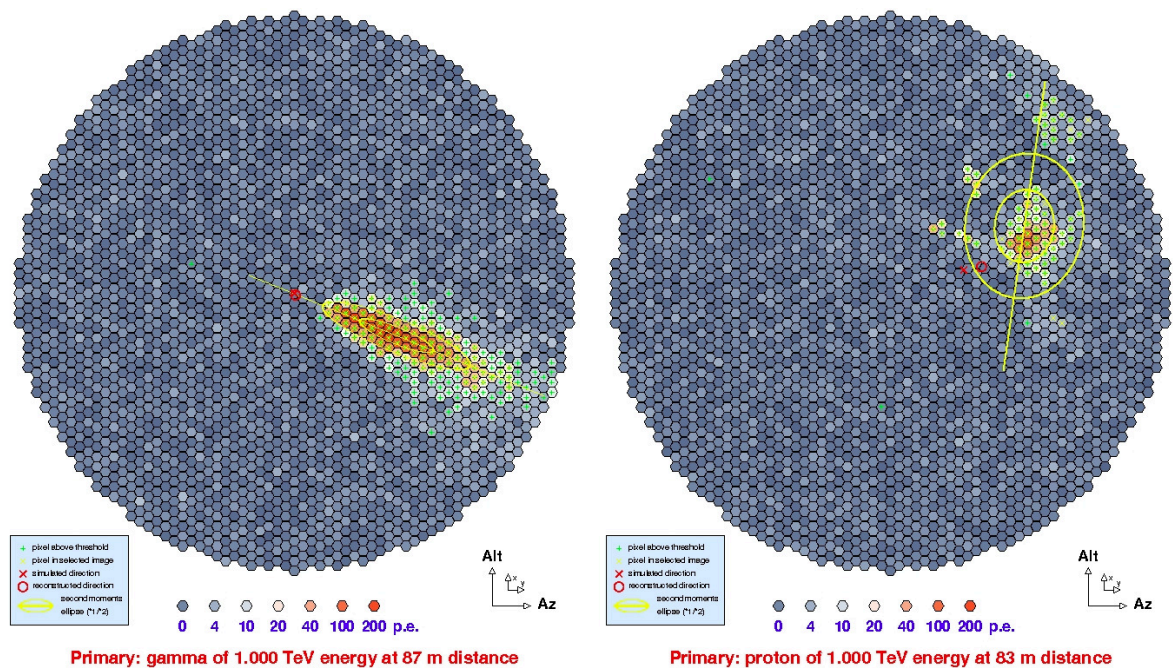
Figure 2.11: A simulated 1 TeV gamma-ray (left) and 1 TeV hadronic (proton) air shower (right) typically captured with the cameras of ground-based imaging atmospheric Cherenkov telescopes. The air showers simulated here occur at similar distances away from the telescope. The different morphology of the air showers makes it relatively easy to distinguish between the two. The gamma-ray (left) has an elliptical shape that points toward the source (red cross) at the centre of the camera, however the hadronic air shower (right) is more dispersed with no certain direction.

Parameterisation of these camera images (called the Hillas parameters, see Section 2.2.3.3) allows for parametric statistical analysis of the images which provides essential information about the shower and crucially enables for the distinction between gamma-ray and hadronic air showers and hence rejection of the cosmic-ray background in the analysis of astrophysical gamma-ray sources.

Finally it should also be mentioned that cosmic-ray electrons incident upon the Earth are also able to initiate electromagnetic air showers that are indistinguishable from gamma-ray-induced air showers. However due their charge and mass, electrons are strongly influenced by the solar and terrestrial magnetic fields at energies $\lesssim 1$ GeV [88]. At energies above ~ 100 GeV, ground-based Cherenkov telescope systems have tended to ignore cosmic-ray electrons due to their low flux at these energies. However, for a next-generation ground-based gamma-ray observatory such as CTA (discussed in Chapter 3) with an energy threshold in the tens of GeV range, cosmic-ray electrons need to be considered, particularly for low-energy observations. This is particularly important for observations of pulsars. Here phase resolving photon arrival times should help to eliminate a significant proportion of the isotropic electron-induced background contribution.

2.2.3.3 Image parameterisation

Parameterisation of the camera images allows computer-based discrimination techniques to be implemented. The standard approach is to implement the Hillas parameterisation scheme which is a function of the second moments obtained from the Cherenkov image. Figure 2.12 illustrates how the Hillas parameters are obtained from the camera images of the Cherenkov air showers. The second order moments and Hillas parameters are defined in Appendix A and a detailed description can be found in Fegan [61].

When using the Hillas parameters to distinguish between gamma-ray and hadronic air showers, the basic approach is to perform many Monte Carlo simulations of both air shower types which provides *a priori* information on the various Hillas parameter ranges [74]. Probability distributions can then be constructed for each of the parameters and using this 'expected' information, cuts can be placed on the images recorded during actual observations of astrophysical gamma-ray sources. Known as the 'standard cuts' method, this widely used procedure helps to reject the cosmic-ray background whilst maintaining a good gamma-ray signal efficiency.
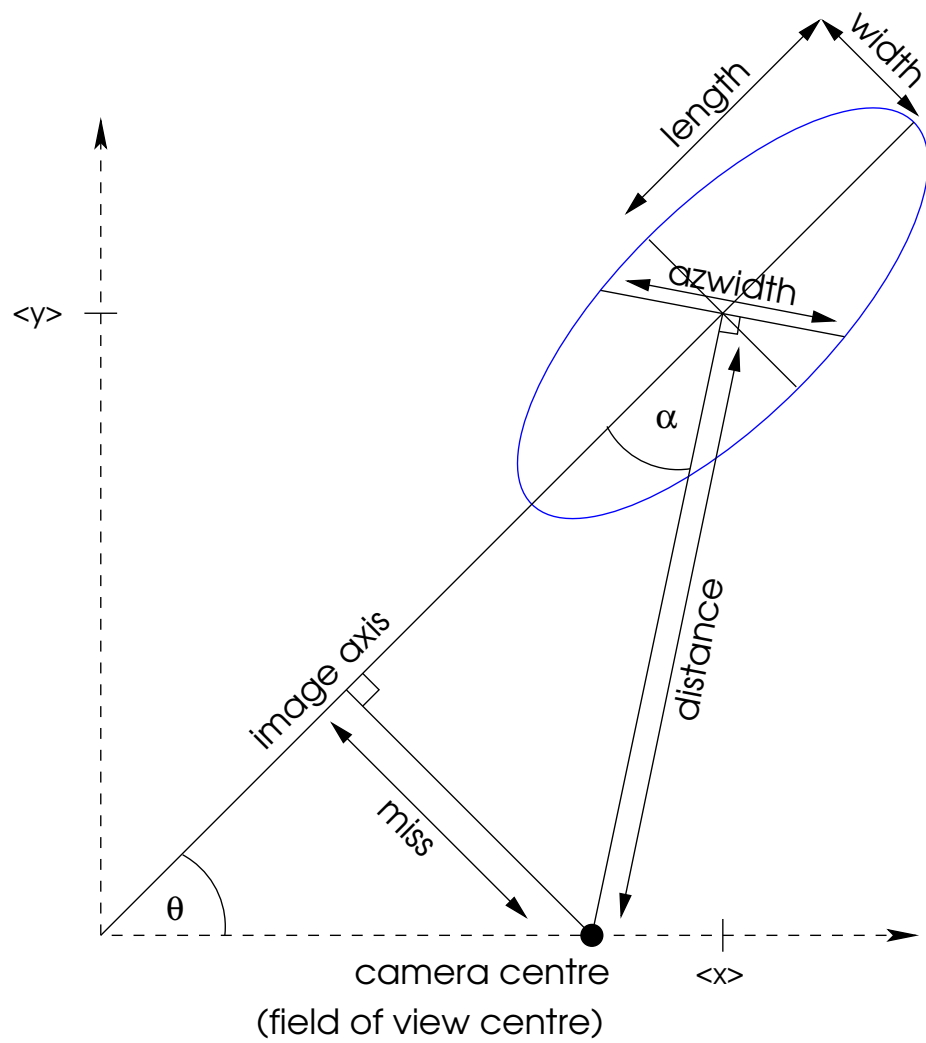
Figure 2.12: Illustrated here are the Hillas parameters obtained from the second moments of the Cherenkov air shower camera images.

2.2.3.4   Stereoscopic techniques & shower reconstruction

Ground-based gamma-ray astronomy can be conducted with a single Cherenkov telescope (see Figure 2.10). However it is preferable to use multiple telescopes because this allows for the stereoscopic reconstruction of air showers. To infer anything meaningful from the observations a number of shower characteristics need to be determined, including the shower-axis orientation in space, the position of the shower core in the observation plane, the angular dimensions of the shower and the depth of shower maximum (Xmax) [83]. Shower parameters are geometrically reconstructed from the camera images and performing this reconstruction from multiple images of the same air shower significantly reduces any uncertainty in these reconstructed parameters. For example, the shower direction is determined by intersecting the primary axes of the elliptical images recorded by the telescope cameras. The *ellipse intersection* method [78] is the most widely accepted method for image reconstruction in ground-based gamma-ray astronomy. Figure 2.13 illustrates the concept of stereoscopic shower imaging (using a 4 telescope array) and reconstruction of shower parameters such as the shower direction and shower core [22].

Finally, it is also worth noting that multiple telescopes allow for a multi-telescope triggering system that improves background rejection in the first instance [64].

2.2.3.5   Mean scaled parameters

The *mean scaled width* method of classifying ground-based gamma-ray telescope camera images as either gamma-ray-like or hadron-like is well established [25]. The method involves the construction of lookup tables that can be used to predict the mean width and length of a gamma-ray-induced air shower as a function of image amplitude (brightness) and shower core distance. For a given event a set of parameters P are obtained from a single camera image. These parameter values can be compared with expected parameters $< P >$ obtained by conducting zenith angle dependent Monte Carlo simulations. Applying this technique across multiple images Equation 2.7 defines the scaled parameter P_{SC} for each triggered
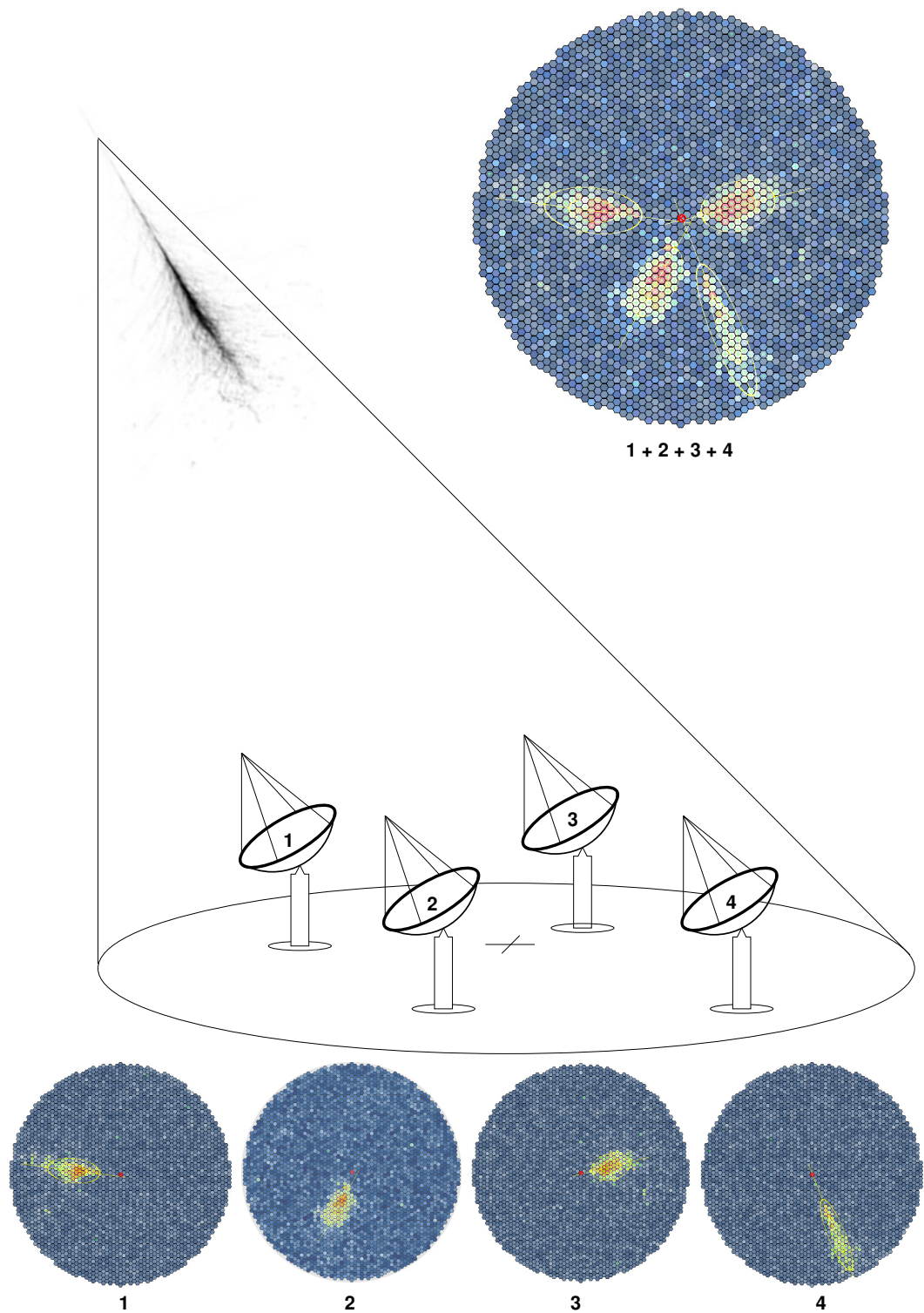
Figure 2.13: Showers are reconstructed using the ellipse intersection method. The basic concept of directional reconstruction is shown here for a 100 GeV simulated gamma-ray-induced air shower using 4 ground-based Cherenkov telescopes.

telescope.

$$P_{SC,i} = \frac{P_i - <P>}{\sigma_i} \tag{2.7}$$

where i is the telescope number and σ the spread. For an array of Cherenkov telescopes the mean scaled parameters are summed and then averaged over the number of telescopes n triggered in the event. This produces a *mean reduced scaled parameter* P_{MRSC} shown in Equation 2.8.

$$P_{MRSC,i} = \sum_{i=1}^{n} \frac{P_{SC,i}}{n} \tag{2.8}$$

Observed background and signal events recorded with ground-based gamma-ray telescopes correspond well with the Monte Carlo simulated *mean reduced scaled widths* (MRSCWs) as shown in Figure 2.14 [25]. Traditional background rejection methods apply a selection or 'shape' cut on these distributions based upon the spectral index of the source being observed. An example of this is the 'standard', 'hard' and 'loose' cut selections used in the H.E.S.S. standard analysis technique detailed in Aharonian et al. [25] and Benbow et al. [35].

The results of the simulation work conducted for this thesis are presented in Chapter 3. Where applicable, results are compared with similar work derived using these traditional background rejection methods.

2.3 Background estimation techniques

This section describes some observational techniques for estimating the background which are used in experiments such as H.E.S.S.. It is conceivable that these methods will continue to be used in future generation ground-based telescope systems such as CTA. It is accepted that Cherenkov events from cosmic-ray air showers dominate the triggering of ground-
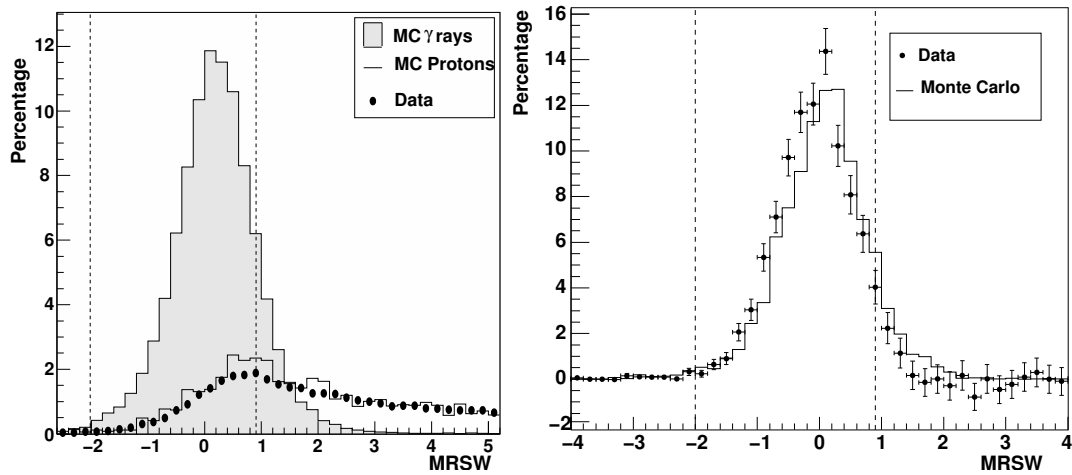
Figure 2.14: Distribution of mean reduced scaled widths from H.E.S.S. [25]. The left panel shows Monte Carlo simulations of gamma-rays (spectral index $\alpha = 2.59$) (grey filled histogram), protons (spectral index $\alpha = 2.7$) (clear histogram) and observational data from an off source region (black dots) prior to making selection cuts. The right panel shows observed data from the Crab nebula (black dots) compared with Monte Carlo simulations (spectral index $\alpha = 2.59$) of this source (clear histogram). All the distributions are for a zenith angle of 50 degrees and the dashed vertical lines illustrate 'standard' H.E.S.S. selection cuts.

based gamma-ray telescopes [64]. Observations of the Crab Nebula by H.E.S.S. reported an average system trigger rate of 240 Hz for 4 telescopes [25]. These triggers are largely cosmic-ray background events meaning it is important to obtain a good measure of this background, particularly as it still needs to be separated from the gamma-ray signal events. Typically this is performed post shower reconstruction and is discussed further in Chapter 3.

Additional factors that need to be taken into account during observations include camera gamma-ray acceptance for example. The acceptance varies across the camera field of view meaning it is always preferential to keep the observed sky area within the central region of the camera in order to maximise the gamma-ray acceptance. For a 5 degree field of view camera this would typically mean the inner 2 degrees [36]. Furthermore the background cosmic-ray flux, although isotropic, triggers the ground-based Cherenkov telescopes in a zenith angle dependent manner. In practice this means that the observed background cosmic-ray trigger rate varies with energy during the course of an observation. In order to take account of these factors observations in ground-based gamma-ray astronomy are typically conducted in *wobble* mode [36].
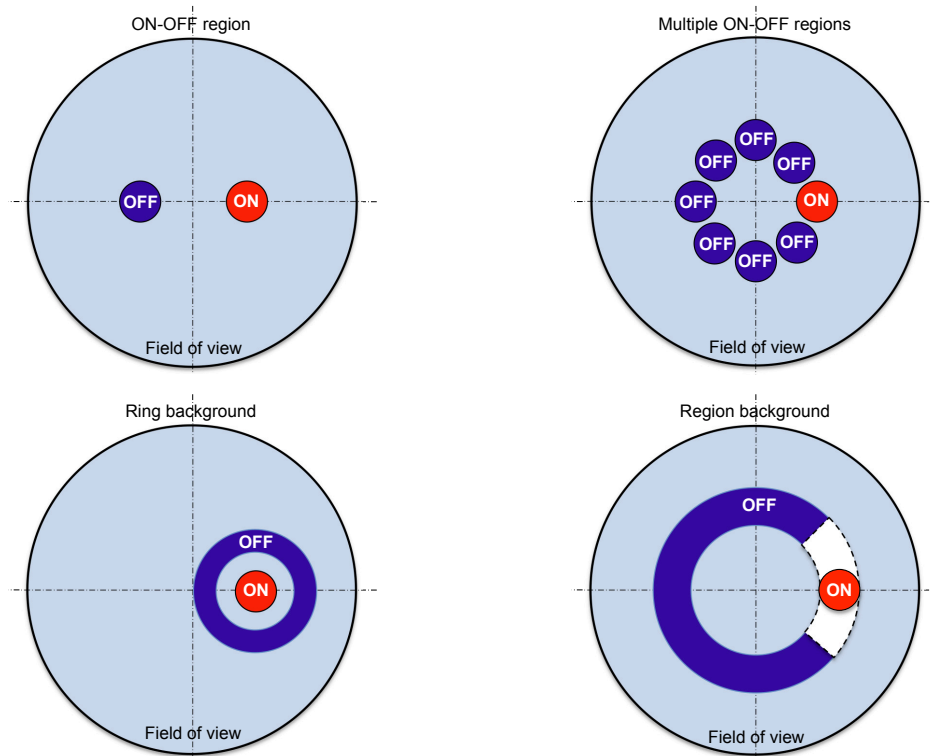
Figure 2.15: Different types of observational techniques employed by ground-based Cherenkov telescopes. The classical ON-OFF region (top left panel), the multiple ON-OFF regions (top right panel), the Ring Background (bottom left panel) and the Region Background (bottom right panel). Adapted from Rowell [105]

Figure 2.15 illustrates different *wobble* approaches that are commonly used for estimating the background during observations with ground-based Cherenkov telescopes such as H.E.S.S. [100]. These include the classical ON-OFF region (top left panel), multiple ON-OFF regions (top right panel), the Ring background (bottom left panel) and the Region background (bottom right panel) [105]. An approach not shown here, is the reflected-region background [36] which is simply a derivative of the multiple ON-OFF regions (top right panel). For the purposes of deriving sensitivity performance (see Section 3.6), this research adopts a background region that is fixed in scale with respect to the ON region. The ON region is defined by the derived angular resolution which varies as a function of energy and hence fixed scaling ensures the background region also varies as a function of energy. Therefore the area ratio of the ON and OFF regions is defined as $\alpha \equiv A_{ON}/A_{OFF} = 0.2$. Figure 2.16 illustrates the sensitivity performance ON-OFF regions which are discussed further in Section 3.6.

Sensitivity performance ON-OFF region
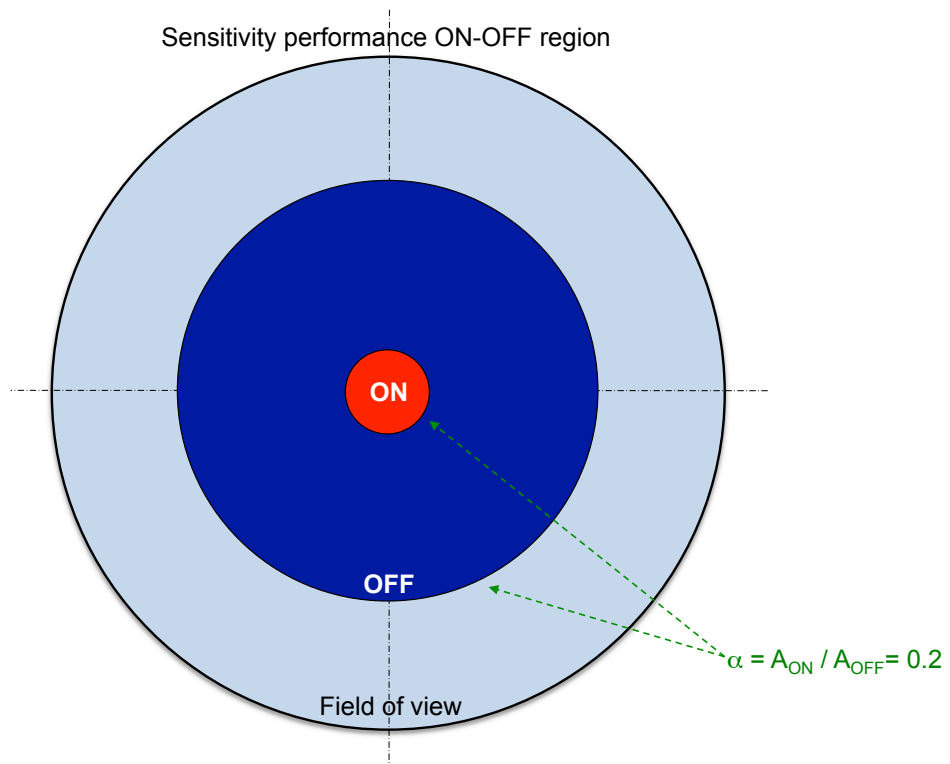
Figure 2.16: Illustration of the ON-OFF region used in this research for the sensitivity performance analysis (Section 3.6). The background OFF region is fixed to be 5 times larger than the ON region for all energies; hence $\alpha \equiv A_{ON}/A_{OFF} = 0.2$.

2.4 Detector calibration

Ground-based gamma-ray telescopes require regular calibration. The purpose of this is to reduce any systematic bias that may be present in the instrumentation. Any bias in the system can influence how much Cherenkov light is measured by the telescope cameras. Although it is not the purpose of this research to discuss all the possible calibration methods that are widely used, it is worth mentioning a few standard calibration procedures that are likely to be used in a future ground-based gamma-ray observatory such as CTA. Various parameters introduced by such procedures are relevant to the simulation and analysis work conducted in this thesis.

2.4.1 Single photo-electron response

H.E.S.S. measures the single photo-electron response on a regular basis by synchronising the telescope trigger to a faint pulsing LED. On average, every third trigger of the LED will produce a single photo-electron in each pixel of the camera. The measured amplitudes for each pixel are used to determine the electrical response for each PMT i.e. the efficiency of the analogue-to-digital signal conversion (ADC). Not all ground-based gamma-ray telescopes measure the single photo-electron response and there is some discussion amongst experts in the field whether this time consuming procedure is absolutely necessary. A preliminary case study focused on the dynamic range performance of CTA has been conducted for this thesis and the findings for the lower dynamic range can be found in Section 4.2.2. In this study the assumed ADC value of 80 (See Figure 2.17) for a single photo-electron is changed in order to determine the effect on performance of CTA within the current Monte Carlo analysis framework.

2.4.2 Image cleaning

Existing ground-based gamma-ray telescopes are regularly calibrated to achieve the best possible sensitivity of the cameras to the very faint Cherenkov light. Despite these efforts the actual images recorded by the camera can still be noisy due to the NSB. The image cleaning process used in this research is similar to that conducted by H.E.S.S., which is a 2-stage process [35]. First, an image pixel is only kept if its amplitude is greater than or equal to a signal of 5 photo-electrons. Secondly, any retained pixel must have a neighbouring pixel with a signal amplitude greater than or equal to 10 photo-electrons. This process is commonly called 'five ten' image cleaning and the result of such a process is to isolate clusters of triggered pixels.

In this chapter the principles and techniques underlying ground-based gamma-ray astronomy were highlighted. Since the discovery of the Crab Nebula in very high-energy gamma-rays by the Whipple telescope in 1989 [113], the imaging atmospheric Cherenkov technique
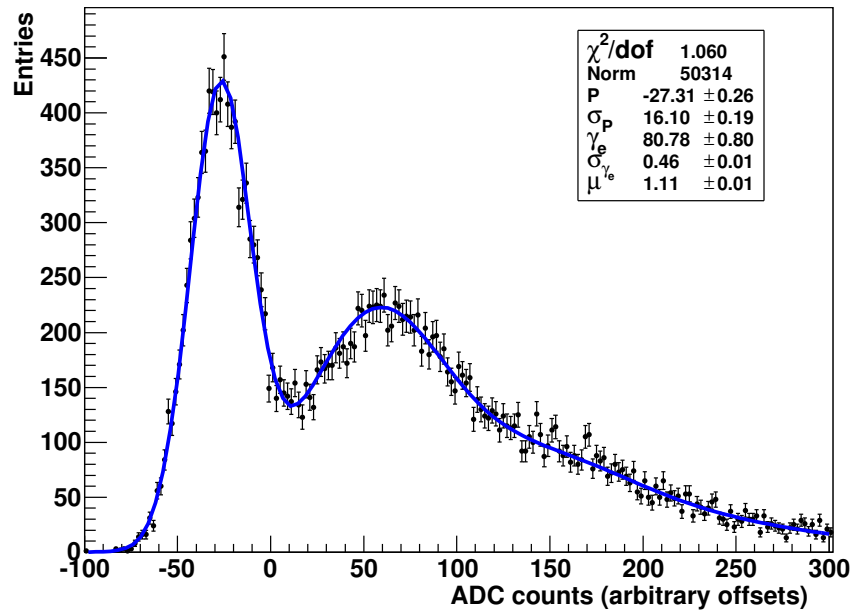
Figure 2.17: Example of the single photo-electron response detected here with H.E.S.S. [24]. This is the typical distribution recorded when an LED pulser is used to illuminate the H.E.S.S. cameras. A parametric function is fit to the data and the second bump is approximated by a Gaussian function. The position of this peak provides the gain in ADC counts for a single photo-electron. In this example the measured value is $\gamma_e = 80.78$ which is essentially the same as the assumed value used in *sim_telarray*. The study conducted in Section 4.2.2 investigates whether changing this value has any adverse effects on CTA performance.

has been successfully used and refined by many experiments mentioned earlier. However, to progress the field and our understanding of the many astrophysical objects which emit gamma-rays, instruments with greater sensitivity are required. Chapter 3 introduces the Cherenkov Telescope Array (CTA) an international initiative to build such an instrument. This includes an assessment of the system's potential performance.

Chapter 3

Toward A Ground-Based Gamma-ray Observatory

The following chapter introduces the Cherenkov Telescope Array (CTA), a next-generation observatory for detecting atmospheric air showers induced by very high-energy gamma radiation originating from a variety of Galactic and extra-galactic sources. This chapter will discuss the motivations, the specifications and possible observatory layouts for such a new instrument. Furthermore, the results of extensive Monte Carlo simulation work are presented in order to assess the expected performance of CTA. These include air shower and telescope simulations through to image reconstruction and background rejection. Sensitivity curves have been generated to provide a measure of array performance which allows for different array layouts and analysis methods to be compared. The procedure for producing the sensitivity curves is discussed, which includes various optimisation cuts that have been made. Particular attention is given to the background rejection method including the post-cut signal and background efficiency. Finally, the potential performance of the array layouts is compared by illustrating the angular and energy resolutions as well as their achievable effective areas and differential sensitivities.

3.1   The Cherenkov Telescope Array

The current generation of ground-based imaging atmospheric Cherenkov telescope systems mentioned in Chapter 2 have helped to establish the technique by discovering many astrophysical sources of gamma radiation, both Galactic and extra-galactic. At the time of writing the catalogue of known very high-energy gamma-ray sources is of order 100 sources [112]. It is believed that improving the sensitivity and lowering the energy threshold of such ground-based gamma-ray astronomy systems will lead to the discovery of more gamma-ray sources. At GeV energies and above the gamma-ray flux incident onto the Earth is low, and the relatively very small effective area of space-based instruments like *Fermi* provide ground-based instruments with a distinct advantage at these energies. This provides the motivation for CTA an international initiative to build a next-generation ground-based gamma-ray observatory that will study the very high-energy gamma-ray sky from $\gtrsim 10$ GeV to $\lesssim 100$ TeV. The conceptual design of CTA calls for a factor 5 - 10 improvement in sensitivity (compared to the current generation of systems) over the energy range $\sim$ 100GeV to $\sim$10TeV [21]. The results of the simulation work carried out in this research confirms that this sensitivity goal is achievable based upon the layouts, simulations and assumptions highlighted in this thesis.

3.1.1   Motivations

The current proposal for CTA is to construct a new facility consisting of a very large system of imaging atmospheric Cherenkov telescopes of different sizes. The physical area coverage of the array is unprecedented for optical telescopes and requires a mammoth engineering effort. However, since CTA was first conceived in 2005 the idea was, and remains, to build the array using proven technologies. The capabilities of CTA are well beyond those achievable by simply upgrading the existing facilities mentioned in Chapter 2. Moreover, CTA will also be the first facility of its kind in the world to operate as an open observatory, acting as the pivotal driving force for exploring the high-energy non-thermal universe within

a multi-wavelength and multi-messenger astrophysics community.

Due to the low flux of ≥ 10 GeV gamma-rays incident onto the Earth, this necessitates the use of instruments with a large effective collecting area. Therefore space based detectors are impractical and effectively discounted. The existing ground-based gamma-ray detection systems, including both water Cherenkov systems and imaging atmospheric Cherenkov systems can achieve sensitivities comparable to the Crab flux and about 1% (for a 25 hour exposure) of the Crab flux respectively. New experiments such as the High-Altitude Water Cherenkov observatory (HAWC) [2] are aiming to improve upon this, however none of these experiments can compete with the sensitivities achievable by CTA within the broad band energy range highlighted above.

3.1.2 Goals & specifications

The following section highlights some of the key specification parameters for existing ground-based gamma-ray systems as well as the CTA performance goals as outlined in the consortium's design concepts publication [21]. Table 3.1 lists the key parameters of the existing ground-based IACT systems.

Table 3.1: Properties of existing IACT systems

Instrument:	Lat: ($°$)	Long: ($°$)	Alt: (m)	Telescopes: #	(m^2)	(m^2)	Pixels: #	FOV: ($°$)	Thresh: (TeV)	Sens: (%Crab)
H.E.S.S.	-23	16	1800	4	107	428	960	5	0.1	0.7
VERITAS	32	-111	1275	4	106	424	499	3.5	0.1	0.7
MAGIC	29	18	2225	2	234	468	576/1039	3.5	0.03	1.0

In addition to the specifications listed in Table 3.1, existing systems can achieve a typical angular resolution of 0.1 degrees at 1 TeV loosening to about 0.2 degrees at 100 GeV. Reconstruction of the gamma-ray source location on the sky can be achieved with an uncertainty of $\pm$ 10 to 20 arcsecs.

The current performance goals for CTA are [21, see]:

1. *Sensitivity.* Over the core energy range of 100 GeV to 10 TeV, CTA aims to have an order of magnitude better sensitivity compared to existing systems. At 1 TeV the goal is to achieve a 1 milli-Crab sensitivity.

2. *Energy Resolution.* CTA is expected to cover a very broad energy spectrum below and above its core range. The CTA system will be sensitive to Cherenkov photons originating from primary gamma-ray energies of $\sim$ 10 GeV to beyond $\sim$ 100 TeV. This is a vast energy coverage spanning 5 orders of magnitude. The goal is to have an energy resolution of under $\sim$ 10 % at energies above 1 TeV.

3. *Angular Resolution.* CTA will be able to reconstruct the shower direction to an angular resolution of $\sim$ 1 arc-minute. This is approximately a factor of 5 better angular resolution compared to existing systems.

4. *Dynamic Range.* CTA sensors should be able to detect single photo-electrons and provide a dynamic range up to 5000 photo-electrons.

3.1.3 Layout proposals

In order to obtain full sky coverage, the CTA consortium proposes to operate two observatory sites; one in the northern hemisphere and one in the southern hemisphere. The southern site will focus on the central Galactic region and all Galactic sources. The northern site will concentrate on extra-galactic sources. Furthermore the southern site's array sensitivity will be optimised to cover the full energy range $\gtrsim$ 10 GeV to $\gtrsim$ 100 TeV. Layout of the telescope arrays on the two separate sites requires a finely-tuned balancing act between cost and performance. Ideally the array performance would purely be driven by the scientific goals and motivations; however, reality demands that the actual performance is trimmed according to cost and technical availability. This thesis will not address the actual monetary costs, but rather where appropriate highlight if the findings in the research affect the overall bottom line.

It was mentioned above that the CTA system will consist of different telescope types. This is driven by the fact that a large energy range coverage is required and thus having an array of identical telescopes over a large area with fixed spacing is not optimal for performance [39] (see Figure 3.1).

Instead it is accepted that the full energy range must be subdivided and telescopes optimised for those energy sub-ranges. In line with this thinking the full energy range can be thought of as three energy ranges; low ($\lesssim 100$ GeV), medium or core (> 100 GeV to < 10 TeV) and high (> 10 TeV). These bounds are for convenience; in practice there are no absolute boundaries but rather a smooth transition from one to the other. The consensus is to have 3 different telescope types that are optimised for each of these sub-energy ranges. For the low energies an area coverage of $\sim 10^4$ m^2 is acceptable because at these energies the event rates are sufficiently high to maintain signal efficiency, despite the larger systematic uncertainties due to the cosmic-ray background. However at low energies there are fewer Cherenkov photons produced in the air showers and hence the showers are very dim. In order to collect enough light to trigger the telescopes it is accepted that the low-energy range is best observed using a few large telescopes with a large collection area. Currently the proposal is to construct 3 or 4 $\sim$23 m diameter telescopes optimised for the low-energy range. In the core energy range, shower observation and reconstruction is well understood from the experiences of the existing ground-based systems. It is generally accepted that a large array of $\sim$12 m class telescopes be utilised to provide coverage of the medium energy range, where an improvement in sensitivity is gained from the larger area, better analysis and reconstruction techniques and better background rejection methods central to the work in this thesis. In the high-energy range, the Cherenkov light intensity is much brighter, but beyond 10 TeV the event rate is relatively low. Conversely high-energy showers occurring at a large distance away from the telescope array can trigger the telescopes because of their high Cherenkov light intensity. Thus it is accepted that smaller telescopes spaced further apart (i.e. covering a larger ground footprint) provide a possible solution for maximising sensitivity performance at the highest energies.
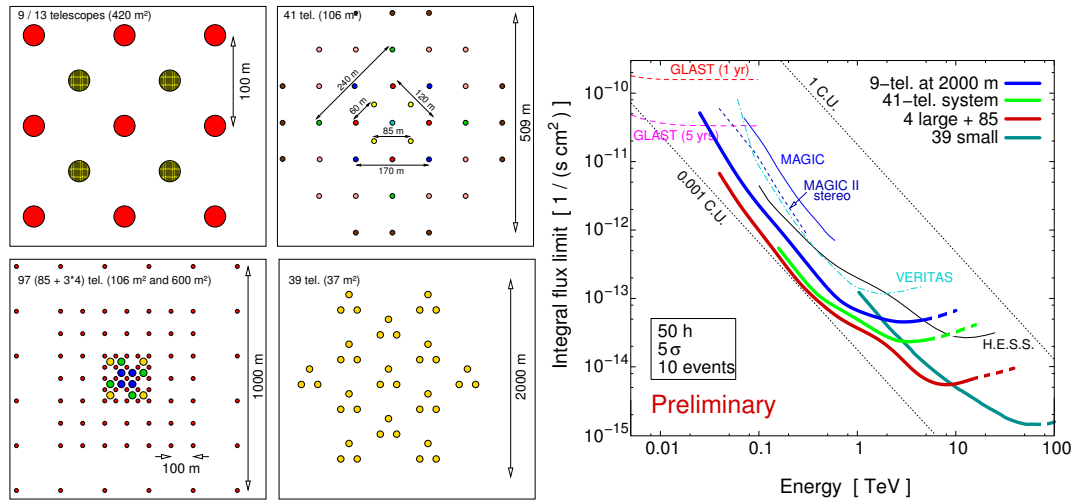
Figure 3.1: A selection of different array layouts (left panel) simulated for altitudes of 1800 m and 2000 m by Bernlöhr [39]. The integral sensitivity performance (right panel) for these preliminary array layouts for a point source at 20 degree zenith angle compared with current instruments. In this example 1 Crab units (C.U.) is $F_{CU}(>E) = 1.78 \times 10^{-7}(E/TeV)^{-1.57}$ [photons m^{-2} s^{-1}]. From this preliminary work by Bernlöhr [39] it is evident that single telescope-type arrays are not adequate to achieve the milli-Crab sensitivity goal within a 50 hour observation for the full energy range.

The production cost of a large-sized telescope (LST) is dominated by its structure, whereas the production cost of a medium-sized telescope (MST) is somewhat equally balanced between the camera and its structure and the production cost of a small-sized telescope (SST) is dominated by the camera. At this stage of the design process it appears as though consensus has been reached for the large and medium sized telescopes. However more work still needs to be done to find the optimal balance between cost and performance of the small-sized telescopes. One option is to have a traditional Davies-Cotton [53] design that is simply a scaled down version of the medium-sized telescopes. An alternative proposal is to have dual-optic Schwarzschild-Couder [108] [51] telescopes, somewhat of a break from the traditional Cherenkov telescope. Although their construction is complex, the immediate benefit of constructing a dual-optic telescope is that the camera plate size can be reduced and hence a significant cost saving can be realised. The research conducted for this thesis does not consider dual-optic telescopes. The sensitivity performance of the final CTA array might be different depending on the findings of the ongoing research into dual-optic telescope performance studies.

Preliminary CTA Monte Carlo studies were conducted by Bernlöhr et al. [42] using different array layouts (shown in Figure 3.1). This preliminary simulation work included a scaled-up 41 telescope version of H.E.S.S., a compact 9 telescope array where each telescope had a much larger collection area of $\sim$ 420 m^2, and a large 97 telescope array with two different telescope sizes. This early work found that by including large telescopes with an increased collection area, it is possible to lower the array threshold energy. In addition, by combining different-sized telescopes (in the case of the 97 telescope array) it is also possible to achieve a low-energy threshold whilst improving background rejection [39]. Much of this work laid the foundations for what became known as the CTA production-run 1 array layout. Figure 3.2 illustrates the CTA production-run 1 array layout that is comprised of 275 telescopes and 3 different telescope types; LST, MST and SST.

Due to limited financial resources it is unrealistic that such a large array could be built. Therefore various smaller subarrays, that are realistically affordable, have been derived from this 275 production-run 1 layout. A total of 14 subarrays were derived from the production-run 1 layout. Preliminary work showed that many of these subarrays could be ignored as their performance was not capable of achieving the CTA sensitivity goals. Therefore this research considers four of the CTA (southern-site) subarray layouts that have the potential to meet the set goals. For convenience these layouts shall be called Subarray-E, Subarray-I, Subarray-J and Subarray-K. Each of these subarray layouts comprise different telescope sizes and are all are shown in Figure 3.3 below. Subarray-E (top left panel) is known as the baseline array and has 4 LSTs ($\sim$23 m diameter), 23 MSTs ($\sim$12 m diameter) and 32 SSTs ($\sim$6 m diameter). Subarray-I (top right panel) consists of 3 LSTs, 18 MSTs and 56 SSTs. Subarray-J (bottom left panel) consists of 3 LSTs, 46 MSTs of which 30 have an 8 degree field of view (red markers) and 16 have a 9 degree field of view (blue markers). Subarray-J has no SSTs. Finally, Subarray-K (bottom right panel) consists of 5 LSTs, no MSTs and 71 SSTs.

In addition to the subarrays shown above it is also worth looking at one further subarray. For convenience this will be called Subarray-B (See Figure 3.4) and is comprised of 37
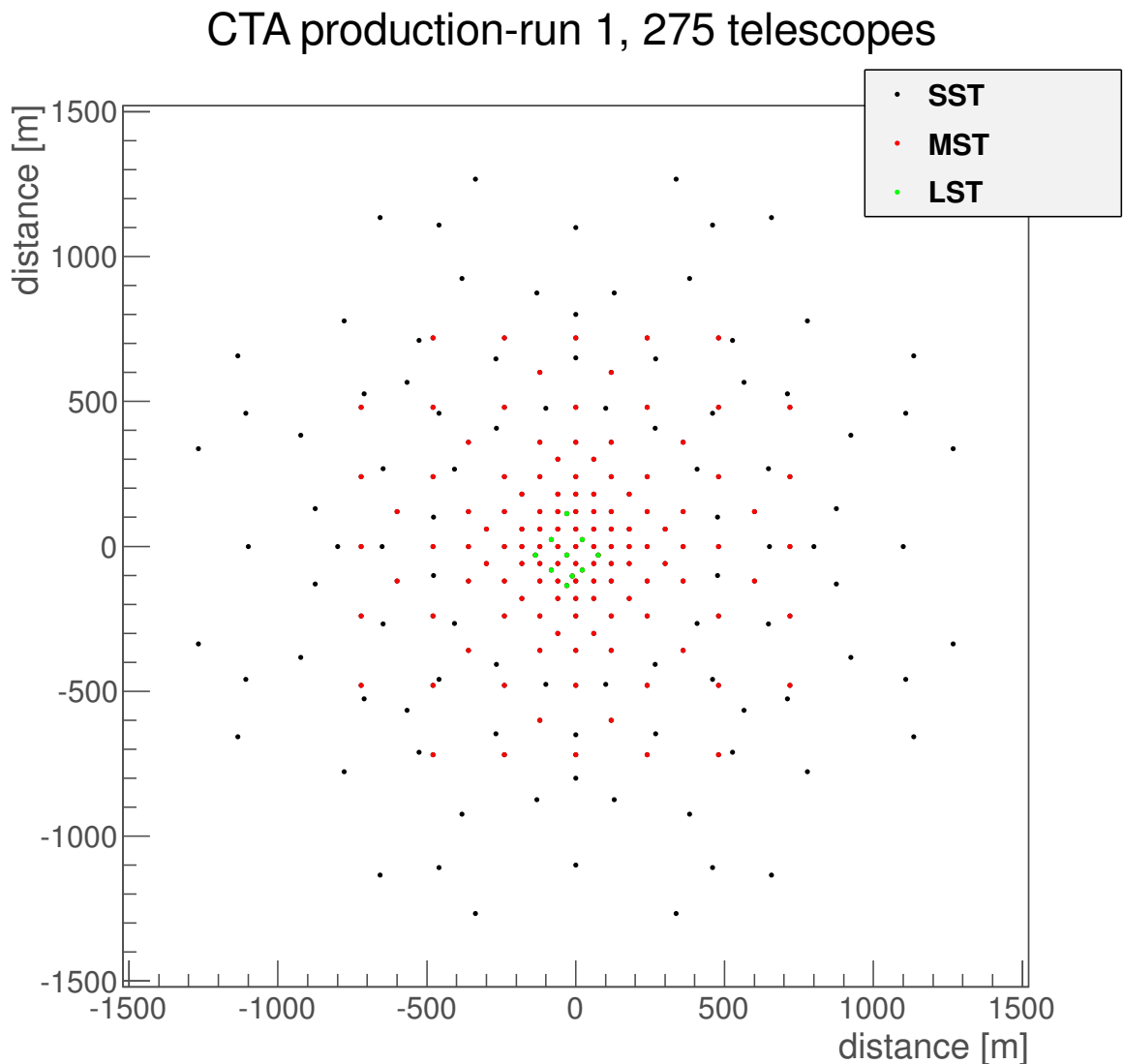
Figure 3.2: The CTA production-run 1 layout comprising 275 telescopes and 3 different telescope types; LSTs (green markers), MSTs(red markers) and SSTs (black markers). The size of the markers are not representative of the telescope size, instead they illustrate where the different types of telescope may be located. It is unlikely that such a large ground-based Cherenkov telescope array would be built unless financial resources were plentiful. This layout was designed by Dr. Konrad Bernlöhr and Prof. Jim Hinton

MSTs and 5 LSTs. Although Subarray-B is not expected to achieve the sensitivity goals across the full CTA energy range, compared to the four subarrays above, Subarray-B is expected to perform extremely well in the low sub 100 GeV energy range thus making this subarray a strong candidate for the study of objects such as pulsars.
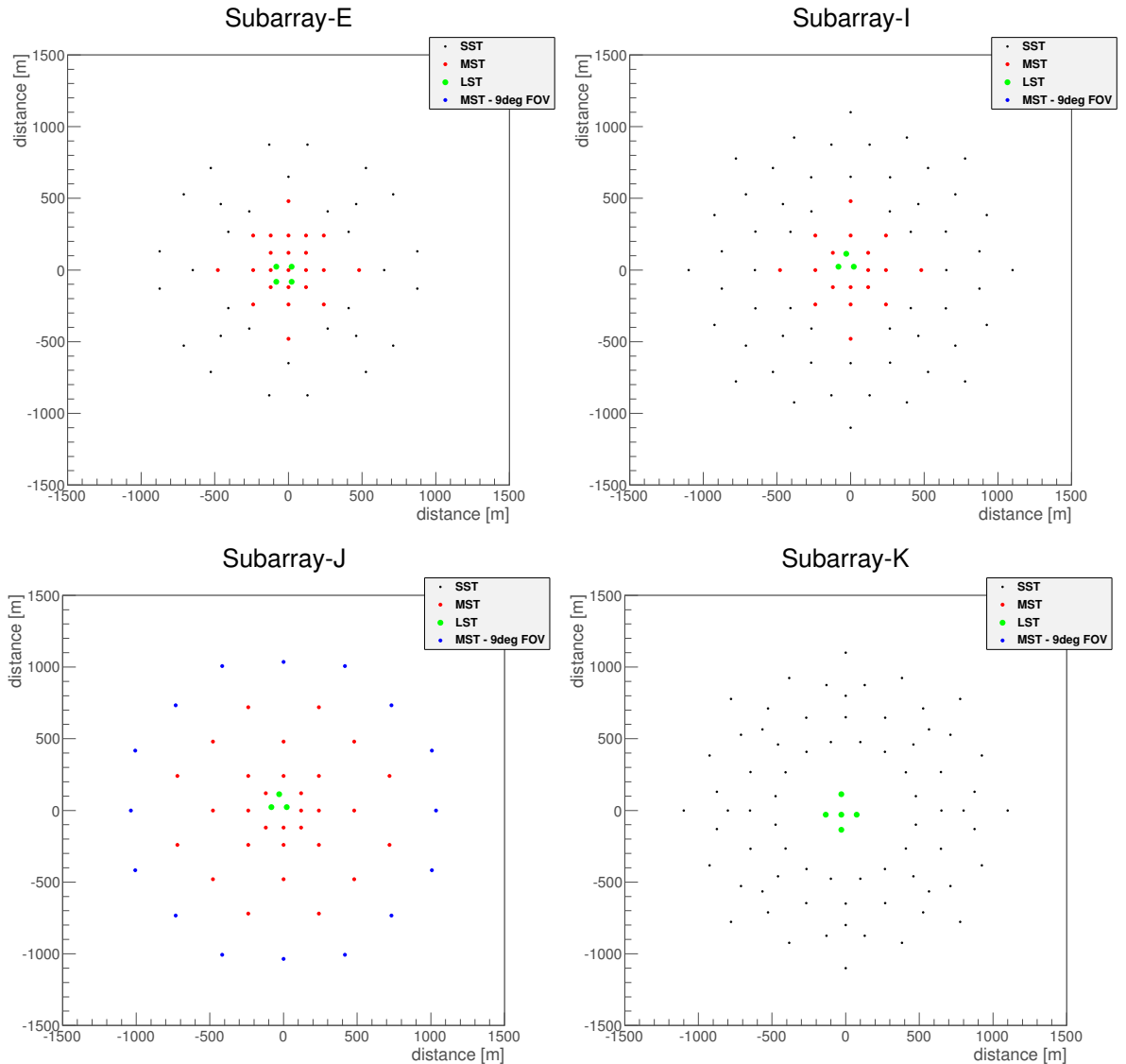
Figure 3.3: Shown here are 4 different potential layouts for the CTA southern site. Subarray-E (top left panel) is known as the baseline array and consists of 3 different telescope types; 4 large sized telescopes (LSTs, ∼23 m diameter, green markers), 23 medium sized telescopes (MSTs, ∼12 m diameter, red markers) and 32 small sized telescopes (SSTs, ∼6 m diameter, black markers). Subarray-I (top right panel) consists of 3 LSTs, 18 MSTs and 56 SSTs. Subarray-J (bottom left panel) consists of 3 LSTs, 46 MSTs and no SSTs. Finally, Subarray-K (bottom right panel) consists of 5 LSTs, no MSTs and 71 SSTs. These layouts were designed by Dr. Konrad Bernlöhr and Prof. Jim Hinton
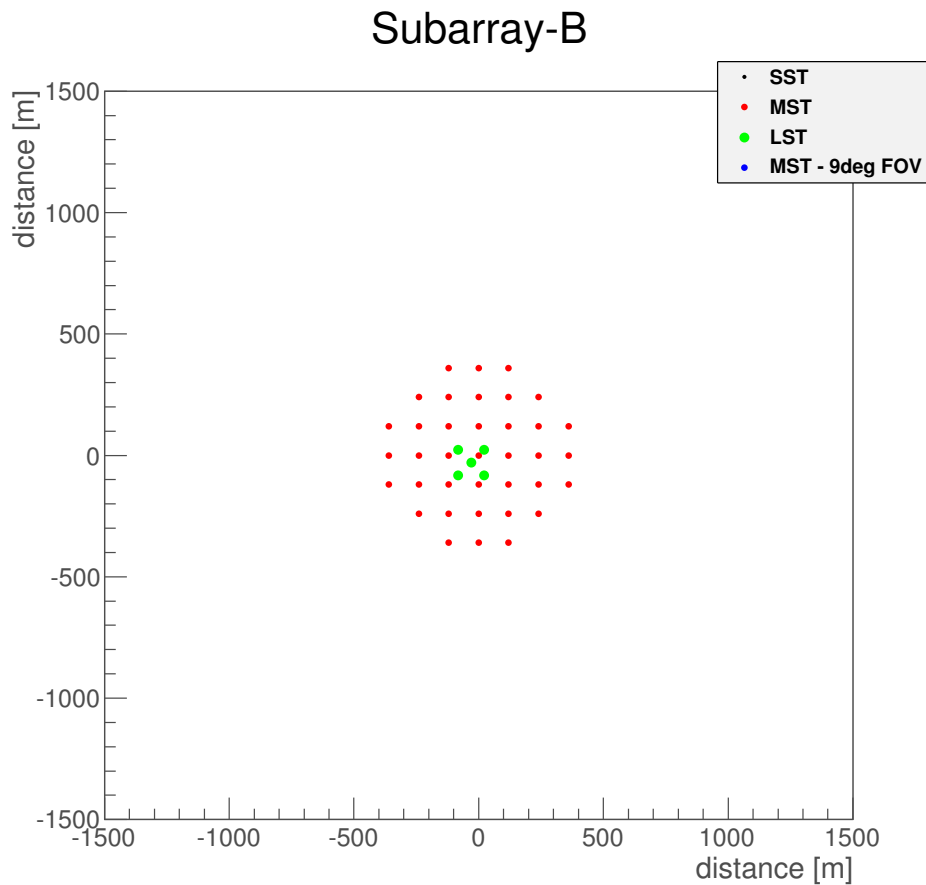
Figure 3.4: CTA Subarray-B comprising 37 medium-sized and 5 large-sized telescopes. This is one of the more compact subarrays that could be potentially interesting for studying astrophysical sources such as pulsars in the low-energy regime below $\approx$ 100 GeV. This layout was designed by Dr. Konrad Bernlöhr and Prof. Jim Hinton

3.2 Performance studies

In order to predict the performance of CTA a comprehensive Monte Carlo simulation has been conducted by many groups across Europe. The work presented here is one of five key contributions toward the CTA Monte Carlo Working Group (MCWG) research specifically focused on analysis and sensitivity of the southern site across the full energy range. Many smaller, focused studies have also been conducted by various people within the MCWG and the results presented here are a small yet important part of a very large effort. Where applicable the results of this research are shown and compared with results from other MCWG contributors. For simplicity these are all denoted as follows: this work (Durham),

Konrad Bernlöhr (MPIK), Abelardo Morelejo (IFAE), Yvonne Beccherini (Paris), Dan Parsons (Leeds) and Gernot Meier (DESY). The key differences between these independently calculated performance studies are highlighted in Section 3.2.1.3. Finally the key steps within the performance study are highlighted as well as how the key performance indicators were calculated.

The Monte Carlo simulation process that has been adopted for this research is simplified for convenience in Figure 3.5.

3.2.1 CTA simulations

As one might imagine, the parameter space for simulating such a facility as CTA is vast. The following list provides an example, but is by no means comprehensive:

- Array layout, including for example site and atmospheric characteristics.

- Telescope sizes, including for example mirror optics and efficiency.

- Telescope camera optics, including for example pixels, field of view and efficiency.

- Telescope electronics, including for example trigger logic and signal pulse shapes.

A starting point for many of these parameters has been provided by the experience gained from the existing ground-based systems. However, extensive simulation is needed (and indeed is still ongoing) to optimise many of these parameters for the final CTA array that can achieve the target sensitivity within budget. The performance study process can be broken down into 4 key areas:

1. Air shower & telescope simulations.

2. Shower reconstruction and analysis.

3. Multivariate-based background rejection.
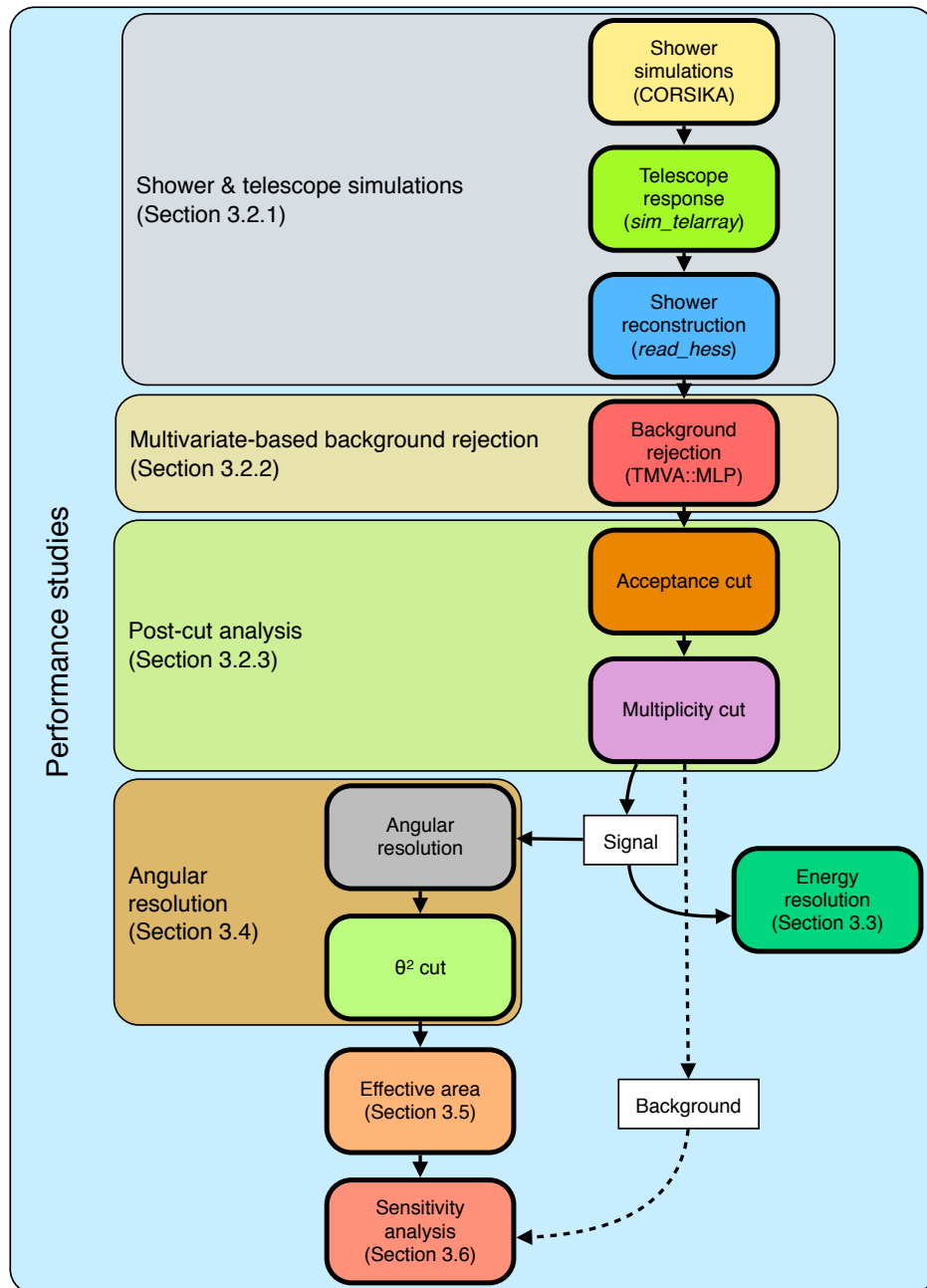
Figure 3.5: Flow-chart to help simplify the Monte Carlo simulation process adopted for this research.

4. Post-cut analysis.

Each of these areas is addressed in the sections that follow.

3.2.1.1 Air shower & telescope simulations

Air shower simulations entail simulating the propagation and interaction of gamma-rays, protons and other particles through the atmosphere all the way to the ground. All air shower simulation has been conducted using the widely used (and tested) CORSIKA [72] software program. Full discussion of CORSIKA is beyond the scope of this thesis; however extensive work has been done to integrate CORSIKA within the telescope simulation package *sim_telarray* by its author Dr. Konrad Bernlöhr [40], [41]. The *sim_telarray* package simulates the detection of the Cherenkov light from the air shower including all the telescope optics and full electronics chain.

The sensitivity performance of Cherenkov telescopes reaches its maximum when observing at zenith angles $\lesssim 30°$ [84]. In addition this is also where the system's minimum energy threshold is expected. Therefore in order to determine CTA's prospects of detecting pulsed emission from astrophysical objects such pulsars, this research only uses archived Monte Carlo simulations of point-like sources conducted at a zenith angle of 20 degrees. In addition, the sensitivity performance of Cherenkov telescopes such as H.E.S.S. has an angular dependence, based upon their point spread functions, when observing objects at large angular distance from the source axis [50]. The off-axis sensitivity performance of CTA has not been considered in this research. Although expected to be very important in the study of extended objects such as pulsar wind nebulae (PWN) it is not critical for the on-axis observations of pulsars. All the shower simulations used for this research assume a source energy distribution of $\frac{dN}{dE} \approx E^{-\gamma}$ where $\gamma = 2$. This is a reasonable assumption that reflects many of the source energy distributions seen. When undertaking a simulation exercise on the scale required for CTA, a very large number of showers needs to be simulated in order to maintain adequate statistics at the detection and post-analysis stages. The following lists the number of events (by primary particle) simulated for the CTA shower simulation archive that have been used in this thesis:

- $\gamma = 2.5 \times 10^9$.

- $p = 50 \times 10^9$.

- $e^- = 2.6 \times 10^9$.

- other heavy particles $= 6 \times 10^6$.

The simulations used approximately 6.4 Terabytes of disc space and took approximately 1100 CPU years to complete. At these scales many thousands of processors were utilised on the European Grid Infrastructure (EGI) [4]. The simulation data generated using the CORSIKA and *sim_telarray* programs were reduced into Data Storage Tree (DST) files. The DST format is a reduced file format that saves computing disc space by not containing all the individual pixel information.

The simulations of the gamma-ray-induced air showers were scattered over a ground area with radius $R_\gamma = 2500$ m and the cosmic-ray initiated air showers were scattered over a ground area with radius $R_{\text{cosmic rays}} = 3000$ m. This radius is defined as the 'air shower scattering radius' and is discussed further in Section 3.5. Finally, the sensitivity results presented in this thesis do not take into account the additional heavy particles as their effect on overall sensitivity performance is expected to be negligible. This is discussed further in Section 3.6.

3.2.1.2 Shower reconstruction and analysis

The shower reconstruction and analysis was performed using the *read_hess* software programme on the DST simulation files produced for each of the four array layouts mentioned above. The *read_hess* software program was developed by Bernlöhr [38] to allow fast and efficient processing of simulation files using the *hessio* file format developed for H.E.S.S. The *read_hess* program is run 3 times on the same DST file in order to:

1. Calculate the expected parameters and fill lookup tables for energy and shape etc.

2. Calculate the mean scaled parameters for each event.

3. Perform the final analysis by applying cut optimisations like energy and shape cuts.

Thus *read_hess* performs a full shower reconstruction from the ellipse intersection of the simulated camera images producing the reconstructed energy, the shower core distance as well as the angle to the shower core for each event. All these calculated parameters and many more are easily exported from *read_hess* into an ntuple ASCII [3] file.

Various cuts and parameters can be supplied to *read_hess* which can affect the analysis. The following list provides a non-comprehensive set of examples:

- *Image amplitude cuts* - the minimum photo-electron (p.e.) amplitude required in each image.

- *Tail cuts* - how pixel clusters are to be defined (see Section 2.4.2).

- *Minimum pixel cuts* - the minimum number of triggered pixels required in each image.

- *Minimum telescopes cuts* - the minimum number of triggered telescopes required in each event.

- *Energy and shape cuts* - place global cuts on images to use only the best data from relatively nearby events.

To determine the sensitivity performance for each of the subarrays highlighted above it is widely accepted that the following cuts be implemented: image amplitude cuts should be $\geq$ 30 p.e. with 5-10 tail cuts, a minimum of 3 pixels per image and 2 telescopes per event. To reduce systematic uncertainties in the directional reconstruction it is possible to increase the number of telescopes required per event, however this may lead to fewer events triggering. The actual cuts implemented for all of the subarrays analysed in this work were a minimum image amplitude of 60 p.e., 5-10 image cleaning tail cuts, a minimum of 3 pixels per image and a minimum of 2 telescopes per event. The energy and shape cuts were ignored because background rejection was performed using an alternative method discussed in the next section.

3.2.1.3   Analysis methods implemented within CTA

As mentioned earlier, in addition to the results calculated for his research, CTA performance results have also been calculated independently by other members of the CTA Monte Carlo Working Group (MCWG) and some of these results are shown in this thesis for the purposes of comparison. It is prudent to have independently calculated performance results to allow for scientific discussion, comparison and continuous improvement. This section highlights some of the key differences between each of the independent results shown in this work. Using the same shower simulations and telescope responses i.e. the same starting point, the general idea is to derive a set of CTA performance results based upon:

1. the standard H.E.S.S. analysis (MPIK results) [25], [52].

2. the standard MAGIC analysis (IFAE results) [28] .

3. the standard VERITAS analysis (DESY results) [90].

4. an approach that uses a sophisticated reconstruction analysis method (e.g. the 3D-model analysis method [85]) to obtain additional shower information which is then input into a neural network to obtain better background rejection [34]. (Paris and Leeds results)

5. a hybrid approach using the H.E.S.S. based shower reconstruction but utilising a neural network for background rejection (this work).

Apart from point number 3 above, all methods use a Hillas based shower reconstruction method (See Chapter 2). However not all methods use the same background rejection methods. Additional information regarding the approaches taken can be found in the references provided above. Finally, the sensitivity calculation (although independently implemented) is the same for each of the methods listed above and this is discussed further in Section 3.6.

3.2.1.4 Uncertainties on the performance results

Calculating, propagating and displaying uncertainties is a very difficult task as the analysis chain is exceptionally long and complicated. The generally accepted rule has been to assume a systematic uncertainty of approximately 15% across all energies. However, in practice this would not reflect the true system performance as a function of energy. For example at low energies it is reasonable to expect the systematic uncertainty to be dominated by the uncertainty associated with shower reconstruction where the background dominates. In addition, the uncertainties associated with the quality of the background rejection method will also be significant. At high energies where the cosmic-ray background no longer dominates, the uncertainties associated with directional reconstruction are diminished. Instead, at high energies statistical uncertainties dominate due to the rather steep gamma-ray flux spectrum and the even steeper cosmic-ray flux spectrum used for determining the sensitivities. In addition, uncertainties in the shower simulations are dominated by the uncertainty in the proton cross-section as well as the uncertainties in the assumed cosmic-ray spectrum. These will have a large impact on the background rates which form part of the sensitivity calculation. It is common for sensitivity curves to be published without error bars and the same approach has been adopted in this work. One approach might be to consider the true sensitivity performance to lie somewhere in between the best and worst independently calculated performance results.

3.2.2 Multivariate-based background rejection

Chapter 2 highlighted the different approaches taken between space-based and ground-based astronomy instruments toward cosmic-ray background rejection. For the ground-based instruments additional analysis needs to be conducted in order to separate the signal events from the background events. As discussed in Chapter 2, existing ground-based Cherenkov systems do this using the standard Hillas method of parameterising the shower images. The method itself is extremely robust, but for CTA to realise its sensitivity goals

additional analysis techniques need to be applied, such as the *3D-model* analysis [85] or the multivariate approach utilising *boosted decision trees (BDTs)* [98] [34]. By implementing a multivariate method, the information contained in many parameters that help to distinguish between signal and background events can be combined to obtain a single response parameter. This response parameter called zeta (ζ) enables events to be classified according to their gamma-ray or cosmic-ray 'likeness'. When utilising a multivariate software package such as TMVA [77], both Ohm et al. [98] and Becherini et al. [34] have shown that significant improvements in performance can be obtained compared to the standard cuts background rejection method. Multivariate methods can be seen as an extension of the standard cuts-based discrimination method. The reasonable cost, availability and processing power of modern desktop (and even laptop) computers enables machine learning algorithms such as artificial neural networks, decision trees, likelihood estimators and Fisher discriminants to be easily implemented. As noted by Ohm et al. [98], one of the main advantages of neural networks and BDTs over likelihood and Fisher discriminants, is their ability to handle nonlinear correlations between parameters. This thesis applies a multi-layer perceptron (MLP) neural network for the background rejection method. It has been suggested that BDTs are the preferred multivariate method for two reasons: they ignore non-discriminating parameters and their decision trail is transparent (unlike the MLP). BDTs and MLPs were implemented in the work presented in this thesis, and it will be shown that the MLPs provide results consistent with sensitivity performances calculated using BDTs, but at a fraction of the time taken. It is conceivable that MLPs be used as a 'real-time' analysis tool for analysing observation data recorded with CTA. This work uses the TMVA implementations of a MLP and BDT, and for convenience these are referred to as TMVA::MLP and TMVA::BDT respectively.

3.2.2.1   Basics of the multi-layer perceptron

A neural network is a biologically-inspired (for example by the human brain) architecture for processing information. One of the key principles of such an architecture is that, like

humans, it learns by example in order to recognise patterns which help to solve a specific problem. The concept of artificial neural networks has been in existence for over half a century, but it is the modern processing power of desktop and laptop computers that have led to their implementation across a wide range of disciplines. Like the human brain, a neural network consists of many interconnected information processing elements called neurons. These work in parallel to solve specific problems. In its most simplistic form, one might provide a neural network with many input parameters and it would return a single output.

Distinguishing between signal events and background events requires processing of many image parameters to recognise patterns as shown in Section 2.2.3.2. Computer learning methods are very efficient at performing these tasks. Thus by providing a neural network with the key parameters that help to distinguish between camera images of gamma-ray and cosmic-ray-induced air showers, it is possible to train a computer to distinguish between images relatively quickly. For ground-based gamma-ray astronomy this can be done by training the neural network using Monte Carlo simulations of both gamma and proton air showers for example. Data from observations or a separate sample of simulated data can then be fed into the neural network for signal/background separation based upon its learning during training.

A feature of an MLP is that the neurons are organised into layers and the connections between layers are directional. Commonly called a feed-forward neural network, this is the type used within this research. Various network architectures were tested in this research, but it was found that no significant improvement of sensitivity performance was achievable for the additional processing time required to complete an optimised more complex network. For example a network consisting of 2 hidden layers (with N+5, N+2 neurons in each) typically required 2 hours for training and testing. However a much simpler 2 hidden-layer network with N, N-1 neurons in each, as shown in Figure 3.6, typically required less than 1 hour to train. For the same separating potential, the BDT required up to 6 hours for training and testing not including the significant additional time needed to read and analyse the

data during the post-cut analysis stage see Section 3.2.3. Sensitivity performance resulting from the different training methods will be illustrated later in this Chapter.
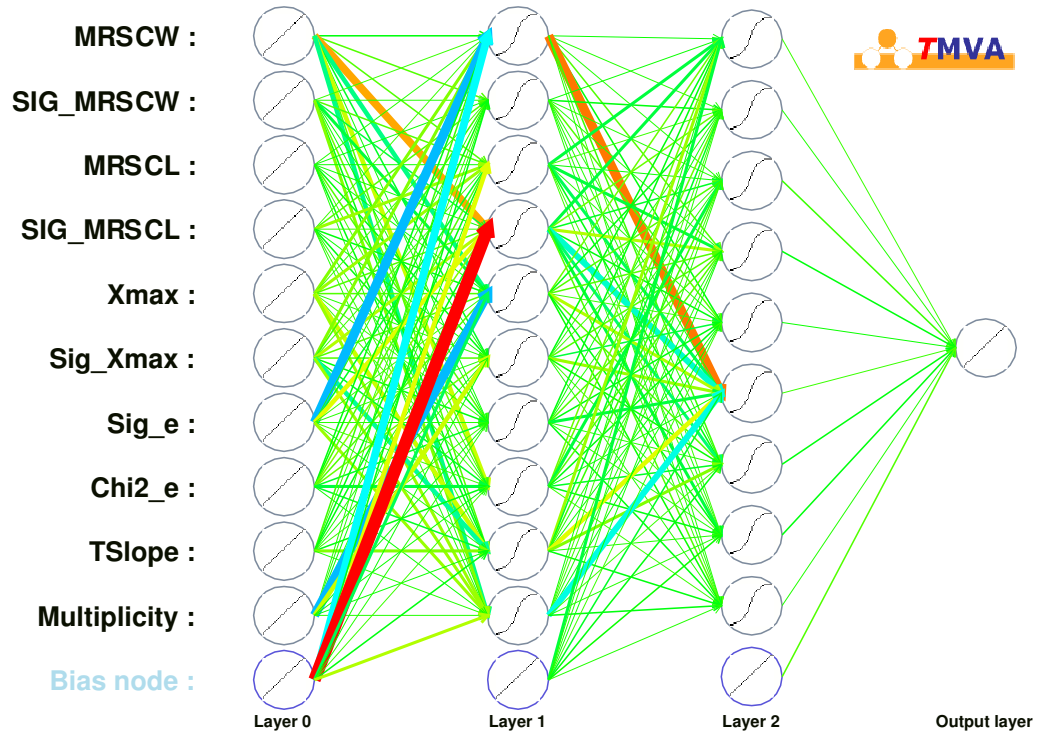
Figure 3.6: A multilayer perceptron neural network, with 2 hidden layers consisting of N, N-1 neurons in each. This simple neural network architecture was implemented for the background rejection conducted in this research. The neural network was implemented using the TMVA software package v 4.1.2. Each of the circles represent the neurons and inside is an illustration of the activation function used within each of these. The MLP implemented for this research uses both linear and non-linear (sigmoid) functions to determine input parameter weightings and hence separating power. The line colours and thickness are representative of the weightings assigned e.g. high (red) to low (green).

Figure 3.6 shows the simple neural network architecture that was implement for the background rejection conducted in this research. The neural network was implemented using the TMVA software package v 4.1.2 shipped within the CERN Root Analysis Framework version 5.30/06 [46]. Each of the circles represent the neurons within which is an illustration of the activation functions used in each. The MLP implemented for this research used both linear and non-linear (*sigmoid*) functions to determine parameter weightings and hence separating power.

The performance of the MLP is dependent upon the input parameters given to the neural network, from which any correlations are determined. The primary parameters needed by

the neural-network are related to the differences between the recorded gamma and hadron camera images i.e. MRSCW, MRSCL and Xmax (see Sections 2.2.3.4 and 2.2.3.5). In addition the spreads of these parameters can also be used to help constrain the widths, lengths and heights of the events. These are the key parameters which should be sufficient to train a basic neural network and achieve reasonable background rejection and are shown in Figure 3.7 .

There are additional parameters (see Figure 3.8) that can be provided to try and make small gains on the overall sensitivity performance, for example the spread of the reconstructed energies divided by reconstructed energy $\sigma_E = \sigma(E)/E_{rec}$ (top left panel). The reconstructed energy is proportional to the total image amplitude and is calculated from a weighted average of all the individual telescope energy reconstructions used to reconstruct the event. Thus one might expect hadronic events to have a larger spread in the reconstructed energies estimated. Similarly if one were to fit a Gaussian to to the reconstructed energies from each of the telescopes, the associated χ^2 value obtained for the fit can be weighted by the number of telescopes used to estimate the reconstructed energies (top right panel). Again for hadronic showers one might expect a larger spread in the uncertainties. Another parameter for training the neural network is the mean time slope (bottom left panel). It is expected that CTA will retain the pixel timing information for the cameras and as the shower develops and subsequently forms an image in the camera, a time gradient is seen [73]. Due to the fact that the cameras tend to image gamma-ray showers from within the light-pool, one might expect these to form more promptly than hadronic showers where the shower core is some distance away from the telescopes. Finally, CTA will provide imaging of showers with different telescope-types as already discussed in Section 3.1.3. Thus it is worth testing whether any correlation exists between shower type and telescope-types triggered for each event. For example, one might expect a higher telescope-type multiplicity for gamma-ray showers as the whole light pool is imaged with the full subarray. However, as hadronic air showers occur more frequently, yet at random locations these may be confined to specific telescope-types. A discrete parameter called 'multiplicity' (bottom right panel)
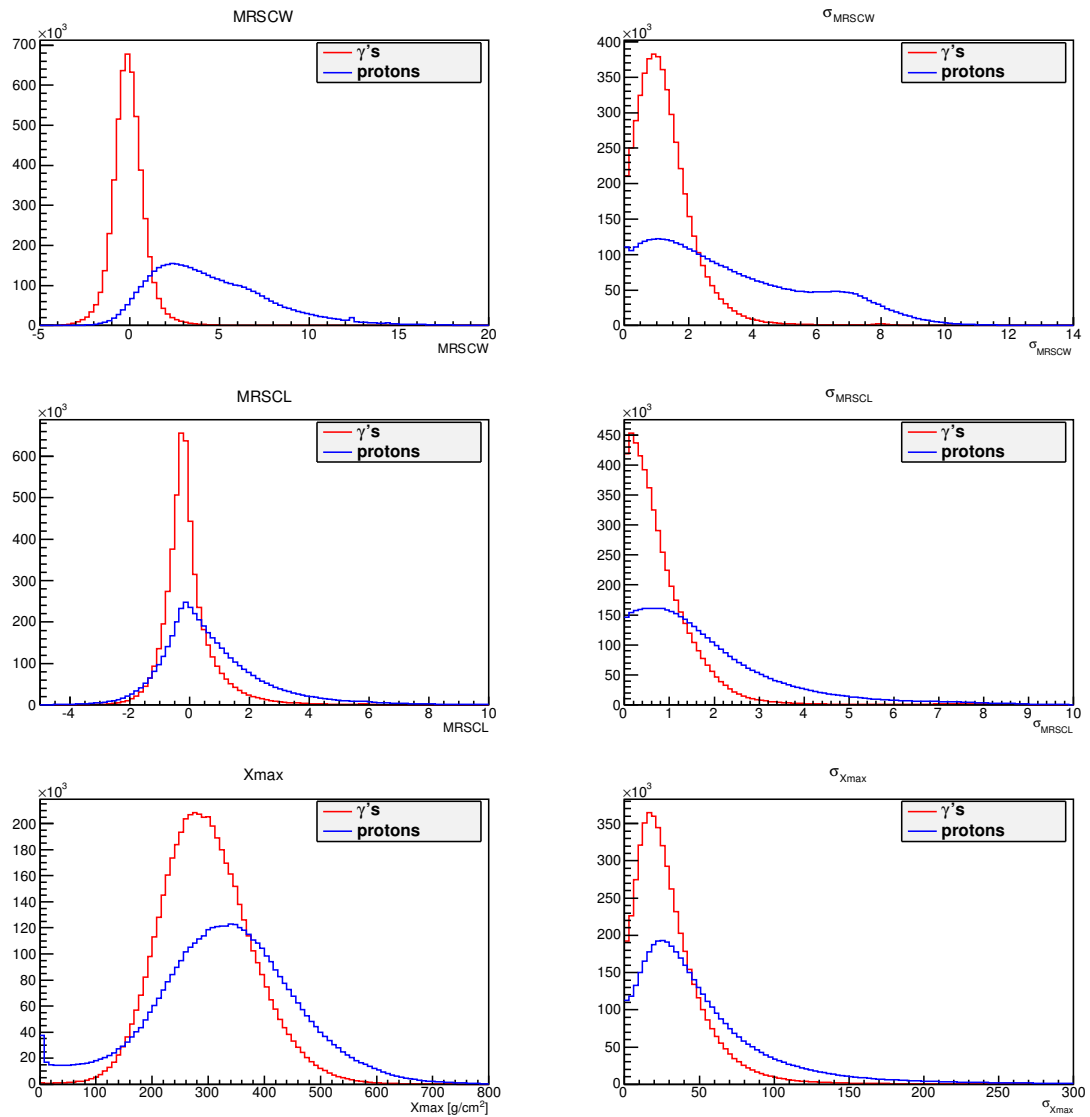
Figure 3.7: Distributions of the six primary training parameters used to train the multilayer perceptron neural network. These include the mean reduced scaled widths (MRSCW) and lengths (MRSCL), the spread of the mean reduced scaled widths (σ_{MRSCW}) and lengths (σ_{MRSCL}), the reconstructed Xmax values as well as their spread (σ_{Xmax}).

was therefore conceived even though it is expected to provide a very small separating power. The multiplicity parameter can be seen as a measure of the combination of telescope-types triggered for each event. These additional parameters are shown in Figure 3.8 for CTA Subarray-I. The number of events will be different for each subarray analysed due to the physical layout of the arrays and the telescope sizes in the array as well as any optimisation cuts made during shower reconstruction and analysis. This includes, but is not limited to, tail cuts and minimum telescope number for example.
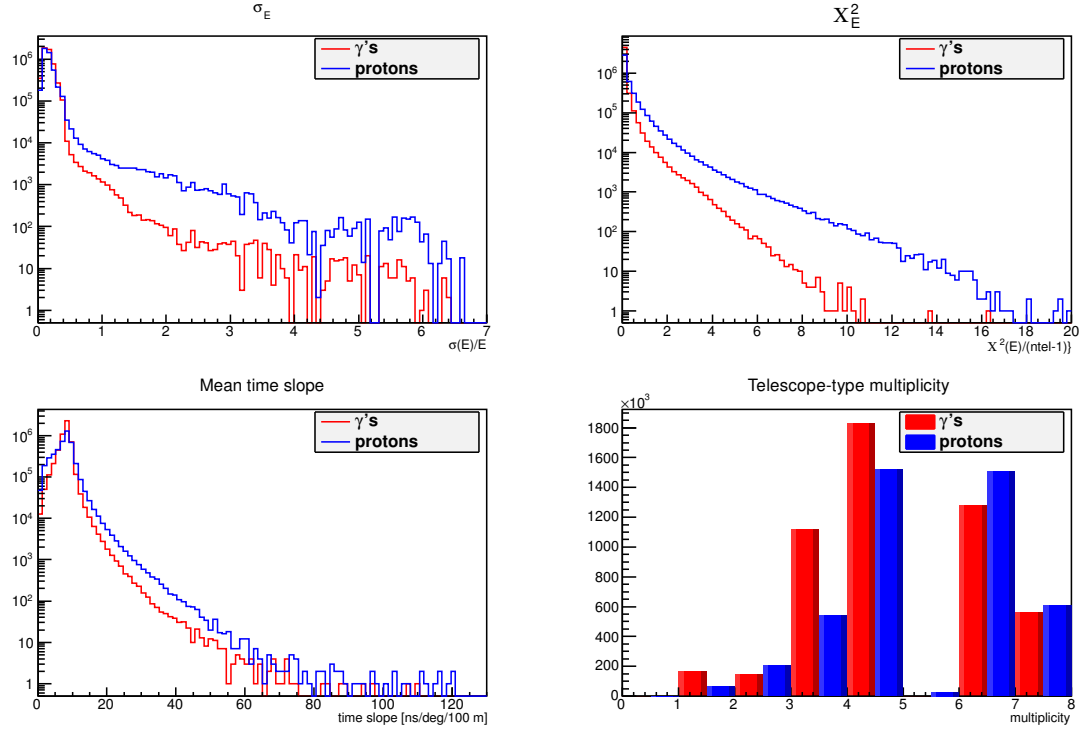
Figure 3.8: Distributions of the additional training parameters used to train the multilayer perceptron neural network. These include spread (σ_E) and chi-squared (χ^2_E) fits of reconstructed energy, the corrected mean time-slope values as well as the new discrete multiplicity parameter. In this particular example no gamma events, and only tens of proton events, triggered the telescope type combination defined as multiplicity = 5 (bottom right panel). This result is dependent upon the physical telescope layout within each subarray.

Table 3.2 lists the TMVA::MLP parameters and the values used in this research. For a detailed description of the different parameters and options available see [77].

Table 3.2: TMVA::MLP settings.

TMVA option	Value
Neuron type	sigmoid
Cycles	600
Hidden layers	N, N-1
Test rate	10
Variable transform	Normalise
Bayesian Regulator	No

3.2.2.2 Basics of the TMVA::BDT

Earlier it was mentioned that within ground-based gamma-ray astronomy a lot of background separation work has been done utilising BDTs. It is beyond the scope of this thesis

to assess the performance of the BDT multivariate method but further reading of Ohm et al. [98] is recommended. Table 3.3 lists the TMVA::BDT parameters and the values used in this research, for comparison with the TMVA::MLP approach. For a detailed description of the different parameters and options available see [77].

Table 3.3: TMVA::BDT settings.

TMVA option	Value
Trees	200
Boost type	AdaBoost
Separation type	Gini Index
Cuts	100
Minimum events	20
Use yes/no leaf	True
Prune method	Cost Complexity
Prune strength	5
Maximum Depth	100

3.2.2.3 Determining the TMVA cut

Implementing a neural network for background rejection within the CTA analysis framework allows for background cosmic-ray air showers to be rejected using a single cut parameter (ζ) known as the TMVA response. However exactly where the cut is made still requires some additional thought and analysis. Figure 3.9 illustrates a typical response from a TMVA::MLP neural network used to successfully separate signal-like events (solid blue) from background-like events (diagonally-lined red). Determining the TMVA cut on such a distribution that includes all events for all energies does not take into account any energy dependence that may exist. For example cosmic-ray protons typically follow a steep power law $E^{-\gamma}$ spectrum with $\gamma = 2.7$, whereas a typical gamma-ray spectrum, and indeed the spectrum used for all gamma simulations in this research, typically follows a spectrum with $\gamma = 2.0$. Above a few TeV it is reasonable to expect a signal-dominated regime whereas at lower energies, certainly under 100 GeV, it is reasonable to expect a much higher cosmic-ray background. With this in mind it is preferential to place all the events into a suitable energy-binning scheme. For this research, and in accordance with other members of the CTA MCWG, an energy binning scheme of 5 bins per decade (in $\log_{10}(E/TeV)$ energies)
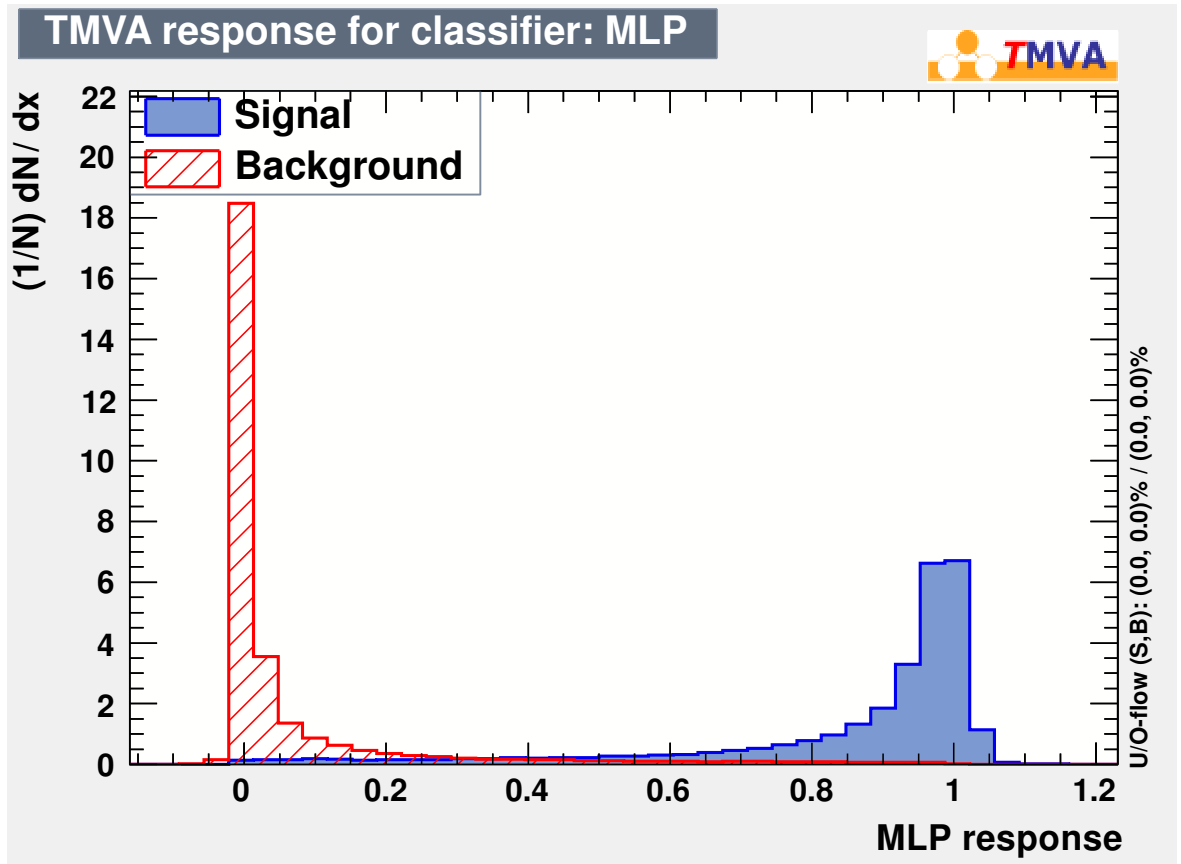
Figure 3.9: A typical MLP response obtained when training a neural network using simulated signal(γ) and background (proton) events. In this example, the neural network response centres signal-like events (solid blue) around 1 and background-like events (diagonally-lined red) around 0. This separation includes all events for all energies and choosing a fixed cut parameter on such a distribution of separated events does not take into account any energy dependence.

has been used.

For this research 5 different methods to derive the ζ cut value have been tested:

1. *Fixed cut method.* The first and simplest method is to choose an arbitrary fixed ζ cut for all energies based upon the MLP response.

2. *Energy-scaled cut method.* The second method chooses the ζ cut value, in each energy bin, to be where the number of signal events are at least 50% greater than the number of background events.

3. *Fixed signal efficiency cut method.* The third method chooses the ζ cut value in each energy bin based upon a predefined fixed post-cut signal efficiency.

4. *Function signal efficiency cut method.* The fourth method chooses the ζ cut value in each energy bin based upon a post-cut signal efficiency that is predefined with a function.

5. *Energy-scaled significance cut method.* Finally, the fifth method chooses the ζ cut value in each energy bin to be where the difference between the signal significance and the background significance is maximised.

For all methods implemented the basic principle is the same. Events with a ζ value less than the chosen cut value are deemed to be background-like and are therefore omitted from the analysis. Events, both signal and background, with a ζ value greater than the chosen cut value are kept for further analysis. The following sections highlight the results from implementing these methods.

3.2.2.4 Fixed cut method

The first method requires choosing an arbitrary fixed ζ cut value for all energies. This fixed cut can be implemented using the standard TMVA response shown in Figure 3.9 above. Alternatively, the response data can be shown as a 2-dimensional histogram binned in energy along the x-axis and response parameter ζ along the y-axis as shown in Figure 3.10. In this example both signal and background events are included in the same histogram. The colour scale on the right indicates red to be the highest density of events and blue the lowest. As expected for standard TMVA response the background-like events are clustered around $\zeta = 0$ and signal-like events are clustered around $\zeta = 1$. An arbitrary fixed cut value of $\zeta = 0.8$ has been chosen (solid blue line) for all energies. It is clear that this method eliminates most of the background events, but it is not immediately obvious which ζ value will provide the best performance results. If the cut is too strict then too many signal events can be lost, similarly if the cut is too loose too many background events will be included into the sensitivity analysis. Moreover the fixed cut approach fails to take into account any energy dependence that exists.
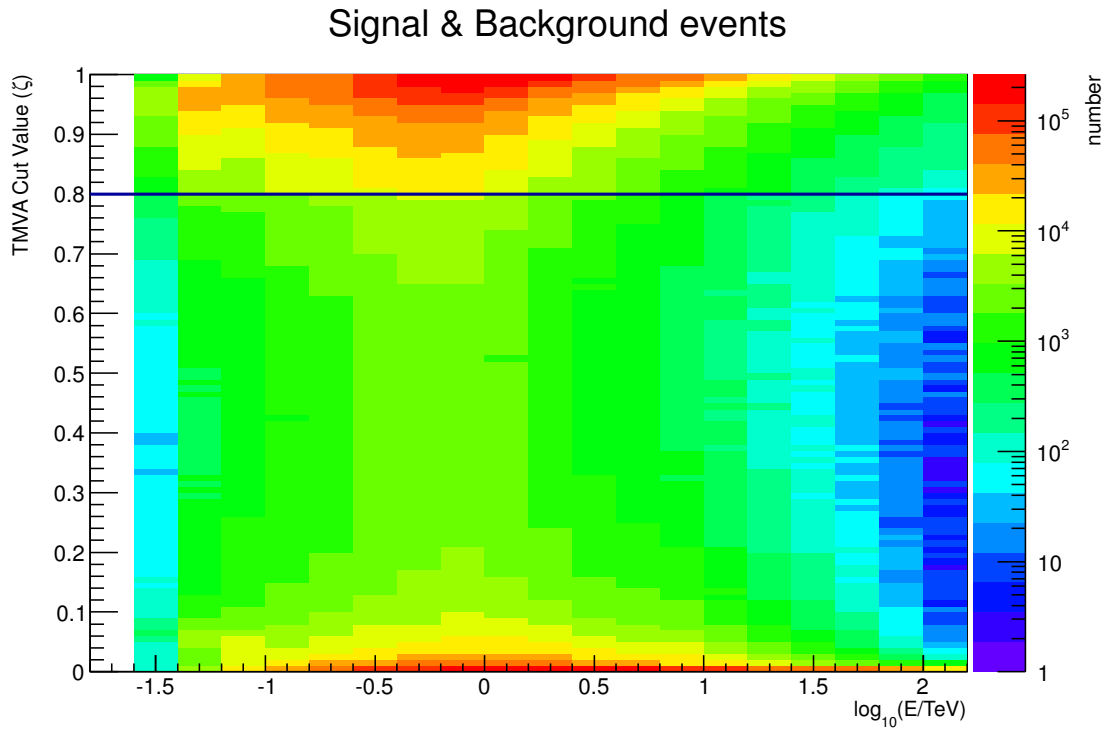
Figure 3.10: A 2-dimensional histogram of the TMVA::MLP response for signal and background events binned in log energy along the x-axis and ζ response parameter along the y-axis. The colour scale on the right shows event number density where blue is the lowest and red the highest. Using the *fixed cut method*, an arbitrary fixed cut value $\zeta = 0.8$ (solid blue line) was chosen for all energies. It is clear that choosing a fixed cut parameter for all energies does not take into account any energy dependence of the events which could significantly affect net performance.

3.2.2.5 Energy-scaled cut method

Unlike the fixed cut method, the second method attempts to take energy dependence into account. This is done by choosing the ζ cut value in each energy bin to be the point at which the number of signal events is at least 50% larger than the number of background events. In practice this requires that the number of signal and background events be evaluated for all response parameters values. Starting from $\zeta = 0$ the event numbers are evaluated until the first instance that the number of signal events is larger than the number of background events. This process continues until the number of signal events are at least 50% larger than the number of background events in that ζ bin. The 50% value is arbitrary, but is designed to take into account any uncertainty that exists when the number of background events fluctuate. Figure 3.11 illustrates the TMVA::MLP separated signal

(red) and background (blue) events for each energy bin. Also shown is the energy-scaled ζ cut parameter (dashed pink line) found for each energy bin. Closer inspection of the 25 GeV energy bin demonstrates how the number of background events can fluctuate as their response value nears $\zeta = 1$. Thus using the first instance where signal events exceed background events is not necessarily accurate for determining the cut parameter. This is especially true for the low-energy bins where there is a larger uncertainty. As shown in Figure 3.11 an overly cautious approach in the low-energy bins can result in too many signal events being cut from the analysis.

3.2.2.6   Fixed signal efficiency cut method

The third method chooses the ζ cut value in each energy bin based upon a predefined post-cut signal efficiency. This can be done by choosing an arbitrary fixed post-cut signal efficiency value for all energies. Figure 3.12 illustrates the predefined fixed post-cut signal efficiency (right panel, red line) which in this example is chosen to be a maximum of 70%. In order to achieve this post-cut signal efficiency the ζ cut values are then determined in each energy bin as shown in the left panel. Also shown in the right panel is the post-cut background efficiency (blue line) that results. It is possible to implement this method using multiple post-cut efficiency values to find the fixed efficiency value that delivers the best sensitivity performance. This is beneficial because the optimum post-cut signal efficiency is expected to be different for each subarray.

Figure 3.13 illustrates the MLP response for the signal events (left panel) and background events (right panel). The derived ζ cut values (solid black line) are also shown. Like the *fixed cut method* in Section 3.2.2.4, it is possible to cut too many signal events in the middle energy regime if the predefined post-cut signal efficiency requires a strict ζ cut. Potentially this can result in a loss of sensitivity performance. However, strict cuts also eliminate a greater number of background events and thus the overall effect on sensitivity may be minimal.
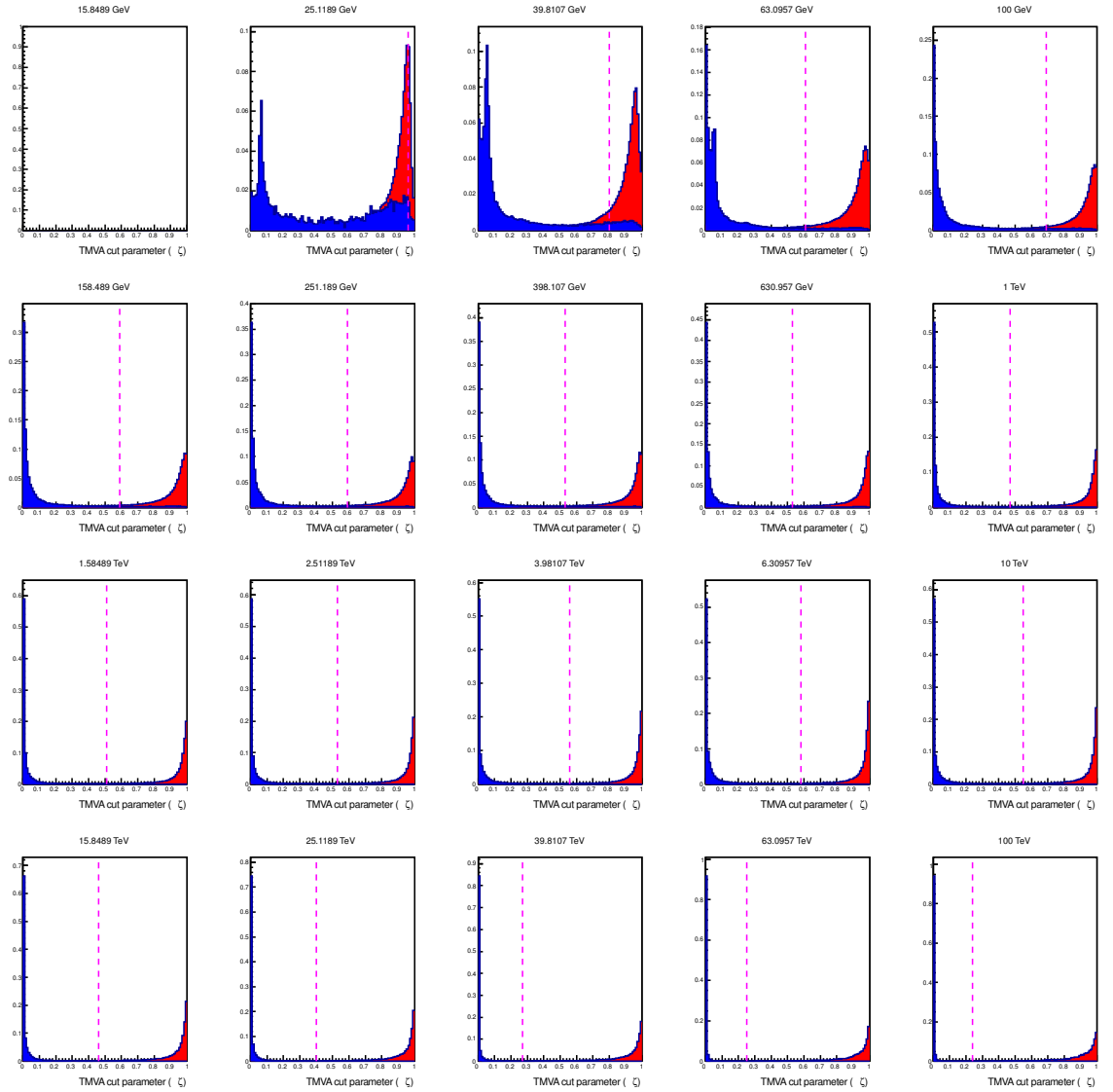
Figure 3.11: CTA Subarray-I MLP response of separated signal (red) and background (blue) events for each energy bin. The y-axis shows the normalised fraction of events and the x-axis shows the MLP response parameter. Also shown is the energy-scaled ζ cut parameter (dashed pink line) found for each energy bin. The *energy-scaled cut method* determines the cut parameter by finding the first instance where the number of signal events is at least 50% greater than the number of background events. An overly cautious approach in the low-energy bins (see 25 GeV energy bin) can result it too many signal events being cut from the analysis.
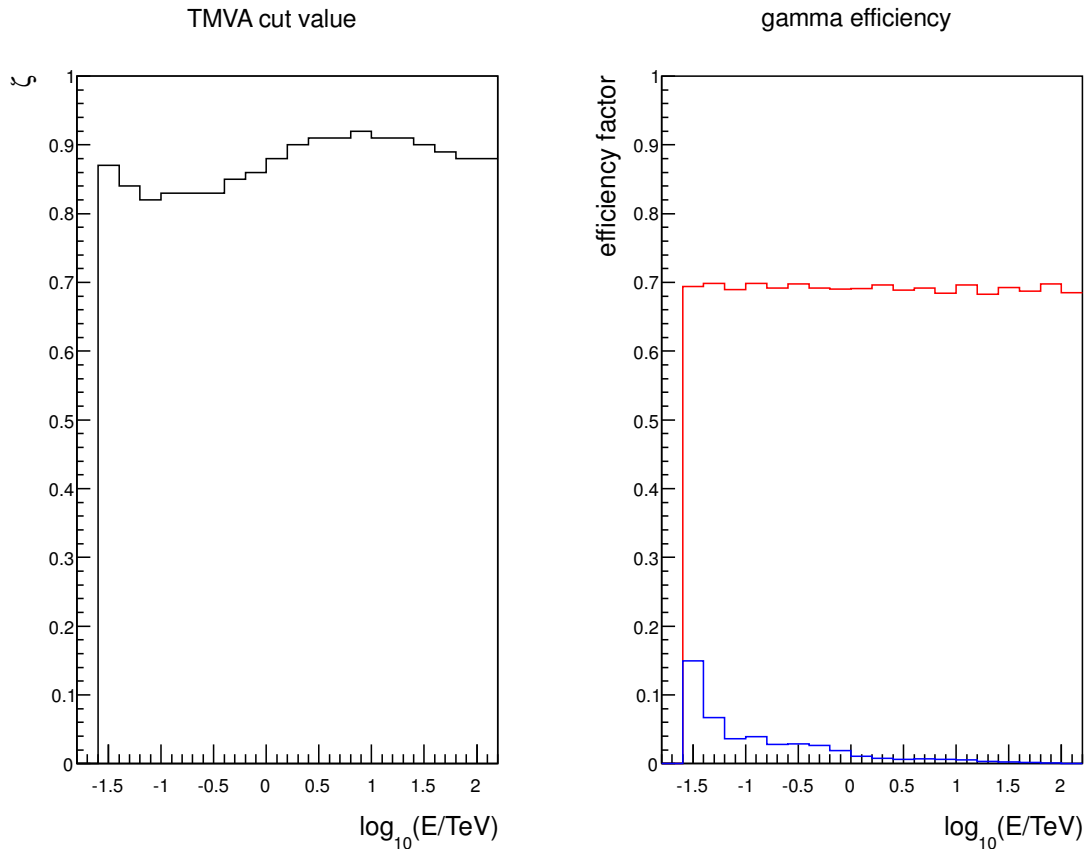
Figure 3.12: The CTA Subarray-I ζ cut parameters for each energy bin (left panel) derived by predefining a fixed post-cut signal efficiency for all energies (right panel, red line). Using the *Fixed signal efficiency cut method*, the post-cut signal efficiency is fixed at an arbitrary value of 70%. Also shown are the background efficiency values (right panel, blue line) that result from deriving the ζ cut values in this manner. With this method the post-cut signal efficiency that delivers the best sensitivity performance can be determined for each subarray.

3.2.2.7   Function signal efficiency cut method

Like the third method, the fourth method chooses the ζ cut value in each energy bin based upon a predefined post-cut signal efficiency. However instead of choosing an arbitrary fixed value, the post-cut signal efficiency is now defined by an arbitrary function. The function chosen to represent the post-cut signal efficiency is a tanh (S-type) function as shown in Equation 3.1.

$$\text{Efficiency}_{\text{Signal}}(E) = (\tanh\left[\log_{10}\left(E/\text{TeV}\right)\right] + 8.9)/10 \tag{3.1}$$

where E is the reconstructed energy. The constants are used to scale the function so that
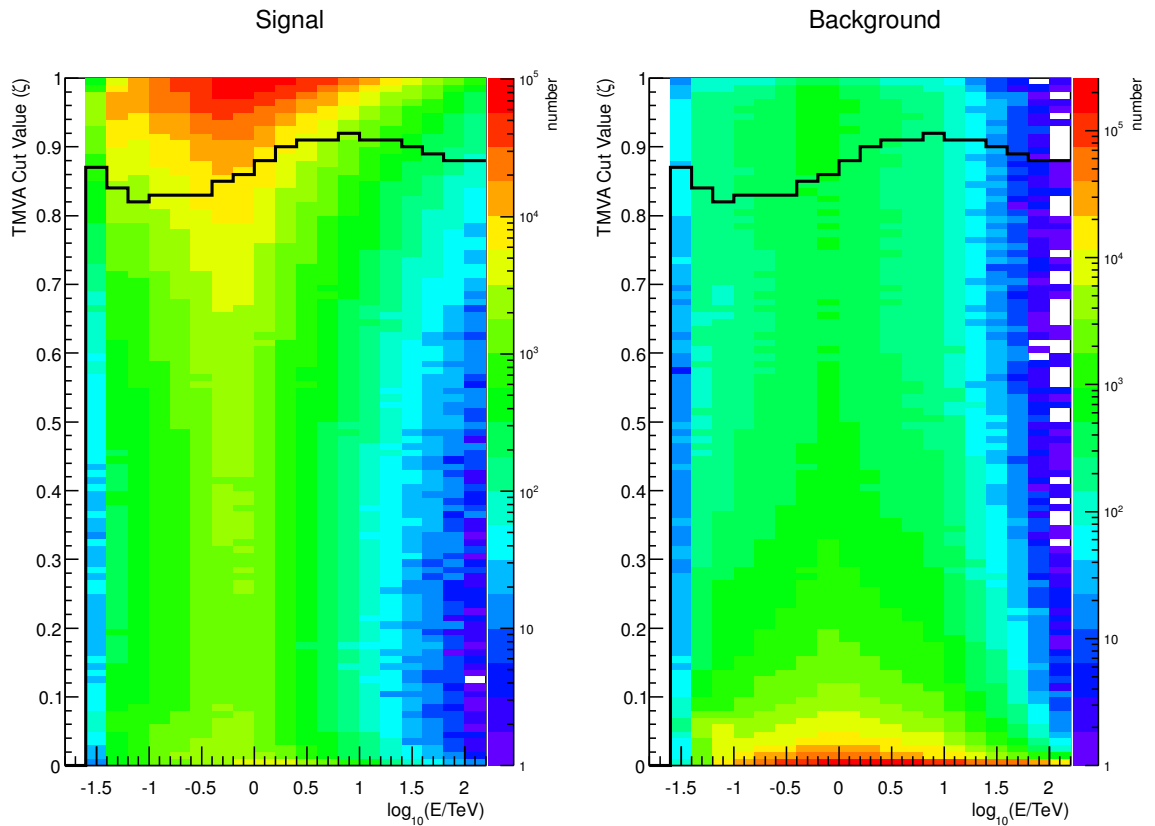
Figure 3.13: The CTA Subarray-I MLP response for signal events (left panel) and background events (right panel) for all energies. Deriving the ζ cut value by predefining a fixed post-cut signal efficiency can result in the loss of too many signal events at medium energies. This is not expected to greatly affect sensitivity performance as a larger number of background events is also likely to be cut.

in the lowest energy bin ($\sim$15 GeV) a post-cut signal efficiency of $\approx 80\%$ is achieved and in the signal dominated high-energy regime the efficiency is ≈ 98 %. Thus, a function can be chosen that best defines how the signal efficiency evolves as a function of energy. For example, due to the larger number of background cosmic-rays at lower energies, it is reasonable to expect a poorer signal efficiency in this regime. However at high energies, say beyond a few TeV, it is also reasonable to expect a signal efficiency close to 100% due to the very low frequency of background cosmic-rays seen at these energies. Figure 3.14 shows the ζ cut values for all energies (left panel) derived by predefining the post-cut signal efficiency (right panel, red line) using an tanh (S-type) function. Also shown is the background efficiency (right panel, blue line) which results from this method.
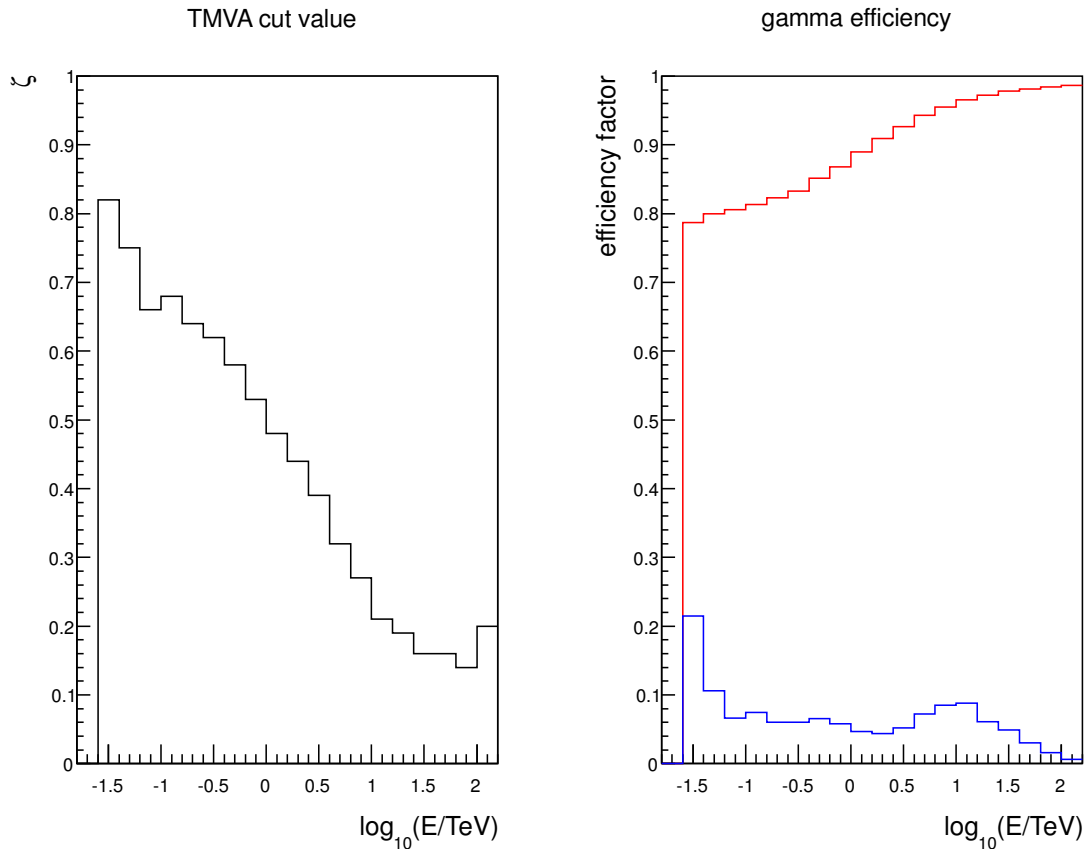
Figure 3.14: CTA Subarray-I ζ cut parameters for each energy bin (left panel) derived using the *function signal efficiency cut method* by predefining the post-cut signal efficiency (right panel, red line) with a tanh (S-type) function. Also shown is the background efficiency values (right panel, blue line) that result from this method. An arbitrary function can be used that best represents the evolution of signal efficiency as a function of energy.

Figure 3.15 illustrates the MLP response for signal events (left panel) and background events (right panel) for all energies. The derived ζ cut values (solid black line) are also shown. This method seems to produce cut values that are more characteristic of the energy dependence of signal and background events. In addition, it is also possible to choose a function that is based upon the observed signal efficiency seen with existing ground-based Cherenkov systems, but these may not be fully representative of the improvements expected with CTA.
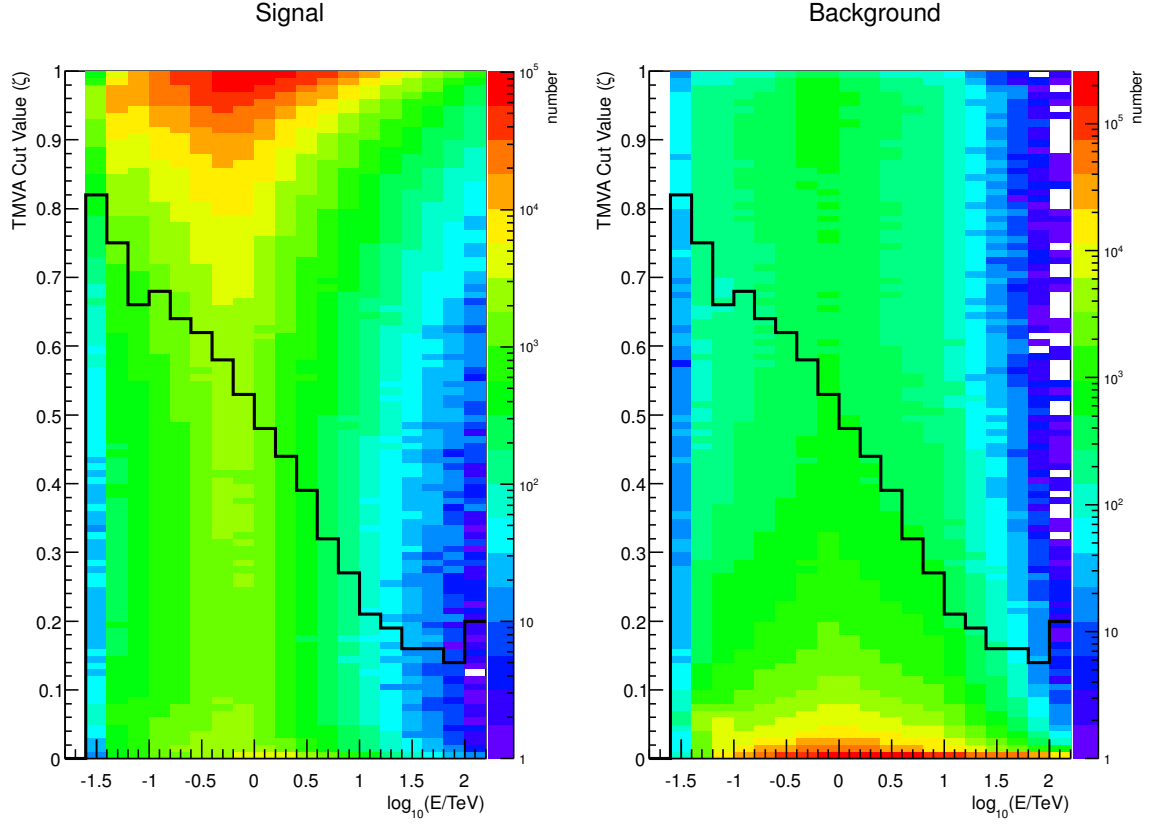
Figure 3.15: CTA Subarray-I MLP response for signal events (left panel) and background events (right panel) for all energies. The derived ζ cut values (solid black line) are also shown. It appears that by using a tanh function to define the post-cut signal efficiency this method produces cut values that are more characteristic to the energy dependence of signal and background events.

3.2.2.8 Energy-scaled significance cut method

The final method chooses the ζ cut value in each energy bin based upon the maximum difference between the signal significance and background significance for that bin. Equations 3.2 and 3.3 show how the significance is calculated for signal and background respectively.

$$\text{Significance}_{\text{Signal}}(\zeta) = \frac{\int_{\zeta}^{1} \text{Signal}}{\sqrt{\int_{\zeta}^{1} \text{Signal} + \int_{\zeta}^{1} \text{Background}}} \qquad (3.2)$$

$$\text{Significance}_{\text{Background}}(\zeta) = \frac{\int_{\zeta}^{1} \text{Background}}{\sqrt{\int_{\zeta}^{1} \text{Signal} + \int_{\zeta}^{1} \text{Background}}} \qquad (3.3)$$

Figure 3.16 illustrates the CTA Subarray-I MLP response for the signal events (red) and

background events (blue) in each energy bin. As mentioned before the MLP response centres signal-like events around 1 and background-like events around 0. Also shown are the background significance values (dashed blue line) calculated using Equation 3.3 and signal significance values (dashed red line) calculated using Equation 3.2. The ζ cut value (dashed pink line) is then chosen to be where the difference between these two significance values is largest.
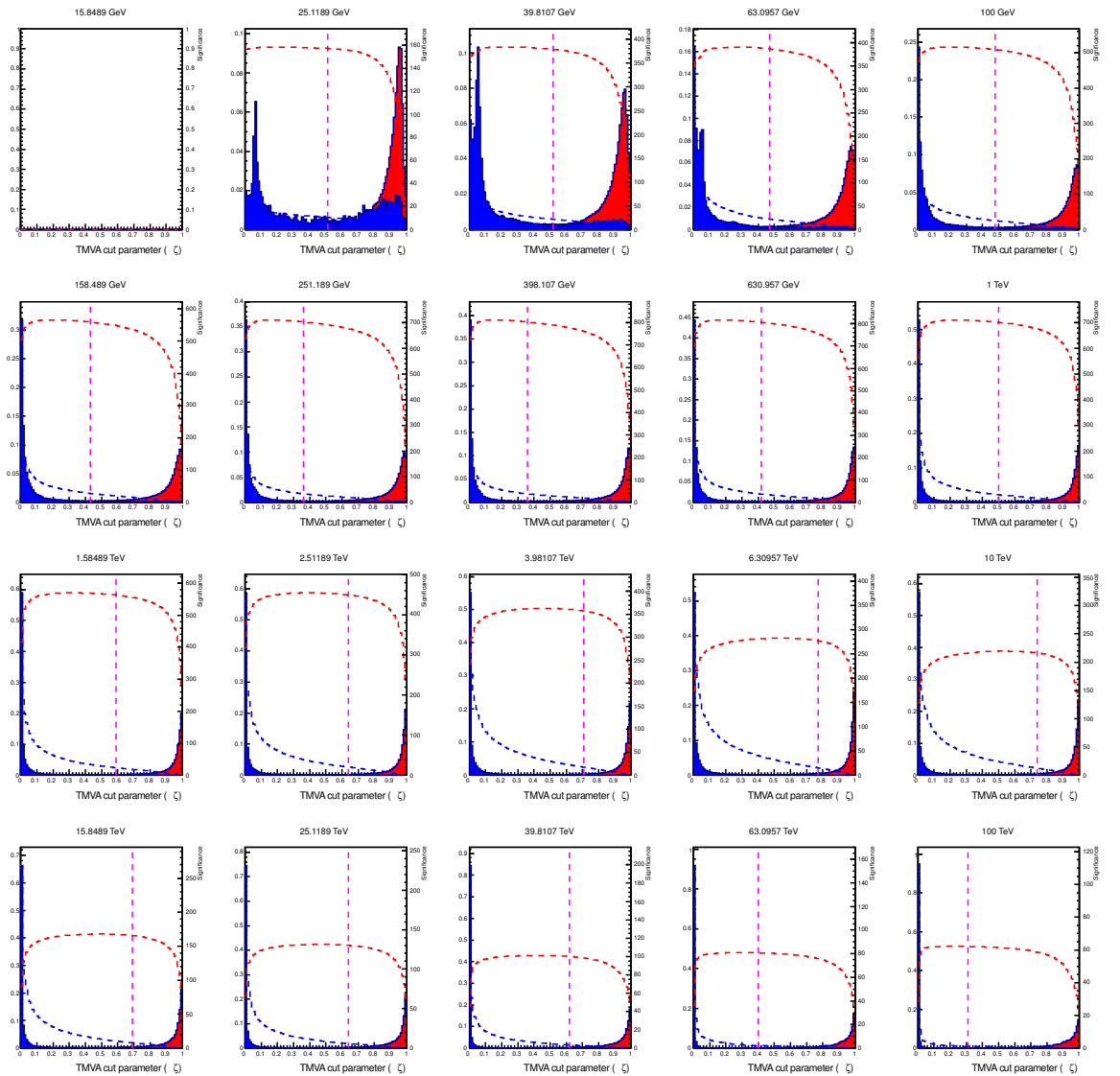
Figure 3.16: CTA Subarray-I MLP response of separated signal (red) and background (blue) events for each energy bin. The y-axis shows the normalised fraction of events and the x-axis shows the MLP response parameter. Using the *energy-scaled significance cut method*, the ζ cut parameter (dashed pink line) in each energy bin is derived by finding the maximum difference between the signal significance (dashed red line) and the background significance (dashed blue line).

The ζ cut parameter derived using the *energy-scaled significance method* appears to closely follow the density distribution of signal events. As a result a greater number of signal events should pass the cut; however, a greater number of background events will also pass the cut. As before, it is not expected that this should significantly affect sensitivity performance.
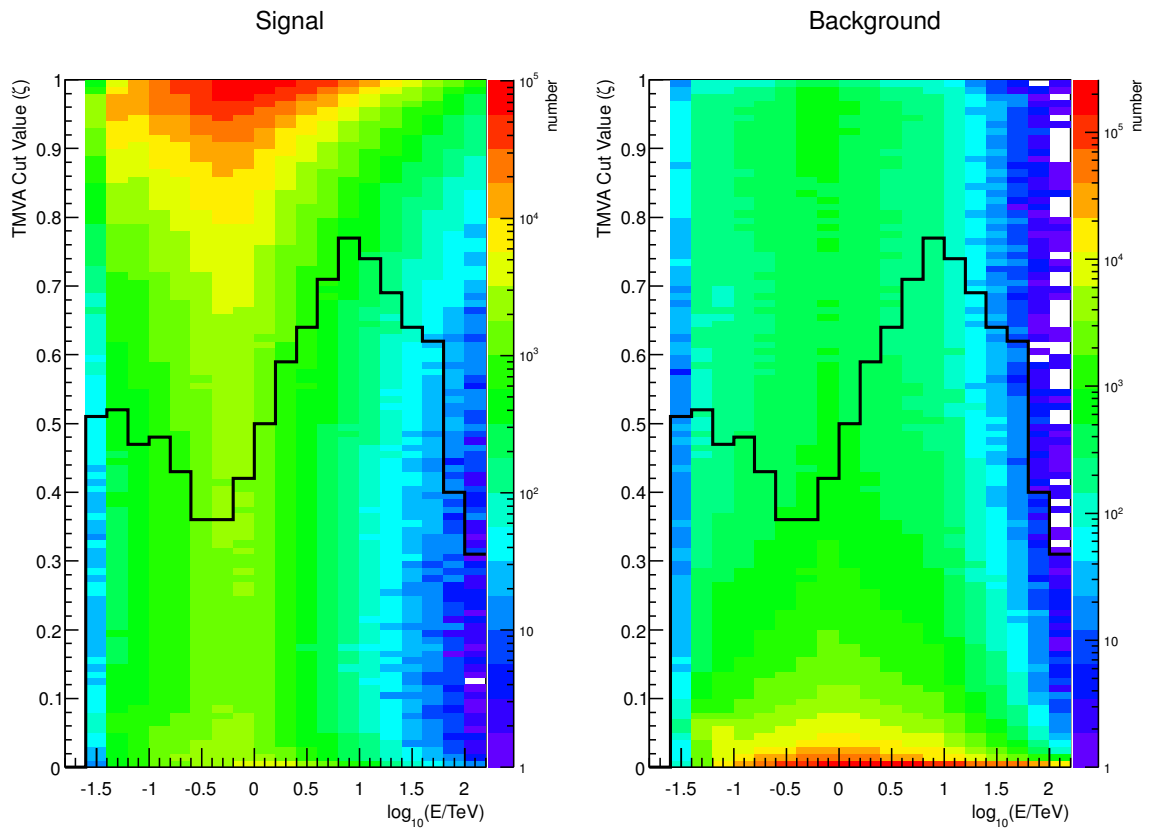
Figure 3.17: CTA Subarray-I MLP response for signal events (left panel) and background events (right panel) for all energies. The derived ζ cut values (solid black line) are also shown. It appears that the *energy-scaled significance cut method* produces cut values which closely follow the density distribution of the signal events and therefore a greater number of signal events should pass the cut.

3.2.3 Post-cut analysis

Within the context of this research, post-cut analysis refers to all analysis and optimisation cuts made after the TMVA response cut has been implemented. For example, this includes implementing acceptance cuts and multiplicity cuts as well as θ^2 cuts based on the derived angular resolution. The post-cut analysis also involves calculating key performance measures such as energy resolution and reconstructed energy bias, angular resolution, effective area and finally flux sensitivity curves.

3.2.3.1 Acceptance cuts

In order to optimise the sensitivity analysis, events passing the TMVA response were cut based on their acceptance level. The acceptance level can be seen as a classification of an event's reconstruction quality. Both signal and background events which failed to meet acceptance level 5 were excluded from further analysis. In practice this means that only the images passing the strictest reconstruction cuts such as tail-cuts (highlighted in Section 3.2.1.2) were permitted for calculation of the performance measures. If the acceptance cut is not implemented there is a significant effect on sensitivity performance. For example, many legitimate gamma-ray event images may extend beyond the edges of the camera and hence be classified incorrectly by the neural network as background. Typically these would be very high-energy events that occur at a large distance from the telescopes. The result is that sensitivity rapidly deteriorates above ≈ 1 TeV. Constraining the sensitivity analysis to include only the best events enables an accurate and reasonable prediction of subarray performance to be calculated.

3.2.3.2 Multiplicity cuts

Multiplicity refers to the number of telescope images used to reconstruct an event. For any given event the number of telescope camera images that successfully record the air shower event is dependent upon the energy of the shower-initiating gamma-ray, as well as the

distance of the shower axis from the telescope. Figure 3.18 shows the distance multiplicity matrix of Subarray-E for both signal (top panel) and background (bottom panel) events before implementing a TMVA::MLP cut. The distance multiplicity matrix shows that fewer telescopes will trigger for dim, low-energy events and a larger number will trigger for higher energy events. However, the triggering low-energy events tend to be relatively nearby and the triggering high-energy events relatively distant. As a result the post-cut analysis must take this energy dependence into account in order to derive optimised performance measures for the CTA subarrays. In practice this is done by implementing a suitable multiplicity cut scheme.
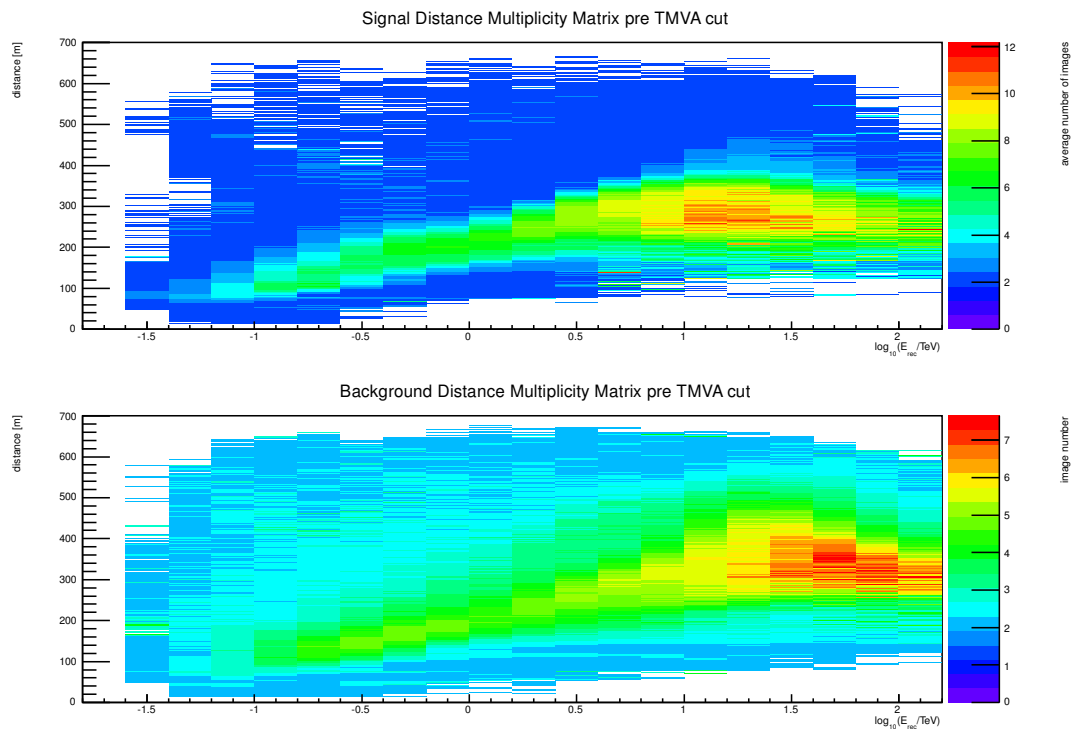
Figure 3.18: The average number of camera images as a function of distance and reconstructed energy seen with Subarray-E for both signal (top panel) and background (bottom panel) events before implementing a TMVA::MLP cut. It is clear that the number of telescopes that trigger and hence the number of camera images recorded for each event is dependent upon energy as well as distance. A suitable multiplicity cut scheme can be derived utilising this information. For both signal and background, x-axis shows the reconstructed energy in $\log_{10}(E/TeV)$, the y-axis is the reconstructed distance (metres) from the telescope to the shower core on the ground and the z-axis shows a colour scale representing the average number of camera images.

The multiplicity cut is expected to affect energy resolution, angular resolution, effective area and hence subarray sensitivity. Two things determine the impact of the multiplicity

cut: the minimum number of images required to pass the cut and the energy at which the cut is enforced. For example, if the image number requirement is too strict at low energies then too few or even no events will pass the cut and hence energy and sensitivity will suffer. On the other hand, angular resolution will improve because a greater number of images used means a smaller uncertainty on the gamma-ray source position. The converse is also true at higher energies. For example, if the image number requirement is too loose at higher energies, then a greater number of events with low image multiplicity will pass and the angular resolution will deteriorate whereas the energy resolution will improve. Therefore the analysis needs to be optimised based upon the goals of the analysis such as achieving the best energy resolution or best angular resolution.

The greater the number of events that pass the multiplicity cut (and any distance cuts), the greater the chance of achieving a better energy resolution performance. However, stereo observation requires that every event is comprised of at least 2 camera images. Therefore the multiplicity cut scheme used to calculate the energy resolution required a minimum of 2 camera images for each event. This rule applied for all event energies and will be discussed further in Section 3.3.

In order to obtain the best performance for angular resolution a different multiplicity cut scheme was used. In this case, the greater the number of images that pass the multiplicity cut, the greater the chance of achieving the best angular resolution performance. The reason for this is that a larger number of images helps to reduce the uncertainty of the source position and hence the reconstructed angle offset. Two methods were tested for doing this and are explained below.

The first method involved defining suitable energy bands through reasonable guesswork, generally based upon the experience obtained with existing Cherenkov telescope systems. For example, the energy threshold of H.E.S.S. (a 4 telescope array) is close to 100 GeV. It is reasonable to expect events which trigger all 4 telescopes to be seen above this threshold energy. However, below this energy events that trigger individual or smaller groups of telescopes might reasonably be expected. At the higher energies above a few TeV, a

reasonable guess might be that a larger number of telescopes than that available in a system like H.E.S.S. might trigger for a given event. Thus in the case of CTA with many more telescopes compared to H.E.S.S. a reasonable guess might be to expect a minimum of 5 or 6 telescopes to trigger for the highest energy events. Table 3.4 below shows a multiplicity cut scheme that was derived using such guesswork.

Table 3.4: Possible multiplicity scheme based upon guesswork of how different sized telescopes may trigger as a function of energy within any given subarray.

Band number	Energies	Minimum image numbers
Band 1	< 40 GeV	2
Band 2	≥ 40 GeV, < 250 GeV	3
Band 3	≥ 250 GeV, < 4 TeV	4
Band 4	≥ 4 TeV, < 10 TeV	5
Band 5	≥ 10 TeV	4

The second method utilised a lookup table (multiplicity matrix) of the average number of images binned by reconstructed energy and the square of the reconstructed image angle offset (θ^2). Figure 3.19 shows the multiplicity matrices constructed for Subarray-B (top left panel), Subarray-E (top right panel), Subarray-I (middle left panel), Subarray-J (middle right panel) and Subarray-K (bottom panel). Each of these multiplicity matrices includes only the events that pass the TMVA cut derived using the *energy-scaled significance cut method* (see Section 3.2.2.8).

From the multiplicity matrices illustrated in Figure 3.19, a multiplicity cut scheme for each of the subarrays was derived by looking for subtle boundaries along the energy axis.

This research tested many different multiplicity cut schemes and there are other approaches that can be implemented in order to find the combinations which provide the best performance. The schemes highlighted in Table 3.5 were the ones used in this work for calculating angular resolution and sensitivity performance.
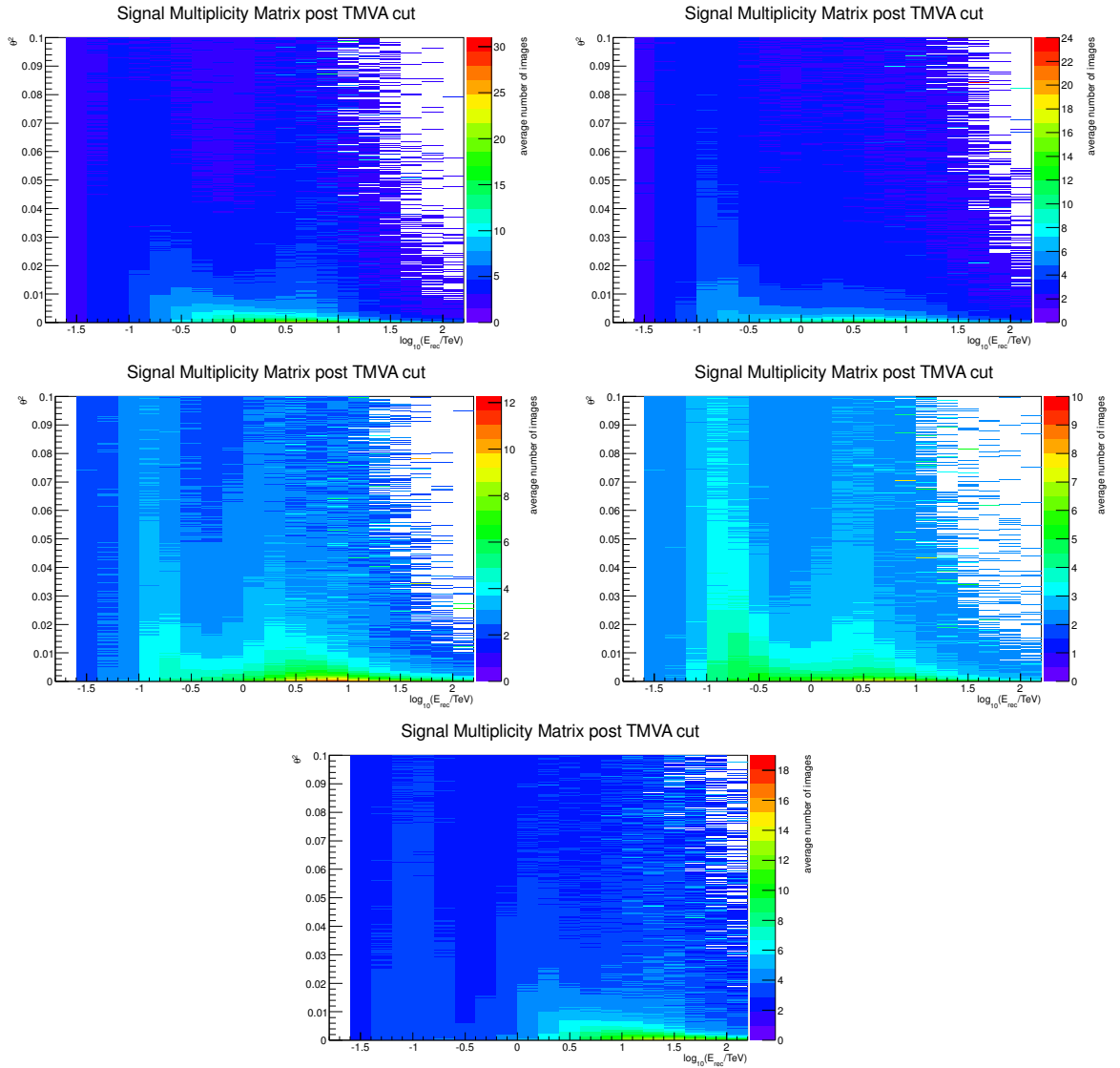
Figure 3.19: Multiplicity matrices constructed for CTA Subarray-B (top left panel), Subarray-E (top right panel), Subarray-I (middle left panel), Subarray-J (middle right panel) and Subarray-K (bottom panel). For each matrix the average number of camera images are binned by reconstructed energy and image angle offset. Any distinctive boundaries in the evolution of the average image numbers as a function of energy will help to define the multiplicity cut scheme. The colour scale on the right shows the average number of images, where blue signifies low and red high. The multiplicity cut schemes derived from these matrices for each subarray are shown in Table 3.5.

Table 3.5: Multiplicity cut schemes derived for each subarray by looking for subtle boundaries along the energy axis in their respective multiplicity matrices shown in Figure 3.19.

Subarray	Scheme Number	Band number	Energies	Minimum image numbers
B	1	Band 1	< 40 GeV	2
		Band 2	≥ 40 GeV, < 150 GeV	3
		Band 3	≥ 150 GeV, < 630 GeV	4
		Band 4	≥ 630 GeV, < 1 TeV	5
		Band 5	≥ 1 TeV, < 6 TeV	4
		Band 6	≥ 6 TeV, < 15 TeV	3
		Band 7	≥ 15 TeV	2
E	1	Band 1	< 40 GeV	2
		Band 2	≥ 40 GeV, < 400 GeV	3
		Band 3	≥ 400 GeV, < 2 TeV	4
		Band 4	≥ 2 TeV, < 25 TeV	3
		Band 5	≥ 25 TeV	2
I	1	Band 1	< 100 GeV	2
		Band 2	≥ 100 GeV, < 2.4 TeV	3
		Band 3	≥ 2.4 TeV, < 10 TeV	4
		Band 4	≥ 10 TeV, < 30 TeV	3
		Band 5	≥ 30 TeV	2
J	1	Band 1	< 40 GeV	2
		Band 2	≥ 40 GeV, < 100 GeV	3
		Band 3	≥ 100 GeV, < 3 TeV	4
		Band 4	≥ 3 TeV, < 10 TeV	5
		Band 5	≥ 10 TeV, < 30 TeV	4
		Band 6	≥ 30 TeV	3
K	1	Band 1	< 40 GeV	2
		Band 2	≥ 40 GeV, < 1 TeV	3
		Band 3	≥ 1 TeV, < 10 TeV	4
		Band 4	≥ 10 TeV, < 30 TeV	5
		Band 5	≥ 30 TeV	4

3.3   Energy resolution results

The energy resolution of an array of Cherenkov telescopes is a measure of the average uncertainty in how well the system can infer the energy of the primary gamma-ray photon that initiates the extensive air shower. For Cherenkov telescopes, the energy resolution is calculated by fitting a Gaussian function to the distributions of reconstructed energy (E_{rec}) divided by the true energy (E_{true}) for each energy bin. The true energies are the CORSIKA simulated energies that follow a source spectrum of E^{-2}. As mentioned in Section 3.2.3.2, for all energies a minimum of 2 telescope images were required to pass the multiplicity cut scheme implemented for optimal energy resolution. The energy resolution for an array of Cherenkov telescopes is calculated by fitting a Gaussian function to the energy binned distributions of E_{rec}/E_{true} as shown in Figure 3.20 for Subarray-E. The distributions of E_{rec}/E_{true} should centre around 1. The half width half maximum (HWHM) of the fitted Gaussian function is then defined as the energy resolution at the 68% confidence level.

3.3.1   Energy reconstruction bias

Any systematic bias in the energy reconstruction can be determined from the mean of the fitted Gaussian function discussed above. Subarray-E appears to exhibit a systematic bias to underestimate the true energies of gamma-ray events as shown in figure Figure 3.21. For most energies this systematic shift is $\lesssim$ 10 %, but below approximately 80 GeV the bias is significant. For example in Figure 3.21 at 30 GeV it can be seen that the bias is approximately 20 %. Such low-energy events are below the array triggering energy threshold and hence a larger uncertainty is expected for their reconstructed energies.

3.3.2   Energy resolution distance cuts

To improve the energy resolution performance, a distance cut is also implemented for all subarrays. This limits the events used for calculating the energy resolution to those that

land very close to the telescopes. For this research, a distance cut of 250 m was used for all subarrays except Subarray-K, which required a looser cut of 350 m. The reason for this is that Subarray-K is comprised mainly of SSTs (71) which are optimised for distant high-energy events. As a result, fewer nearby events trigger and to maintain statistics a looser distant cut is required.

Implementing a distance cut has an effect on the derived energy resolution as shown in Figure 3.22. In total 7 different distance cuts were tested 150 m (beige line), 250 m (black line), 350 m (red line), 450 m (green line), 550 m (blue line), 650 m (yellow line) and finally a test making no distance cut (pink line). It is clear that energy resolution is sensitive to distance cuts at the highest energies $\gtrsim$ 1 TeV, and particularly at energies above a few TeV. For example at an energy of approximately 30 TeV [$\log_{10}$(E/TeV) $\approx$ 1.5] the energy resolution values calculated implementing a 250 m distance cut (black line) are approximately 23% better than those calculated without making a distance cut (pink line). This is expected from the distance-energy dependence shown in Figure 3.18. Furthermore, if the distance cut is too strict (beige line) then too many events are lost and the energy resolution results become nonsensical. As mentioned earlier, a distance cut of 250 m works for most of the arrays analysed, but the actual value used is dependent on the array being analysed.
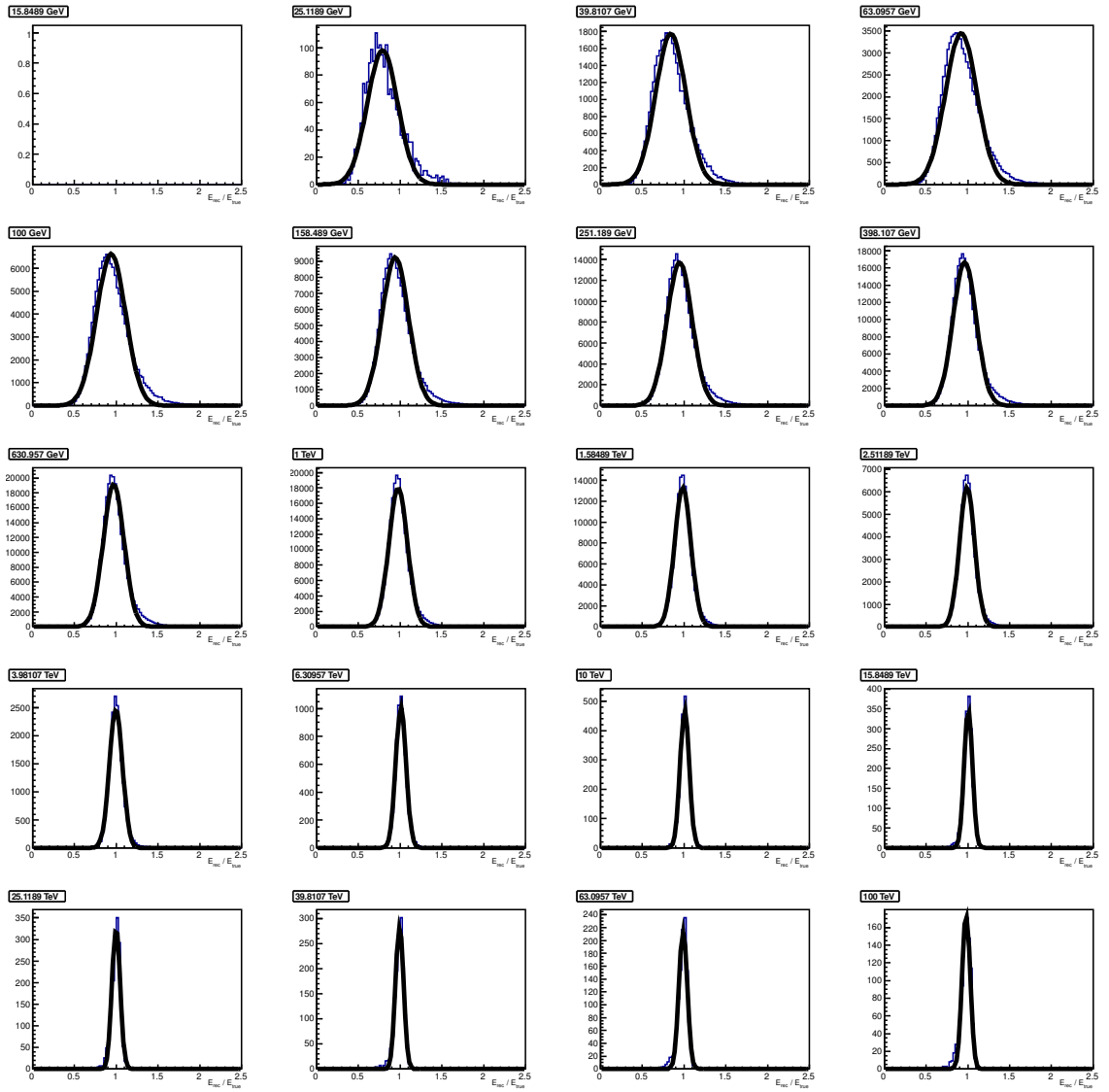
Figure 3.20: The energy binned distributions of E_{rec}/E_{true} for Subarray-E. The distributions all centre toward 1 and a Gaussian function is fitted. The half width half maximum (HWHM) of the fitted Gaussian function is defined to be the 68% confidence level energy resolution.
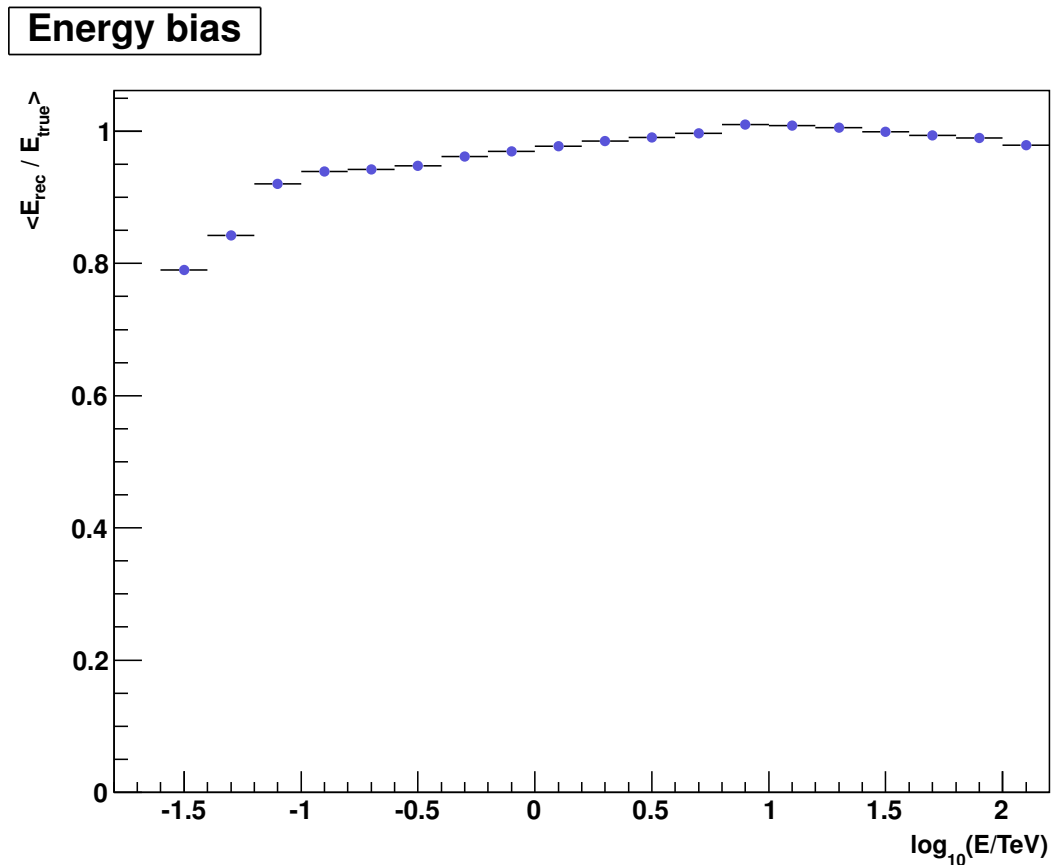
Figure 3.21: The reconstructed energy bias of Subarray-E. The bias is equal to the mean of the Gaussian function fitted to the energy binned distributions of E_{rec}/E_{true}. It appears that Subarray-E systematically underestimates the true energies of gamma-ray events. For most energies this systematic bias is $\lesssim 10\%$. However for energies below $\lesssim 80$ GeV the bias is significant, for example at 30 GeV the bias is approximately 20%. This is because such low-energy events are below the array threshold, resulting in poorly reconstructed images.
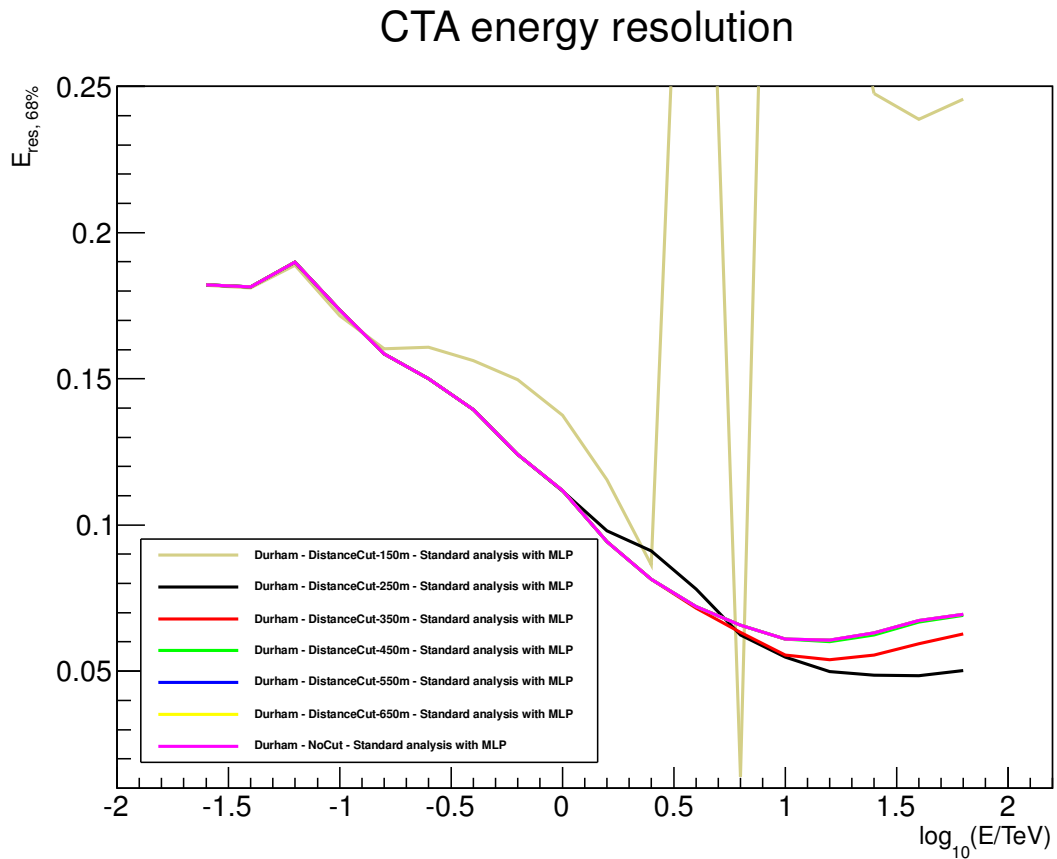
Figure 3.22: Derived energy resolution as a function of energy for Subarray-E calculated using different distance cut values. In total 7 different distance cuts were tested 150 m (beige line), 250 m (black line), 350 m (red line), 450 m (green line), 550 m (blue line), 650 m (yellow line) and finally a test making no distance cut (pink line). At an energy of approximately 30 TeV $[\log_{10}(\mathrm{E/TeV}) \approx 1.5]$ the energy resolution values calculated implementing a 250 m distance cut black line) are approximately 23% better than those calculated without making a distance cut (pink line). It is clear that energy resolution is sensitive to distance cuts particularly at the highest energies $\gtrsim 1$ TeV. This is expected due to the distance-energy dependence shown in Figure 3.18. If the cut is too strict (beige line) this results in a lack of statistics.

3.3.3   Energy resolution of subarrays analysed

The energy resolution results calculated for all of the subarrays analysed are shown in Figure 3.23. Subarray-B appears to be the best performing subarray for energy resolution. This is because Subarray-B is relatively compact and comprised of 5 LSTs and 37 MSTs, meaning it has a comparatively large light collecting area with lower triggering thresholds, thereby optimising the subarray for nearby events. The other subarrays appear to have a similar energy resolution performance except for Subarray-E, which suffers at energies 800 GeV $\lesssim$ E $\lesssim$ 10 TeV due to the more widely spaced and lower number of MSTs (18).
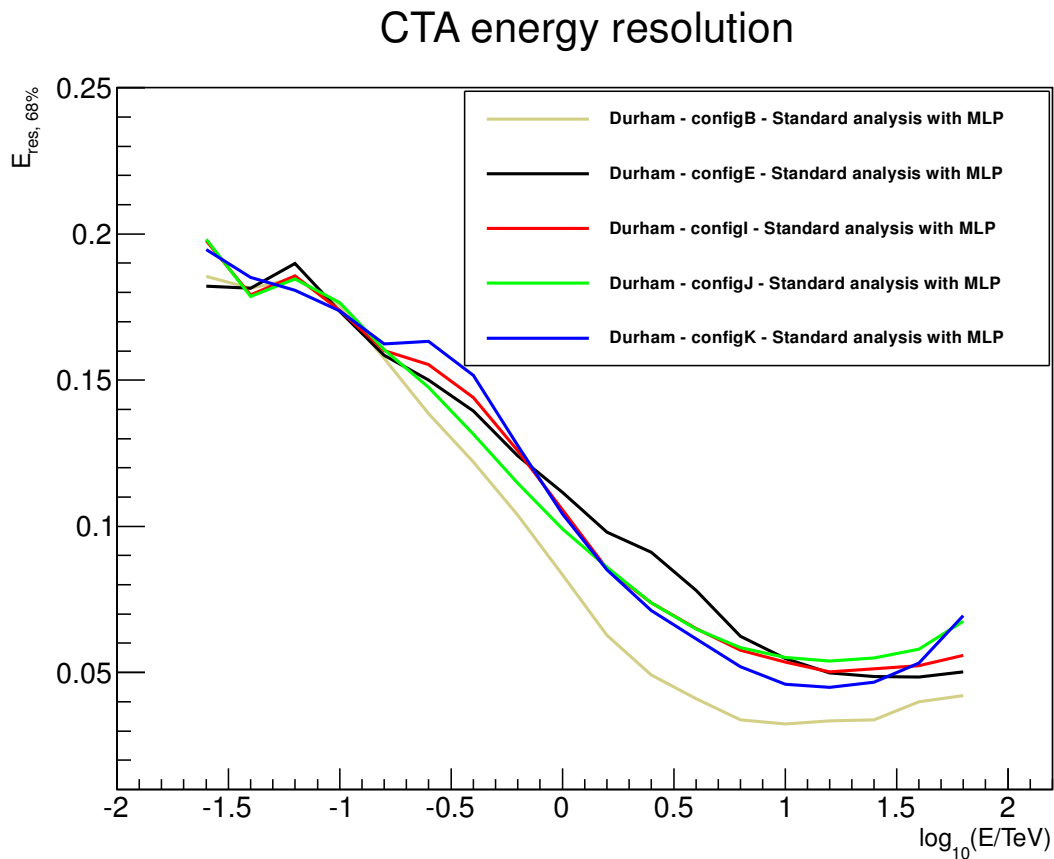
Figure 3.23:   Derived energy resolution as a function of energy for all analysed subarrays. Subarray-B appears to be the best performing subarray for energy resolution. This is because Subarray-B is relatively compact and comprised of 5 LSTs and 37 MSTs, meaning it has a comparatively large light collecting area with lower triggering thresholds, optimising the subarray for nearby events. The other subarrays all have a similar energy resolution performance.

3.3.4 Energy resolution: comparison of TMVA cut methods

When comparing the energy resolution performances derived using different methods to determine the TMVA::MLP cut parameter, it appears as though this has very little effect as shown in Figure 3.24. However, this is somewhat dependent on the values chosen for the *fixed cut method* (Section 3.2.2.4), the *fixed signal efficiency method* (Section 3.2.2.6) and the *function signal efficiency method* (Section 3.2.2.7).
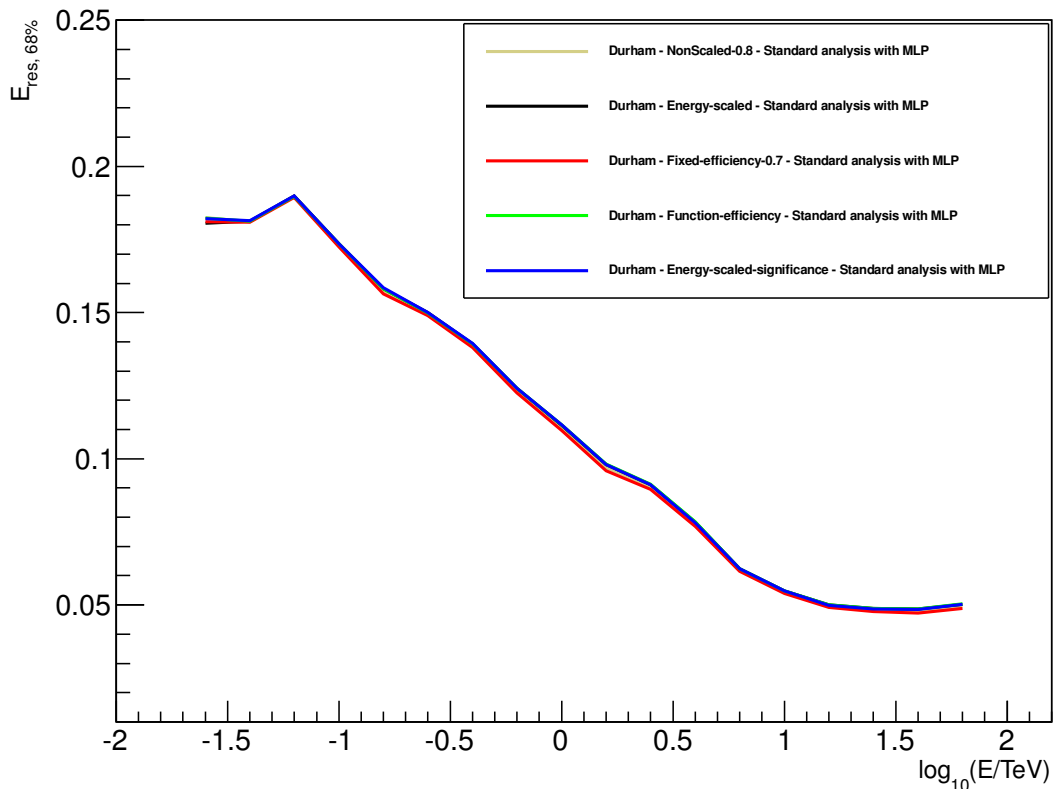
Figure 3.24: Derived energy resolution values as a function of energy for Subarray-E calculated using different methods to derive the TMVA::MLP cut parameter. It appears that energy resolution performance is not sensitive to the different methods used to derive the TMVA cut.

Further investigation of the *fixed cut method* shows that different fixed cut values have very little effect on the result as illustrated in Figure 3.25. The reason for this is that energy resolution is only dependent upon the signal events and the closer to zero the TMVA::MLP cut is made, the larger the number of signal events included in the angular resolution calculation. However, the increase is small relative to the number of signal events located

closer to a TMVA::MLP response value of $\zeta = 1$. Therefore using the *fixed cut method* is somewhat flawed in that it is possible to make a cut without consideration of the signal or background 'likeness' of the events. Hence caution is advised when using this method.
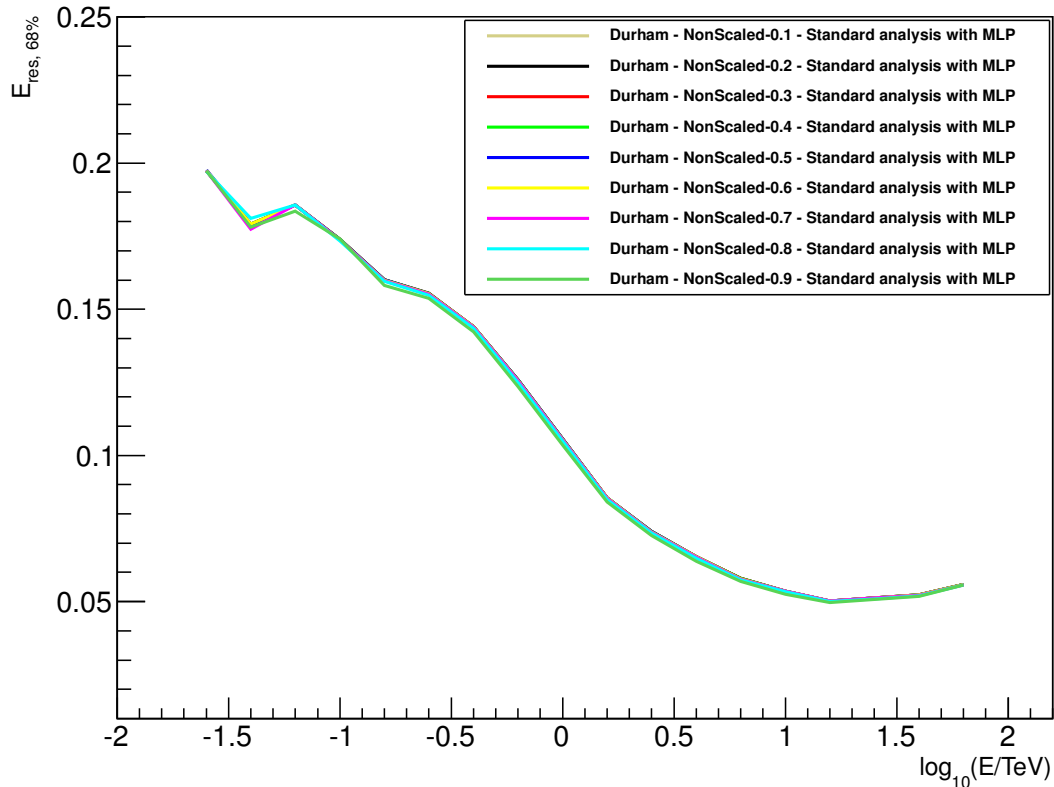
Figure 3.25: Derived energy resolution values as a function of energy for Subarray-I calculated using different values for the *fixed* TMVA::MLP cut parameter. Using the *fixed cut method*, the derived energy resolution does not appear to be sensitive to the fixed cut value chosen. However, this method makes no consideration of the signal or background 'likeness' and hence caution is advised.

Energy resolution performance does appear to be sensitive towards the different values chosen for the *fixed signal efficiency method* of deriving the TMVA::MLP cut parameter as shown in Figure 3.26. For example, at an energy of 30 GeV [$\log_{10}(E/TeV) = -1.5$] the energy resolution derived using a fixed signal efficiency of 30% (beige line) is approximately 6% better than the energy resolution derived using a fixed signal efficiency of 70% (blue line), as shown in Figure 3.26.
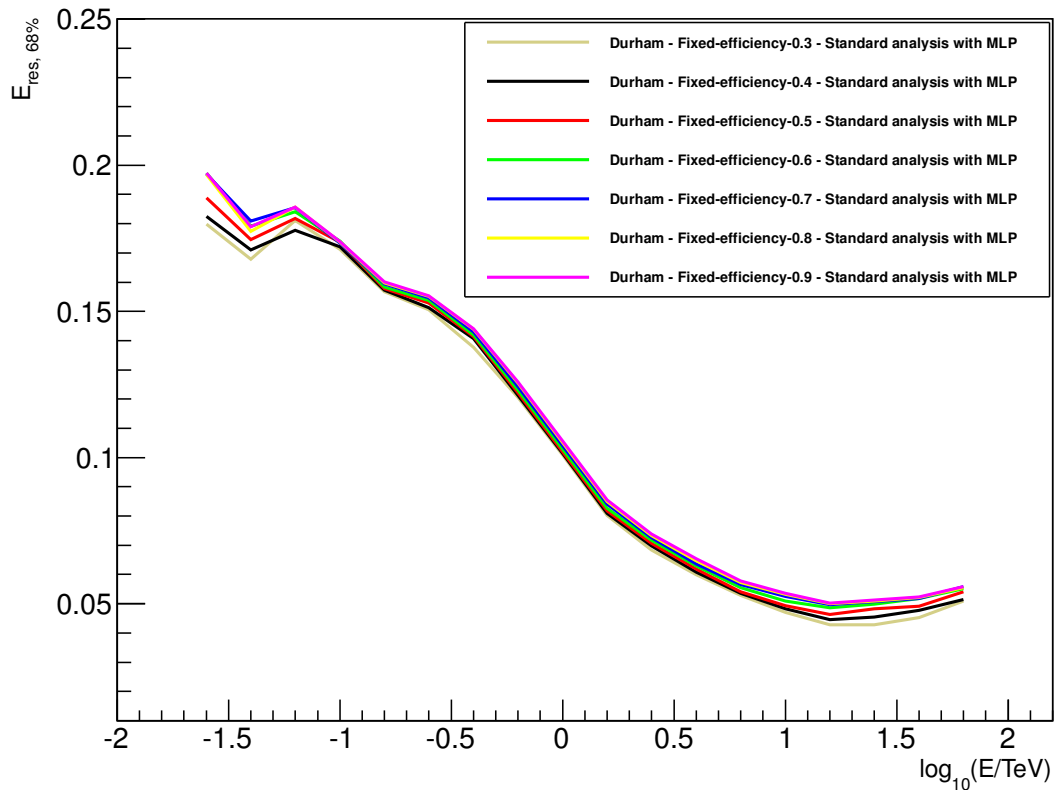
Figure 3.26: Derived energy resolution values as a function of energy for Subarray-I calculated using different values for the *fixed signal efficiency method* of deriving the TMVA::MLP cut parameter. The derived values for energy resolution appear to be sensitive to the cut value chosen for this particular method of deriving the TMVA::MLP cut parameter. For example at an energy of 30 GeV [$\log_{10}(E/TeV)$ = -1.5] the energy resolution derived using a fixed signal efficiency of 30% (beige line) is approximately 6% better than the energy resolution derived using a fixed signal efficiency of 70% (blue line).

3.3.5 Energy resolution: comparison of analysis methods

The energy resolution results for Subarray-E derived by key members of the CTA MCWG are shown in Figure 3.27. It appears that the energy resolution calculated in this research (Durham blue line) using a TMVA::MLP for background rejection is improved at energies $\lesssim$ 250 GeV and $\gtrsim$ 15 TeV. This is in comparison with the energy resolution values calculated using the traditional standard cuts background rejection method (MPIK black line). The definition of energy resolution is the same in each of these results, which have all been calculated using independent analysis methods. In most cases the same shower simulations have been used, but not necessarily the same reconstruction methods, background rejection

or post-cut analysis methods. Moreover, what has not been considered is the effect of the shower reconstruction analysis on energy resolution, in particular image amplitude cuts. This research uses a fixed image amplitude cut of 60 photo-electrons for all energies, whereas analyses performed by other members of the CTA MCWG may optimise amplitude cuts as a function of energy.
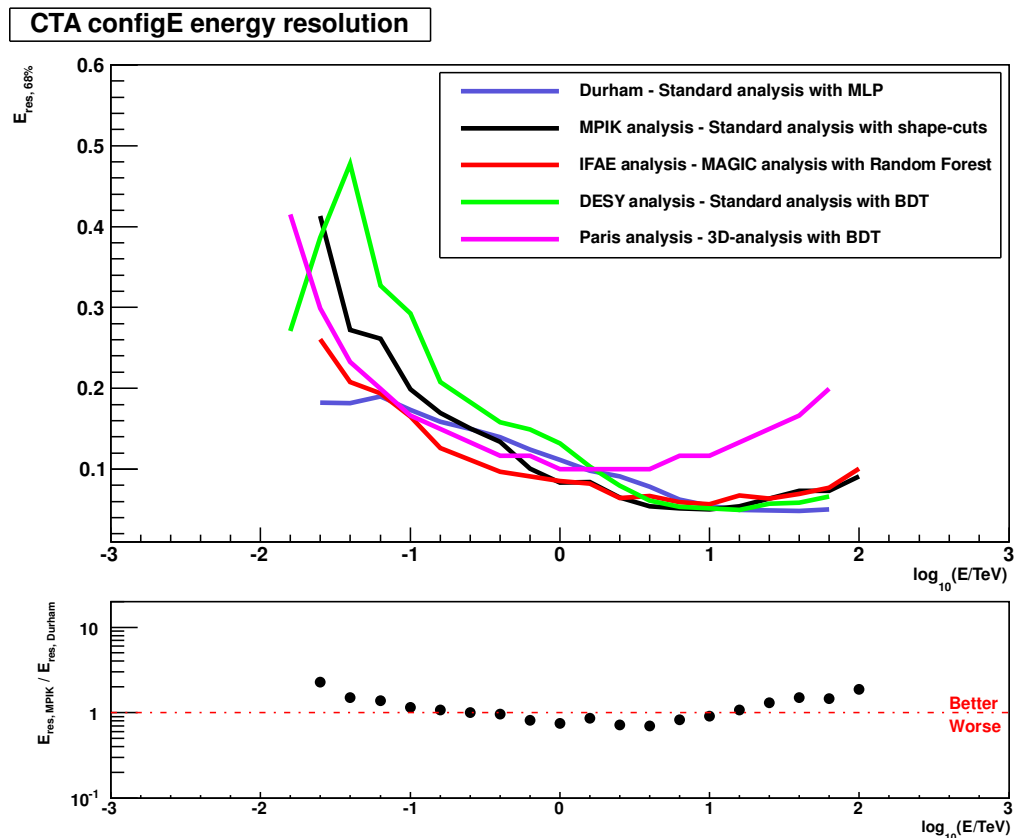
Figure 3.27: Derived energy resolution values as a function of energy for Subarray-E calculated by different members of the CTA MCWG. The different analysis approaches are highlighted in the legend. The sub-figure compares the energy resolution calculated in this research (Durham blue line) using the TMVA::MLP background rejection method versus the energy resolution calculated using the traditional standard cuts background rejection method (MPIK black line). It appears that this research results in an improved energy resolution for events with energies $\lesssim$ 250 GeV and $\gtrsim$ 15 TeV.

3.3.6 Energy resolution: comparison of TMVA methods

Finally, the energy resolution was also calculated for Subarray-E using events that passed a background rejection scheme based upon the TMVA::BDT multivariate analysis method.

Figure 3.28 shows two sets of angular resolution results derived using different background rejection schemes. The first set was calculated using a background rejection scheme based on the TMVA::BDT method (blue line) and the second was calculated using a background rejection scheme based on the TMVA::MLP method (red line). In both cases the cut parameter was derived using the *energy-scaled significance method* (see Section 3.2.2.8). In addition the same multiplicity cut scheme (see Table 3.5) was used for both sets of results. The subfigure compares the performance of the two energy resolution results calculated with different TMVA background rejection schemes. The energy resolutions resulting from the two TMVA background rejection methods are identical. The settings used for the two TMVA methods are detailed in Tables 3.3 and 3.3.
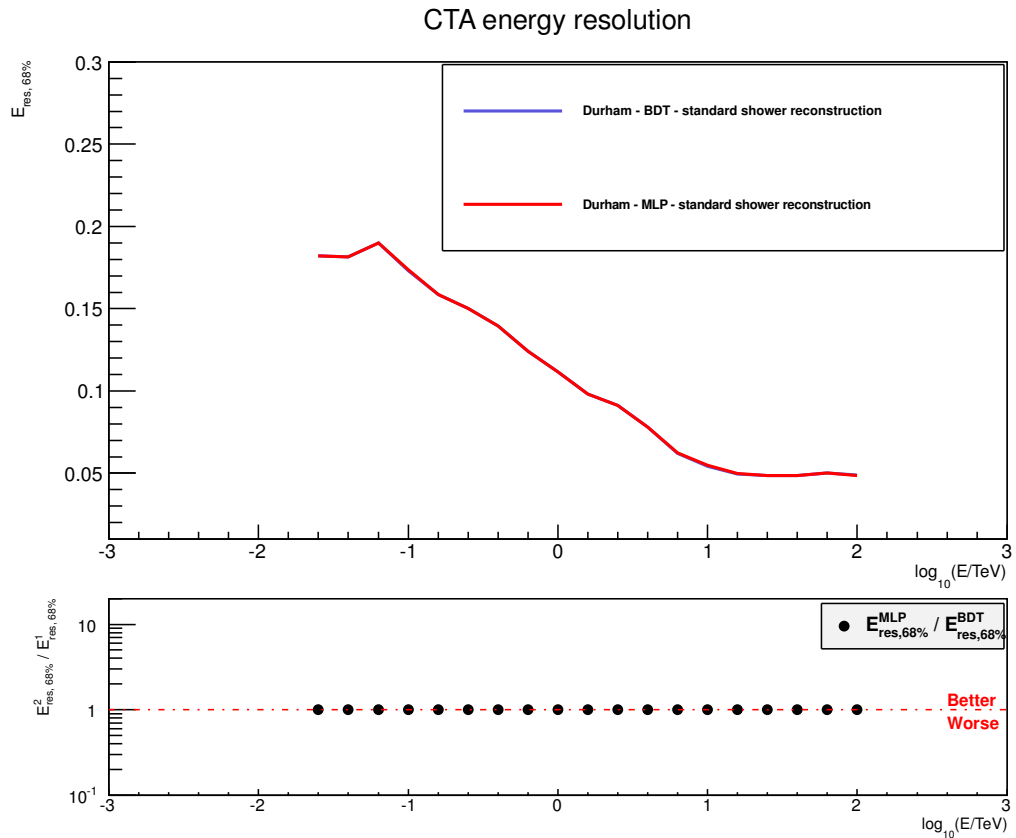
Figure 3.28: Derived energy resolution values as a function of energy for Subarray-E calculated using different background rejection schemes. One set of energy resolution results were calculated using a background rejection scheme based on the TMVA::BDT method (blue line) and the other was calculated using a background rejection scheme based on the TMVA::MLP method (red line). In both cases the cut parameter was derived using the *energy-scaled significance method*. In addition the same multiplicity cut scheme was used for both sets of results. The subfigure compares the performance of the two energy resolution results using the two different background rejection schemes. There is no difference between the energy resolution values calculated using these two different background rejection schemes

3.4 Angular resolution results

The angular resolution of an array of Cherenkov telescopes is the minimum angle at which the system can resolve two separate sources. In practice the angular resolution for an array of Cherenkov telescopes is a function of the spread of reconstructed point-source positions. This research only considers on-axis point source simulations; the results would be different when considering off-axis observations of extended sources. Figure 3.29 illustrates a typical distribution of reconstructed image offset angles with respect to the shower axis seen when observing gamma-ray point sources. There are a number of reasons for this event distribution, including atmospheric effects, electronic noise and optical efficiency, as well as uncertainties in the reconstruction methods. All of these factors limit the spatial resolving power of the telescope system. Although arguably more important for morphology studies of extended sources, a good angular resolution as well as pointing accuracy is important for proper source identification when undertaking point source observations. In practice the angular resolution for an array of Cherenkov telescopes is typically defined as the angular distance (or radius) within which 68%, 80% or 95% of the events are contained. The 68% confidence level, also used by CTA colleagues, is the one used for the results presented in this thesis.

3.4.1 Angular resolution of subarrays analysed

The angular resolution results calculated for all of the subarrays analysed are shown in Figure 3.30. The angular resolution values were calculated using the events that have passed both the energy-scaled significance TMVA::MLP cut as well as the individual subarray multiplicity cut schemes highlighted in Table 3.5. The angular resolution results suggest that Subarray-B provides the best angular resolution in the approximate energy range 200 GeV $\lesssim$ E $\lesssim$ 10 TeV. This is due to the compact layout and number of MSTs (37) within this array. Perhaps surprisingly Subarray-B does not perform as well as expected in the low-energy regime below $\lesssim$ 100 GeV, despite the fact it has 5 LSTs. The angular resolution of Subarray-B below

Reconstructed angle to shower axis core
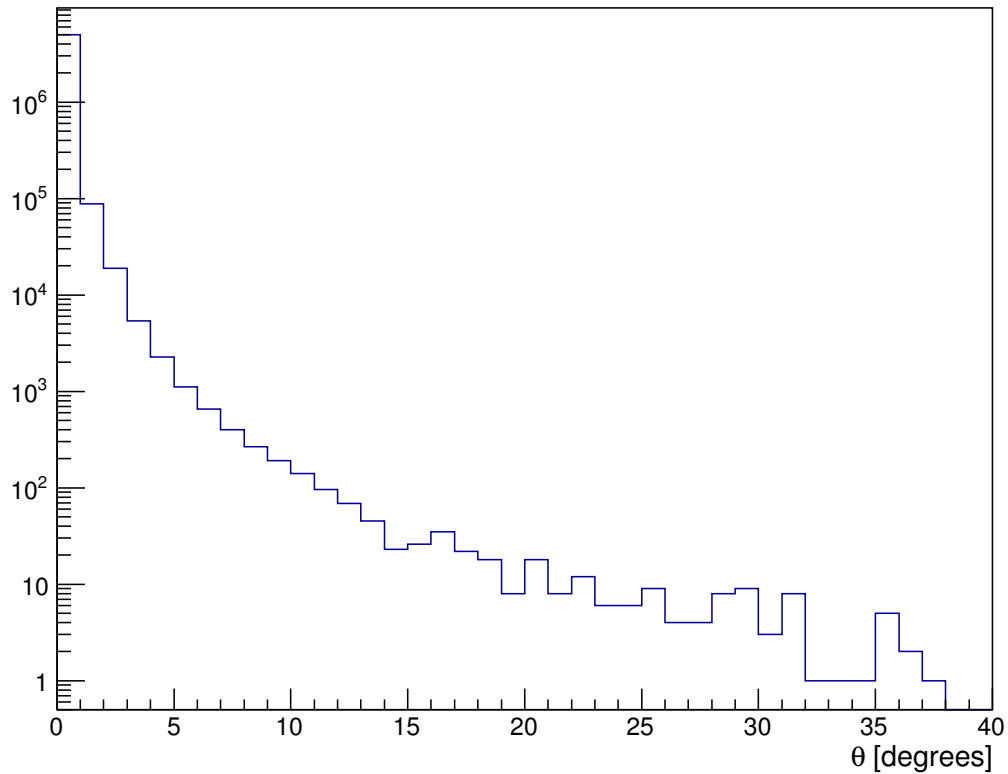
Figure 3.29: Distribution of reconstructed image offset angles with respect to the shower core axis from a simulated gamma-ray point source observed with CTA Subarray-I. In ground-based gamma-ray astronomy the angular resolution for an array of Cherenkov telescopes is a function of this observed spread in reconstructed image angle offsets.

100 GeV might improve if a stricter multiplicity cut is used for these energies. Subarray-K (which also has 5 LSTs) performs the best in this low-energy regime. However, as this particular subarray possesses no MSTs there is a distinctive bump in the angular resolution at energies between 150 GeV $\lesssim$ E $\lesssim$ 2 TeV. Compared to the other arrays, Subarray-E performs well in the low-energy regime, but it is the worst performing array for angular resolution in the high-energy regime above $\gtrsim$ 2 TeV. This is due to the lower number of SSTs (32) which, compared to the SSTs in Subarray-I, are spaced much further apart. In terms of angular resolution Subarray-J performs consistently well for all energies. With only 3 LSTs Subarray-I is the worst performing subarray for angular resolution at energies below $\lesssim$ 100 GeV. Like Subarray-K, Subarray-I also has a distinctive bump in its angular resolution performance at energies between 150 GeV $\lesssim$ E $\lesssim$ 2 TeV. This is due to the

smaller number of MSTs (18) spaced further apart.
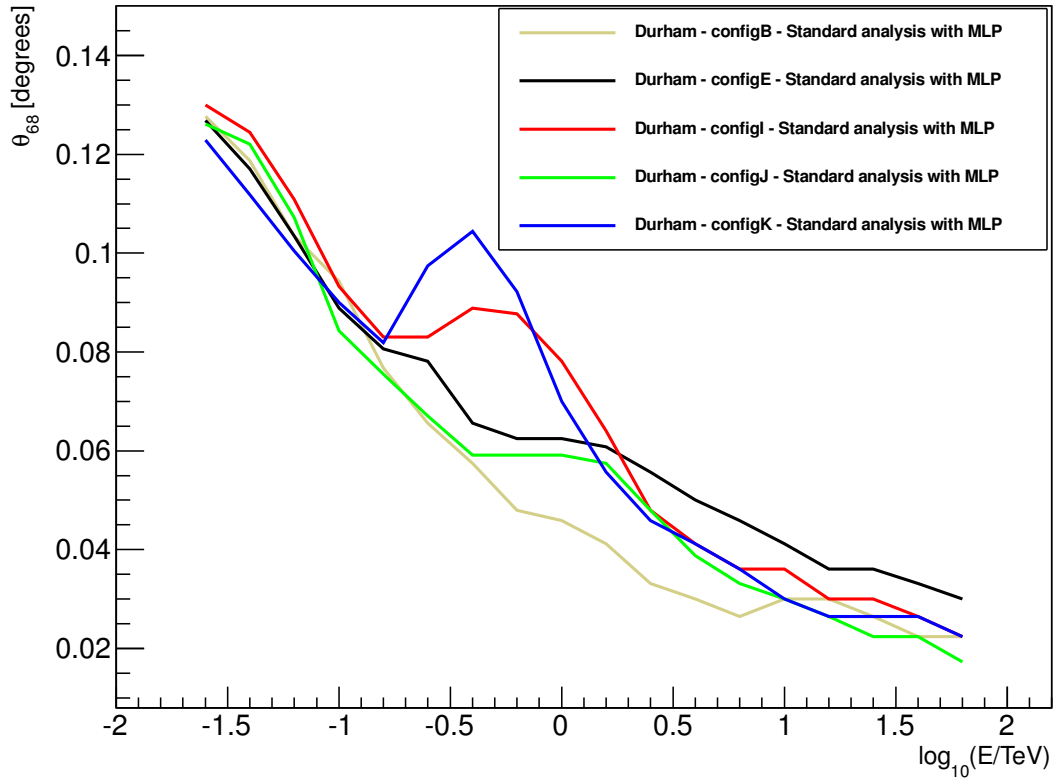
Figure 3.30: The derived angular resolution values as a function of energy for each of the analysed subarrays. The angular resolution of an array of Cherenkov telescopes is defined as the angular distance within which 68% of the detected events are contained. These angular resolution values were calculated using events that have passed both the energy-scaled significance TMVA::MLP cut parameter as well as the individual subarray multiplicity cut schemes highlighted in Table 3.5. When comparing the subarrays it is clear that the angular resolution performance for Subarray-I and Subarray-K worsens between 150 GeV $\lesssim$ E $\lesssim$ 2 TeV where a clear bump is visible. This is due to Subarray-I having fewer (18), more widely-spaced MSTs and Subarray-K having no MSTs.

3.4.2 Angular resolution: comparison of TMVA cut methods

The derived angular resolution as a function of energy for Subarray-E using different methods to select the TMVA::MLP cut parameter is shown in Figure 3.31. It is clear that no significant difference in performance results from using a particular method to derive the TMVA::MLP cut parameter, but this is somewhat dependent on the values chosen for the *fixed* TMVA::MLP cut (Section 3.2.2.4), the *fixed signal efficiency method* (Section

3.2.2.6) and the *function signal efficiency method* (Section 3.2.2.7).

CTA angular resolution

Figure 3.31: The derived angular resolution values as a function of energy for Subarray-E calculated using different methods to derive the TMVA::MLP cut parameter. It appears that angular resolution performance is not significantly sensitive to the different methods used to derive the TMVA cut.

Further investigation of the *fixed cut method* shows that wherever the fixed cut is placed there is little effect on the angular resolution (See Figure 3.32). As with energy resolution, the angular resolution is only dependent upon the signal events and the closer to zero the TMVA::MLP cut is made, the larger the number of signal events included in the angular resolution calculation. However, the increase is small relative to the number of signal events located closer to a TMVA::MLP response value of $\zeta = 1$. Therefore, the *fixed cut method* is somewhat flawed because it is possible to make a cut without consideration of the signal or background 'likeness' of the events. As before, caution is advised with the *fixed cut method*.

Performing the same test for the *fixed signal efficiency method* of deriving the TMVA::MLP
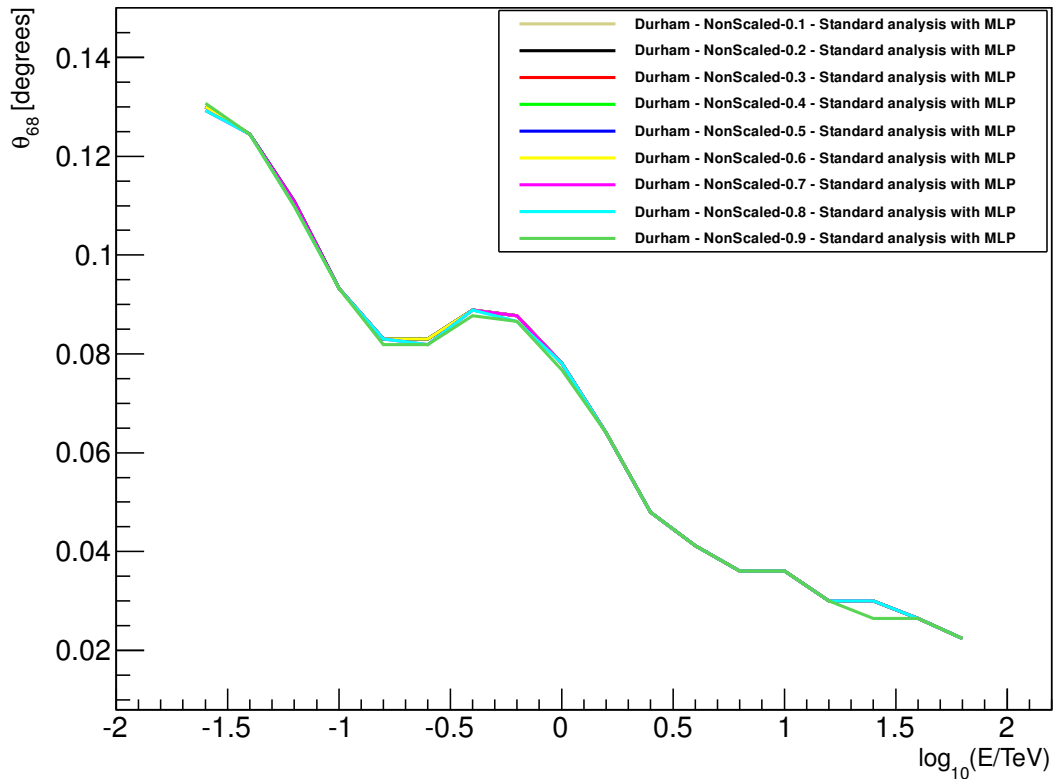
Figure 3.32: The derived angular resolution values as a function of energy for Subarray-I calculated using different values for the *fixed* TMVA::MLP cut parameter. Using the *fixed cut method*, the derived angular resolution does not appear to be sensitive to the fixed cut value chosen.. However caution is advised with the *fixed cut method* as it is possible to make a cut without consideration for signal or background event 'likeness'.

cut parameter (Section 3.2.2.6), it appears as though the derived angular resolution does become sensitive to the efficiency values chosen, as seen in Figure 3.33. Deviations in the resulting angular resolutions occur between 100 GeV and 1 TeV. This could be due to the fact that Subarray-I has a smaller number of MSTs (18), which enhances the effect of changing the required post TMVA cut signal efficiency. As angular resolution is only dependent on the signal events, insisting on a lower post-cut signal efficiency may actually increase the number of events within the constraining radius. At approximately 315 GeV [$\log_{10}(E/TeV) \approx$ -0.5] in Figure 3.33 the angular resolution derived using a fixed signal efficiency of 30% (beige line) is approximately 6% better than using a fixed signal efficiency of 90% (pink line). Thus the the derived angular resolution values are not particularly sensitive to the chosen method used for deriving the TMVA::MLP cut parameter. Instead

the derived angular resolution is more sensitive to the multiplicity cut scheme used shown in Section 3.4.3.
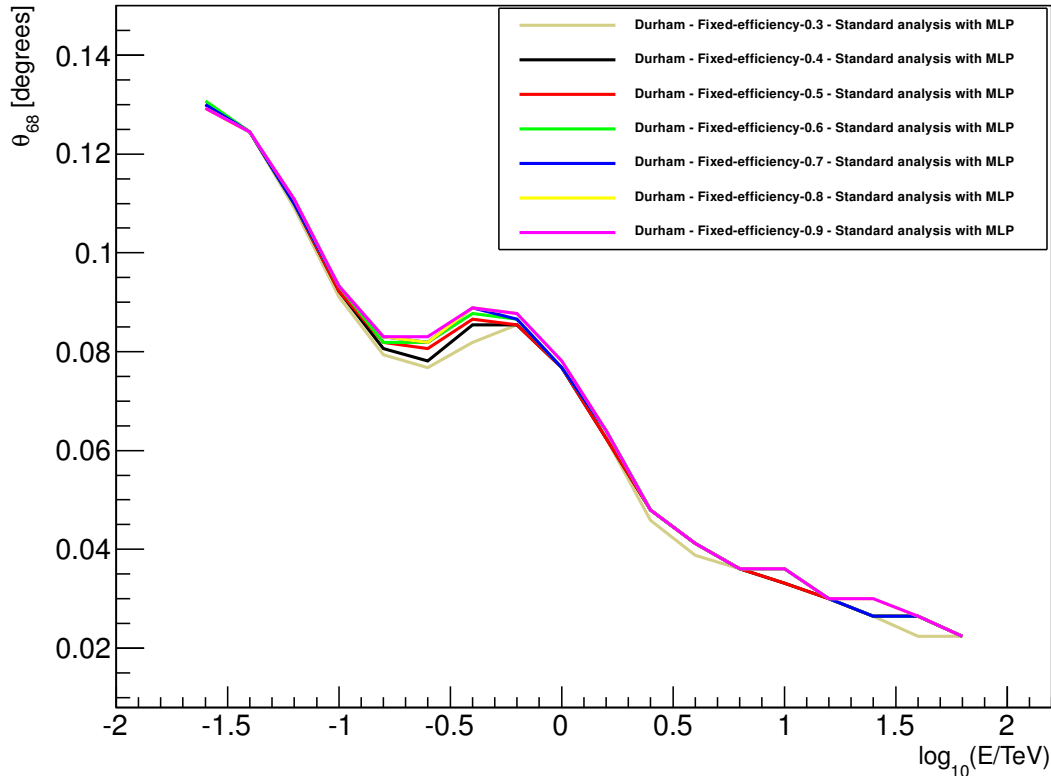
Figure 3.33: The derived angular resolution values as a function of energy for Subarray-I calculated using different values for the *fixed signal efficiency method* of deriving the TMVA::MLP cut parameter. Again the derived values for angular resolution do not appear to be significantly sensitive to the cut value chosen for this particular method of deriving the TMVA::MLP cut parameter. For example at approximately 315 GeV [$\log_{10}(E/TeV) \approx$ -0.5] the angular resolution derived using a fixed signal efficiency of 30% (beige line) is approximately 6% better than using a fixed signal efficiency of 90% (pink line).

3.4.3   Angular resolution: comparison of multiplicity cuts

The angular resolution results derived using different multiplicity cut schemes are shown in Figure 3.34. It is clear that the derived angular resolution values are sensitive to the total number of images required for a multiplicity cut scheme. Furthermore, the angular resolution is also sensitive to the energies at which any image multiplicity cut scheme is enforced. Analysing the difference between the best and worst angular resolution results

shown in Figure 3.34, it is clear that at an energy of 10 TeV [$\log_{10}(E/TeV) = 1.0$] the angular resolution values shown by the green line are approximately 33% better than the values shown by the beige line. In this particular case having a stricter cut at higher energies improves the angular resolution.

Figure 3.34: Derived angular resolution values as a function of energy for Subarray-E calculated using different multiplicity cut schemes. The red line shows the angular resolution values derived using the "best guess" multiplicity cut scheme outlined in Table 3.4. The green line shows the angular resolution values derived using the same energy bands defined in this scheme, but a different image number requirement. The black line shows the angular resolution values derived using the multiplicity matrix optimised cut scheme outlined in Table 3.5 and the beige line shows the angular resolution values derived using the same image number requirement as this scheme, but different energy bands where the cut takes effect. It appears that angular resolution is sensitive to the multiplicity cut scheme used. For example at 10 TeV [$\log_{10}(E/TeV) = 1.0$] the green line angular resolution values are approximately 33% better than the beige line values. In this particular case a stricter multiplicity cut at higher energies improves the angular resolution.

3.4.4 Angular resolution: comparison of analysis methods

The angular resolution results for Subarray-E derived by key members of the CTA MCWG are shown in Figure 3.35. The definition of angular resolution is the same in each of these results, but they have all been calculated using independent analysis methods. In some cases the same shower simulations have been used, but not necessarily the same reconstruction methods, background rejection or post-cut analysis methods. First, it is clear that all the independently calculated angular resolution results are consistent. Secondly it appears as though the angular resolution results calculated in this research (Durham, blue line) utilising a TMVA::MLP for background rejection are better at energies below 150 GeV compared to the angular resolution results calculated using the traditional background rejection (standard cuts) method (MPIK black line). However for energies above 150 GeV, the angular resolution results calculated using the standard cuts background rejection method are better. It may be possible to improve the angular resolution results by testing more multiplicity cut schemes. These findings appear consistent with the results of DESY (green line) and Paris (pink line), also derived utilising a multivariate method. The results for Subarray-B, Subarray-I, Subarray-J and Subarray-K are all available in Appendix B. The observations made above for Subarray-E appear consistent for all the other subarray results.
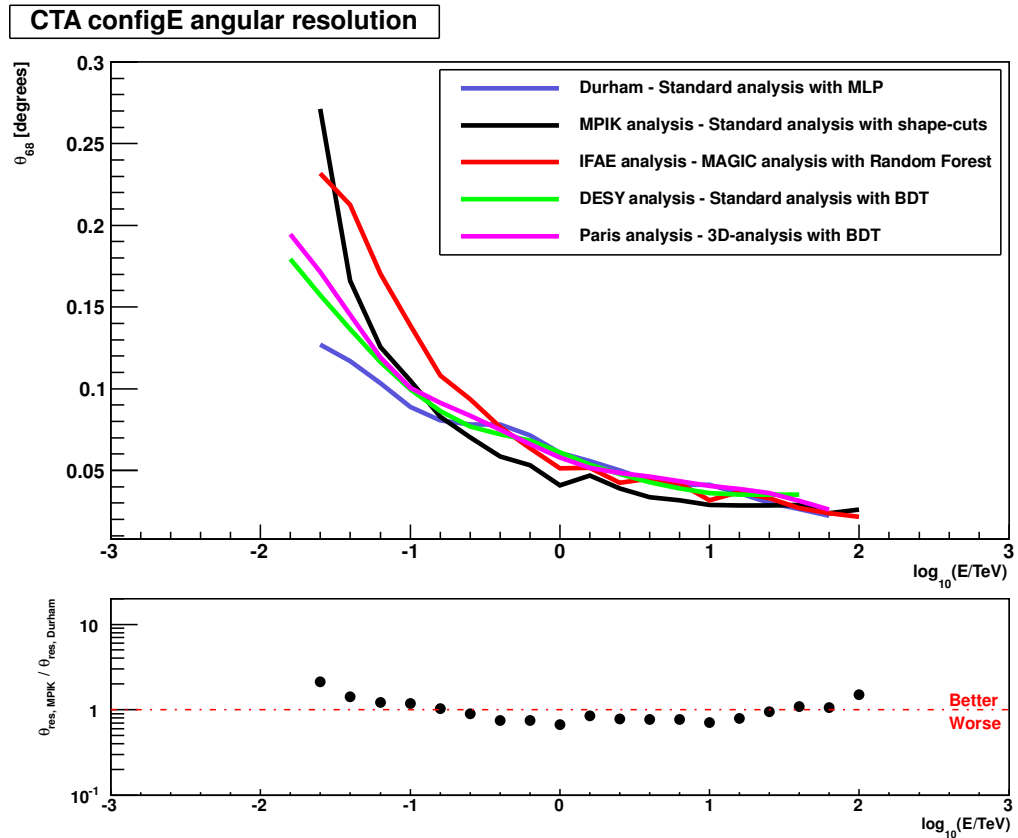
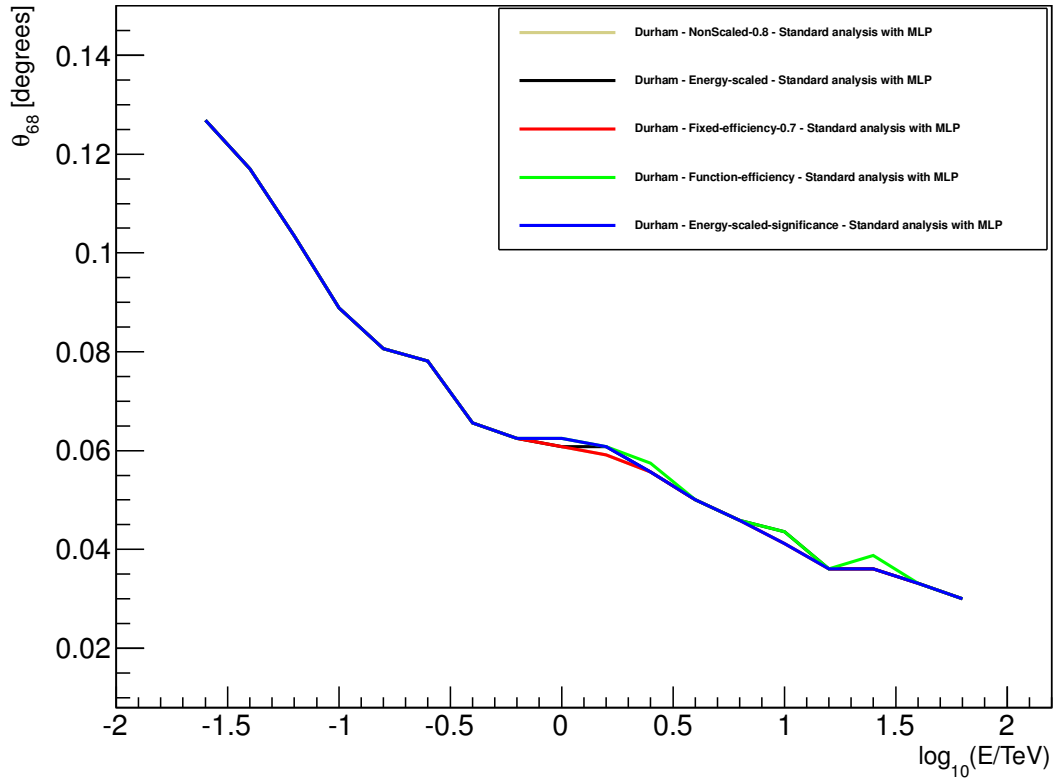**Figure 3.35:** Derived angular resolution values as a function of energy for Subarray-E calculated by different members of the CTA MCWG. The different analysis approaches are highlighted in the legend. The sub-figure compares the angular resolution results calculated for this research (Durham, blue line) versus the angular resolution results calculated using the traditional background rejection approach (MPIK, black line). It appears as though using the TMVA::MLP for background rejection results in better angular resolution at energies below $\lesssim$ 150 GeV but slightly worse performance for energies above this. This improved performance at low energies is consistent with the DESY (green line) and Paris (pink line) angular resolution results that also use a multivariate background rejection scheme.

3.4.5   Angular resolution: comparison of TMVA methods

Finally the angular resolution was also calculated for Subarray-E using events that passed a background rejection scheme based upon the TMVA::BDT multivariate analysis method. Figure 3.36 shows two sets of angular resolution results derived using different background rejection schemes. The first set of angular resolution results are calculated using a background rejection scheme based on the TMVA::BDT method (blue line) and the second is calculated using a background rejection scheme based upon the TMVA::MLP method (red line). In both cases the cut parameter was derived using the *energy-scaled significance method* (see Section 3.2.2.8). In addition the same multiplicity cut scheme (see Table 3.5) was used for both sets of results. The subfigure compares the performance of the two angular resolution results using the different background rejection schemes. The angular resolution values calculated using the TMVA::MLP scheme result in a better performance at energies 400 GeV $\lesssim$ E $\lesssim$ 1.6 TeV. For example, the angular resolution results calculated using the TMVA::MLP scheme are $\sim$25% better at $\sim$600 GeV [$\log_{10}$(E/TeV) $\approx$ -0.2]. It is clear that both angular resolution results are consistent and a significant time advantage is gained by using the much faster TMVA::MLP method with no loss in performance. The settings used for the two TMVA methods are detailed in Tables 3.3 and 3.3.
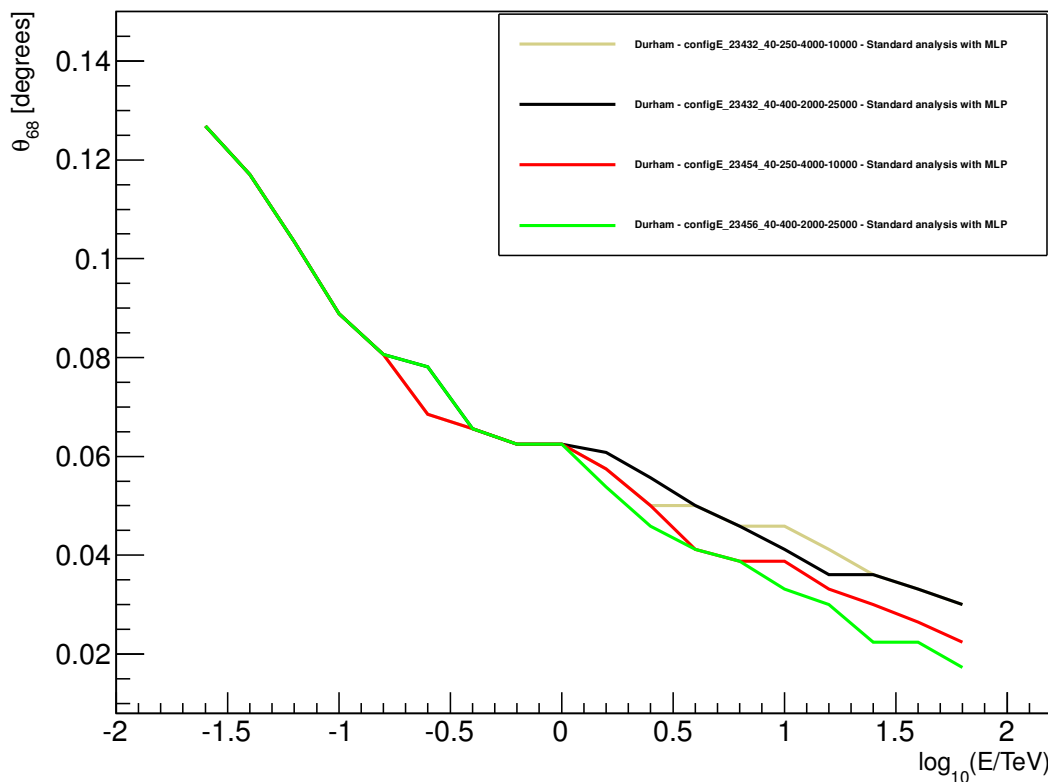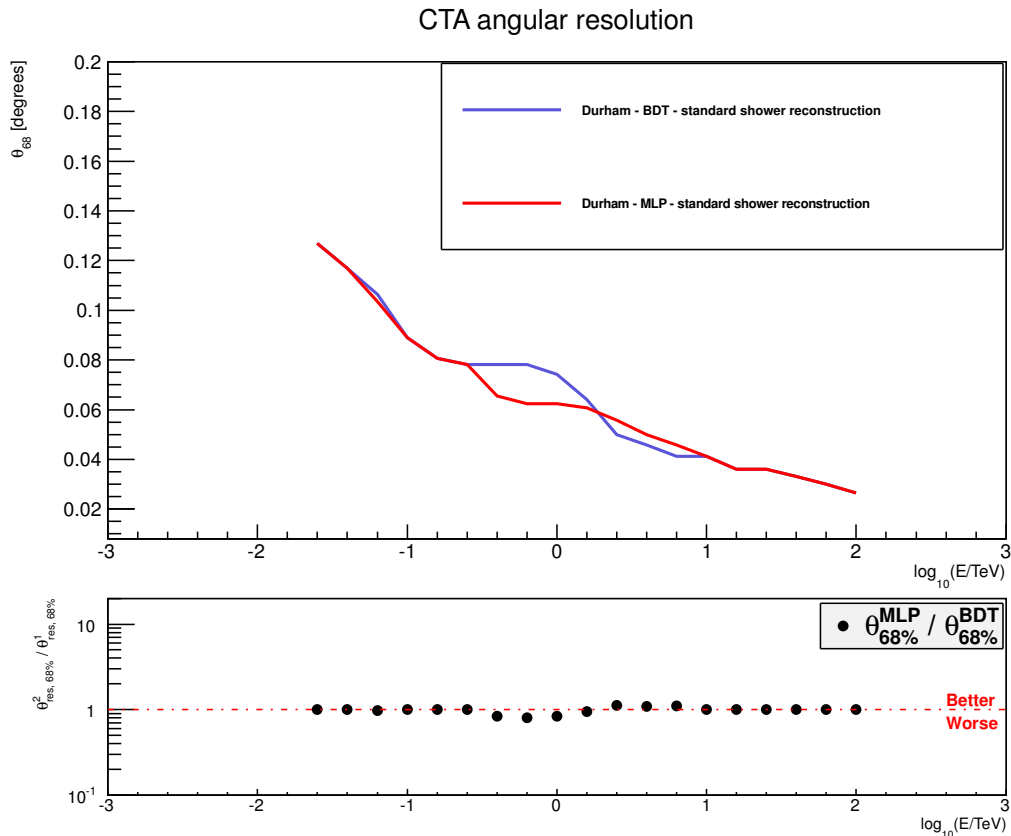
Figure 3.36: Derived angular resolution values as a function of energy for Subarray-E calculated using different background rejection schemes. One set of angular resolution results were calculated using a background rejection scheme based on the TMVA::BDT method (blue line) and the other was calculated using a background rejection scheme based on the TMVA::MLP method (red line). In both cases the cut parameter was derived using the *energy-scaled significance method*. In addition the same multiplicity cut scheme was used for both sets of results. The subfigure compares the performance of the two angular resolution results using the different background rejection schemes. It appears as though the angular resolution values calculated using the TMVA::MLP background rejection scheme result in a relatively better performance at energies between 400 GeV $\lesssim$ E $\lesssim$ 1.6 TeV. For example the angular resolution results calculated using the TMVA::MLP are approximately 25% better at 630 GeV [$\log_{10}(E/TeV) = -0.2$].

3.4.6   Angular resolution: optimisation cuts quality factor

To optimise the sensitivity performance calculations, all signal events passing the TMVA::MLP cut, the acceptance cut and the multiplicity cut are also required to pass a θ^2 cut based on the derived angular resolution. The derived angular resolutions presented here for each subarray are used to eliminate signal events with a large reconstructed angle offset. Again this is to ensure that only the best events are used in order to obtain a true measure of the CTA system performance. In addition the angular resolution defines the ON region which is used for determining CTA's sensitivity performance. Therefore the angular cut made on the background events is defined by the ratio between the ON and OFF regions.

To assess the quality of the cuts made in this sensitivity analysis it is appropriate to calculate the *quality factor* defined in Equation 3.4

$$Q = \frac{N_{\text{signal passing cut}} / N_{\text{signal triggered}}}{\sqrt{N_{\text{background passing cut}} / N_{\text{background triggered}}}} \tag{3.4}$$

where $N_{\text{signal passing cut}}$ is the number of simulated gamma events passing each cut, $N_{\text{signal triggered}}$ is the number of simulated gamma events triggering the telescopes, $N_{\text{background passing cut}}$ is the number of proton events passing each cut and $N_{\text{background triggered}}$ is the number of simulated proton events triggering the telescopes.

Figure 3.37 illustrates the *quality factor* calculated for events passing: the TMVA::MLP cut (black line), the acceptance cut (red line), the multiplicity cut (green line) and the θ^2 cut (blue line). It is clear that each of the cuts implemented improves the quality factor and hence the sensitivity performance. In addition the *quality factor* provides a gauge of the relative power of each cut.
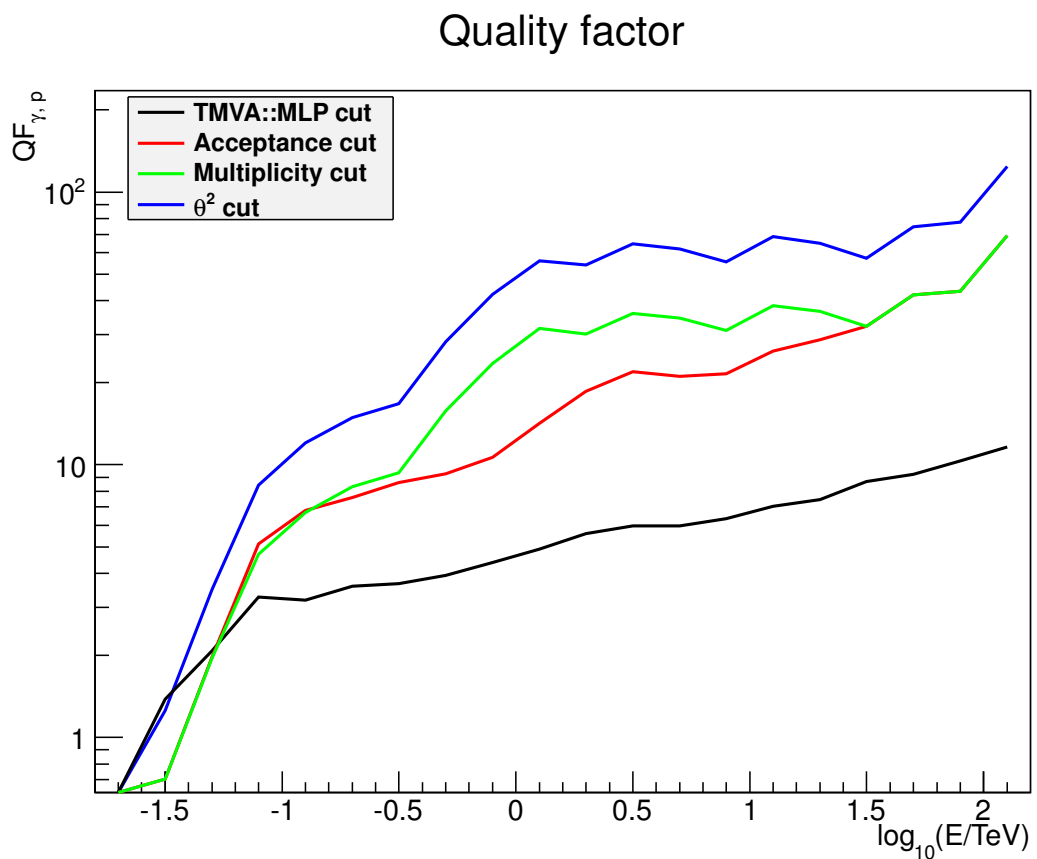
Figure 3.37: The calculated *quality factor* (see Equation 3.4) for the fraction of signal and background events passing: the TMVA::MLP cut (black line), the acceptance cut (red line), the multiplicity cut (green line) and the θ^2 cut (blue line). It is clear that each of the cuts implemented improves the quality factor and hence the sensitivity performance.

3.5   Effective area results

The sensitivity performance of Cherenkov telescopes used in ground-based gamma-ray as-
tronomy is proportional to their effective area, which is really a function of telescope light
collection area, camera efficiency and mirror efficiency. In addition, external factors such
as atmospheric scattering and night sky background light levels can also have an impact
on the effective area, meaning effective area is much larger than the simple scale of the
telescope. In addition, for an array of Cherenkov telescopes such as CTA, the array effective
area is essentially equal to the sum of all the individual telescope effective areas. Due to the
low flux of very high-energy gamma-ray photons incident onto the Earth, a large effective
area is essential for making statistically significant detections of their astrophysical sources.

The accepted method for calculating effective area in the case of Cherenkov telescopes is
shown in Equation 3.5.

$$A_{\text{eff}} = \frac{N_{\text{triggered}}}{N_{\text{simulated}}} \times \pi R^2 \tag{3.5}$$

where $N_{\text{triggered}}$ is the number of triggered events passing all cuts, $N_{\text{simulated}}$ the number of
events simulated and R is the geometrical radius of the total telescope array collecting area,
which is related to the air shower scattering radius. For this work the number of triggered
events passing all cuts is defined as the number of events passing the TMVA::MLP cut
parameter, the acceptance cut and the multiplicity cut as well as the θ^2 cut highlighted in
Section 3.4. In addition the MCWG defines $R_\gamma = 2500$ m and $R_{\text{cosmic-rays}} = 3000$ m for
calculating the respective signal and background effective areas. The background effective
area is calculated when deriving the background rate needed for flux sensitivity calculations,
which are discussed in Section 3.6. Effective area as an array performance measure only
refers to the signal effective area.

Effective area is also dependent on the air shower zenith angle. For observations conducted
at very large zenith angles, the effective area increases; due to the increased distance
between the telescope and the shower depth maximum (Xmax), the air shower develops

over a much larger area. Conversely, the energy threshold increases due to the greater air mass. To ensure the lowest possible threshold energy it is usual practice to maintain very small zenith angles when observing astrophysical sources.

3.5.1 Effective area of subarrays analysed

The effective area for each of the analysed subarrays is shown in Figure 3.38. These were calculated using signal events that passed the TMVA::MLP cut parameter derived using the *energy-scaled significance method* (see Section 3.2.2.8), acceptance cuts and the subarray specific multiplicity cut schemes highlighted in Table 3.5. In addition, the signal events passed the θ^2 cut derived for each subarray shown in Figure 3.30. Subarray-B appears to be the best performing subarray for effective area at low energies $\lesssim$ 250 GeV. Again this is because Subarray-B is comprised of 5 LSTs and 37 MSTs. However, at higher energies Subarray-B becomes the worst performing subarray. Subarray-I achieves the highest effective area $\gtrsim$ 1 TeV and Subarray-E performs relatively well at both low and high energies.

3.5.2 Effective area: comparison of TMVA cut methods

Once again the method used to derive the TMVA::MLP cut parameter has very little effect on the derived effective area as shown in Figure 3.39.

Further investigation of the *fixed cut method* shows that using different cut values has very little effect on the derived effective area as illustrated in Figure 3.40. However the concerns highlighted in Sections 3.3.4 and 3.4.2 regarding this method should be taken into consideration.

In addition the effective area is sensitive to the different values chosen for the *fixed signal efficiency method* of deriving the TMVA::MLP cut parameter as shown in Figure 3.41. For example, at an energy of approximately 2.5 TeV [$\log_{10}(E/TeV) \approx 0.4$] the effective area
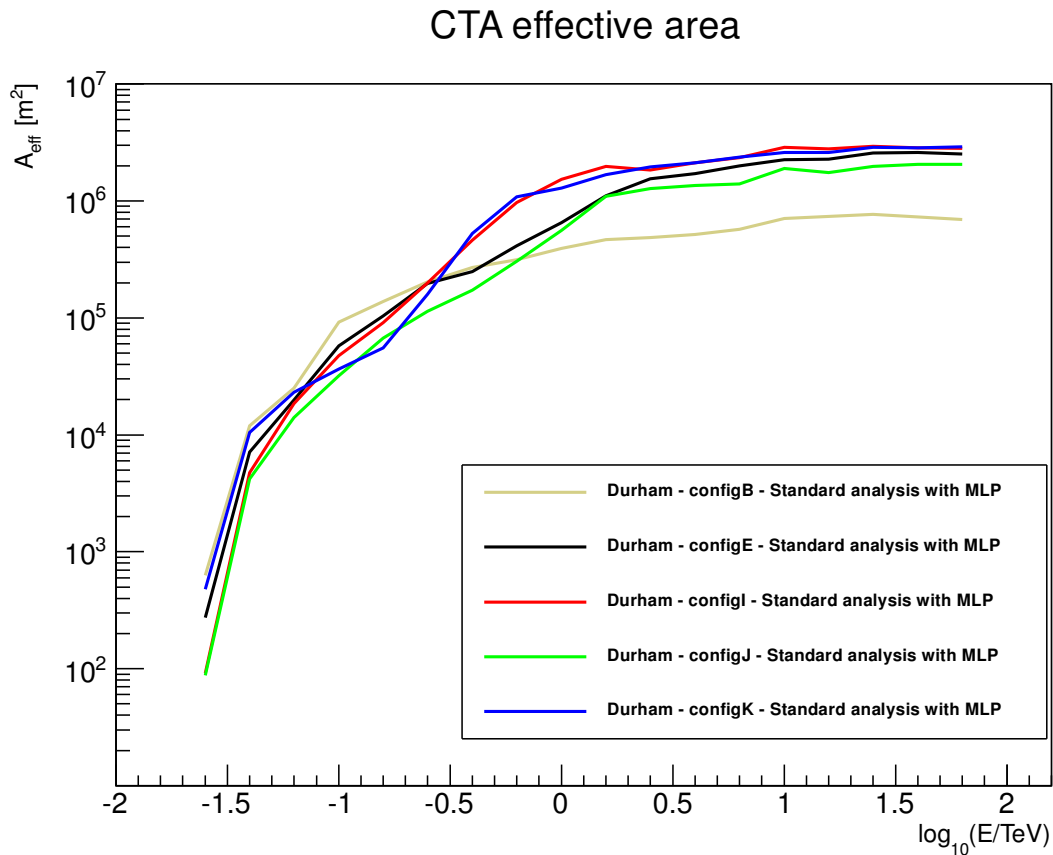
Figure 3.38: Effective area as a function of energy for all analysed subarrays. Subarray-B appears to be the best performing subarray for effective area at low energies below $\lesssim 250$ GeV. Again this is because Subarray-B is comprised of 5 LSTs and 37 MSTs. However at higher energies Subarray-B becomes the worst performing subarray. Subarray-I achieves the highest effective area $\gtrsim 1$ TeV and Subarray-E performs relatively well at both low and high energies.

value derived using a fixed signal efficiency of 30% (beige line) is approximately 60% smaller than the effective area value derived using a fixed signal efficiency of 90% (pink line).

3.5.3   Effective area: comparison of multiplicity cuts

The derived effective area values are also sensitive to the multiplicity cut scheme used as shown in Figure 3.42. It is clear that the derived effective area values are sensitive to the total number of images required for a multiplicity cut scheme. Furthermore the effective area is also sensitive to the energies at which any image multiplicity cut scheme is enforced. When analysing the difference between the best and worst effective area results, as shown in Figure 3.42, it is clear that at an energy of 10 TeV the effective area values shown by
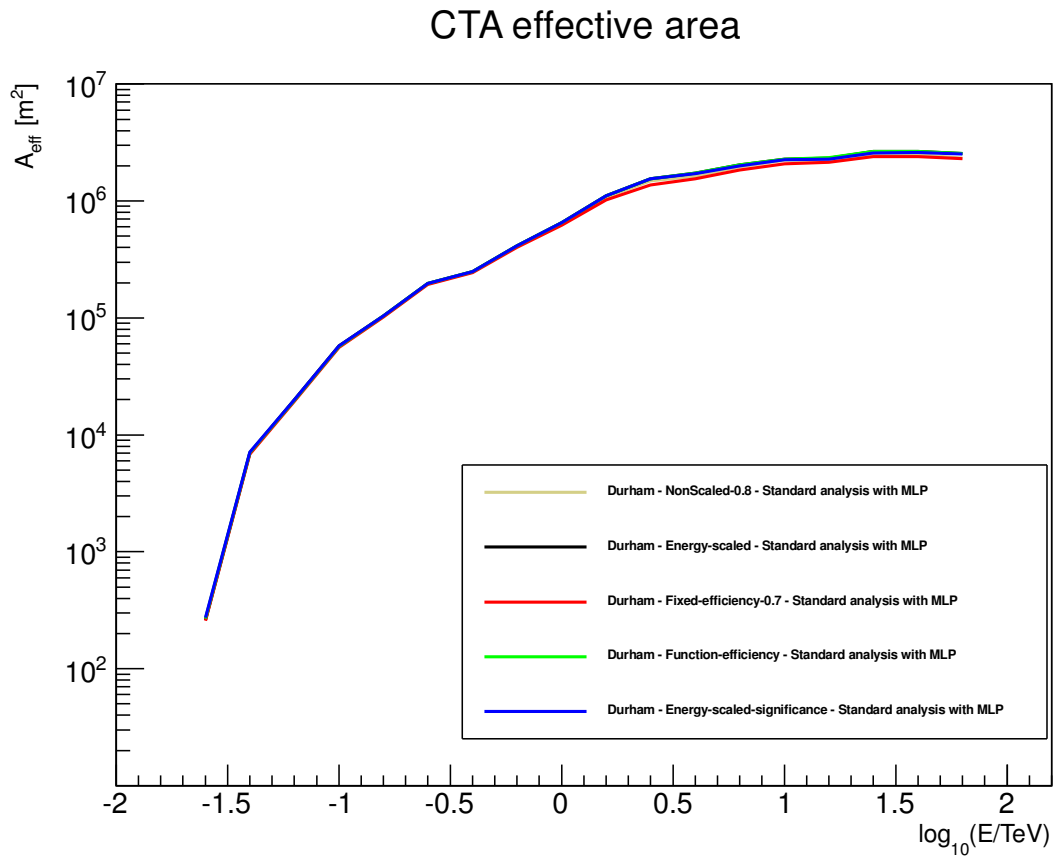
Figure 3.39: Effective area as a function of energy for Subarray-E calculated using different methods to derive the TMVA::MLP cut parameter. It appears that the effective area is not significantly sensitive to the different methods used to derive the TMVA::MLP cut.

the green line are approximately 40% smaller than the values shown by the beige line. In this case using a stricter multiplicity cut scheme for the higher energies has reduced the subarray's effective area.
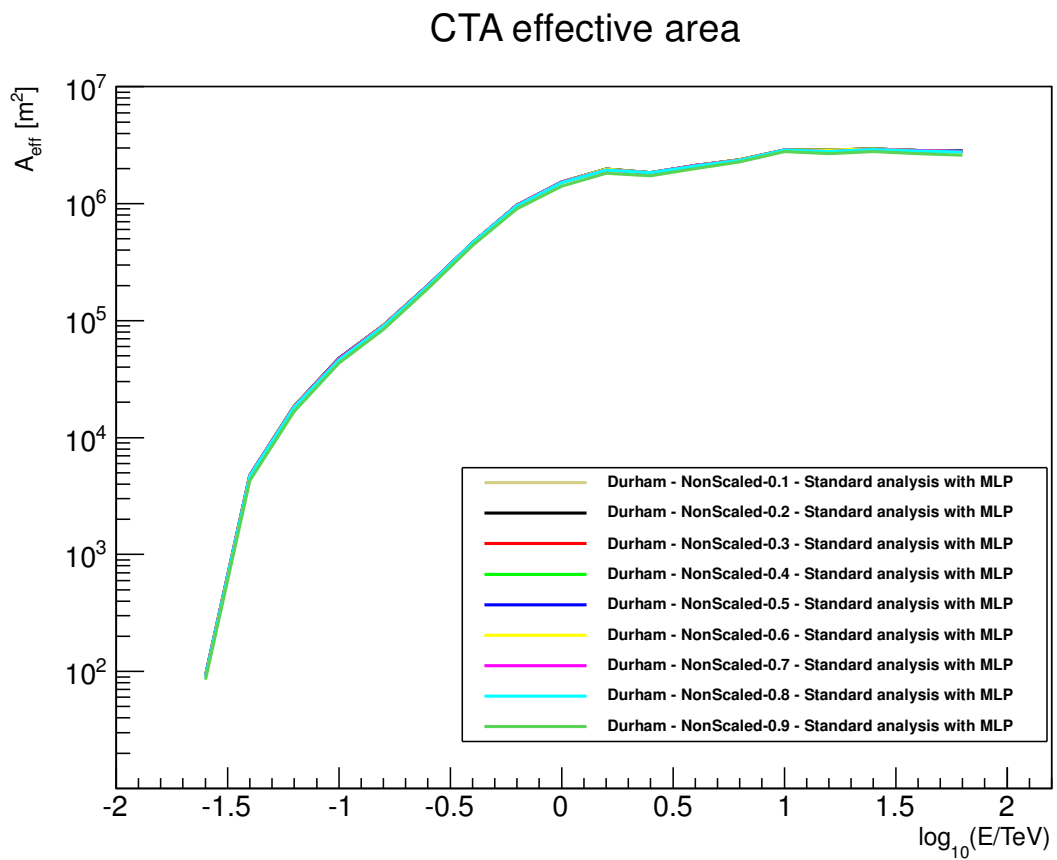
Figure 3.40: Effective area as a function of energy for Subarray-I calculated using different values for the *fixed* TMVA::MLP cut parameter. Again the derived values for the effective area do not appear to be sensitive to the cut value chosen for this particular method of deriving the TMVA::MLP cut parameter. However the concerns highlighted in Section 3.4 regarding the *fixed cut method* should be taken into consideration.
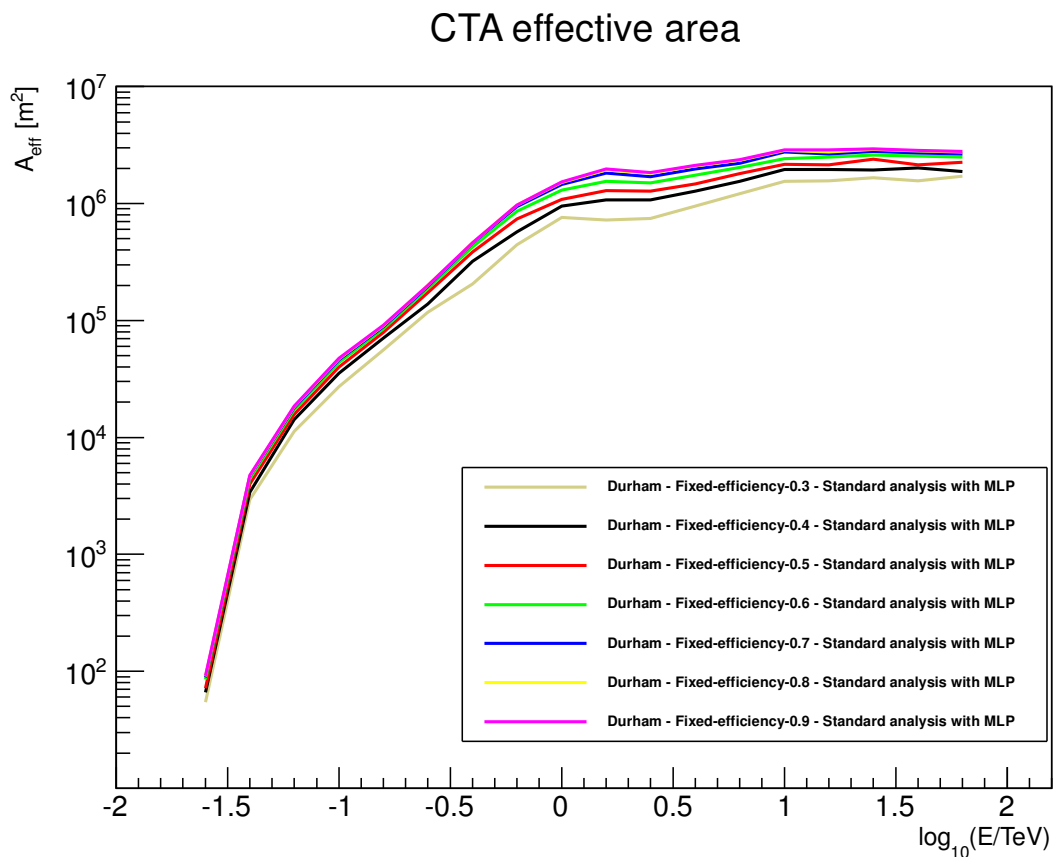
Figure 3.41: Effective area as a function of energy for Subarray-I calculated using different values for the *fixed signal efficiency method* of deriving the TMVA::MLP cut parameter. The effective area values appear to be sensitive to the cut value chosen for this particular method of deriving the TMVA::MLP cut parameter. For example at an energy of approximately 2.5 TeV [$\log_{10}(E/TeV) \approx 0.4$] the effective area value derived using a fixed signal efficiency of 30% (beige line) is approximately 60% smaller than the effective area value derived using a fixed signal efficiency of 90% (pink line).
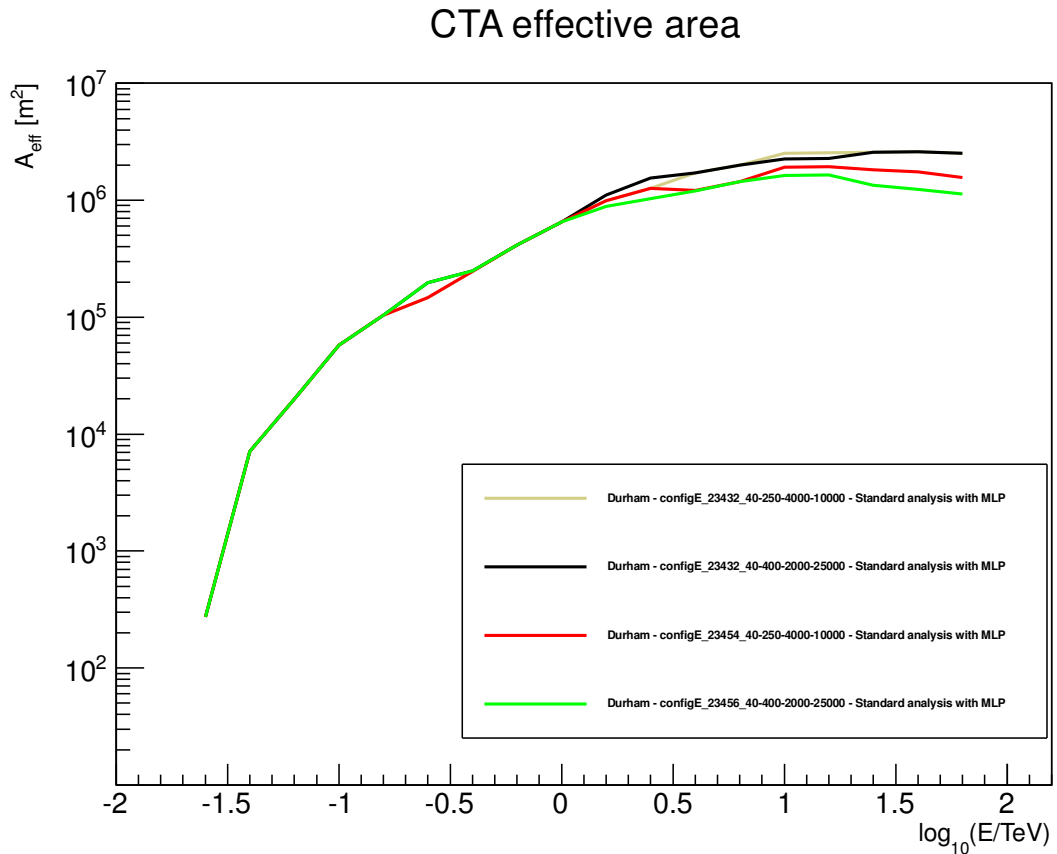
Figure 3.42: Effective area as a function of energy for Subarray-E calculated using different multiplicity cut schemes. The red line shows the effective area values derived using the "best guest" multiplicity cut scheme outlined in Table 3.4. The green line shows the effective area values derived using the same energy bands defined in this scheme, but a different image number requirement. The black line shows the effective area values derived using the multiplicity matrix optimised cut scheme outlined in Table 3.5 and the beige line shows the effective area values derived using the same image number requirement as this scheme, but different energy bands where the cut takes effect. It appears that effective area is sensitive to the multiplicity cut scheme used. For example at an energy of 10 TeV the green line effective area values are approximately 40% smaller than the beige line values. In this case implementing a stricter multiplicity cut at higher energies decreases the subarray effective area.

3.5.4   Effective area: comparison of methods

The effective area results for Subarray-E derived by key members of the CTA MCWG are shown in Figure 3.43. The definition of effective area is the same in each of these results; however they have all been calculated using independent analysis methods. In most cases the same shower simulations have been used, but not necessarily the same reconstruction methods, background rejection or post-cut analysis methods. All the independently calculated effective area results appear consistent with one another. It is clear that the effective area values of this research (Durham blue line) calculated using the TMVA::MLP background rejection method result in an improvement between energies of 60 GeV $\lesssim$ E $\lesssim$ 16 TeV compared to the effective area values calculated using the traditional standard cuts background rejection method.

3.5.5   Effective area: comparison of TMVA methods

Finally the effective area was also calculated for Subarray-E using events that passed a background rejection scheme based upon the TMVA::BDT multivariate analysis method. Figure 3.44 shows two sets of angular resolution results derived using different background rejection schemes. The first set was calculated using a background rejection scheme based on the TMVA::BDT method (blue line) and the second was calculated using a background rejection scheme based on the TMVA::MLP method (red line). In both cases the cut parameter was derived using the *energy-scaled significance method* (see Section 3.2.2.8). In addition the same multiplicity cut scheme (see Table 3.5) was used for both sets of results. The subfigure compares the performance of the two effective area results calculated with different TMVA background rejection schemes. The effective area performance is more or less the same in the low-energy regime, but the TMVA::BDT separated events do appear marginally better at an energy of approximately 60 GeV. The main difference in performance between the methods appears to be from approximately 400 GeV where the TMVA::BDT separated events result in an improved effective area. For example at approximately 630 GeV
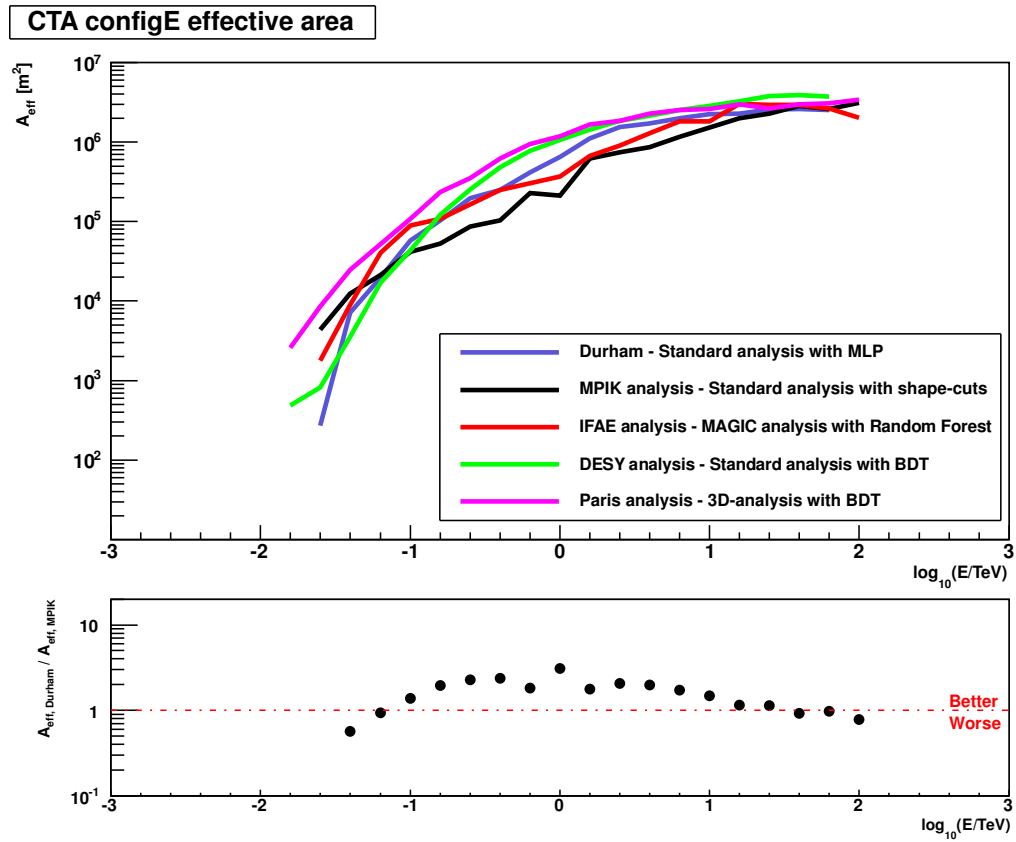
Figure 3.43: Effective area values as a function of energy for Subarray-E calculated by different members of the CTA MCWG. The different analysis approaches are highlighted in the legend. The sub-figure compares the performance of effective area values calculated in this research (Durham blue line) using the TMVA::MLP background rejection method versus the effective area values calculated using the traditional standard cuts background rejection method (MPIK black line). It is clear that this research results in improved effective area values for energies between 60 GeV $\lesssim$ E $\lesssim$ 16 TeV.

[$\log_{10}(E/TeV) \approx$ -0.2] the TMVA::BDT separated effective area values are approximately a factor 1.5 times better than the TMVA::MLP separated effective area values. From approximately 1.5 TeV the TMVA::MLP separated effective area values are marginally better than the TMVA::BDT separated values however these are small relative differences. The settings for the two TMVA methods used are detailed in Tables 3.3 and 3.3.

3.5.6   Effective area: optimisation cuts

To assess the impact of the implemented analysis cuts on the derived effective area performance, it is appropriate to calculate the effective area for each of the analysis cuts

implemented. Figure 3.45 illustrates the derived effective area as a function of energy for Subarray-E calculated using the gamma-ray events passing: the TMVA::MLP cut (red line), the acceptance cut (green line), the multiplicity cut (blue line) and the theta cut (yellow line). Also shown is the effective area using the total number of gamma-ray events triggering the telescopes (black line). This can be thought of as the maximum effective area achievable for the given subarray, in this case Subarray-E. It appears that the acceptance cut significantly reduces the effective area for all energies; whereas the multiplicity cut scheme appears to be optimised for the lowest and highest energies, but not the medium energies from a few hundred GeV to a few TeV.
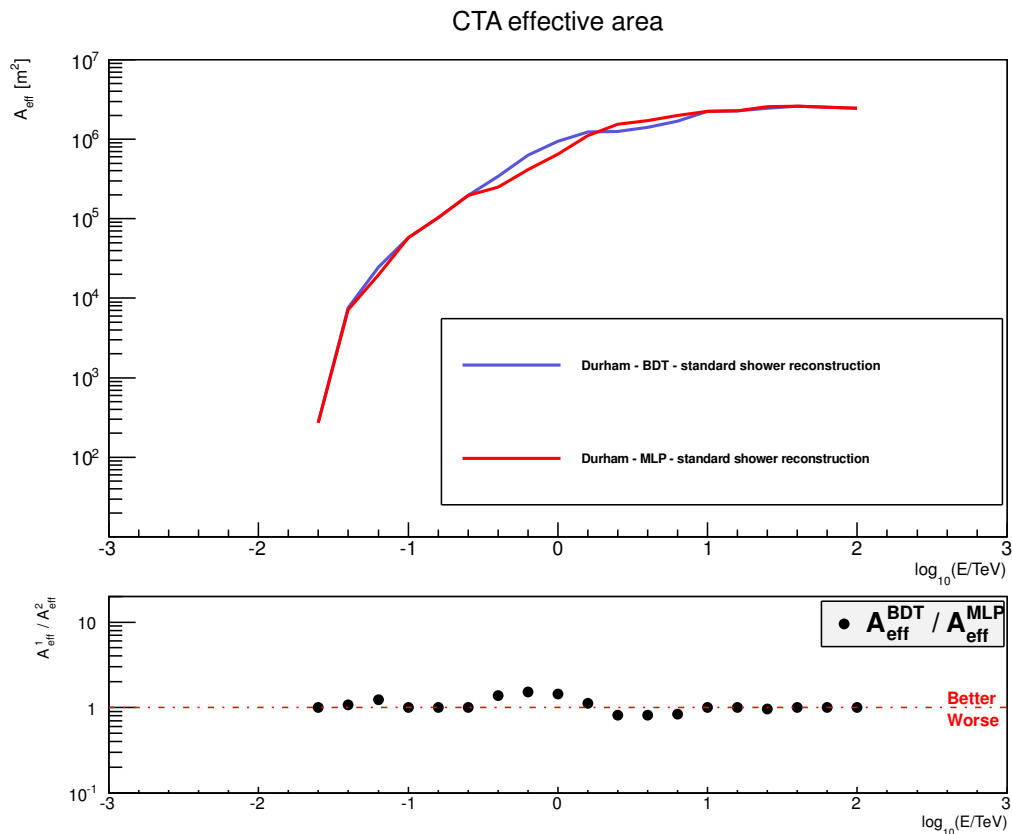
Figure 3.44: Effective area as a function of energy for Subarray-E calculated using different background rejection schemes. One set of effective area results were calculated using a background rejection scheme based on the TMVA::BDT method (blue line) and the other was calculated using a background rejection scheme based on the TMVA::MLP method (red line). In both cases the cut parameter was derived using the *energy-scaled significance method*. In addition the same multiplicity cut scheme was used for both sets of results. The subfigure compares the performance of the two effective area results using the two different background rejection schemes. The main difference in performance between the methods appears to be from approximately 400 GeV where the TMVA::BDT separated events result in an improved effective area. For example at approximately 630 GeV [$\log_{10}(E/\text{TeV}) \approx$ -0.2] the TMVA::BDT separated effective area values are approximately a factor 1.5 times better than the TMVA::MLP separated effective area values.
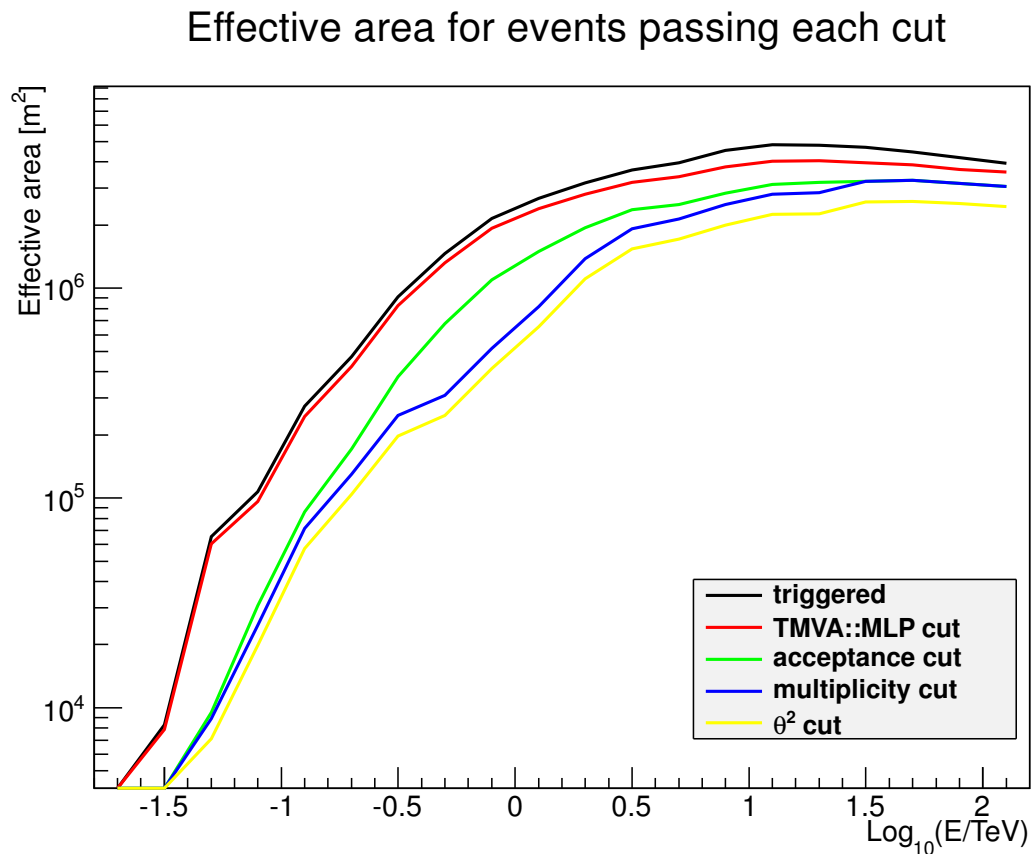
Figure 3.45: Effective area as a function of energy for Subarray-E calculated using the gamma-ray events passing : the TMVA::MLP cut (red line), the acceptance cut (green line), the multiplicity cut (blue line) and the theta cut (yellow line). Also shown is the effective area using the total number of gamma-ray events triggering the telescopes (black line). It appears that the acceptance cut significantly reduces the effective area for all energies; whereas the multiplicity cut scheme appears to be optimised for the lowest and highest energies, but not the medium energies from a few hundred GeV to a few TeV.

3.6 Sensitivity performance results

The post-cut analysis work conducted so far in this research has provided a measure of performance for different proposed CTA subarrays in terms of how well the source position can be determined, how well the energy of the air shower initiating gamma-ray can be inferred and finally a measure of the scale of each subarray's effective area. The final performance measure is to use these calculated values in order to determine the ability of each subarray to detect gamma-rays amongst the much larger cosmic-ray background. In other words, how sensitive is each subarray to the number of gamma-ray signal events compared to the much greater number of hadronic background events? The sensitivity of CTA is defined as the gamma-ray flux needed in order to make a significant detection of an astrophysical gamma-ray source. For ground-based gamma-ray astronomy the accepted level of significance is 5σ in a 50 hours observation. This research determines significance using the accepted method presented by Li and Ma [86] and Equation 3.6 shows how σ is defined.

$$\sigma_{\text{Li\&Ma}} = \sqrt{2} \left\{ N_{\text{ON}} \ln\left[\frac{1+\alpha}{\alpha}\left(\frac{N_{\text{ON}}}{N_{\text{ON}} + N_{\text{OFF}}}\right)\right] + N_{\text{OFF}} \ln\left[(1+\alpha)\left(\frac{N_{\text{OFF}}}{N_{\text{ON}} + N_{\text{OFF}}}\right)\right] \right\}^{\frac{1}{2}}$$
(3.6)

where N_{ON} is the number of counts in the ON region, N_{OFF} the number of counts in the OFF region and α is a normalisation factor between the two regions. The radius that defines the ON region is the derived angular resolution as a function of energy. The OFF region is fixed at a factor 5 larger than the ON region (see Section 2.3). Thus the significance shown in Equation 3.6 is the probability that the difference between N_{ON} and N_{OFF} is not due to any fluctuations in the background events. Hence the number of excess events N_{excess} is calculated using Equation 3.7.

$$N_{\text{excess}} = N_{\text{ON}} - \alpha N_{\text{OFF}}$$
(3.7)

The magnitude of the astrophysical source signal is then approximated to be the number of excess events.

The first step in the sensitivity calculation is to approximate both the signal and background event rates for the ON and OFF regions respectively. For an unknown source, the differential sensitivity is a good measure of the subarray's performance which is proportional to its effective area. If the expected source spectrum is known, it is possible to calculate the integral flux sensitivity by folding in the gamma-ray source spectrum. Two populations of cosmic-ray particles have been considered within the sensitivity calculations: protons and electrons. The results presented here do not take into account the additional heavy particles. These can be included by scaling the proton rate by a factor 1.33, but the effect on net sensitivity is negligible and therefore ignored in this work. Equation 3.8 shows the proton spectrum used in the background rate calculations Sanuki et al. [107] and Bernlöhr [private comm.].

$$\Phi_{\text{proton}} = 0.096 \left(\frac{E}{\text{TeV}}\right)^{-2.7} \qquad [\text{m}^{-2}\ \text{s}^{-1}\ \text{sr}^{-1}\ \text{TeV}^{-1}] \tag{3.8}$$

Equation 3.9 shows the parameterisation, kindly provided by Dr. Konrad Bernlöhr [private comm.], of the electron spectrum used which includes the '*Fermi* shoulder' [16] [1]. The process adopted involved calculating the triggering rates for the two populations of cosmic-rays followed by their sum to find the total background trigger rate.

$$\begin{aligned} \Phi_{\text{electron}} = {} & 6.85 \times 10^{-9} \left(\frac{E}{\text{TeV}}\right)^{-3.21} \\ & + 3.186 \times 10^{-7}\ \exp\left[-\frac{\left(\log(E) - \log(0.107)\right)^2}{0.776\sqrt{2}}\right] \quad [\text{cm}^{-2}\ \text{s}^{-1}\ \text{sr}^{-1}\ \text{TeV}^{-1}] \end{aligned} \tag{3.9}$$

The proton trigger rates $R_{\text{trigger}}^{\text{proton}}(E)$ were calculated using Equation 3.10 [96] which can also be used to calculate the electron trigger rate by substituting in the appropriate electron values.

$$R_{trigger}^{proton}(E_{low}; E_{high}) = \frac{N_{trig}^{proton}}{N_{sim}^{proton}} \, A \, \Omega \, \frac{\Phi_{proton}}{\gamma - 1} \left(E_{low}^{1-\gamma} - E_{high}^{1-\gamma} \right) \qquad [\text{Hz}] \qquad (3.10)$$

where N_{trig}^{proton} is the number of proton events passing the TMVA::MLP cut parameter, the acceptance cut and the multiplicity cut, N_{sim}^{proton} is the number of proton shower events simulated, A the background collecting area, Ω the solid angle observed by the telescopes which is defined by the square of the angular resolution for each energy bin, Φ_{proton} is the flux normalisation factor for the assumed proton spectrum in Equation 3.8, γ is the spectral index used in Equation 3.8 and E_{low} and E_{high} are the lower and upper limits of the energy bins. The number of OFF events is then simply $R_{trigger}^{proton+electron} \times \Delta T$ where ΔT is the observation period. The post-reconstruction proton trigger rate for Subarray-E, before all cuts, is estimated to be $\sim$3.4 kHz.

Then using the Li & Ma significance method (Equation 3.6) the number of ON events is obtained for a 5σ above background observation of 50 hours. The number of excess events is then calculated using Equation 3.7. Assuming a small bin width, the number of excess events can be approximated as in Equation 3.11.

$$N_{excess}(E) \approx \Delta T \, \frac{dF}{dE} \, A_{eff,signal}(E_{bin}) \, \Delta E \qquad (3.11)$$

this can be rearranged to find the differential flux

$$\frac{dF}{dE} = \frac{N_{excess}(E)}{\Delta T \times \Delta E \times A_{eff,signal}(E_{bin})} \qquad (3.12)$$

where ΔE is the fixed bin width, ΔT the observation time and $A_{eff,background}(E)$ the signal effective area. The differential flux can be calculated in many different units, but the most common astronomical units of erg cm^{-2} s^{-1}, found by multiplying the result from Equation 3.12 by E_{bin}^2, are used in this research.

Section 3.1.2 showed the CTA sensitivity performance goals with respect to the very high-energy gamma-ray 'standard candle' source the Crab nebula. For comparison, on all the sensitivity results that follow the differential Crab spectrum as measured by the HEGRA (High-Energy Gamma-Ray Astronomy) system of IACTs is shown as well as the 10%, 1% and 0.1% (milli-Crab) Crab spectrum values. The differential Crab spectrum used is shown in Equation 3.13 [23].

$$\frac{dF_{Crab}}{dE} = 2.79 \times 10^{-11} \left(\frac{E}{TeV} \right)^{-2.59} \qquad [cm^{-2}\ s^{-1}\ TeV^{-1}] \qquad (3.13)$$

For consistency the differential Crab spectrum is scaled to the appropriate energy units of erg.

3.6.1 Sensitivity performance of subarrays analysed

Differential sensitivity performance as a function of energy calculated for each of the analysed subarrays is shown in Figure 3.46. Subarray-B (beige line) and Subarray-K (blue line) appear to be the best performing subarrays at low energies $\lesssim$ 100 GeV, but this is expected because both of these arrays possess the most LSTs (5). Subarray-E (black line) also performs strongly at the low energies despite having one fewer LST. Due to their large number of SSTs Subarray-I (red line) and Subarray-K (blue line) are the best performing subarrays at energies $\gtrsim$ 500 GeV. Subarray-K (blue line) has a distinctive bump in its sensitivity curve at approximately 250 GeV. This is because Subarray-K has no MSTs and hence a discontinuity is created between the low and high-energy regimes. With the same LST (3) and inner MST layout, Subarray-J (green line) and Subarray-I (red line) are the worst performing subarrays $\lesssim$ 150 GeV. As already mentioned Subarray-B (beige line) is the best performing subarray at energies $\lesssim$ 500 GeV. However for energies > 500GeV Subarray-B rapidly loses sensitivity becoming the worst performing subarray at high energies due its compact layout and lack of SSTs. Also shown in Figure 3.46 is the HEGRA Crab spectrum (thin black line), 10% of the HEGRA Crab spectrum (dashed black line), 1% of the HEGRA

Crab spectrum (dotted black line) and 0.1% of the HEGRA Crab spectrum (dot-dashed black line) called the milli-Crab level. None of the analysed subarrays reach the milli-Crab level for differential flux sensitivity. All of the subarrays except Subarray-B are below the 1% Crab spectrum sensitivity level for a large proportion of CTA's core energy range from approximately 40 GeV to 10 TeV.
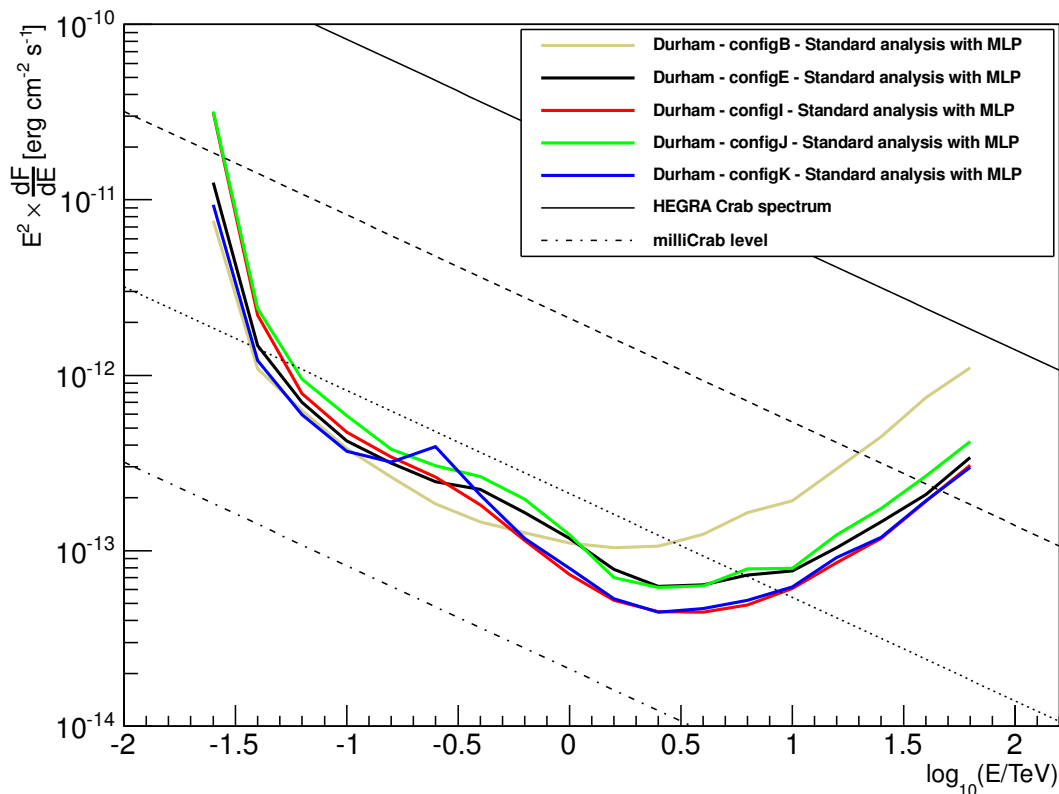
Figure 3.46: Differential sensitivity as a function of energy for all analysed subarrays. Subarray-B (beige line) and Subarray-K (blue line) are the best performing arrays at low energies below $\lesssim 100$ GeV, but this is expected because both of these arrays possess the most LSTs (5). Subarray-E (black line) also performs strongly at the low energies despite having one less LST. Due to their large number of SSTs Subarray-I (red line) and Subarray-K (blue line) are the best performing subarrays at energies above $\gtrsim 500$ GeV. Subarray-K (blue line) has a distinctive bump in its sensitivity curve at approximately 250 GeV. This is because Subarray-K has no MSTs and hence a discontinuity is created between the low and high-energy regimes. Also shown are the HEGRA (High-Energy Gamma-Ray Astronomy) Crab spectrum (thin black line), 10% of the HEGRA Crab spectrum (dashed black line), 1% of the HEGRA Crab spectrum (dotted black line) and 0.1% of the HEGRA Crab spectrum (dot-dashed black line) called the milli-Crab level.

3.6.2 Sensitivity performance: comparison of TMVA cut methods

Once again the method used to derive the TMVA::MLP cut parameter appears to have very little effect on the derived differential flux sensitivity as shown in Figure 3.47. However, the preference is to use the *energy scaled significance method* as it appears to perform well for all energies and its results are not dependent upon any input values.
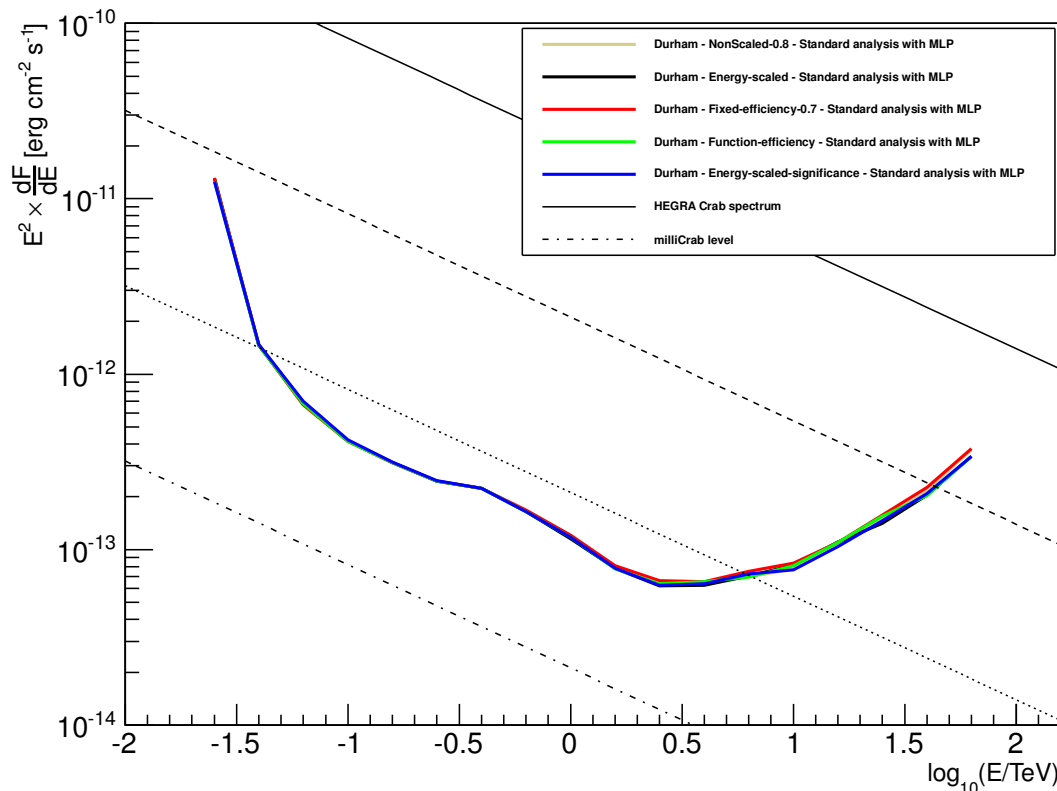
Figure 3.47: Differential sensitivity as a function of energy for Subarray-E calculated using different methods to derive the TMVA::MLP cut parameter. It appears that the differential sensitivity is not sensitive to the different methods used to derive the TMVA::MLP cut.

Again, further investigation of the *fixed cut method* shows that using different cut values has very little effect on the derived differential sensitivities as illustrated in Figure 3.48. However the concerns highlighted in Sections 3.3.4 and 3.4.2 regarding this method should be taken into consideration.

Performing the same test on different values chosen for the *fixed signal efficiency method* of
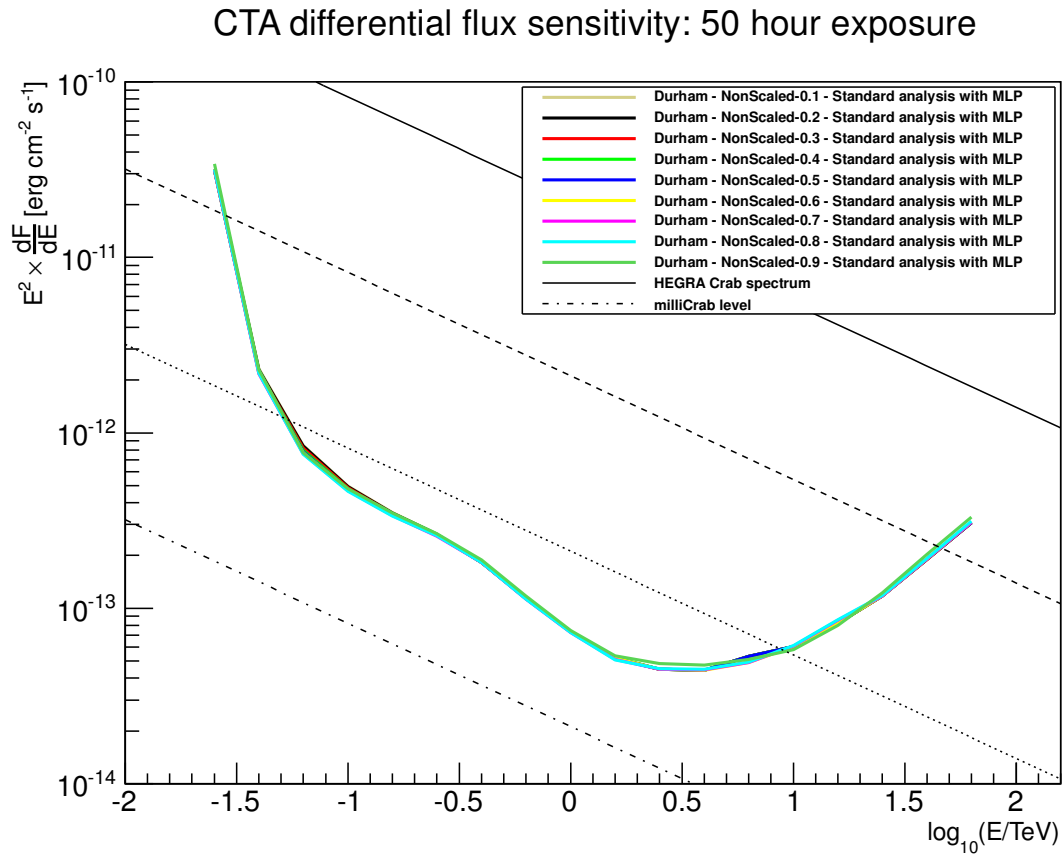
Figure 3.48: Differential sensitivity as a function of energy for Subarray-I calculated using different values for the *fixed* TMVA::MLP cut parameter. The derived values for the differential sensitivity do not appear to be sensitive to the cut value chosen for this particular method of deriving the TMVA::MLP cut parameter. However the concerns highlighted in Section 3.4 regarding the *fixed cut method* should be taken into consideration.

deriving the TMVA::MLP cut parameter, as shown in Figure 3.41, it appears that differential sensitivity performance is sensitive toward these chosen values. For example at an energy of 1 TeV [$\log_{10}(E/TeV) = 0$] the differential sensitivity value derived using a fixed signal efficiency of 30% (beige line) is approximately 53% less sensitive than the differential sensitivity value derived using a fixed signal efficiency of 90% (pink line).
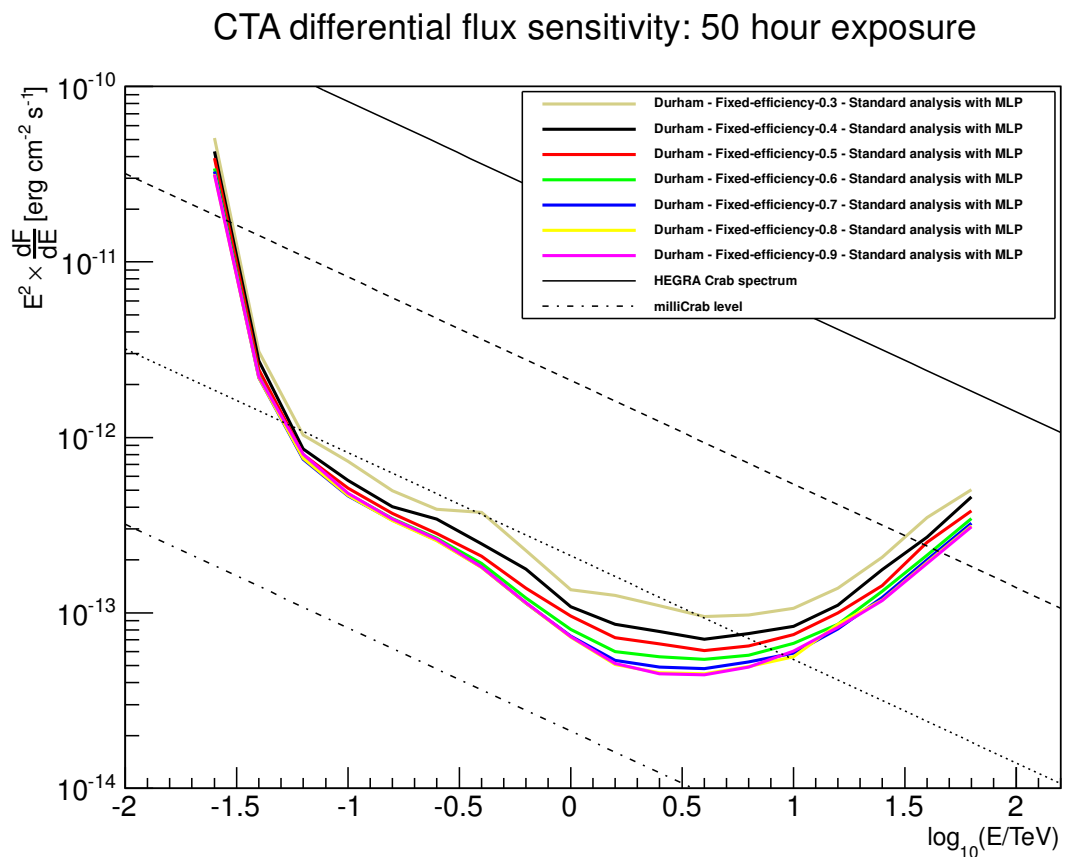
Figure 3.49: Differential sensitivity as a function of energy for Subarray-I calculated using different values for the *fixed signal efficiency method* of deriving the TMVA::MLP cut parameter. The derived differential sensitivity values appear to be sensitive to the cut value chosen for this particular method of deriving the TMVA cut parameter. For example at an energy of 1 TeV [$\log_{10}(E/\text{TeV})$ = 0] the differential sensitivity value derived using a fixed signal efficiency of 30% (beige line) is approximately 53% less sensitive than the differential sensitivity value derived using a fixed signal efficiency of 90% (pink line).

3.6.3   Sensitivity performance: comparison of multiplicity cuts

Differential sensitivity performance as a function of energy for Subarray-E calculated using different multiplicity cut schemes (highlighted in Tables 3.4 and 3.5) is shown in Figure 3.50. The differential sensitivity results appear sensitive to the total number of images required for a multiplicity cut scheme. Furthermore, the differential sensitivity also appears sensitive to the energies at which the image multiplicity cut scheme is enforced. When analysing the difference between the best and worst differential sensitivity results shown in Figure 3.50, it is clear that at an energy of approximately 3 TeV [$\log_{10}(E/TeV) \approx 0.5$] the differential sensitivity values shown by the green line are approximately 15% less sensitive than the values shown by the black line. The green line multiplicity cut gets stricter for high energies and hence a loss in sensitivity performance is seen.

Figure 3.50: Differential sensitivity performance as a function of energy for Subarray-E calculated using different multiplicity cut schemes. The red line shows the differential sensitivity values derived using the "best guest" multiplicity cut scheme outlined in Table 3.4. The green line shows the differential sensitivity derived using the same energy bands defined in this scheme, but a different image number requirement. The black line shows the differential sensitivity values derived using the multiplicity matrix optimised cut scheme outlined in Table 3.5 and the beige line shows the differential sensitivity values derived using the same image number requirement as this scheme, but different energy bands where the cut takes effect. It appears that differential sensitivity is sensitive to the multiplicity cut scheme used. For example at approximately 3 TeV [$\log_{10}(E/TeV) \approx 0.5$] the green line differential sensitivity values are approximately 15% less sensitive than the black line values.

3.6.4 Sensitivity performance: comparison of analysis methods

The differential sensitivity performances for Subarray-E derived by key members of the CTA MCWG are shown in Figure 3.51. The definition of differential sensitivity is the same in each of these results however they have all been calculated using independent analysis methods. In some cases the same shower simulations have been used, but not necessarily the same reconstruction methods, background rejection or post-cut analysis methods. It appears that by implementing a multivariate background rejection scheme as has been done in this research (Durham blue line), it is possible to achieve a significant gain in sensitivity over the traditional standard cuts background rejection method (MPIK black line). The greatest improvement in performance appears to be at low energies below a few hundred GeV and at high energies above a few TeV. Also shown are the Paris results (pink curve) that have been derived using a more advanced reconstruction method (3D analysis method) compared to the standard Hillas style reconstruction method used by the other results shown here. By combining an improved reconstruction method as well as a multivariate based background rejection method, significant improvements in sensitivity performance can be achieved meaning that it might be possibly for CTA to achieve a differential flux sensitivity at the milli-Crab level.
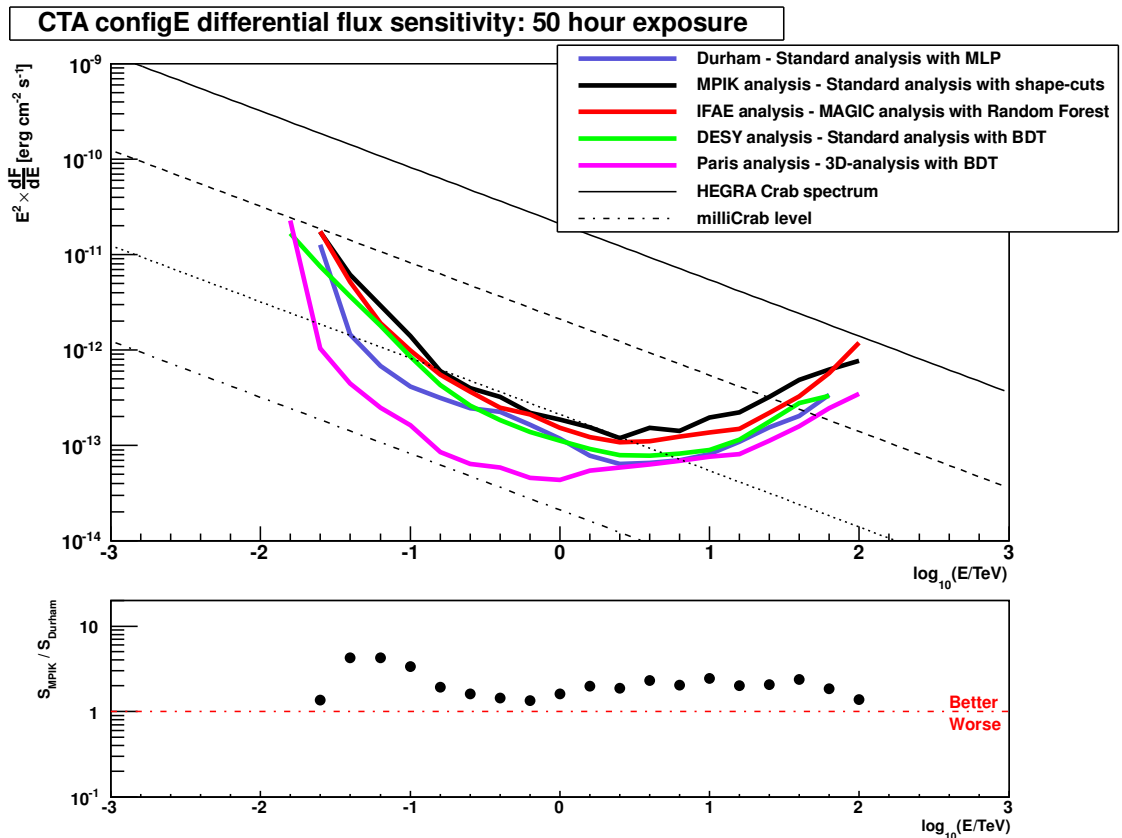
Figure 3.51: Differential sensitivity performance as a function of energy for Subarray-E calculated by different members of the CTA MCWG. The different analysis approaches are highlighted in the legend. The sub-figure compares the differential flux sensitivity values calculated in this research (Durham blue line) using a TMVA::MLP background rejection method versus the differential flux sensitivity values calculated using the tradition standard cuts background rejection method (MPIK black line). This research shows that a significant gain in sensitivity performance can be achieved particularly at low energies below a few hundred GeV and at the high energies above a few TeV. Also shown are the Paris results (pink curve) that have been derived using a more advanced reconstruction method (3D analysis method) compared to the standard Hillas style reconstruction method used by the other results shown here. Again by combining an improved reconstruction method as well as a multivariate based background rejection method, significant improvements in sensitivity performance can be achieved.

3.6.5 Sensitivity performance: comparison of TMVA methods

The differential sensitivity was also calculated for Subarray-E using events that passed a background rejection scheme based upon the TMVA::BDT multivariate analysis method. Figure 3.52 shows two sets of differential sensitivity results derived using different background rejection schemes. The first set was calculated using a background rejection scheme based on the TMVA::BDT method (blue line) and the second was calculated using a background rejection scheme based on the TMVA::MLP method (red line). In both cases the cut parameter was derived using the *energy-scaled significance method* (see Section 3.2.2.8). In addition, the same multiplicity cut scheme (see Table 3.5) was used for both sets of results. The subfigure compares the performance of the two differential sensitivity results calculated with different TMVA background rejection schemes. The TMVA::BDT separated values show a small improvement in differential sensitivity at energies between approximately 400 GeV and 1.5 TeV; however, these are small relative differences and the results are consistent with one another. It may be possible to improve the differential sensitivity performance calculated using a TMVA::MLP based background rejection scheme by optimising the network architecture or even by creating three separate neural networks based on the energy regimes, at no significant time cost. The settings for the two TMVA methods used are detailed in Tables 3.3 and 3.3.
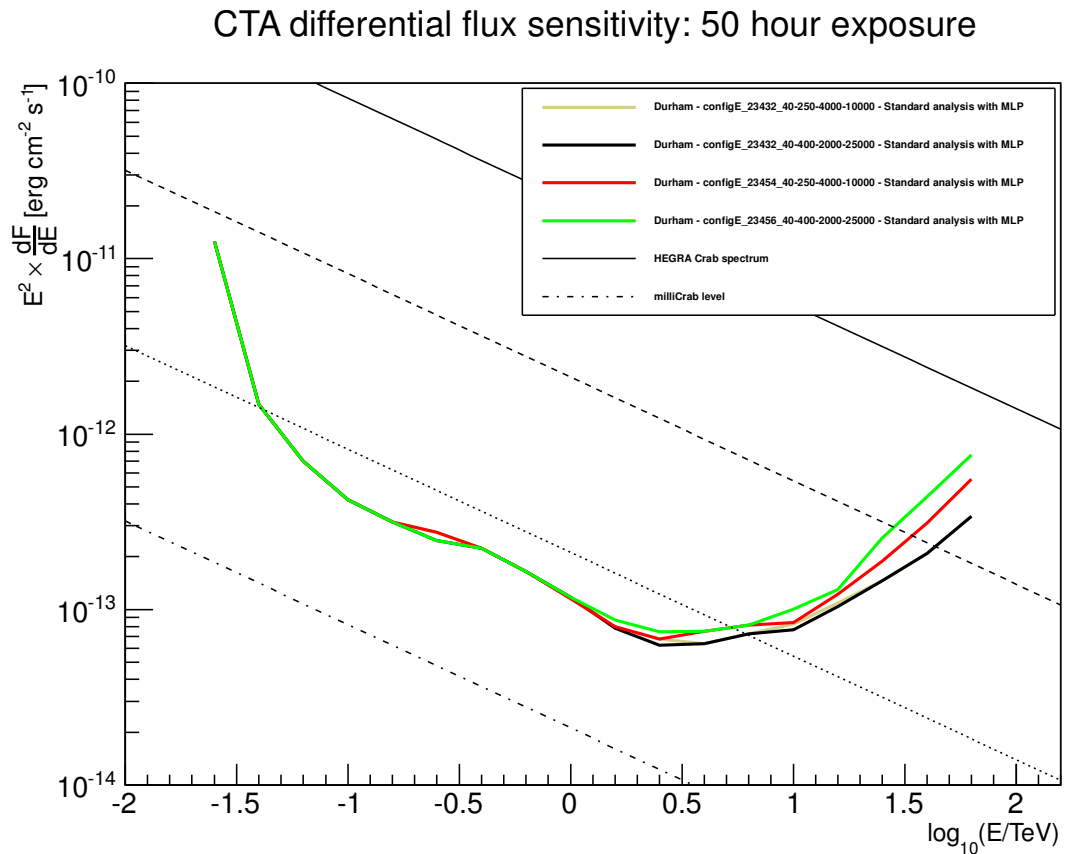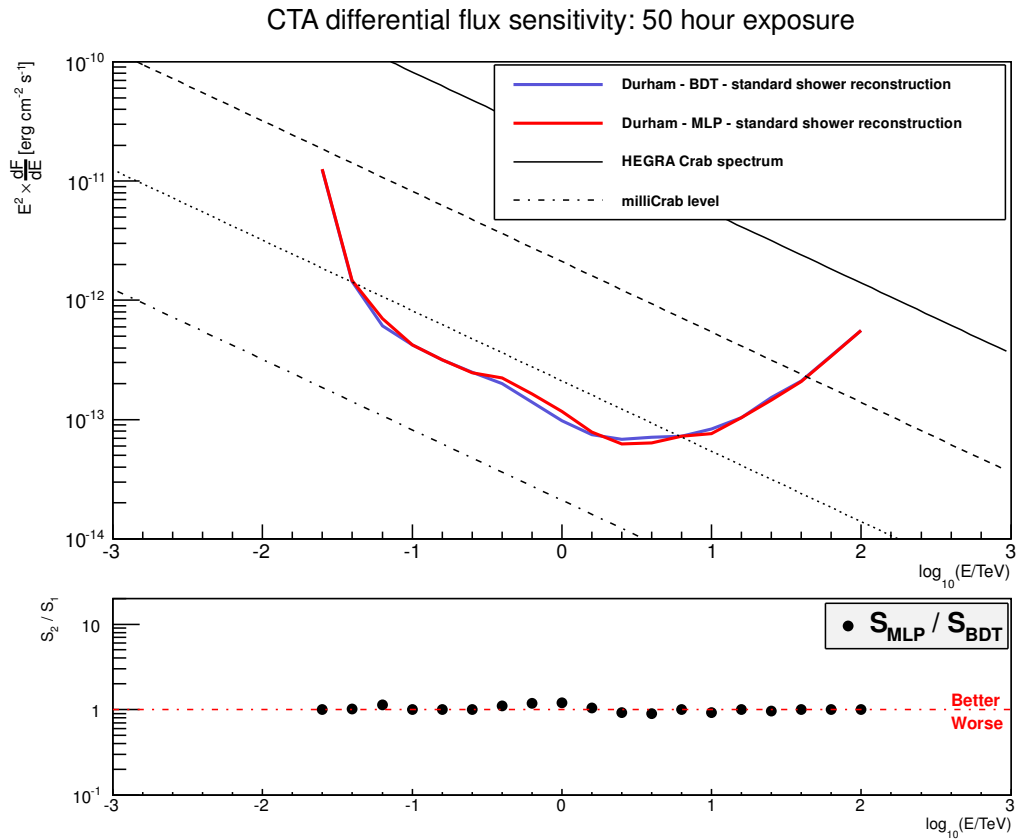
Figure 3.52: Differential sensitivity performance as a function of energy for Subarray-E calculated using different background rejection schemes. One set of differential sensitivity results were calculated using a background rejection scheme based on the TMVA::BDT method (blue line) and the other was calculated using a background rejection scheme based on the TMVA::MLP method (red line). In both cases the cut parameter was derived using the *energy-scaled significance method*. In addition the same multiplicity cut scheme was used for both sets of results. The subfigure compares the performance of the two differential sensitivity results using the two different background rejection schemes. Again the differential sensitivity values resulting from the two background rejections schemes appear to be consistent. The TMVA::BDT separated values show a small improvement in differential sensitivity at energies between approximately 400 GeV and 1.5 TeV however these are small relative differences.

3.6.6 Integral flux sensitivity performance

For a given source spectrum like that in Equation 3.13 for the Crab nebula and using Equations 3.6 and 3.7 it is possible to estimate the number of excess gamma-ray events above the cosmic-ray background. Then integrating over the array effective area for the duration of the observation period and folding in the integral of the Crab nebula spectrum it is possible to calculate the integral sensitivity of the array as shown in Equation 3.14.

$$S_\gamma(E) = \frac{E^{-(\gamma-1)}}{\gamma - 1} \frac{N_{\text{excess}}(E)}{\Delta T} \left(\int_E^\infty A_{\text{eff}}(E)dE \right)^{-1} \times \left(\frac{1}{E_{\text{low}}} \right) \qquad [\text{cm}^{-2}\ \text{s}^{-1}] \qquad (3.14)$$

where γ is the spectral index, $N_{\text{excess}}(E)$ the number of excess gamma-ray events, ΔT the observation period, $A_{\text{eff}}(E)$ the effective area and E_{low} the low edge of the energy bin. Figure illustrates the integral sensitivity limit of CTA baseline Subarray-E (blue line) compared with the integral flux limits (taken from Figure 3.1) of *Fermi* 5 year performance (magenta line), MAGIC-I single telescope (dashed green line), MAGIC-II stereo (solid green line), VERITAS (cyan line) and H.E.S.S. (red line). Even without using improved reconstruction methods, this research demonstrates that achieving an order of magnitude better sensitivity performance over the energy range from 100 GeV to 10 TeV (compared to existing ground-based Cherenkov telescopes such as MAGIC, VERITAS and H.E.S.S.) is within CTA's reach. The integral sensitivity performance derived in this research for Subarray-E achieves the goal of milli-Crab sensitivity at an energy of 1 TeV.
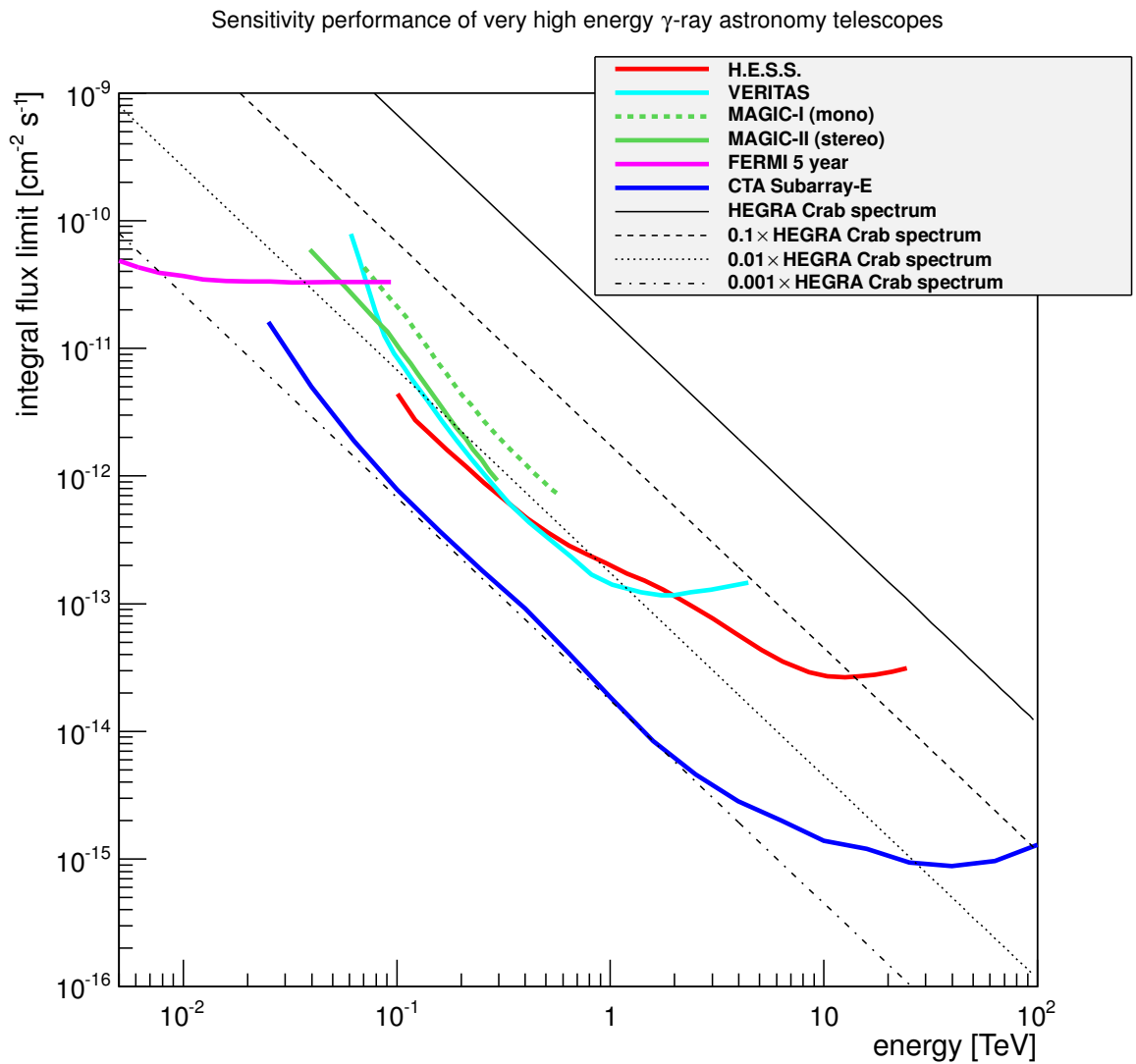
Figure 3.53: The integral sensitivity flux limit of CTA baseline Subarray-E (blue line) compared with the integral sensitivity limits (taken from Figure 3.1) of *Fermi* 5 year performance (magenta line), MAGIC-I single telescope (dashed green line), MAGIC-II stereo (solid green line), VERITAS (cyan line) and H.E.S.S. (red line). The integral sensitivity performance derived in this research for Subarray-E achieves the milli-Crab sensitivity at 1 TeV goal.

3.7 Performance study conclusions

This research has shown that implementing a TMVA::MLP neural network is an effective tool for separating the gamma-ray-like signal events from the cosmic-ray-like background events. Compared to the widely used TMVA::BDT method, the TMVA::MLP is much quicker and sensitivity performance is consistent with that derived using a TMVA::BDT background rejection method. The parameters used to train the neural network have different separating powers. These input parameters, or combination of input parameters, will affect the ability of the neural network to separate signal from background. Apart from the primary shape parameters, additional parameters such as the average time gradient can be used to make small gains in sensitivity performance. Choosing where to make the signal and background cut is best done using a method such as the *energy-scaled significance method* (Section 3.2.2.8) shown in this work. This particular method provides the best sensitivity performances, makes full consideration of the background and is not dependent upon any specific input parameters. During the post-cut analysis of events passing the background separation, the acceptance cut has a significant effect at all energies on the effective area performance; however this cut ensures only the best images are used for sensitivity performance. The multiplicity cut is very efficient at eliminating background events from the sensitivity analysis providing a sensible scheme is used that does not eliminate too many signal events. This work provides a suitable method for determining a multiplicity cut scheme in order to achieve the best sensitivity performance.

Based upon the findings of this research, the following observations are made when comparing against the results of independently calculated sensitivity performances and against CTA's performance goals highlighted in Section 3.1.2.

- the results achieved in this research are amongst the best within the CTA MCWG.

- the baseline Subarray-E integral flux sensitivity results achieve the milli-Crab sensitivity goal at 1 TeV.

- the baseline Subarray-E energy resolution results are within 15% of the goal resolution of $\lesssim$10% at 1 TeV. The other subarrays tested achieved this goal.

- the baseline Subarray-E angular resolution results achieve a reconstructed shower direction performance of $\sim$4 arc-minutes at 1 TeV and $\sim$7 arc-minutes at 40 GeV.

- telescope layout and shower reconstruction method are extremely important for sensitivity performance.

It's clear that for a given set of telescope responses, the array layout and shower reconstruction method appear to have the largest impact on achievable sensitivity performance. This is clearly seen when comparing the methods implemented in this research across different array layouts or comparing against the Paris analysis which uses the 3D-analysis reconstruction method.

Finally if CTA is to detect pulsed gamma-ray emission from pulsars, a good sensitivity is required at energies $\lesssim$ 100 GeV. Even for a large telescope array such as CTA this is a challenge, mainly because of the large cosmic-ray background which includes an increasing number of air showers resulting from background electrons as the array energy threshold decreases. The electromagnetic air showers resulting from electrons at these energies are indistinguishable from gamma-ray-induced air showers, meaning that both the TMVA and standard cuts rejection methods would fail to separate signal from background adequately. Furthermore, the uncertainties in the gamma-ray arrival direction increase at these low energies as shown by the angular resolution results. However despite these challenges, the results of this research, and the independent research conducted by other members of the MCWG, suggest that CTA will provide a significant improvement in sensitivity over existing ground-based imaging atmospheric Cherenkov systems.

Before discussing CTA's prospects of detecting pulsed gamma-ray emission from pulsars (Chapter 5), the results of three small focused studies which use many of the analysis methods highlighted above are presented in Chapter 4.

Chapter 4

Performance Studies: High altitude CTA site and dynamic range

The following chapter presents the results of three specific studies undertaken for the CTA Monte Carlo working group (MCWG). The first study addresses the effect of site altitude on the overall array sensitivity. The second and third studies address two specific questions relating to the dynamic range of the pixels to be used in the cameras; first the amplitude at which the pixels can be saturated before adversely affecting subarray performance, and secondly how changing the photo-electron to digital counts ratio affects subarray performance. Each of these focused studies have made a contribution to the decision making regarding the future construction of CTA, in particular the benefit versus cost challenges.

4.1 Site altitude studies

All of the results presented so far have been simulated for a telescope array situated at an altitude of 2000 m. It has been suggested that building a system of low-energy threshold Cherenkov telescopes at a higher altitude ($\gtrsim$ 3500 m) will help to improve the efficiency of the system [22] particularly at low energies ($\lesssim$ 100 GeV). At high altitude the telescope

system is physically closer to the air shower meaning that the Cherenkov light has less distance and atmosphere to traverse before being detected by the telescope system. Moreover, less Cherenkov light is scattered away from the camera field of view and hence the Cherenkov light intensity should be higher. An improved performance in this low-energy regime will enable better overlap between the *Fermi* space-based telescope and the ground-based Cherenkov telescopes. This is particularly important for modelling and determining the energy spectra of pulsars.

The work presented here is an independent analysis of the high-altitude air shower simulations conducted by Farnier and Lenain [60] (ISDC) in order to assess the potential performance of a high altitude CTA site. The goal of this study is to independently verify their results and to compare the performance measures of the baseline Subarray-E (see Figure 3.3 top left panel) for two different site altitudes: 2000 m and 3700 m.

For this study, the Monte Carlo air shower simulations were conducted for different primary particles (gamma, proton and electron) using CORSIKA and the CTA system response was simulated using the *sim_telarray* and *read_hess* software packages. All simulations were conducted as described in Section 3.2.1.1; however, the number of simulated events is different, as listed in Table 4.1. There is roughly an order of magnitude difference between the number of simulated gamma events at 2000 m and 3700 m, but this is not expected to adversely affect the end results.

Table 4.1: Summary of the number of events simulated for the high-altitude study.

Site altitude	Gammas	Electrons	Protons
2000 m	2.5×10^9	2.6×10^9	5×10^{10}
3700 m	6.46×10^8	1.41×10^9	1.38×10^{10}

Table 4.2 provides a summary of the simulation details for both the 2000 m and the 3700 m studies.

The angular resolution, the energy resolution and bias, the effective area and the differential sensitivity have all been calculated following the methods described in Chapter 3.

Table 4.2: High-altitude study summary.

Details	2000 m	3700 m
image amplitude	60 p.e.	60 p.e.
image cleaning	5-10	5-10
min. pixels	3	3
min. tels	2	2
significance	5σ	5σ
exposure	50 hours	50 hours
energy binning	5 per dec.	5 per dec.
min. gammas	10 per bin	10 per bin
min. background	5% per bin	5% per bin

4.1.1 Angular resolution results

Figure 4.1 shows the derived angular resolution as a function of energy for Subarray-E situated at two different altitudes: 3700 m (blue line) and 2000 m (black line). The angular resolution for the 3700 m site, is improved for energies $\lesssim$ 60 GeV [$\log_{10}$(E/TeV) $\approx$ -1.2], but at energies between 250 GeV $\lesssim$ E $\lesssim$ 1.5 TeV the angular resolution performance deteriorates relative to a 2000 m altitude site (black line). Above approximately 1.5 TeV the angular resolution performance of Subarray-E for the two different altitudes is relatively similar.

The angular resolution performance (see Figure 4.2) calculated in this study for Subarray-E at an altitude of 3700 m (blue line) is significantly better at energies $\lesssim$ 100 GeV [$\log_{10}$(E/TeV) = -1] compared to the angular resolution performance calculated by ISDC (cyan line) and indeed the angular resolution performances of Subarray-E at a 2000m site (black and pink lines). However, at higher energies between 150 GeV $\lesssim$ E $\lesssim$ 1.5 TeV the angular resolution performance appears to deteriorate relative to the 2000 m altitude sites as well as that calculated by ISDC. At energies above approximately 150 GeV the angular resolution performance calculated by MPIK using the standard reconstruction with a shape-cuts background rejection method performs the best. It is not absolutely clear whether this is due to the background rejection method favouring higher energy events or

Figure 4.1: Angular resolution as a function of energy for Subarray-E calculated for two different site altitudes: 3700 m (blue line) and 2000 m (black line). Angular resolution performance for a high altitude Subarray-E appears improved at energies $\lesssim$ 60 GeV [$\log_{10}$(E/TeV) $\approx$ -1.2]. However at energies between 250 GeV $\lesssim$ E $\lesssim$ 1.5 TeV the angular resolution performance deteriorates relative to a 2000 m altitude site.

if the better performance is simply the result of a well optimised multiplicity cut scheme.
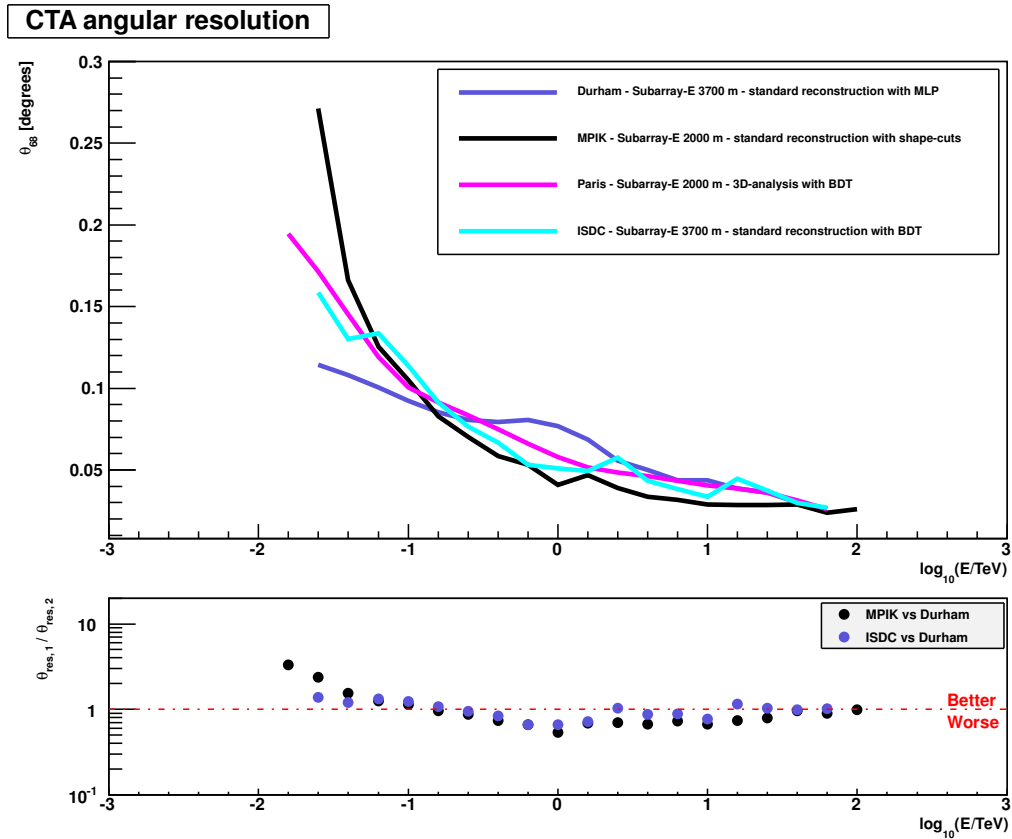
Figure 4.2: Angular resolution values as a function of energy for Subarray-E calculated independently for two different site altitudes using different analysis methods. The angular resolution performance derived in this work for Subarray-E at 3700 m (blue line) is compared against the independently calculated performance for Subarray-E at 3700 m by ISDC (cyan line). Also shown are the angular resolution performances for Subarray-E at 2000 m calculated by MPIK (black line) using the standard reconstruction with shape-cuts background rejection [35], and Paris (pink line) using the 3D-analysis reconstruction [85] and a BDT background rejection method [34]. The angular resolution performance calculated in this work appears to be significantly better at energies $\lesssim 100$ GeV [$\log_{10}(\text{E/TeV}) = -1$] compared to the angular resolution performance calculated by ISDC and indeed the performances of Subarray-E at a 2000m site. However at higher energies between 150 GeV $\lesssim$ E $\lesssim$ 1.5 TeV the angular resolution performance calculated in this research appears to deteriorate relative to the 2000 m altitude sites as well as that calculated by ISDC. At energies above approximately 150 GeV the angular resolution performance calculated by MPIK using the standard reconstruction with a shape-cuts background rejection method performs the best.

4.1.2   Energy resolution results

Figure 4.3 shows the derived energy resolution as a function of energy for Subarray-E situated at: 3700 m (blue line) and 2000 m (black line). The energy resolution performance of the 3700 m site appears improved at energies 50 GeV $\lesssim$ E $\lesssim$ 1.5 TeV. However at energies greater than approximately 1.5 TeV [$\log_{10}$(E/TeV) $\approx$ 0.2] the energy resolution performance of Subarray-E at high altitude begins to deteriorate relative to Subarray-E at an altitude of 2000 m. At an energy of approximately 60 TeV [$\log_{10}$(E/TeV) $\approx$ 1.8] the 2000 m altitude Subarray-E energy resolution performance is nearly 50% better than that of Subarray-E at 3700 m. Perhaps somewhat surprising is that the energy resolution performance of Subarray-E at 3700 m altitude for energies $\lesssim$ 50 GeV [$\log_{10}$(E/TeV) $\approx$ -1.3] is not significantly better than that of Subarray-E at 2000 m.

The energy resolution performance calculated in this study (see Figure 4.4) for Subarray-E at an altitude of 3700 m (blue line) is significantly better at energies $\lesssim$ 100 GeV [$\log_{10}$(E/TeV) = -1] compared to the energy resolution performance calculated by ISDC (cyan line) and indeed the performances of Subarray-E at a 2000m site (black and pink lines). For example, the sub-figure shows that at an energy of approximately 25 GeV [$\log_{10}$(E/TeV) $\approx$ -1.6] the energy resolution calculated in this work is roughly a factor 2 better than that calculated by ISDC and MPIK and approximately 30% better than the performance calculated by Paris. At higher energies above $\gtrsim$ 2 TeV [$\log_{10}$(E/TeV) $\approx$ 0.3] the energy resolution performance of Subarray-E at 2000 m calculated by MPIK using the standard reconstruction with a shape-cuts background rejection method is the best.

4.1.3   Effective area results

Figure 4.5 shows the derived effective area as a function of energy for Subarray-E situated at 3700 m (blue line) and 2000 m (black line). The effective area performance of the 3700 m site is approximately a factor 3 greater for energies around 15 GeV [$\log_{10}$(E/TeV) $\approx$ -1.8] compared to Subarray-E at 2000 m altitude (black line). However at energies greater than
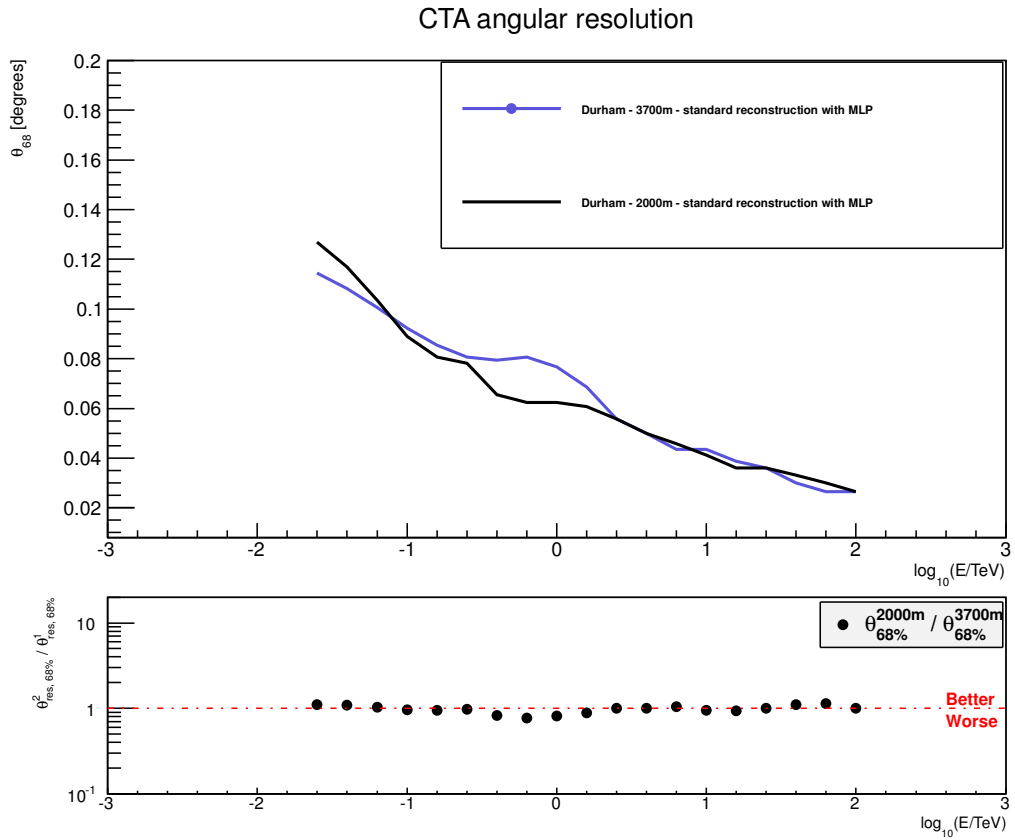
Figure 4.3: Energy resolution as a function of energy for Subarray-E calculated for two different site altitudes: 3700 m (blue line) and 2000 m (black line). Energy resolution performance for a high altitude Subarray-E appears improved at energies 50 GeV $\lesssim$ E $\lesssim$ 1.5TeV. At energies greater than approximately 1.5 TeV [$\log_{10}(E/TeV) \approx 0.2$] the energy resolution performance of Subarray-E at high altitude begins to deteriorate relative to Subarray-E at an altitude of 2000 m. At an energy of approximately 60 TeV [$\log_{10}(E/TeV) \approx 1.8$] the Subarray-E energy resolution performance is nearly 50% better than that of Subarray-E at 3700 m.

Figure 4.4: Energy resolution as a function of energy for Subarray-E calculated independently for two different site altitudes using different analysis methods. The energy resolution performance derived in this work for Subarray-E at 3700 m (blue line) is compared against the independently calculated performance for Subarray-E at 3700 m by ISDC (cyan line). Also shown are the energy resolution performances for Subarray-E at 2000 m calculated by MPIK (black line) using the standard reconstruction with shape-cuts background rejection, and Paris (pink line) using the 3D-analysis reconstruction and a BDT background rejection method. The energy resolution performance calculated in this work appears to be significantly better at energies $\lesssim$ 100 GeV [$\log_{10}(E/TeV) = -1$] compared to the energy resolution performance calculated by ISDC and indeed the performances of Subarray-E at a 2000m site. For example, the sub-figure shows that at an energy of approximately 25GeV [$\log_{10}(E/TeV) \approx -1.6$] the energy resolution calculated in this work is roughly a factor 2 better than that calculated by ISDC. At higher energies above $\gtrsim$ 2 TeV [$\log_{10}(E/TeV) \approx 0.3$] the energy resolution performance of Subarray-E at 2000 m calculated by MPIK using the standard reconstruction with a shape-cuts background rejection method performs the best.

approximately 1.5 TeV [$\log_{10}(E/TeV) \approx 0.2$] the effective area performance of Subarray-E at high altitude begins to deteriorate relative to Subarray-E at an altitude of 2000 m.
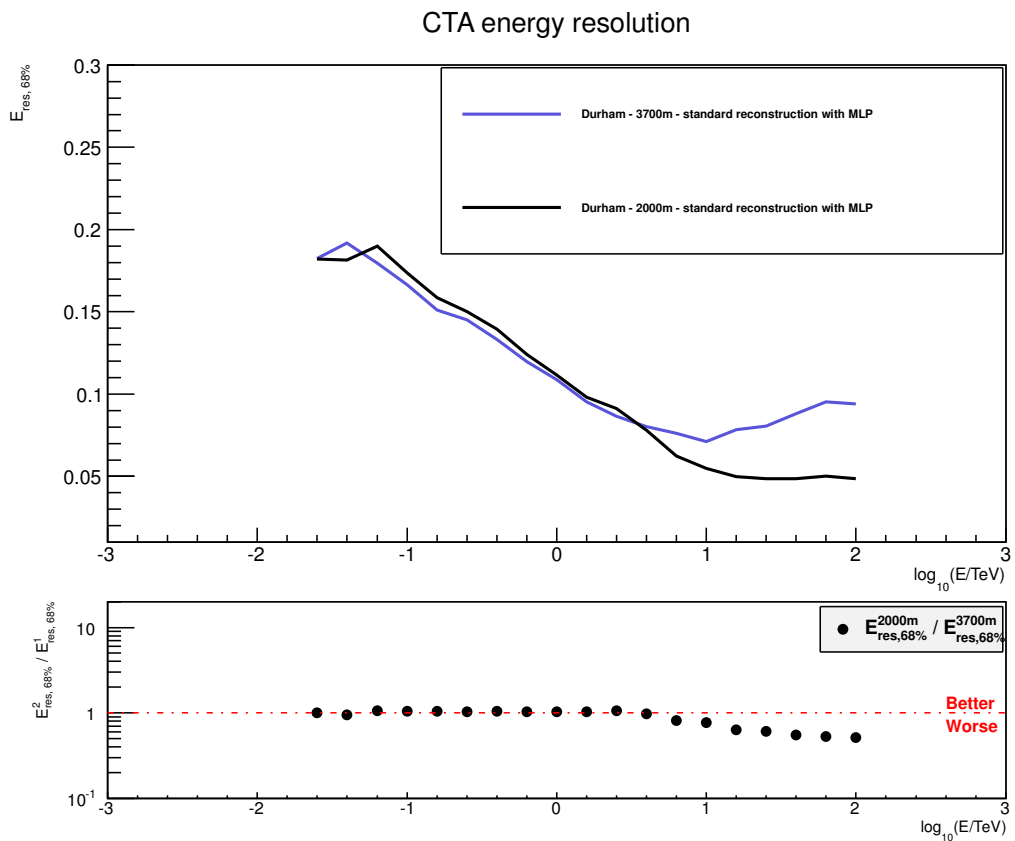

Figure 4.5: Effective area as a function of energy for Subarray-E calculated for two different site altitudes: 3700 m (blue line) and 2000 m (black line). The sub-figure shows that the effective area performance for a 3700 m altitude Subarray-E is approximately a factor 3 greater at energies of approximately 15 GeV [$\log_{10}(E/TeV) \approx -1.8$] compared to a 2000 m altitude Subarray-E. However at energies greater than approximately 1.5 TeV [$\log_{10}(E/TeV) \approx 0.2$] the effective area performance of Subarray-E at high altitude begins to deteriorate relative to Subarray-E at an altitude of 2000 m.

The effective area performance calculated in this work (see Figure 4.6) for Subarray-E at an altitude of 3700 m (blue line) is better at energies $\lesssim$ 2.5 TeV [$\log_{10}(E/TeV) \approx 0.4$] compared to the effective area performance calculated by ISDC (cyan line). At energies of approximately 15 GeV the effective area performance calculated in this work is significantly better, approximately a factor 5 greater, than that calculated by ISDC. Somewhat surprisingly, the effective area performance of Subarray-E at 2000 m altitude calculated by MPIK (black line) and Paris (pink line) for energies $\lesssim$ 40 GeV [$\log_{10}(E/TeV) \approx -1.4$], are

both significantly better than the effective area performances calculated in this work and by ISDC. Indeed, the performance calculated by Paris using the 3D-analysis reconstruction method is better than all the other analyses for all energies, suggesting that using an improved reconstruction technique can provide significant gains in sensitivity performance even for a lower level site.

4.1.4 Differential sensitivity results

Figure 4.7 shows the derived differential sensitivity as a function of energy for Subarray-E situated at 3700 m (blue line) and 2000 m (black line). The differential sensitivity performance of the 3700 m site is approximately a factor 2 greater for energies of around 15 GeV [$\log_{10}(E/TeV) \approx$ -1.8] compared to Subarray-E at 2000 m altitude (black line). However at energies greater than approximately 1.5 TeV [$\log_{10}(E/TeV) \approx 0.2$] the differential sensitivity performance of Subarray-E at high altitude begins to deteriorate relative to Subarray-E at an altitude of 2000 m.

The differential sensitivity performance calculated in this work (see Figure 4.8) for Subarray-E at an altitude of 3700 m (blue line) appears to be better at energies $\lesssim$ 125 GeV [$\log_{10}(E/TeV) \approx$ -0.9] and $\gtrsim$ 1.25 TeV [$\log_{10}(E/TeV) \approx 0.1$] compared to the differential sensitivity performance calculated by ISDC. At energies $\lesssim$ 60 GeV [$\log_{10}(E/TeV) \approx$ -1.2] the differential sensitivity performance calculated in this work is at least 1.5 times better than that calculated by ISDC. The differential sensitivity performance for Subarray-E at 2000 m altitude calculated by MPIK is the worst performing relative to the other results shown here for energies below approximately 1.5 TeV [$\log_{10}(E/TeV) \approx 0.2$]. The differential sensitivity performance for Subarray-E at 2000 m calculated by Paris using the 3D-analysis reconstruction method is the best performing for all energies. At an energy of approximately 15 GeV [$\log_{10}(E/TeV) \approx$ -1.8] the Paris calculated differential sensitivity performance is approximately a factor 6 better than the performances of Subarray-E at 3700 m calculated in this work.
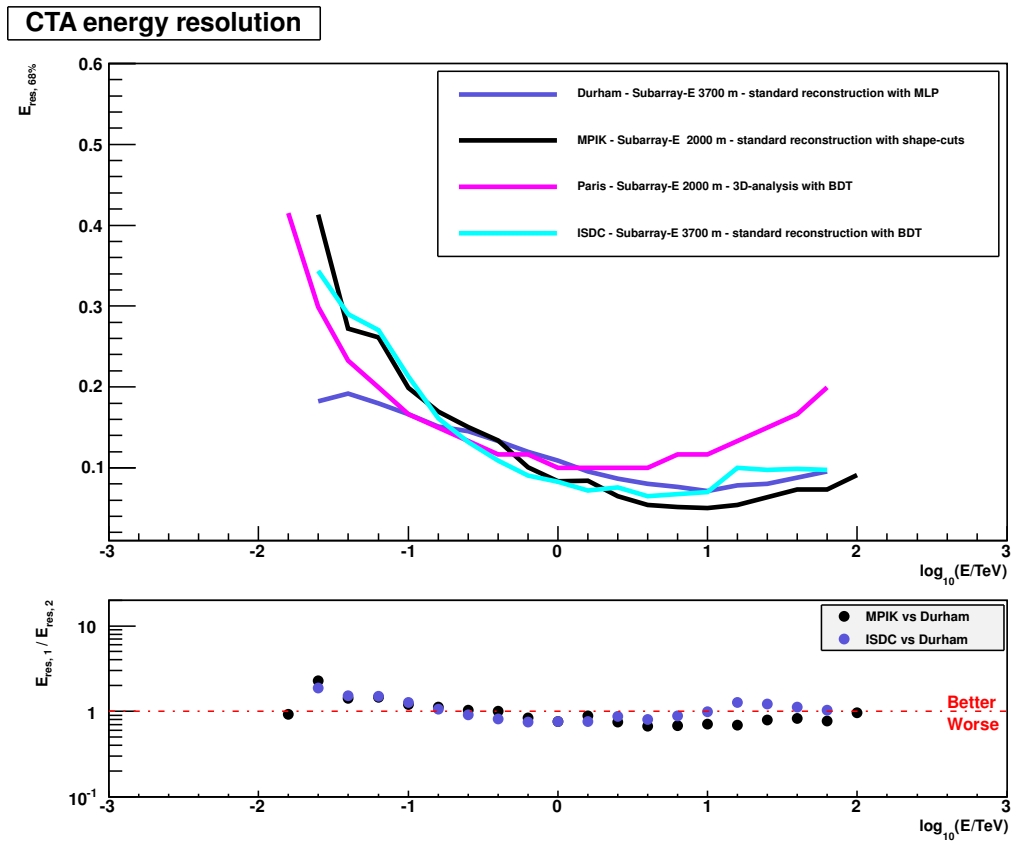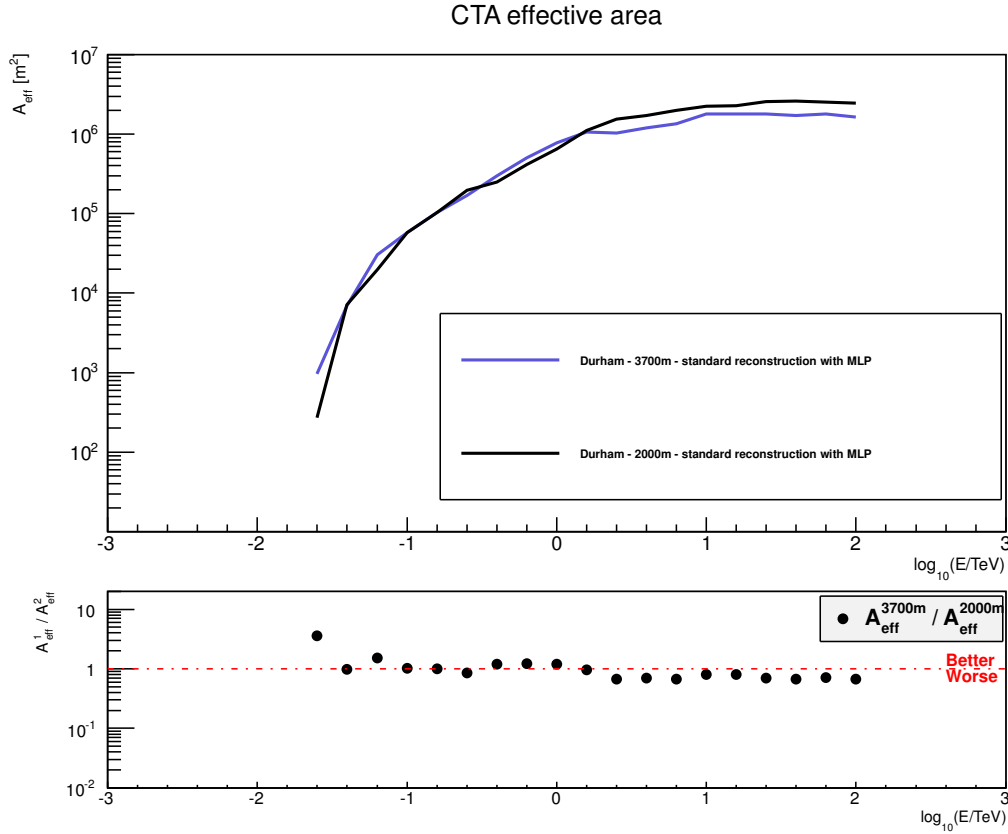
Figure 4.6: Effective area as a function of energy for Subarray-E calculated independently for two different site altitudes using different analysis methods. The effective area performance derived in this work for Subarray-E at 3700 m (blue line) is compared against the independently calculated performance for Subarray-E at 3700 m by ISDC (cyan line). Also shown are the effective area performances for Subarray-E at 2000 m calculated by MPIK (black line) using the standard reconstruction with shape-cuts background rejection, and Paris (pink line) using the 3D-analysis reconstruction and a BDT background rejection method. The effective area performance calculated in this work appears to be better at energies $\lesssim$ 2.5 TeV [$\log_{10}$(E/TeV) $\approx$ 0.4] compared to the effective area performance calculated by ISDC. At energies of approximately 15 GeV the effective area performance calculated in this work is significantly better, approximately a factor 5 greater, than that calculated by ISDC. Somewhat surprisingly, the effective area performance of Subarray-E at 2000 m altitude calculated by MPIK and Paris for energies $\lesssim$ 40 GeV [$\log_{10}$(E/TeV) $\approx$ -1.4], are both significantly better than the effective area performances calculated in this work and by ISDC. Indeed, the performance calculated by Paris using the 3D-analysis reconstruction method is better than all the other analyses for all energies.
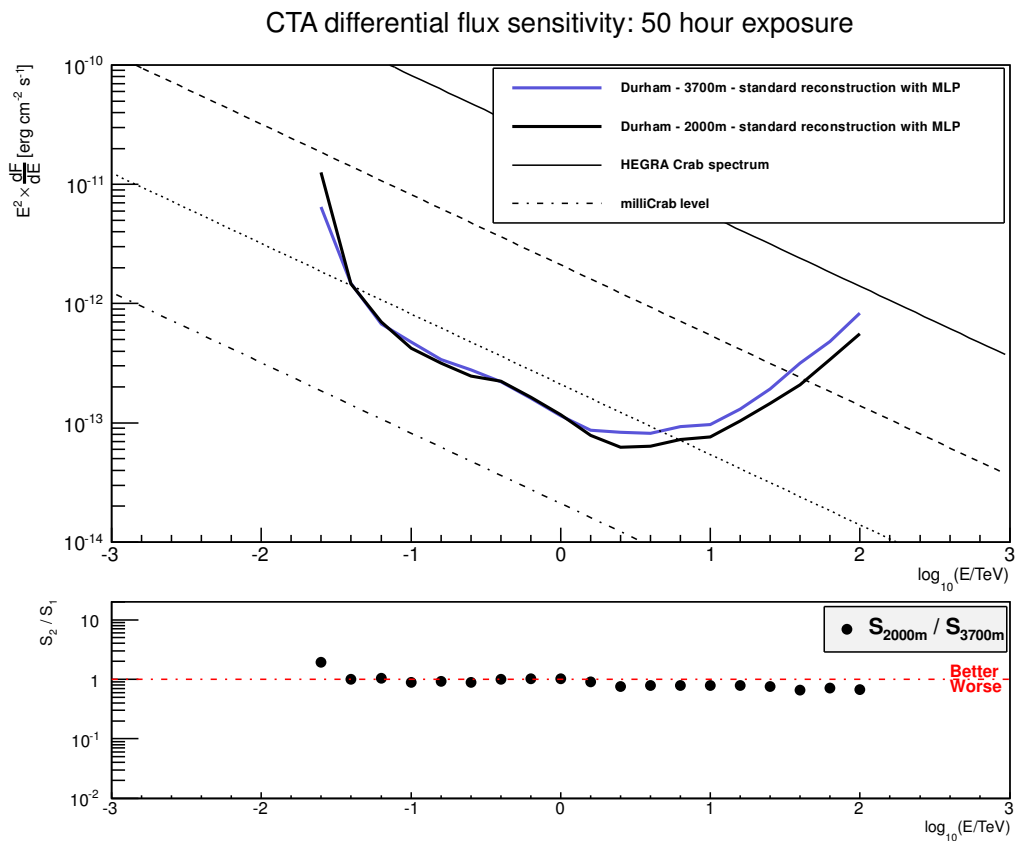
Figure 4.7: Differential sensitivity as a function of energy for Subarray-E calculated for two different site altitudes: 3700 m (blue line) and 2000 m (black line). The sub-figure shows that the differential sensitivity performance for a 3700 m altitude Subarray-E is approximately a factor 2 greater at energies of approximately 15 GeV [$\log_{10}$(E/TeV) $\approx$ -1.8] compared to a 2000 m altitude Subarray-E. However at energies greater than approximately 1.5 TeV [$\log_{10}$(E/TeV) $\approx$ 0.2] the differential sensitivity performance of Subarray-E at high altitude begins to deteriorate relative to Subarray-E at an altitude of 2000 m.
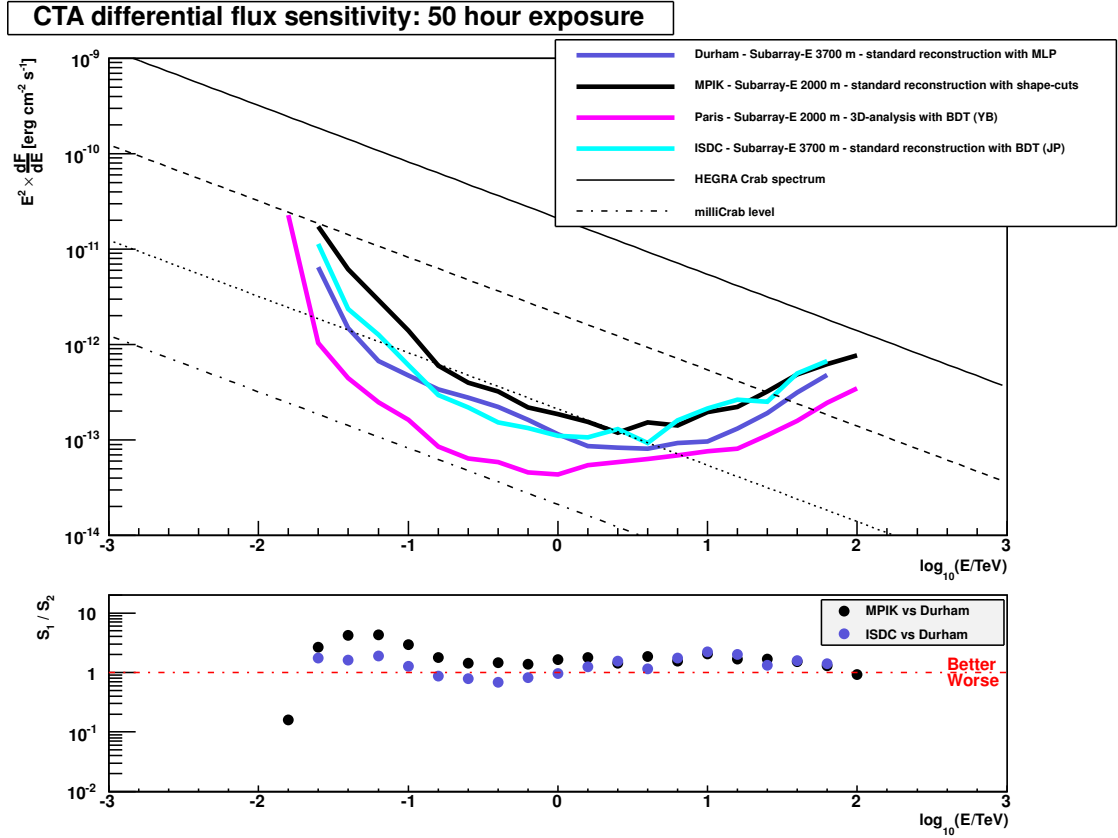
Figure 4.8: Differential sensitivity as a function of energy for Subarray-E calculated independently for two different site altitudes using different analysis methods. The differential sensitivity performance derived in this work for Subarray-E at 3700 m (blue line) is compared against the independently calculated performance for Subarray-E at 3700 m by ISDC (cyan line). Also shown are the differential sensitivity performances for Subarray-E at 2000 m calculated by MPIK (black line) using the standard reconstruction with shape-cuts background rejection, and Paris (pink line) using the 3D-analysis reconstruction and a BDT background rejection method. The differential sensitivity performance calculated in this work appears to be better at energies $\lesssim$ 125 GeV [$\log_{10}(E/\text{TeV}) \approx$ -0.9] and $\gtrsim$ 1.25 TeV [$\log_{10}(E/\text{TeV}) \approx$ 0.1] compared to the differential sensitivity performance calculated by ISDC. At energies $\lesssim$ 60 GeV [$\log_{10}(E/\text{TeV}) \approx$ -1.2] the differential sensitivity performance calculated in this work is at least a factor 1.5 better than that calculated by ISDC. The differential sensitivity performance for Subarray-E at 2000 m altitude calculated by MPIK is the worst performing relative to the other results shown here for energies below approximately 1.5 TeV [$\log_{10}(E/\text{TeV}) \approx$ 0.2]. The differential sensitivity performance for Subarray-E at 2000 m calculated by Paris using the 3D-analysis reconstruction method is the best performing for all energies. At an energy of approximately 15 GeV [$\log_{10}(E/\text{TeV}) \approx$ -1.8] the Paris calculated differential sensitivity performance is approximately a factor 6 better than the performances of Subarray-E at 3700 m calculated in this work.
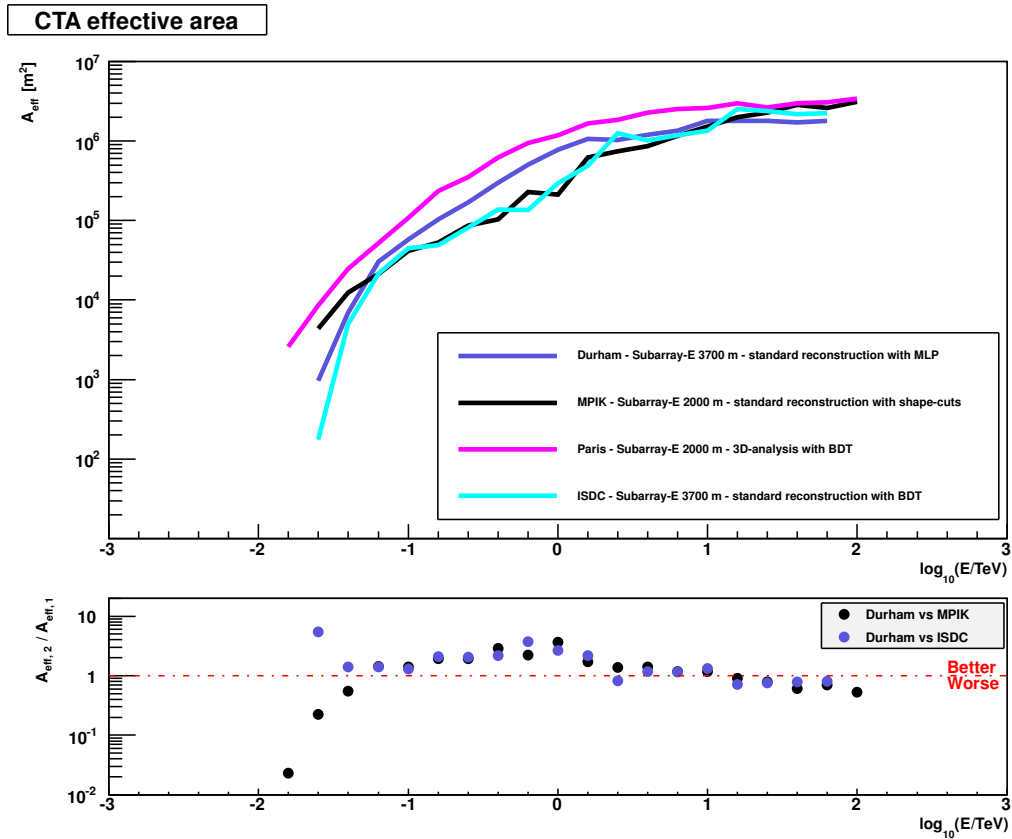
4.1.5   High altitude-site study conclusions

From this study it can be concluded that there is a gain in differential sensitivity within the low-energy regime $\lesssim 100$ GeV if the subarray is situated at an altitude of 3700 m compared to 2000 m. However this only appears to be the case when comparing performance against results derived using the traditional reconstruction and background rejection methods or when comparing against the performance results for a lower altitude array derived using the same analysis methods. It appears that using a more sophisticated reconstruction method, such as the 3D-analysis method, provides a significantly improved differential sensitivity performance even for an array situated at a lower altitude.

If comparing performance results with like for like reconstruction and analysis over the full core energy range it can be concluded that the subarray situated at an altitude of 2000 m performs at least equally as well as a subarray situated at an altitude of 3700 m above energies of approximately 40 GeV. For energies larger than roughly 1.5 TeV the subarray located at 2000 m consistently performs about 20% better than the same subarray situated at 3700 m. As was noted in the conclusions of Farnier and Lenain [60] the high altitude array does not take into account any physical optimisation of the array for the higher altitude. For example the telescope focal lengths, the pixel spacing, camera trigger thresholds and even the telescope layout are all identical. Thus the findings of this study are consistent with those of Farnier and Lenain [60]. What this study does show is that improved analysis methods, which are much cheaper to implement, can potentially provide equal if not significantly better performance compared to constructing a large telescope array at high altitudes which is sure to bring additional cost and complication.

4.2 Dynamic range studies

The second and third focused studies undertaken for the CTA MCWG involved performing simulations to test the dynamic range response of the camera pixels. The motivation for conducting these studies was to address two specific questions:

1. At which amplitude can the pixels be saturated before adversely affecting subarray performance?

2. Must CTA have a dynamic range that covers the single photo-electron (SPE)?

Understanding the limits of dynamic range is essential for being able to make a decision on the type of photomultiplier tubes (PMTs) that should be used in the camera systems. Fitting the cameras with PMTs that have a very broad dynamic range can be costly. However, fitting the cameras with PMTs that have a low dynamic range can result in them becoming saturated too quickly and images which do not represent the true light level. This could affect the performance parameters of CTA including energy resolution and flux sensitivity. Section 3.1.2 highlighted that the current design requirements of the CTA sensors are that they should be able to detect single photo-electrons and provide a dynamic range up to 5000 photo-electrons. The research conducted here attempts to use Monte Carlo simulations to help answer the two questions above within the context of the CTA performance goals, and determine whether the design requirements are correct. The research was carried out as two separate studies and is detailed in the following sections.

4.2.1 Upper dynamic range study

The upper dynamic range study focused solely on addressing the first question highlighted above. It has been suggested by White et al. [115] that each CTA sub-system (LST, MST and SST) should operate without any detrimental effects such as saturation up to the following energies: 5 TeV for the LST, 30 TeV for the MST and 300 TeV for the

SST. In this research, the initial approach adopted was to calculate the angular and energy resolution performance using only simulated gamma events obtained from CORSIKA air shower simulations. A set of mono-energetic (5 TeV) gamma-ray air showers was simulated and processed with *read_hess* only for the LSTs with the following cut requirements: a minimum of 2 telescopes, a minimum image amplitude of 60 photo-electrons, a minimum of 3 pixels and 5-10 tail cuts image cleaning. From a total of 7225 events only 157 events triggered the LSTs. After the image amplitude cuts this was reduced to 47 events and after the shape cuts this was reduced further to 21 events. Finally, after the camera angle cut, only 1 event was left clearly insufficient for any sort of study. Therefore as a time saving measure, some archived 20 degree zenith angle point-source gamma-ray shower simulations following an E^{-2} energy spectrum were used and processed for Subarray-E at 2000 m. The number of events used and passing various cuts are detailed in Appendix C. The approach adopted in this preliminary study was to select an energy bin immediately after the one containing 5 TeV, to allow for statistical effects resulting from the simulated spectrum. Moreover, this preliminary study only considered the LST upper dynamic range performance within the energy bin $\log_{10}(E/TeV) = 0.8$ (approximately 6 TeV).

Two methods were adopted to test the effects of pixel saturation on image reconstruction. The first method, named the *ignore* method consisted of setting a pixel saturation level in units of photo-electrons (p.e.). In practice this required that in every camera image, if the recorded number of photo-electrons for an individual pixel exceeded the saturation level, the number of photo-electrons for that pixel were set equal to the saturation level. The fact that the image was saturated is ignored and the image is passed for use within the shower reconstruction. Such a procedure might be described as 'induced' saturation of the camera images. This procedure was conducted for a number of different photo-electron amplitude levels to test where performance might be adversely affected.

Figure 4.9 illustrates the derived angular resolution performance as a function of saturation amplitude in photo-electrons (p.e.), calculated using the *ignore* method for the LSTs of Subarray-E at energies of approximately 6 TeV [$\log_{10}(E/TeV) = 0.8$]. It appears that per-
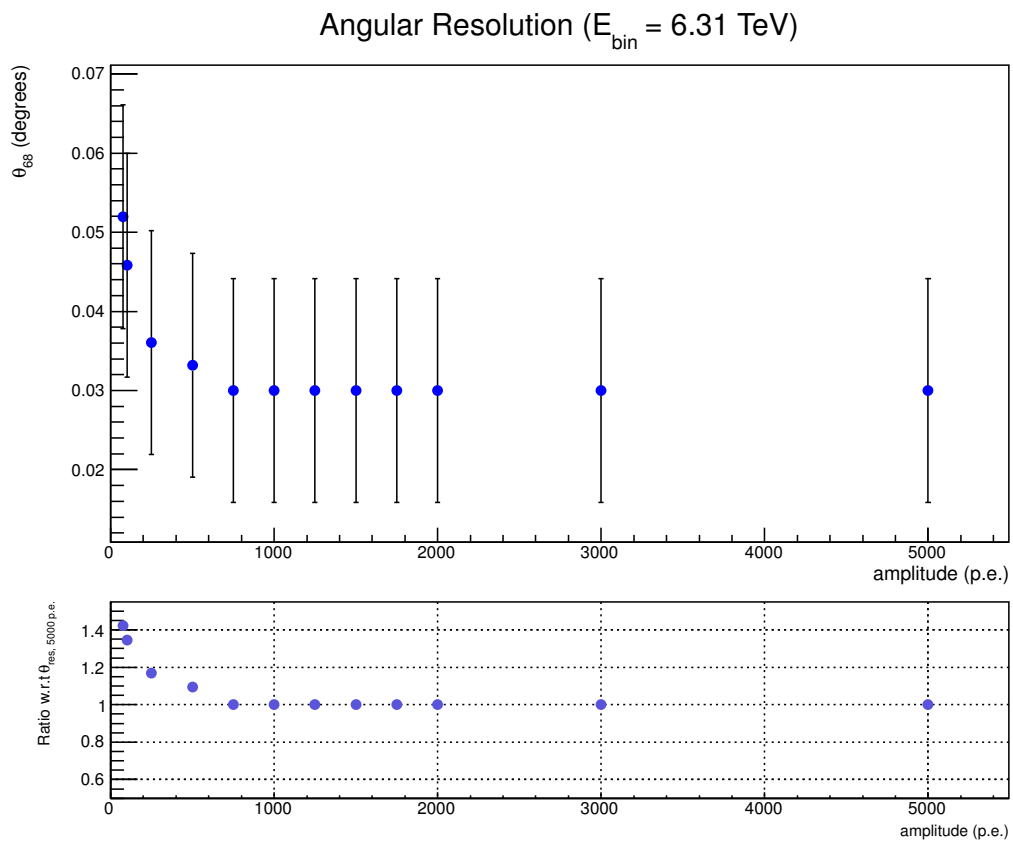
Figure 4.9: Angular resolution values as a function of saturation amplitude in photo-electrons (p.e.) calculated using the *ignore* method for the LSTs of Subarray-E in the energy bin $\log_{10}(\text{E/TeV}) = 0.8$ (approximately 6 TeV). It appears that the angular resolution performance remains stable, despite the induced saturation, to amplitudes of approximately 750 p.e. As shown in the sub-figure, below 750 p.e. the derived angular resolution performance gets gradually worse and is ~35% worse at 100 p.e. compared to the performance at 5000 p.e. The error bars show the square root of the θ^2 bins widths.

formance remains stable with induced saturation to amplitudes as low as approximately 750 p.e. As shown in the sub-figure, below 750 p.e. the derived angular resolution performance gets gradually worse and is ∼35% worse at 100 p.e. compared to the performance at 5000 p.e.

Figure 4.10: The derived energy resolution performance as a function of saturation amplitude in photo-electrons (p.e.) calculated using the *ignore* method. The performance values were calculated for the LSTs of Subarray-E at energies of approximately 6 TeV [$\log_{10}(E/TeV) = 0.8$]. The energy resolution performance appears to remain stable, despite camera saturation, for all amplitudes tested. The maximum difference in performance is at 500 p.e., which is ∼6% worse than energy resolution performance at 5000 p.e. The error bars show the uncertainty calculated for the HWHM found by fitting a Gaussian function to the E_{rec}/E_{true} distributions.

Figure 4.10 illustrates the energy resolution performance as a function of saturation amplitude in photo-electrons (p.e.). The LST energy resolution performance at approximately 6 TeV, appears to remain stable for all amplitudes tested despite the induced camera saturation. The maximum difference in performance is at 500 p.e., which is ∼6% worse than the energy resolution performance at 5000 p.e.
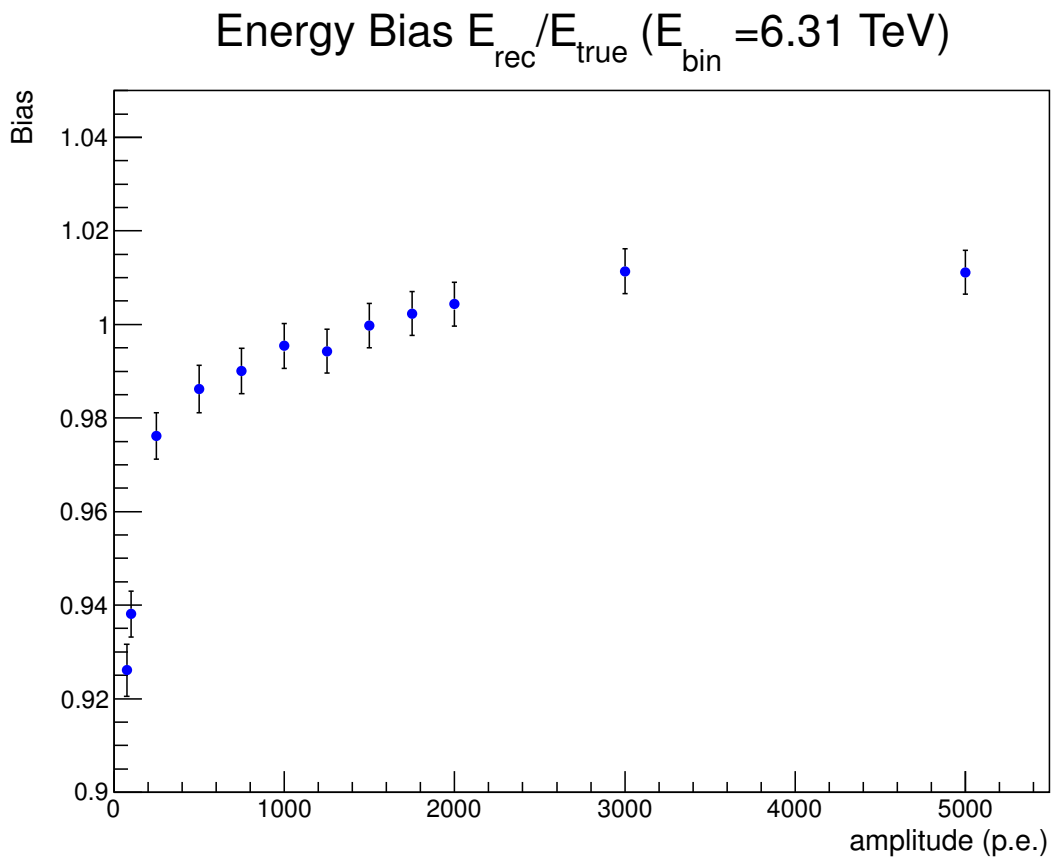
Figure 4.11: The derived energy bias performance as a function of saturation amplitude in photo-electrons (p.e.) calculated using the *ignore* method. The performance values were calculated for the LSTs of Subarray-E at energies of approximately 6 TeV [$\log_{10}(E/\text{TeV}) = 0.8$]. The energy bias is $< 5\%$, despite camera saturation, from 250 p.e. to 5000 p.e. The maximum difference in performance is at 75 p.e., where an event's reconstructed energy is systematically underestimated to about $\sim 7\%$ of the event's true energy. The error bars show the standard error calculated for the mean of the E_{rec}/E_{true} distributions.

Figure 4.11 illustrates the energy bias performance as a function of saturation amplitude in photo-electrons (p.e.). The energy bias is $< 5\%$, despite camera saturation, from 250 p.e. to 5000 p.e. The maximum difference in performance is at 75 p.e., where an event's reconstructed energy is systematically underestimated to about $\sim 7\%$ of the event's true energy.
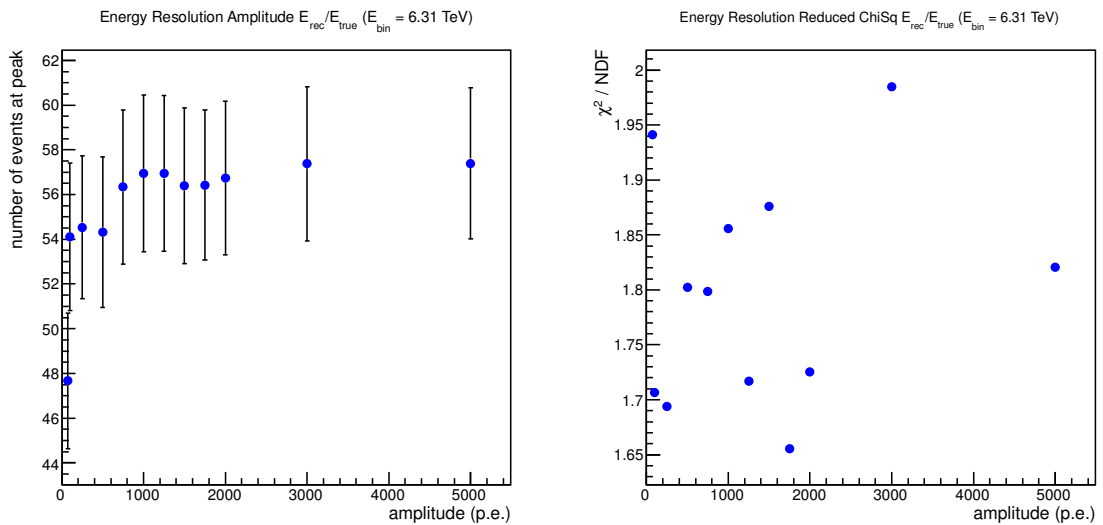
Figure 4.12: Amplitude (left panel) and χ^2 values (right panel) as a function of saturation amplitude in photo-electrons (p.e.) calculated when deriving the energy resolution performance of the LSTs using the *ignore* method. It appears as though the number of events at the peak of the E_{rec}/E_{true} distributions remains relatively stable within approximately 10% for all amplitudes except 75 p.e. The error bars (left panel) show the uncertainty calculated for the amplitudes of the Gaussian function fitted to the E_{rec}/E_{true} distributions.

Figure 4.12 illustrates the amplitude (left panel) and the χ^2 (right panel) from the Gaussian function fitted to the E_{rec}/E_{true} distributions. It appears as though the number of events at the peak of the E_{rec}/E_{true} distributions (see Figure 4.12, left panel) remains relatively stable within approximately 10% for all amplitudes except 75 p.e.

The second method, named the ***throw*** method, again consisted of setting a pixel saturation level in units of photo-electrons (p.e.), but on this occasion, when a camera pixel exceeded the pixel limit the whole image was eliminated from the shower reconstruction. In practice this can be considered a worst case scenario and one that is not likely to occur.
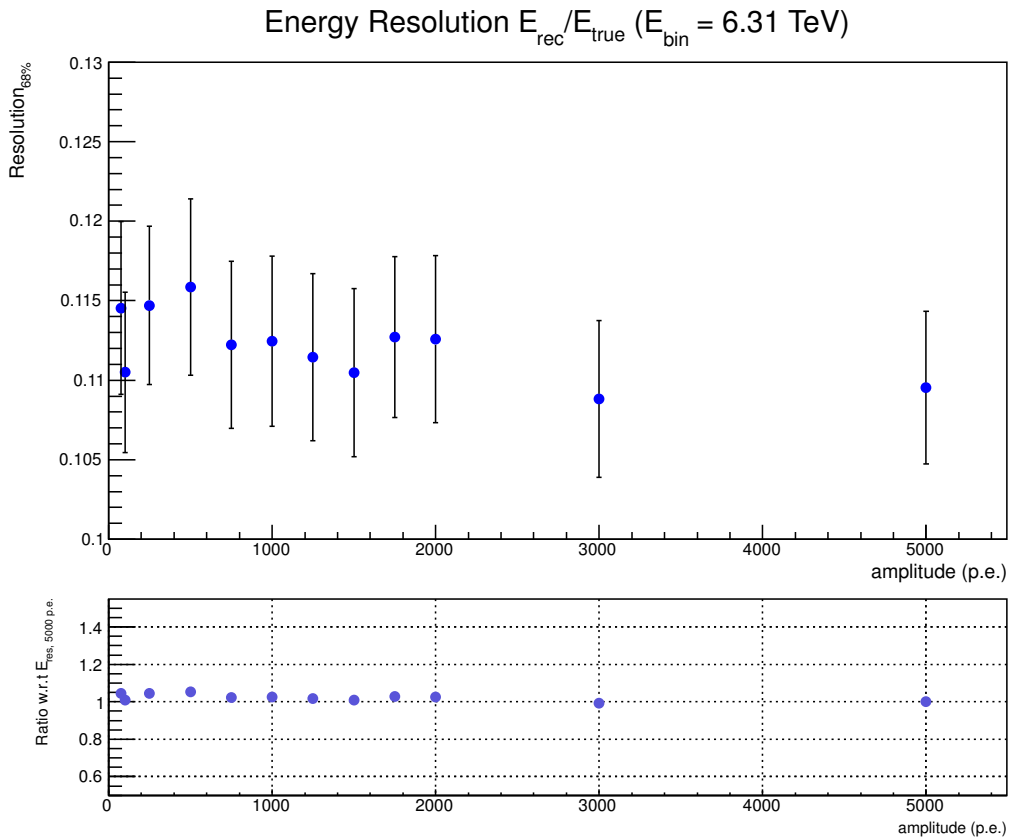
Figure 4.13 illustrates the derived angular resolution performance as a function of saturation amplitude in photo-electrons (p.e.), calculated using the *throw* method for the LSTs of

Figure 4.13: Angular resolution values as a function of saturation amplitude in photo-electrons (p.e.) calculated using the *throw* method for the LSTs of Subarray-E in the energy bin $\log_{10}(E/\text{TeV}) = 0.8$ (approximately 6 TeV). It appears that angular resolution performance is almost immediately affected under the *throw* method. For example the angular resolution performance at 3000 p.e. is approximately 10% worse than at 5000 p.e. and when moving to even lower amplitude levels the angular resolution continues to deteriorate relative to the angular resolution performance at 5000 p.e. At at amplitude of 250 p.e. the angular resolution performance is roughly 60% worse compared to the performance ta 5000 p.e. At the amplitudes tested below 250 p.e. no images pass the saturation cut and hence no angular resolution performance can be derived. The error bars show the square root of the θ^2 bins widths.

Subarray-E in the $\log_{10}(E/TeV) = 0.8$ energy bin (approximately 6 TeV). It appears that angular resolution performance is almost immediately affected under the *throw* method. For example, the angular resolution performance at 3000 p.e. is approximately 10% worse than at 5000 p.e. and when moving to even lower amplitude levels the angular resolution continues to deteriorate relative to the angular resolution performance at 5000 p.e. At at amplitude of 250 p.e. the angular resolution performance is roughly 60% worse compared to the angular resolution performance at 5000 p.e. At the amplitudes tested below 250 p.e. no images pass the saturation cut and hence no angular resolution performance can be derived.

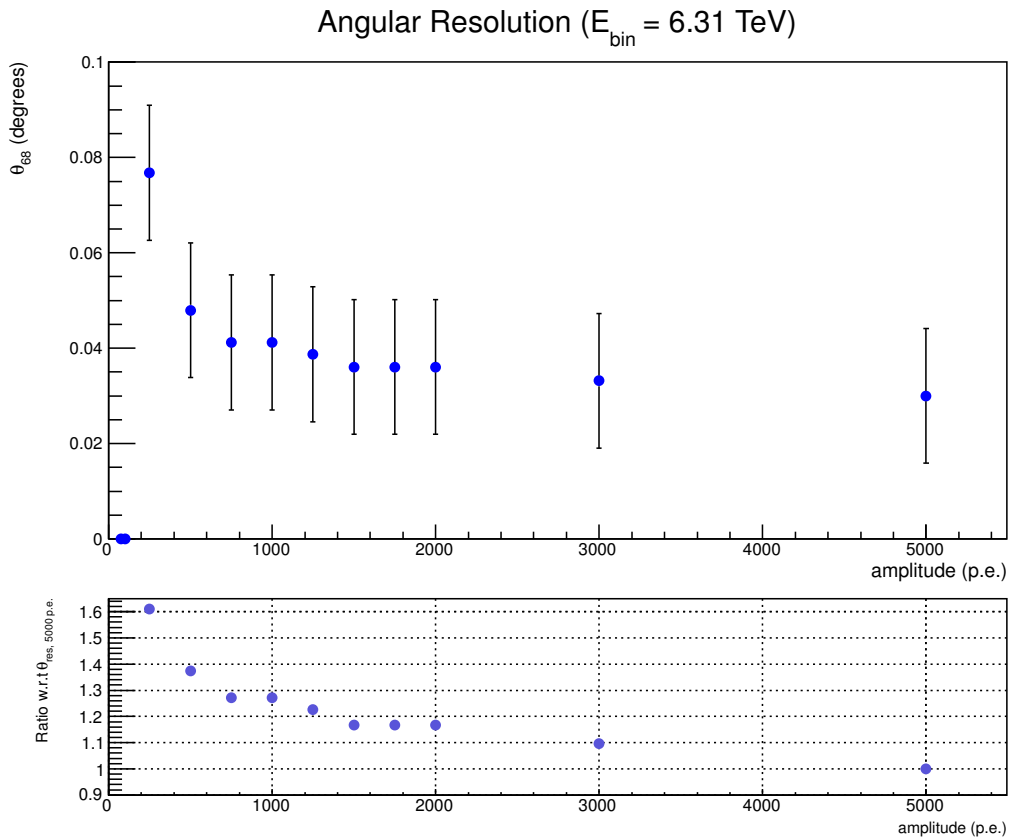Figure 4.14 illustrates the energy resolution performance as a function of saturation amplitude in photo-electrons (p.e.) calculated using the *throw* method for the LSTs of Subarray-E at energies in the $\log_{10}(E/TeV) = 0.8$ (approximately 6 TeV) energy bin. The energy resolution performance is also strongly affected by the loss of images at the saturation amplitude. Reducing the saturation amplitude results in a larger number of images being thrown from the analysis and hence a loss in energy resolution performance. For example, at 3000 p.e. the energy resolution performance is approximately 11% worse compared to the energy resolution performance at 5000 p.e., and at a saturation amplitude of 250 p.e. the derived energy resolution performance is approximately 40% worse. As in the case of angular resolution derived using the *throw* method, no events pass the saturation cuts for the tested amplitudes below 250 p.e.

Figure 4.15 illustrates the energy bias performance as a function of saturation amplitude in photo-electrons (p.e.) calculated using the *throw* method. For all the amplitudes tested, it appears that the reconstructed event energies are overestimated to within 5% their true energies. This is a very small effect considering the much larger effect seen on the angular and energy resolutions when too many images are thrown away.

Figure 4.16 illustrates the amplitude (left panel) and the χ^2 (right panel) from the Gaussian function fitted to the E_{rec}/E_{true} distributions.

Using both the *ignore* and *throw* methods to test at which amplitude saturation effects start
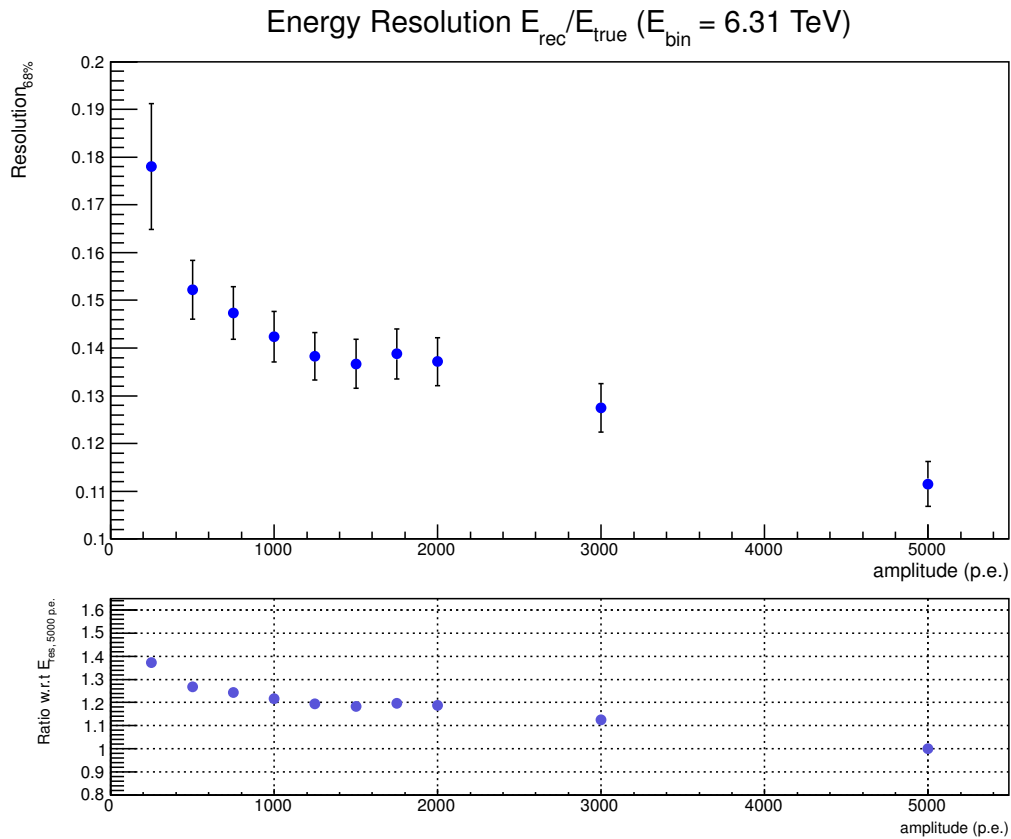
Figure 4.14: The derived energy resolution performance as a function of saturation amplitude in photo-electrons (p.e.) calculated using the *throw* method. The performance values were calculated for the LSTs of Subarray-E at energies of approximately 6 TeV [$\log_{10}(E/TeV) = 0.8$]. The energy resolution performance is almost immediately affected by the loss of images at the saturation amplitude. For example at 3000 p.e. the energy resolution performance is approximately 11% worse compared to the energy resolution performance at 5000 p.e. Reducing the saturation amplitude results in a larger number of images being thrown from the analysis and hence a loss in energy resolution performance. At a saturation amplitude of 250 p.e. the derived energy resolution performance is approximately 40% worse compared to the energy resolution performance at 5000 p.e. The error bars show the uncertainty calculated for the HWHM found by fitting a Gaussian function to the E_{rec}/E_{true} distributions.
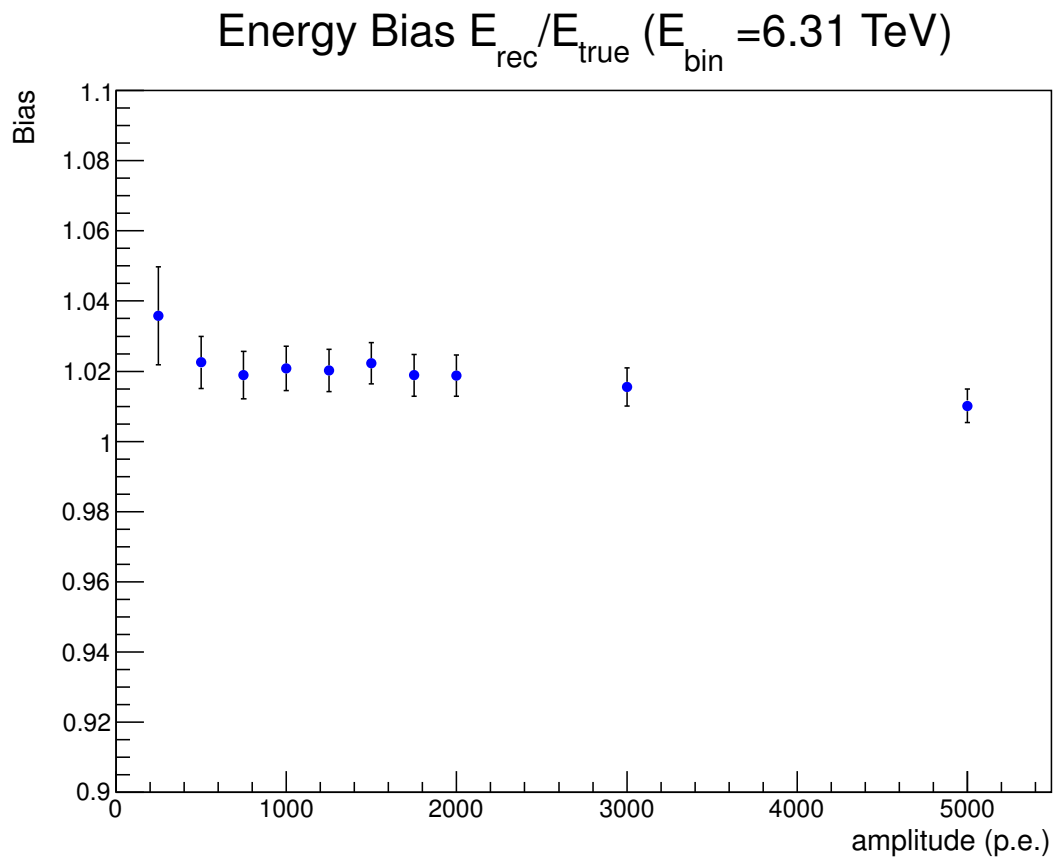
Figure 4.15: The derived energy bias performance as a function of saturation amplitude in photo-electrons (p.e.) calculated using the *throw* method. The performance values were calculated for the LSTs of Subarray-E at energies of approximately 6 TeV [$\log_{10}(E/TeV) = 0.8$]. For the *throw* method, it appears that for all the amplitudes tested, the reconstructed event energies are overestimated to within 5% their true energies. This is a very small effect considering the much larger effect on the angular and energy resolutions when too many images are thrown away. The error bars show the standard error calculated for the mean of the E_{rec}/E_{true} distributions.
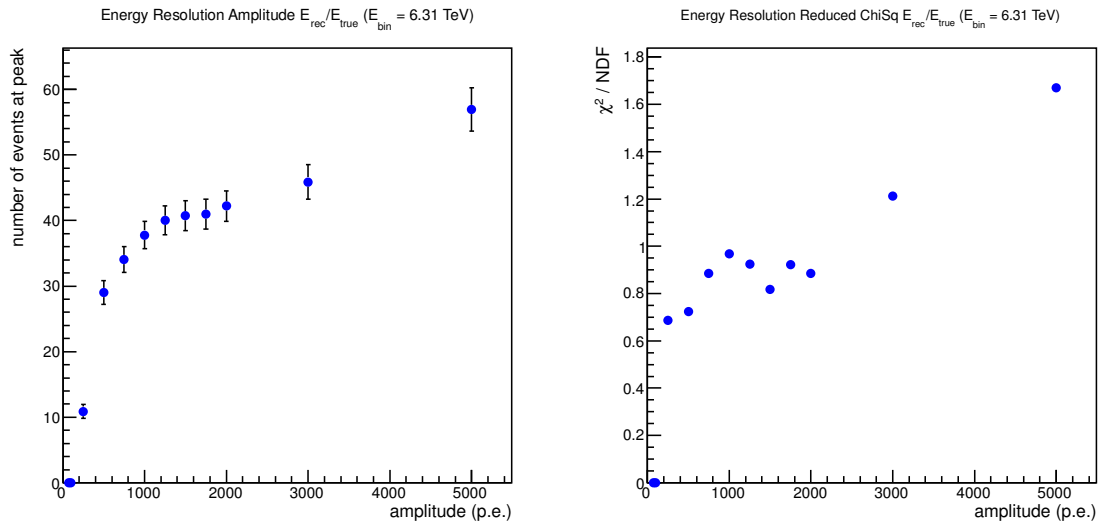
Figure 4.16: Amplitude (left panel) and χ^2 values (right panel) as a function of saturation amplitude in photo-electrons (p.e.) calculated when deriving the energy resolution performance of the LSTs using the *throw* method. The error bars (left panel) show the uncertainty calculated for the amplitudes of the Gaussian function fitted to the E_{rec}/E_{true} distributions.

to affect LST performance, it appears as though energy and angular resolution performance are not significantly affected above amplitudes of approximately 2000 p.e. With induced saturation the performances remain relatively stable above amplitudes of approximately 1000 p.e. and it is only in the worst case scenario, where whole images are lost, that adverse affects on performance are seen at larger amplitudes. In the case of the *throw* method, the loss in performance seen when the saturation amplitude is decreased is mainly due to a greater number of images being lost from the reconstruction. In the case of the *ignore* method, the loss of performance seen when the saturation amplitude is decreased is believed to be related to the reconstructed width of each image (see Figure 4.17). As a result, images are systematically reconstructed to an energy below their true energy. Furthermore, it is not yet known how this may affect performance once background is included in the study.

No Saturation   500 p.e.   100 p.e.
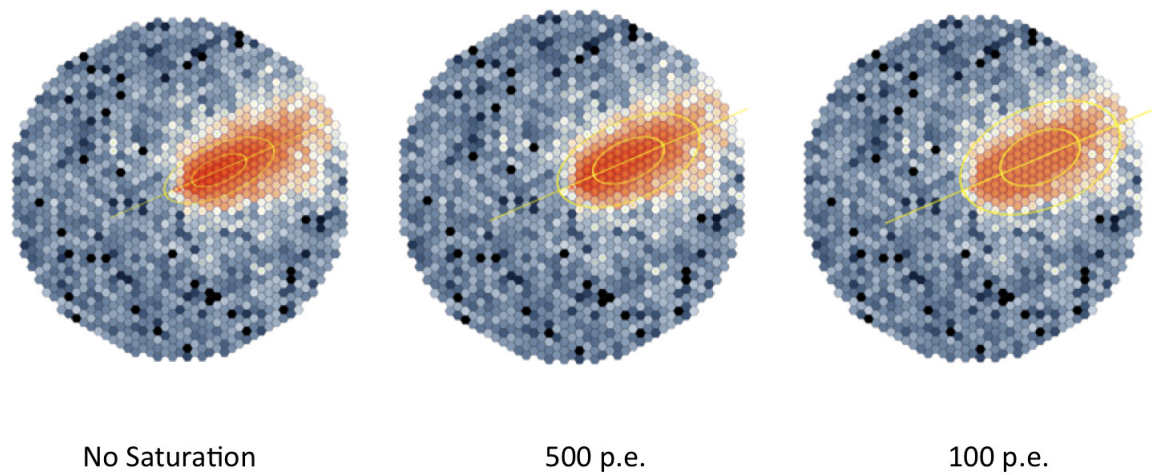
Figure 4.17: The reconstructed image widths (yellow ellipses) before (left) and after induced saturation at amplitudes of 500 p.e. (centre) and 100 p.e. (right). Images are reconstructed with a larger width and systematically reconstructed to energies lower than the true energy. D. Parsons [private comm.]

4.2.2   Lower dynamic range study

The lower dynamic range study focused solely on addressing the single photo-electron (SPE) question. A set of mono-energetic shower simulations was performed for the energies highlighted by White et al. [115], 30 GeV, 100 GeV and 1 TeV, to test each of the different telescope designs. For this particular study none of the sub-arrays highlighted in Section 3.1.3 were used. Instead a small, compact array was designed for this study comprising a total of 9 telescopes. This included 3 LSTs, 3 MSTs and 3 SSTs as illustrated in Figure 4.18. The reason for constructing this array was simply because the large 275 telescope production run 1 array was too large, and a small array significantly shortened the time to process the simulations. The scale of the array should not alter the telescope pixel performance, so a small array is adequate for testing of the lower dynamic range.

In practice, the only way to address the SPE question highlighted above through simulation and analysis is to test how low the assumed digital counts to photo-electron (DC/PE) ratio can be set before performance is adversely affected. Within the context of the CTA simulation and analysis framework (the *sim_telarray* and *read_hess* software packages) this proved quite challenging as there is no way to do this directly. However it was possible to test the system performance based on different values of FADC (Flash Analogue-to-Digital Converter) amplitude which is directly related to the assumed DC/PE ratio:

$$\text{Amplitude}_{\text{FADC}} = \left\lfloor \frac{(\text{DC/PE})}{(\Sigma_{\text{FADC}}\Delta T)/C_{\max}} \right\rfloor \tag{4.1}$$

where $\lfloor\ \rfloor$ is the floor function [8], Σ_{FADC} is the sum of the FADC trace signal in units of mV, ΔT is the time step in nanoseconds and $C_{\max}$ the maximum counts for a single FADC time step in units of mV. Within *sim_telarray* the FADC amplitude is fixed at 14 which corresponds to a DC/PE ratio of 80. Other values that are assumed to be fixed in *sim_telarray* include $\Sigma_{\text{FADC}} = 203.2$ mV, $\Delta T = 0.5$ ns and $C_{\max} = 18.8$ mV. Based on these assumptions Table 4.3 highlights the different FADC amplitude values and their associated DC/PE ratios.
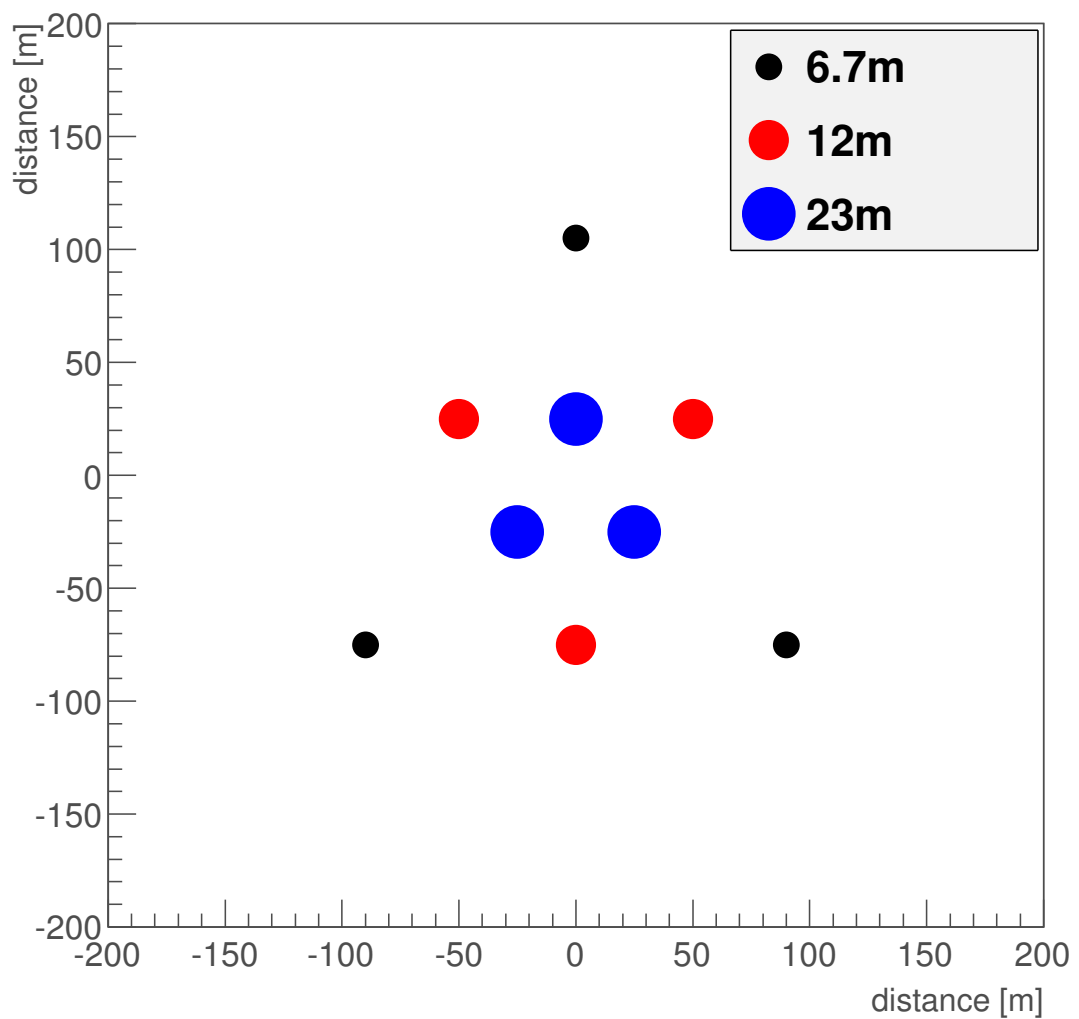
Figure 4.18: The single photo-electron (SPE) test array layout. This compact array consists of three different telescope types and was constructed to test the SPE performance of the different CTA cameras. The array is comprised of 9 telescopes in total including 3 LSTs (blue dots, ∼23 m diameter), 3 MSTs (red dots, ∼12 m diameter) and 3 SSTs (black dots, ∼6.7 m diameter). The size of the dots represents the different telescope sizes, but is not to scale.

Table 4.3: The calculated FADC amplitude values and their associated DC/PE ratios.

FADC amplitude	Actual value	DC/PE ratio
1	1.85	10
3	3.70	20
5	5.55	30
7	7.40	40
9	9.25	50
11	11.10	60
14	14.80	80

Current Cherenkov telescope systems like H.E.S.S. assume that DC/PE = 80 and accordingly the FADC amplitude = 14. The approach then was to adjust these FADC amplitude values according to Table 4.3 within *sim_telarray* to see how the performance measures were affected.

4.2.2.1 Lower dynamic range: LST performance results

Figure 4.19 illustrates the derived angular resolution performance as a function of FADC amplitude calculated for the LSTs in the SPE test array using 30 GeV mono-energetic gamma-ray air shower simulations. The sub-figure in Figure 4.19 shows that the derived angular resolution performance of the LSTs remains relatively stable when the FADC amplitude values are adjusted to reflect a change in the assumed DC/PE ratio.

Figure 4.20 illustrates the energy resolution performance as a function of FADC amplitude calculated for the LSTs in the SPE test array for 30 GeV mono-energetic gamma-ray air shower simulations. Energy resolution performance appears to remain relatively stable within ~5% for FADC amplitudes from 3 to 14. However at FADC=1 the energy resolution performance of the LSTs is approximately 11% better than the energy resolution performance at FADC=14.

Figure 4.21 illustrates the amplitude (left panel) and the reduced χ^2 values (right panel) as functions of FADC amplitude. These values result from the Gaussian function fit to the E_{rec}/E_{true} distributions when calculating energy resolution. It is believed that the lower
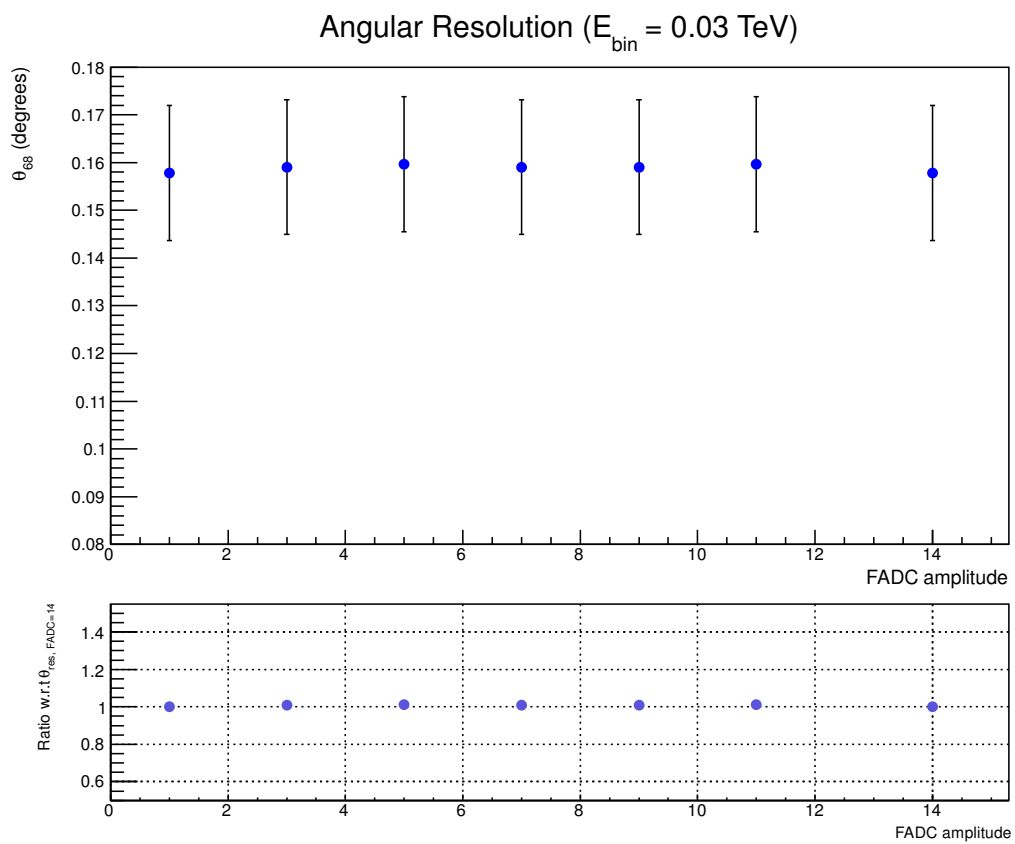
Figure 4.19: The derived angular resolution performances as a function of FADC amplitude for the LSTs of the SPE test array using 30 GeV mono-energetic gamma-ray air shower simulations. As shown in the sub-figure the derived angular resolution performance of the LSTs remains stable when the FADC amplitude values are adjusted to reflect a change in the assumed DC/PE ratio. The error bars show the square root of the θ^2 bins widths.

Figure 4.20: Energy resolution performance as a function of FADC amplitude for the LSTs of the SPE test array using 30 GeV mono-energetic gamma-ray air shower simulations. It appears as though energy resolution performance remains relatively stable within ~5% for FADC amplitudes from 3 to 14. However at FADC=1 the energy resolution performance of the LSTs is approximately 11% better than the energy resolution performance at FADC=14. The error bars show the uncertainty calculated for the HWHM found by fitting a Gaussian function to the E_{rec}/E_{true} distributions.

number of events at FADC=1 (left panel) results in an improved energy resolution compared to the energy resolution performance for other FADC values.
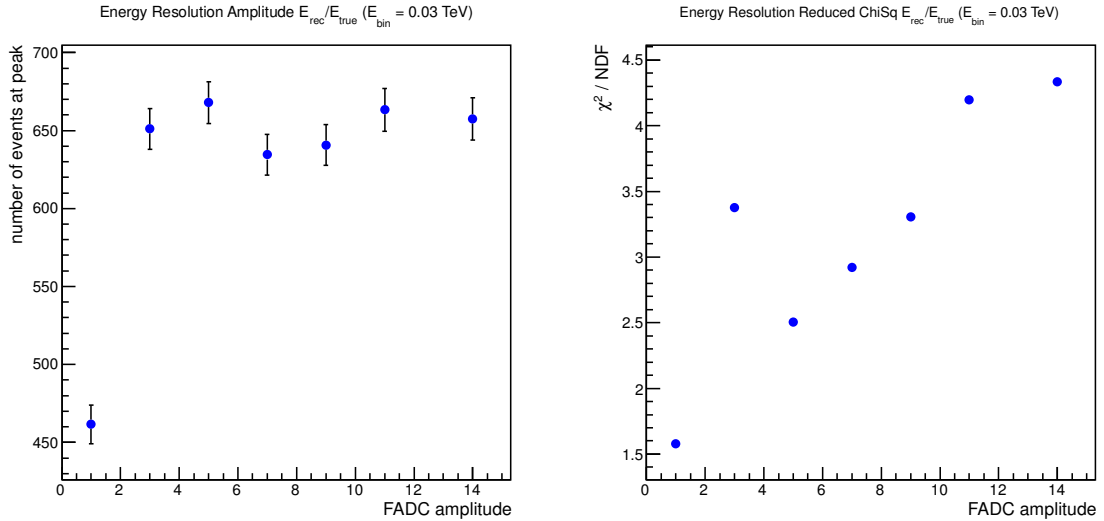
Figure 4.21: Amplitude (left panel) and χ^2 values (right panel) as a function of FADC amplitude calculated when deriving the energy resolution performance of the LSTs in the SPE test array. It is believed that the lower number of events at FADC=1 results in an improved energy resolution compared to the energy resolution performance for other FADC values. The error bars (left panel) show the uncertainty calculated for the amplitudes of the Gaussian function fitted to the E_{rec}/E_{true} distributions.

Figure 4.22 illustrates the energy bias performance as a function of FADC amplitude calculated for the LSTs in the SPE test array for 30 GeV mono-energetic gamma-ray air shower simulations. Energy bias performance remains relatively stable for all FADC values. However at FADC=1 the reconstructed event energies are systematically underestimated by approximately 2% of their true energy.

#### 4.2.2.2   Lower dynamic range: MST performance results

Figure 4.23 illustrates the derived angular resolution performance as a function of FADC amplitude calculated for the MSTs in the SPE test array using 100 GeV mono-energetic gamma-ray air shower simulations. The sub-figure in Figure 4.23 shows that the derived angular resolution performance of the MSTs remains relatively stable, within ~5%, when the FADC amplitude values are adjusted to reflect a change in the assumed DC/PE ratio.
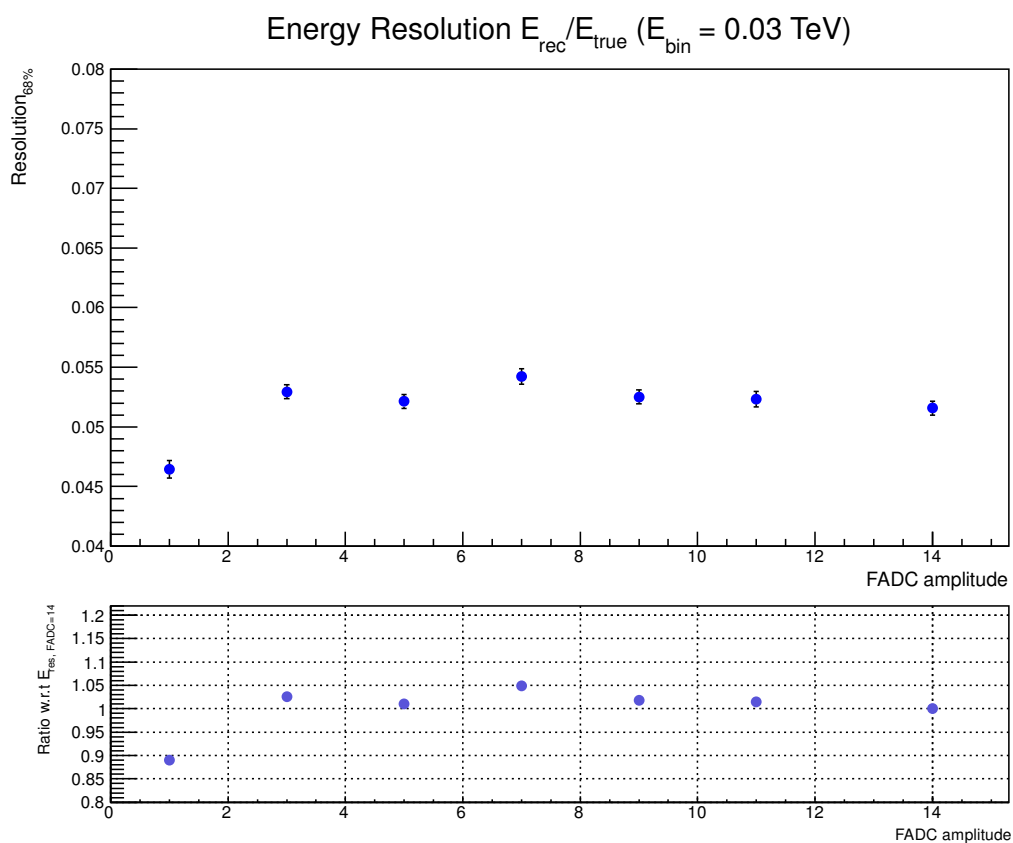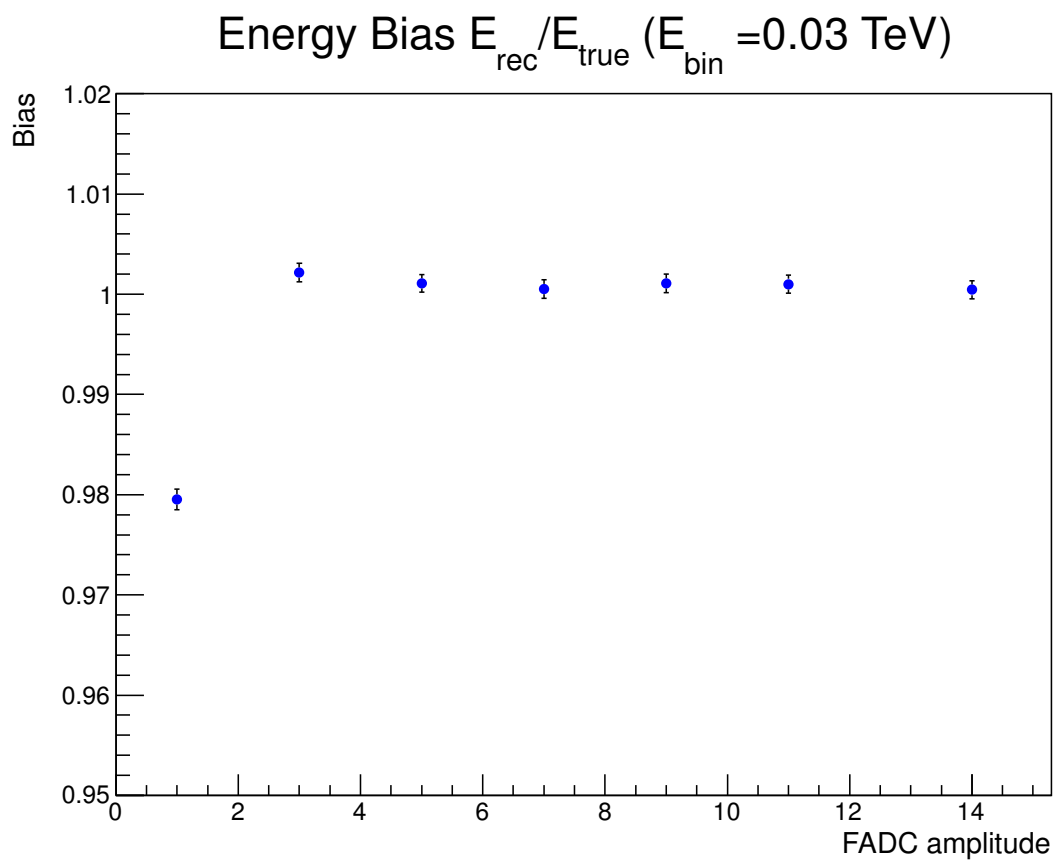
Figure 4.22: Energy bias performance as a function of FADC amplitude for the LSTs of the SPE test array using 30 GeV mono-energetic gamma-ray air shower simulations. It appears as though energy bias performance remains relatively stable for all FADC values. However at FADC=1 the event energies are systematically underestimated by approximately 2% of their true energy. The error bars show the standard error calculated for the mean of the E_{rec}/E_{true} distributions.

Figure 4.23: The angular resolution performances as a function of FADC amplitude for the MSTs of the SPE test array using 100 GeV mono-energetic gamma-ray air shower simulations. As shown in the sub-figure the derived angular resolution performance of the MSTs remains relatively stable, within $\sim$5%, when the FADC amplitude values are adjusted to reflect a change in the assumed DC/PE ratio. The error bars show the square root of the θ^2 bins widths.

Figure 4.24 illustrates the energy resolution performance as a function of FADC amplitude for the MSTs in the SPE test array for 100 GeV mono-energetic gamma-ray air shower simulations. The energy resolution performance remains relatively stable within 5% for FADC amplitude values from 3 to 14. However at FADC=1 the energy resolution performance of the MSTs is approximately 25% better than the energy resolution performance at FADC=14.

Figure 4.24: Energy resolution performance as a function of FADC amplitude for the MSTs of the SPE test array using 100 GeV mono-energetic gamma-ray air shower simulations. It appears as though energy resolution performance remains relatively stable within 5% for FADC amplitude values from 3 to 14. However at FADC=1 the energy resolution performance of the MSTs is approximately 25% better than the energy resolution performance at FADC=14. The error bars show the uncertainty calculated for the HWHM found by fitting a Gaussian function to the E_{rec}/E_{true} distributions.

Figure 4.25 illustrates the amplitude (left panel) and the reduced χ^2 values (right panel) as functions of FADC amplitude. These values result from the Gaussian function fit to the E_{rec}/E_{true} distributions when calculating energy resolution. As in the case of the LSTs, a

lack of events at FADC=1 (left panel) results in an improved energy resolution compared to the energy resolution performance for other FADC values.
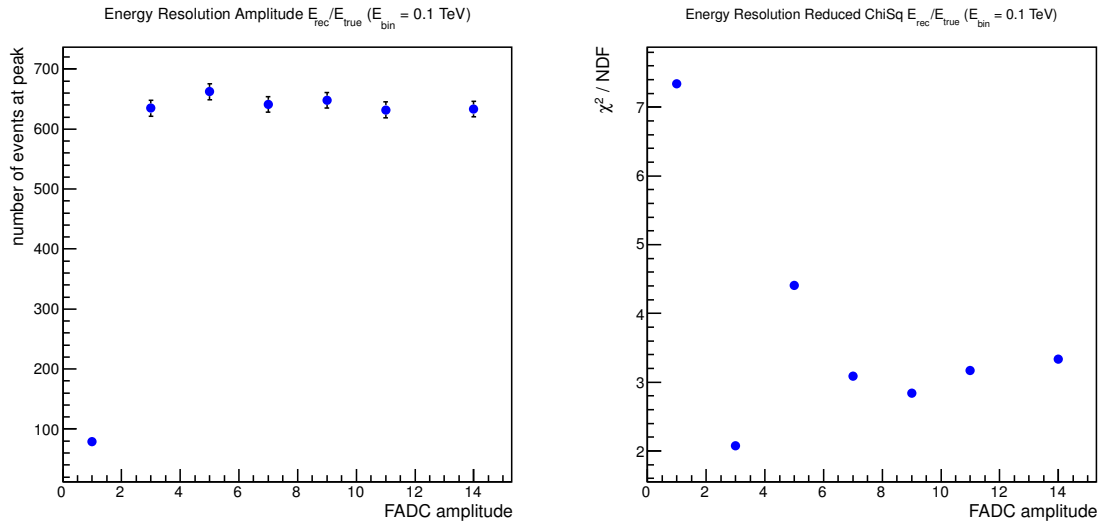
Figure 4.25: Amplitude (left panel) and χ^2 values (right panel) as a function of FADC amplitude calculated when deriving the energy resolution performance of the MSTs in the SPE test array. It is believed that a lack of events at FADC=1 results in an improved energy resolution compared to the energy resolution performance for other FADC values. The error bars (left panel) show the uncertainty calculated for the amplitudes of the Gaussian function fitted to the E_{rec}/E_{true} distributions.

Figure 4.26 illustrates the energy bias performance as a function of FADC amplitude for the MSTs in the SPE test array for 100 GeV mono-energetic gamma-ray air shower simulations. For the tested FADC amplitudes from 3 to 14 there does not appear to be any energy bias in the reconstruction. However at FADC=1 the reconstructed event energies are systematically underestimated by nearly 5% of their true energy.

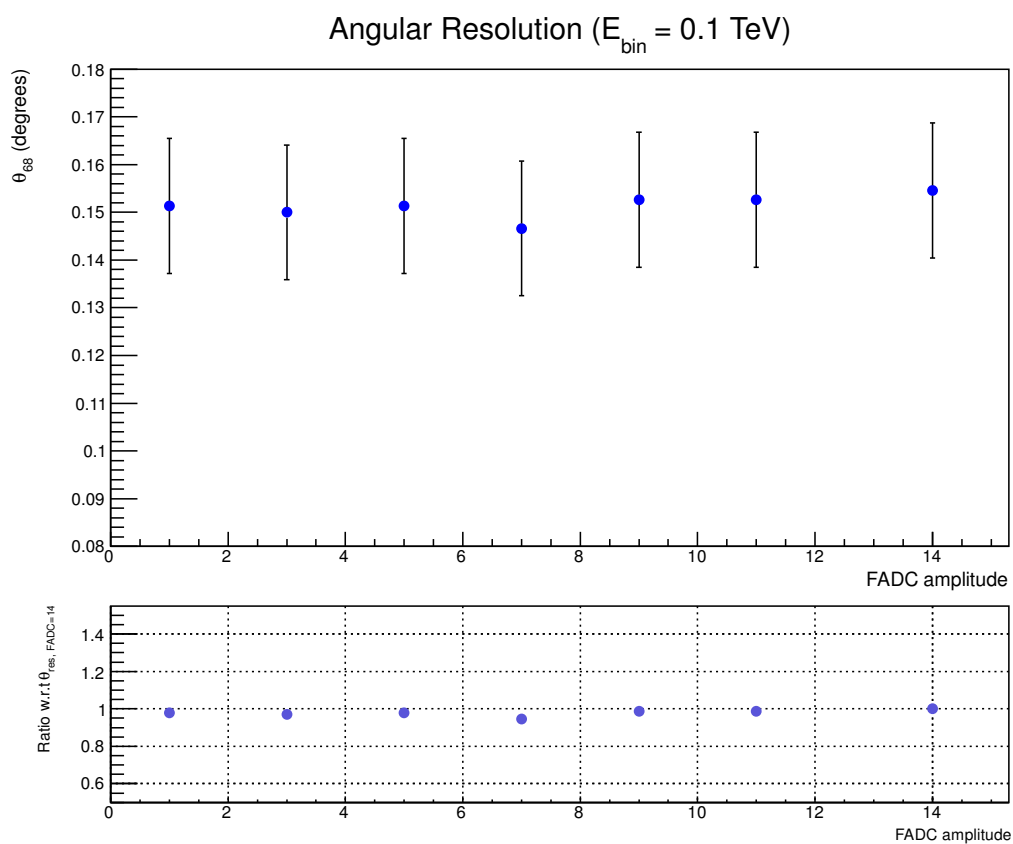### 4.2.2.3   Lower dynamic range: SST performance results

Figure 4.27 illustrates the derived angular resolution performance as a function of FADC amplitude calculated for the SSTs in the SPE test array using 1 TeV mono-energetic gamma-ray air shower simulations. The sub-figure in Figure 4.27 shows that the derived angular resolution performance of the SSTs remains relatively stable, for all FADC values tested except FADC=1, when the FADC amplitude values are adjusted to reflect a change in the

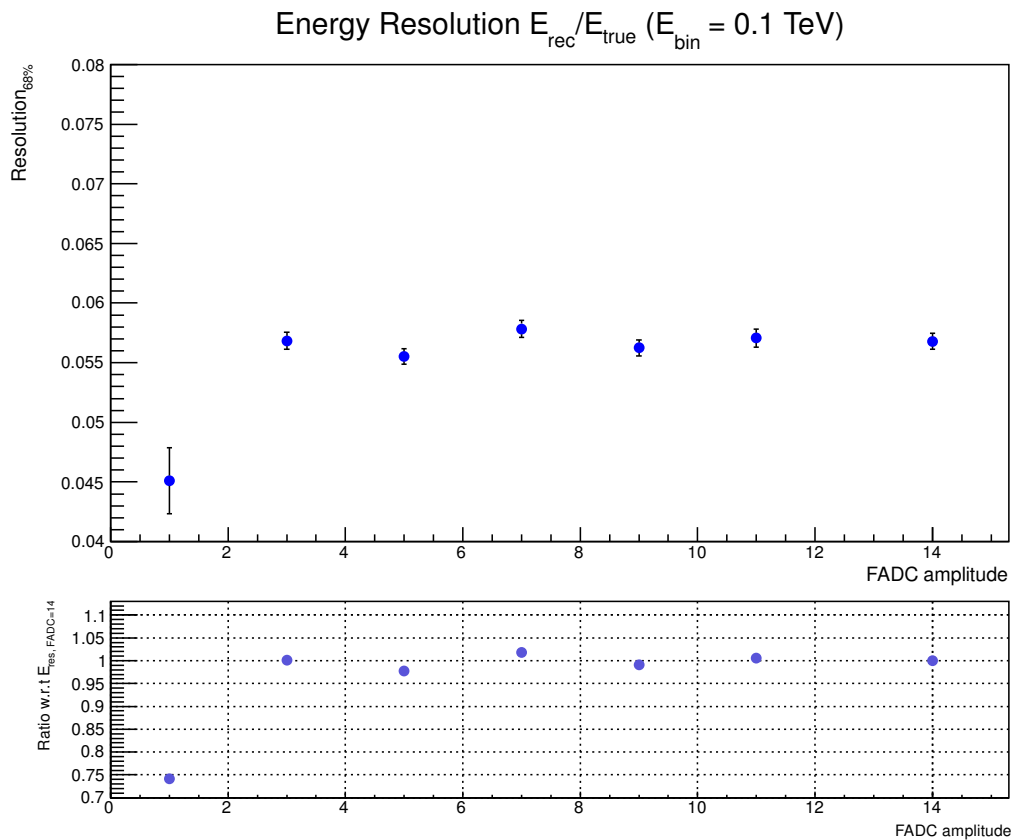**Figure 4.26:** Energy bias performance as a function of FADC amplitude for the MSTs of the SPE test array using 100 GeV mono-energetic gamma-ray air shower simulations. For the tested FADC amplitudes from 3 to 14 there does not appear to be any energy bias in the reconstruction. However at FADC=1 the reconstructed event energies are systematically underestimated by nearly 5% of their true energy. The error bars show the standard error calculated for the mean of the E_{rec}/E_{true} distributions.

assumed DC/PE ratio. At FADC=1 the angular resolution performance is approximately 45% worse than at FADC=14.

Figure 4.27: Angular resolution performances as a function of FADC amplitude for the SSTs of the SPE test array using 1 TeV mono-energetic gamma-ray air shower simulations. As shown in the sub-figure the derived angular resolution performance of the SSTs remains relatively stable, for all FADC values tested except FADC=1, when the FADC amplitude values are adjusted to reflect a change in the assumed DC/PE ratio. At FADC=1 the angular resolution performance is approximately 45% worse than at FADC=14. The error bars show the square root of the θ^2 bins widths.

Figure 4.28 illustrates the energy resolution performance as a function of FADC amplitude for the SSTs in the SPE test array for 1 TeV mono-energetic gamma-ray air shower simulations. Energy resolution performance appears to remain relatively stable, within 2%, for the tested FADC amplitude values 5 to 14. At FADC=3 the energy resolution performance of the SSTs is approximately 7% better than the energy resolution performance at FADC=14, and at FADC=1 the energy resolution performance is about 3% worse than at FADC=14.

Figure 4.29 illustrates the amplitude (left panel) and the reduced χ^2 values (right panel)
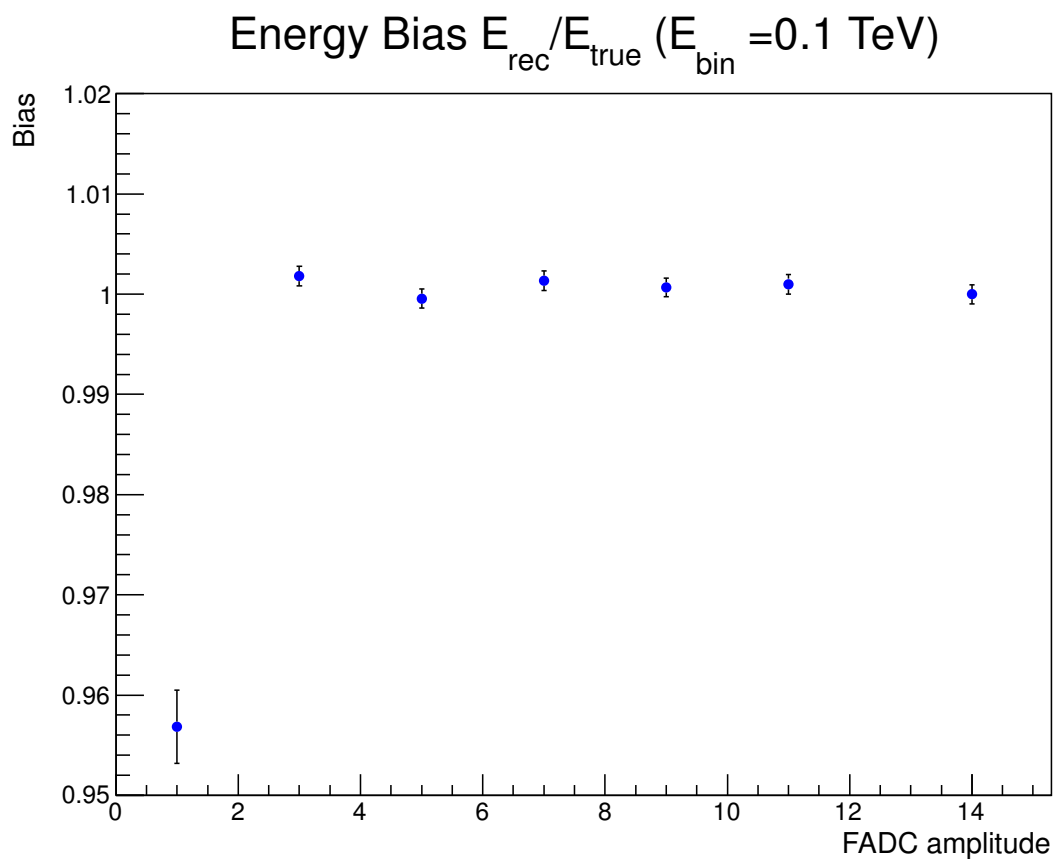
Figure 4.28: Energy resolution performance as a function of FADC amplitude for the SSTs of the SPE test array using 1 TeV mono-energetic gamma-ray air shower simulations. It appears as though energy resolution performance remains relatively stable, within 2%, for the tested FADC amplitude values 5 to 14. At FADC=3 the energy resolution performance of the SSTs is approximately 7% better than the energy resolution performance at FADC=14, and at FADC=1 the energy resolution performance is about 3% worse than at FADC=14. The error bars show the uncertainty calculated for the HWHM found by fitting a Gaussian function to the E_{rec}/E_{true} distributions.

as functions of FADC amplitude. These values result from the Gaussian function fit to the E_{rec}/E_{true} distributions when calculating energy resolution. It appears that not enough events are present in the analysis at FADC=1 (left panel) and the small increase in the number of events at FADC=3 may also contribute to the small improvement in energy resolution at this FADC amplitude. It is also believed that a greater number of shower simulations will improve the χ^2 fit values as seen in the case of the LST where there is a much greater number of triggered events.
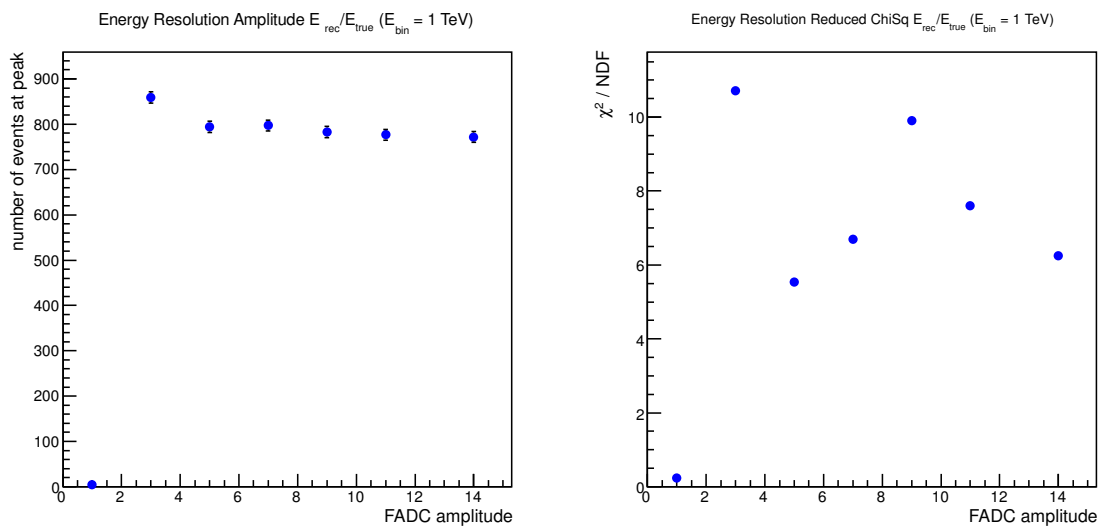
Figure 4.29: Amplitude (left panel) and χ^2 values (right panel) as a function of FADC amplitude calculated when deriving the energy resolution performance of the SSTs in the SPE test array. It appears that not enough events are present in the analysis at FADC=1 and the increased number of events at FADC=3 may be the reason for the small improvement in energy resolution at this FADC amplitude. The error bars (left panel) show the uncertainty calculated for the amplitudes of the Gaussian function fitted to the E_{rec}/E_{true} distributions.

Figure 4.30 illustrates the energy bias performance as a function of FADC amplitude for the SSTs in the SPE test array for 1 TeV mono-energetic gamma-ray air shower simulations. There appears to be no bias in the event energy reconstruction for the tested FADC amplitudes from 3 to 14. However at FADC=1 the reconstructed event energies appear to be systematically underestimated by approximately 3% their true energy.
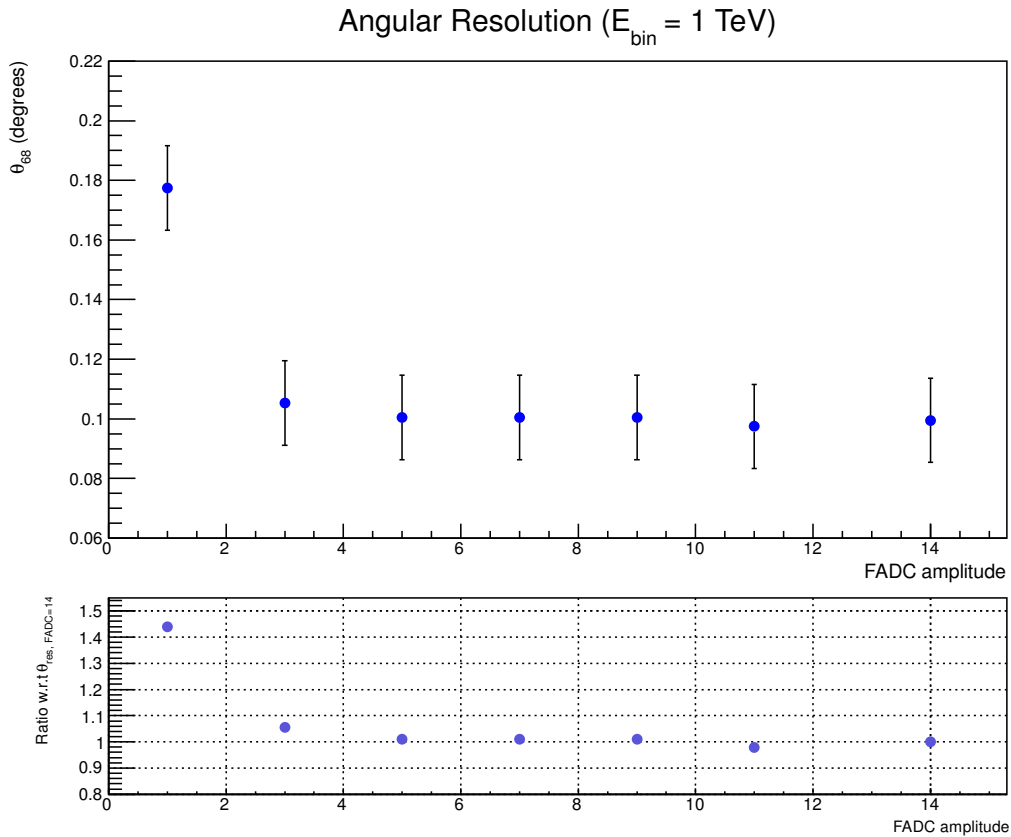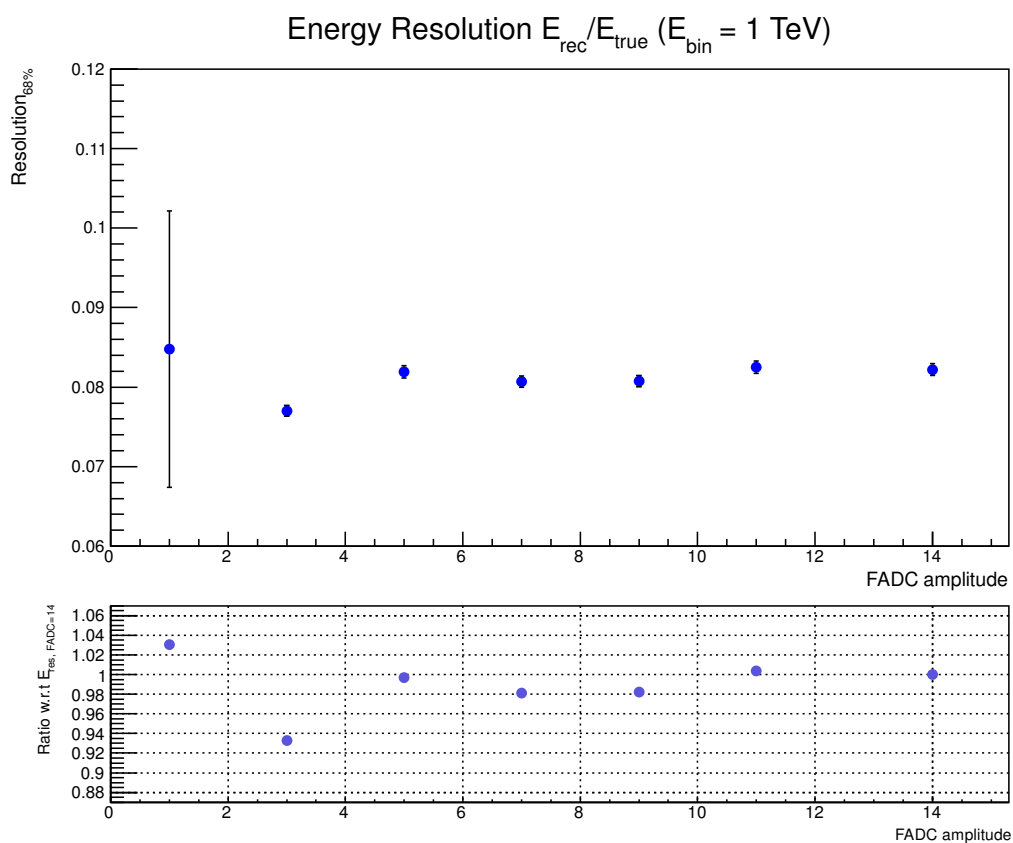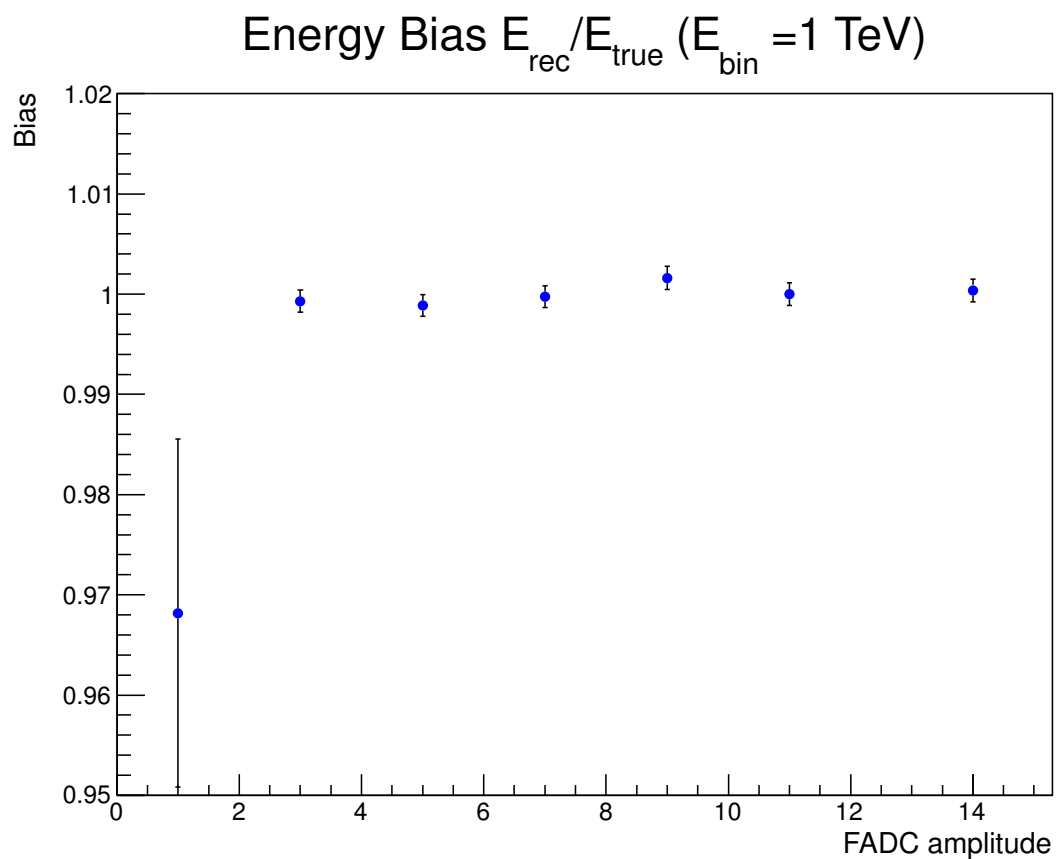
Figure 4.30: Energy bias performance as a function of FADC amplitude for the SSTs of the SPE test array using 1 TeV mono-energetic gamma-ray air shower simulations. There appears to be no bias in the event energy reconstruction for the tested FADC amplitudes from 3 to 14. However at FADC=1 the reconstructed event energies appear to be systematically underestimated by approximately 3% their true energy. The error bars show the standard error calculated for the mean of the E_{rec}/E_{true} distributions.

4.2.3 Dynamic range conclusions

First, it can be concluded that for the upper dynamic range study that energy and angular resolution performance are not adversely affected when the cameras are saturated at an amplitude of approximately 1500 p.e. In fact it appears that when the cameras are saturated above 1000 p.e. the performances remain relatively stable. It is only in the worst case scenario, where whole images are lost, that the performance analysis appears to be significantly affected, this being at the $\sim$10% level for amplitudes around 3000 p.e. and $\lesssim$20% for amplitudes between roughly 1250 p.e. and 2000 p.e. Therefore this preliminary study of upper dynamic range performance suggests that CTA's upper dynamic range goal of 5000 p.e. may be reduced for the LSTs to 2000 p.e., possibly even to $\sim$1700 p.e. as recommended by White et al. [115], and will not lead to any adverse effects on the derived energy and angular resolution performances. However, a more complete understanding of the systematic effects resulting from induced saturation can only be achieved once background has been included into this study.

The findings from the lower dynamic range study suggest that reducing the assumed DC/PE ratio for all telescope types does not adversely affect the derived energy and angular resolution performance. These simulations suggest that, within the context of the current CTA analysis framework, resolving the single photo-electron is a financial and time cost that CTA does not need to incur.

It is recommended that further work be carried out on the two dynamic range studies presented here. In particular the upper dynamic range needs to be tested using mono-energetic gamma-ray shower simulations for all three telescope types. This requires running many time consuming shower simulations at very high energies (30 TeV and 300 TeV). The lower dynamic range study can now be extended by increasing the number of events simulated and by including background simulations to allow a full background rejection analysis leading to the production of sensitivity curves. Determining whether there is any adverse effect on sensitivity performance as a result of adjusting the FADC amplitude values will provide a comprehensive study of the lower dynamic range for CTA.

Chapter 5

Prospects for detecting pulsed gamma-ray emission with CTA

The following chapter presents the results of an analysis of data recorded with the Large Area Telescope (LAT) instrument aboard the Fermi Gamma-Ray Space Telescope (*Fermi*). A discussion of the data reduction and timing analysis is presented. Using the recommended binned likelihood method, the differential energy spectra for the Crab and Vela pulsars are derived. Finally, using the sensitivity performances derived in this research, the prospects for detecting pulsed gamma-ray emission with the CTA telescope system are also discussed.

5.1 Pulsar observations

A short introduction of pulsars was provided in Chapter 1 which included discussion of their inferred spin-down energies $\dot{E}$ as well as their key measurable parameters; period P and period derivative $\dot{P}$. Figure 5.1 illustrates the $P - \dot{P}$ diagram for known radio and gamma-ray pulsars. From this diagram the distinction between the millisecond pulsars and the 'normal' pulsars is clear and it is suggested that the millisecond pulsars result from a different formation history and mostly exist in binary systems [82]. This work is concentrated on the 'normal' pulsars where it appears that those detected with gamma-ray

emission tend to have large spin-down energies. In particular the Crab pulsar (highlighted in Figure 5.1) appears relatively unique in terms of its inferred $\dot{E}$ and whether its properties can be applied to pulsars like Vela (also highlighted) for example which is 2 orders of magnitude less energetic is questionable [82]. However, there is still hope that pulsars like Vela have only gone undetected with ground-based Cherenkov telescopes due to a lack of sensitivity at the energies of interest from the current generation of instruments. Based on this assumption, it is a useful exercise to analyse *Fermi* observations of the Crab and Vela pulsars against the sensitivity performances derived for CTA in this work, in order to speculate on CTA's prospects for detecting pulsed gamma-ray emission from pulsars.

5.2 Observations of the Crab and Vela pulsars with *Fermi*

In order to determine the prospects for detecting pulsed gamma-ray emission from sources such as pulsars, some observational data recorded with the *Fermi* LAT were analysed. The goal was to analyse data from two prominent gamma-ray sources: the Crab pulsar [RA (right ascension) = 83.6331°, DEC (declination) = 22.0145° (J2000)] and the Vela pulsar [RA = 128.836°, DEC = −45.1764° (J2000)].

For the results presented here, the data used for the Crab pulsar was collected between 4th August 2008, 54682.6 Modified Julian Date (MJD) and 4th January 2010 (55200 MJD). For the Vela pulsar observations the data used were collected between 4th August 2008 (54682.6 MJD) and 2nd July 2009 (55014 MJD). The reason for choosing these observational periods was to coincide with the validity of the respective pulsar ephemerides (see Section 5.2.2). Photon files were obtained for a 10 degree radius centred on the respective objects covering the energy range from 100 MeV to 300 GeV. The data were reduced using the NASA *Fermi* provided *ScienceTools-v9r23p1-fssc-20111006-i386-apple-darwin10.8.0* software package. Details on all the tools can be found in the online *Cicerone* [5] and a description of the *Fermi* recommended Likelihood analysis which was used in this research can be found in

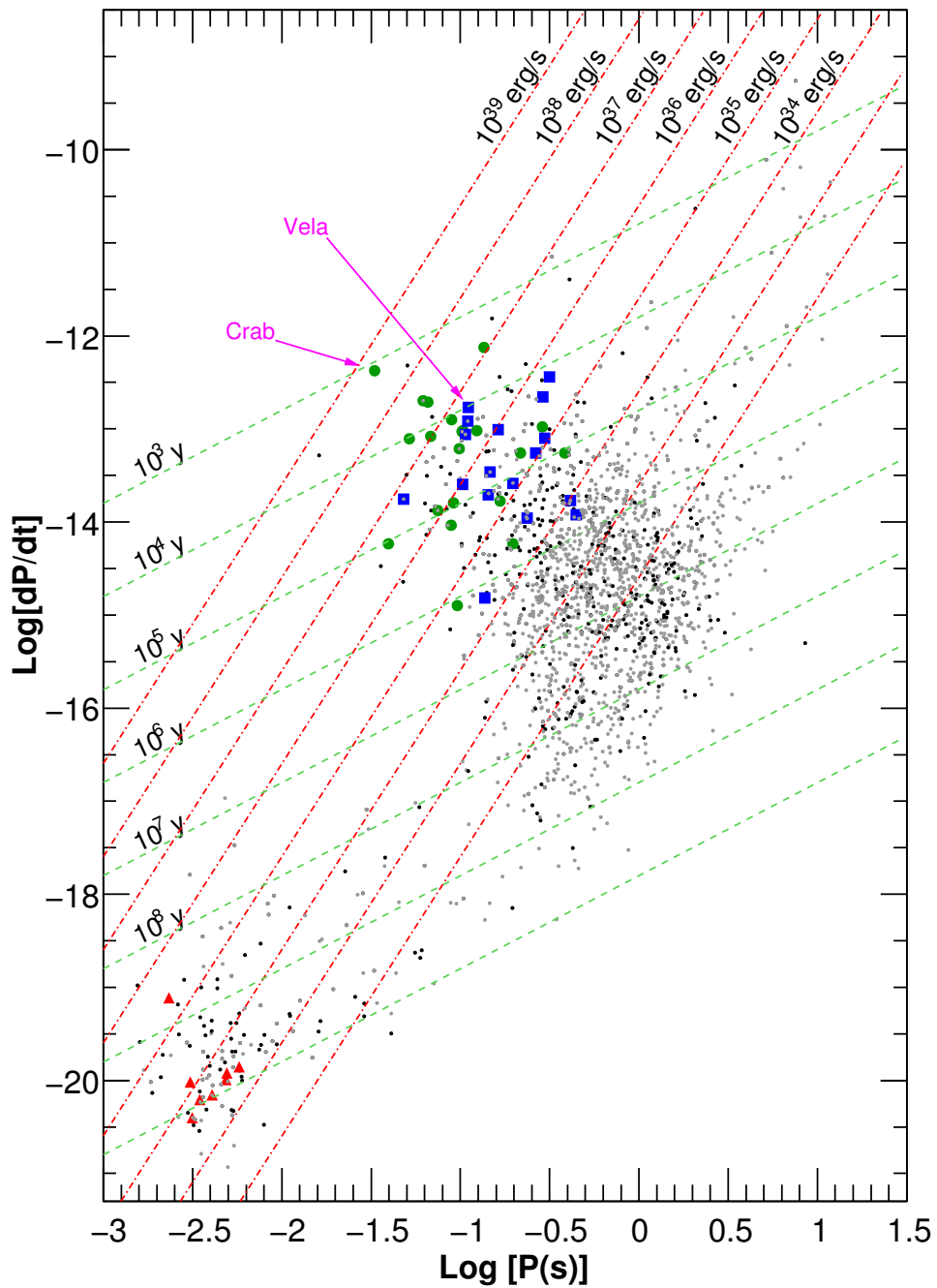**Figure 5.1:** The $P - \dot{P}$ diagram for known radio and gamma-ray pulsars. Shown here are the the fixed $\dot{E}$ values (dashed-dot line), the spin-down age of the pulsars (dashed line), *Fermi* detected gamma-ray pulsars (blue squares), *Fermi* detected millisecond gamma-ray pulsars (red triangles), radio-loud gamma-ray pulsars (green circles) and all other radio-loud pulsars (black and grey dots) [17].

Abdo et al. [15].

5.2.1   Data reduction of *Fermi* LAT pulsar observations

Using the *gtselect* tool, the downloaded photon files were filtered to include only events within the energy range from 100 MeV to 100 GeV. The reason for trimming the upper energy bound is to minimise the large statistical errors seen with *Fermi* observations at these energies. This is only done in the flux derivations and not in the image count maps where the statistical error is of low importance. In addition a maximum zenith angle of 105 degrees was stipulated as recommended in the *Cicerone*. Then using the *gtmktime* tool, an energy-dependent zenith angle cut was also made limiting the analysis to events within an energy-dependent region of interest (ROI) centred on the respective sources: the Crab pulsar and the Vela pulsar. Equation 5.1 shows how the maximum angular acceptance for each energy bin was derived for the Crab pulsar, which is the same as the approach adopted by Abdo et al. [19].

$$\theta_{\mathrm{max}} = \mathsf{max}(6.68 - 1.76 \times \log 10(\mathsf{E_{MeV}}, 1.3))[\mathrm{degrees}] \tag{5.1}$$

where *max* is a function that determines the maximum value between two given numbers. For analysis of the Vela pulsar a similar approach to that adopted by Abdo et al. [18] was used in this work and is shown in Equation 5.2.

$$\theta_{\mathrm{max}} = \mathsf{max}(1.6 - 3 \times \log 10(\mathsf{E_{GeV}}, 1.3))[\mathrm{degrees}] \tag{5.2}$$

again where *max* is a function that determines the maximum value between two given numbers. In both cases it is suggested that such energy-dependent angular cuts allow for consideration of the system performance and also ensure that the signal-to-noise ratio is maximised. Additional spacecraft status information was also used to clean the events further. The following flags denote the spacecraft conditions required for events to pass into

the analysis: DATA_QUAL=1, LAT_CONFIG=1 and ABS(ROCK_ANGLE)<52. Briefly, these mean that the data recorded is good, the telescope was functioning properly and the spacecraft was never positioned such that it had the Earth's limb within its field of view. Full explanation of the definitions can be found in the *Cicerone* [5]. Table 5.1 provides a summary of the number of counts analysed.

Table 5.1: Summary of the number of observed counts for the Crab and Vela pulsars.

Source	Total counts	Total OFF pulse counts	Total ON pulse counts
Crab pulsar	339857	101212	138989
Vela pulsar	395180	80019	303893

5.2.2   Timing solution of *Fermi* LAT pulsar observations

Proper analysis of pulsed gamma-ray emission from pulsars requires a timing model. This allows a phase to be assigned to each of the detected photons based upon their time of arrival (TOA). Typically in very high-energy gamma-ray astronomy, pulsar timing models are provided by timing analyses conducted with radio telescopes such as the Parkes Radio Telescope [6]. The timing solution used for the Crab pulsar is detailed in Ackermann et al. [20] and the timing solution used for the Vela pulsar is that detailed in Abdo et al. [18]. In this research the *Fermi* detected photons were phase folded according to their TOA using the *tempo2* [76] [59] [75] timing analysis software in conjunction with the *tempo2 fermi-plugin* [102]. The *tempo2* software package adjusts the photon TOAs so that they represent arrival times within an inertial reference frame. Full discussion of how this is done is beyond the scope of this thesis, but briefly this is done by transforming each detected photon TOA at Earth (or on a satellite in orbit around the Earth) to a TOA in the pulsar's frame of reference. The motion of the Earth around the Solar System Barycentre is taken into account as well as any orbital effects encountered by the pulsar, particularly if it is in a binary system. In addition, delays caused by other factors such as gravitational effects are also taken into account in order to reconstruct the pulse emission time. Figures 5.2 and

5.3 show the phase resolved light-curves for the Crab and Vela pulsars respectively.

Figure 5.2: The phase resolved light-curve (top left panel) for the Crab pulsar for > 100 MeV gamma-ray events observed with the *Fermi* gamma-ray space telescope during the period 4th August 2008 (54682.6 MJD) and 4th January 2010 (55200 MJD) (right panel). The light-curve was generated using the *tempo2* timing analysis software package with the *fermi-plugin*. The timing solution used was that detailed in Ackermann et al. [20]. In addition to phase folding the light-curve, the *tempo2 fermi-plugin* also produces the H-test [54] Test Significance (TS) as a function of time (bottom left panel) which illustrates the uniformity of the barycentre corrected photon arrival times. The dashed line (top left panel) shows the average event number for all phases.

Figure 5.2 shows the phase resolved light-curve for the Crab pulsar derived using gamma-ray photon events observed with *Fermi* between energies of 100 MeV and 300 GeV. Two phase rotations are shown for convenience. Two distinct peaks are seen at the approximate phases of $\phi_1 = 0.99$ and $\phi_2 = 0.38$. The peaks are asymmetric and there appear to be distinctive ON and OFF pulse regions. Following Abdo et al. [19], the ON-pulse region is defined as being between the following two phase intervals: $0.27 > \phi_{ON,Crab} < 0.47$ and $0.87 > \phi_{ON,Crab} < 1.07$. The OFF-pulse region is defined as $0.52 > \phi_{OFF,Crab} < 0.87$.

There also appears to be a *bridge* between ϕ_1 and ϕ_2; however, for the purposes of this study these photons will be ignored.

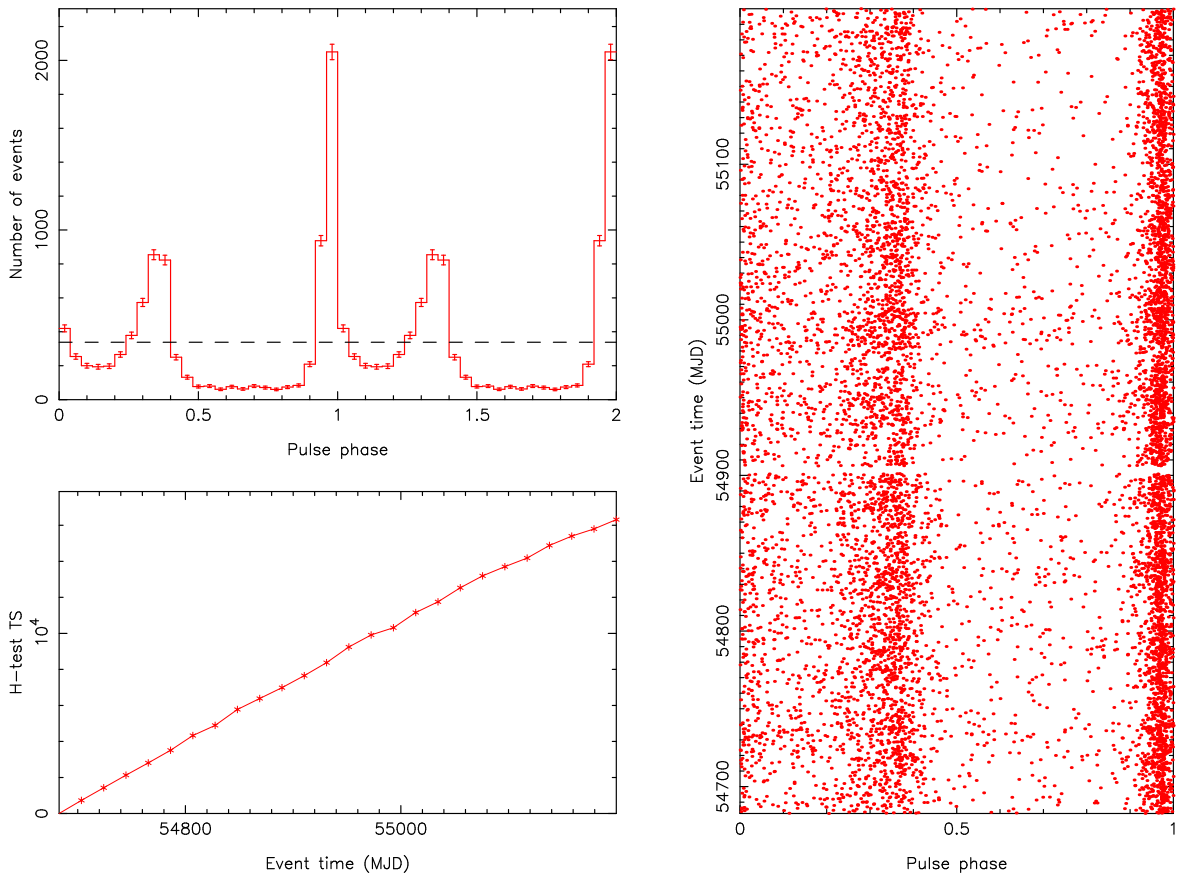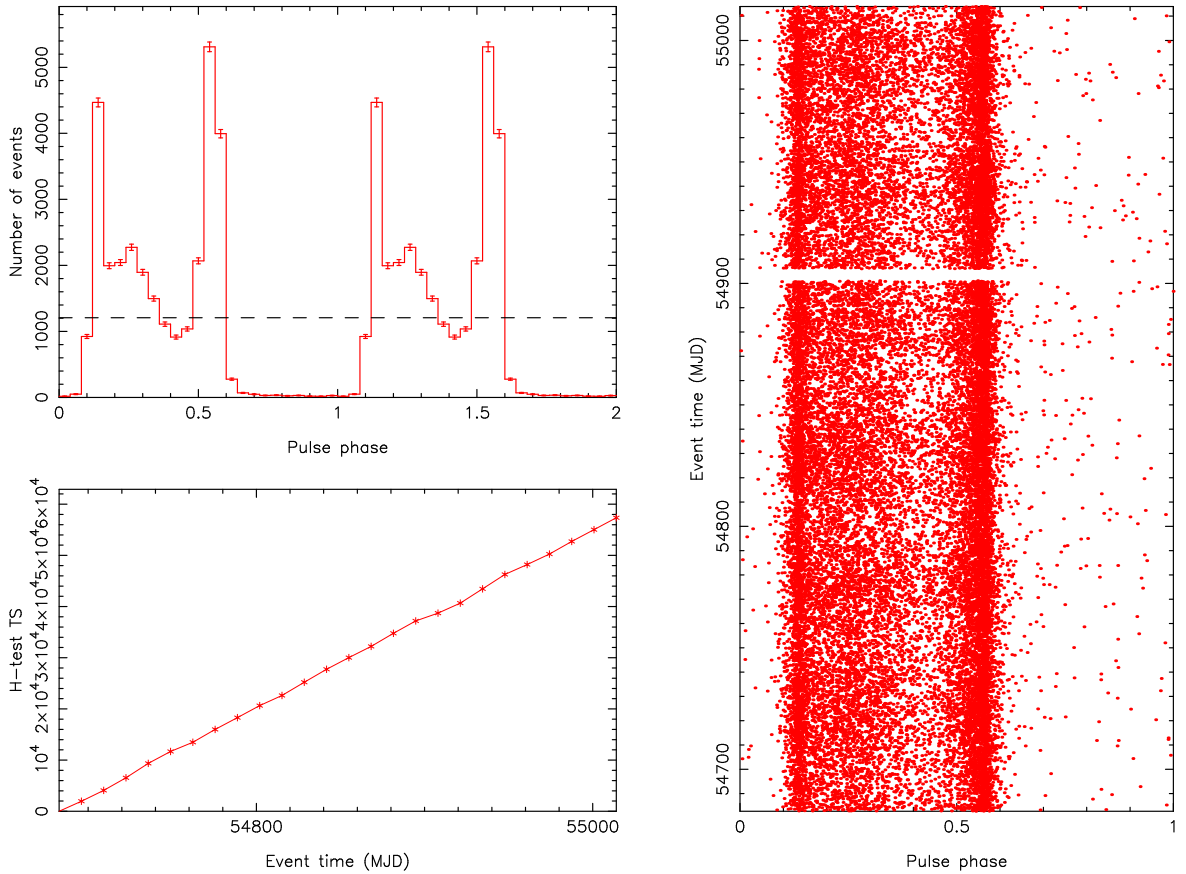**Figure 5.3:** The phase resolved light-curve for the Vela pulsar for >100 MeV gamma-ray events observed with the *Fermi* gamma-ray space telescope during the period 4th August 2008 (54682.6 MJD) and 2nd July 2009 (55014 MJD). The light-curve was generated using the *tempo2* timing analysis software package with the *fermi-plugin*. The timing solution used was that detailed in Abdo et al. [18]. Also shown is the H-test Test Significance (TS) as a function of time (bottom left panel). The dashed line (top left panel) shows the average event number for all phases.

Figure 5.3 shows the phase resolved light-curve for the Vela pulsar derived using gamma-ray photon events observed with *Fermi* between energies of 100 MeV and 300 GeV. Again two phase rotations are shown for convenience. Two distinct peaks are seen at the approximate phases of $\phi_1 \sim 0.15$ and $\phi_2 \sim 0.55$. Like the Crab pulsar, the phase resolved light-curve of the Vela pulsar has distinctive ON-pulse and OFF-pulse regions. The regions defined in Abdo et al. [14] were the ones used for this research. The ON-pulse region is defined as being between the following two phase intervals: $0.05 > \phi_{ON,Vela} < 0.65$. The OFF-pulse region is defined as $0.65 > \phi_{OFF,Crab} < 1.05$. Unlike the Crab pulsar, it appears that Vela

has a very prominent bridge region between ϕ_1 and ϕ_2. For the purposes of this research the photon events arriving with these phases have been included within the ON-pulse region. In the work carried out by Abdo et al. [18], it was shown that at energies above a few GeV the distinctive pulse at ϕ_1 reduces and the pulse within the bridge region at $\phi_3 \sim 0.29$, becomes more prominent.

Using the ON-pulse regions highlighted above for the Crab and Vela pulsar respectively, the observed photon events were reduced further to exclude all photons from the analysis that do not fall within these ON-pulse regions.

5.2.3   Binned likelihood analysis of *Fermi* LAT pulsar observations

The events were analysed using the *Fermi* LAT binned likelihood analysis method. The basic procedure is described online [7]; this has been adapted for the ON-pulse analysis described in this thesis. A three-dimensional counts cube was generated using the *gtbin* tool. The counts cube is simply a counts map binned in energy slices. The *Fermi* team recommends a binning scheme of 10 bins per decade to allow for rapid variations in the effective area below a few hundred MeV. However, for this research the events were binned into 15 equally-spaced logarithmic energy bins from 100 MeV to 100 GeV. This scheme was used to match the binning scheme implemented in the derivation of the CTA sensitivity curves, and therefore to allow a detailed comparison of the *Fermi* data with the sensitivity curves derived in this thesis. Equation 5.3 shows how the size of the counts cube was defined.

$$\text{Counts Cube Size}_{\text{pixels}} = 2 \times \big(\text{ROI}_{\text{total}} + \ 10 \text{ degrees}\big)\big/\delta \tag{5.3}$$

where $\delta = 0.2$ is the recommended number of degrees per pixel and $\text{ROI}_{\text{total}}$ the full 10 degree region of interest. This results in a counts cube size of 200 x 200 pixels. The same scheme was used for both the Crab pulsar and the Vela pulsar observations.

Figure 5.4: Smoothed count maps of gamma-ray events > 100 MeV from the Crab pulsar region observed with *Fermi* between 4th August 2008 (54682.6 MJD) and 4th January 2010 (55200 MJD). The top panel illustrates the events arriving in the OFF pulse phase and the bottom panel the ON pulse phase. The grid shows right ascension (RA) on the horizontal axis and declination (DEC) on the vertical axis in units of degrees (J2000 catalogue). Both images are centred on the Crab pulsar (RA $= 83.6331°$, DEC $= 22.0145°$). In the top panel there appears to be another gamma-ray source with an extended component located in the 10 degree ROI at RA $\approx 93°$ DEC $\approx 22°$. Images created using SAOImage DS9 developed by Smithsonian Astrophysical Observatory [80].
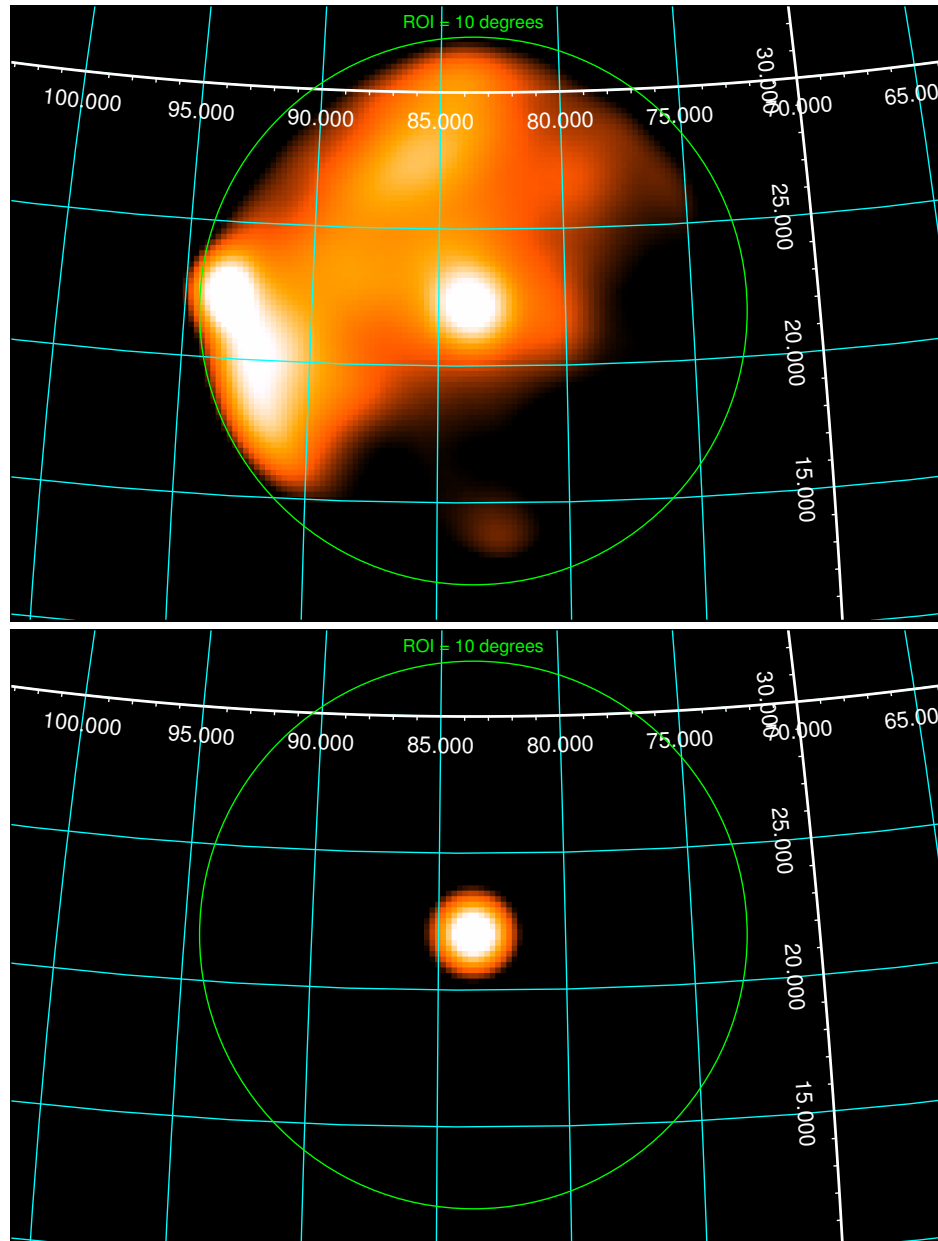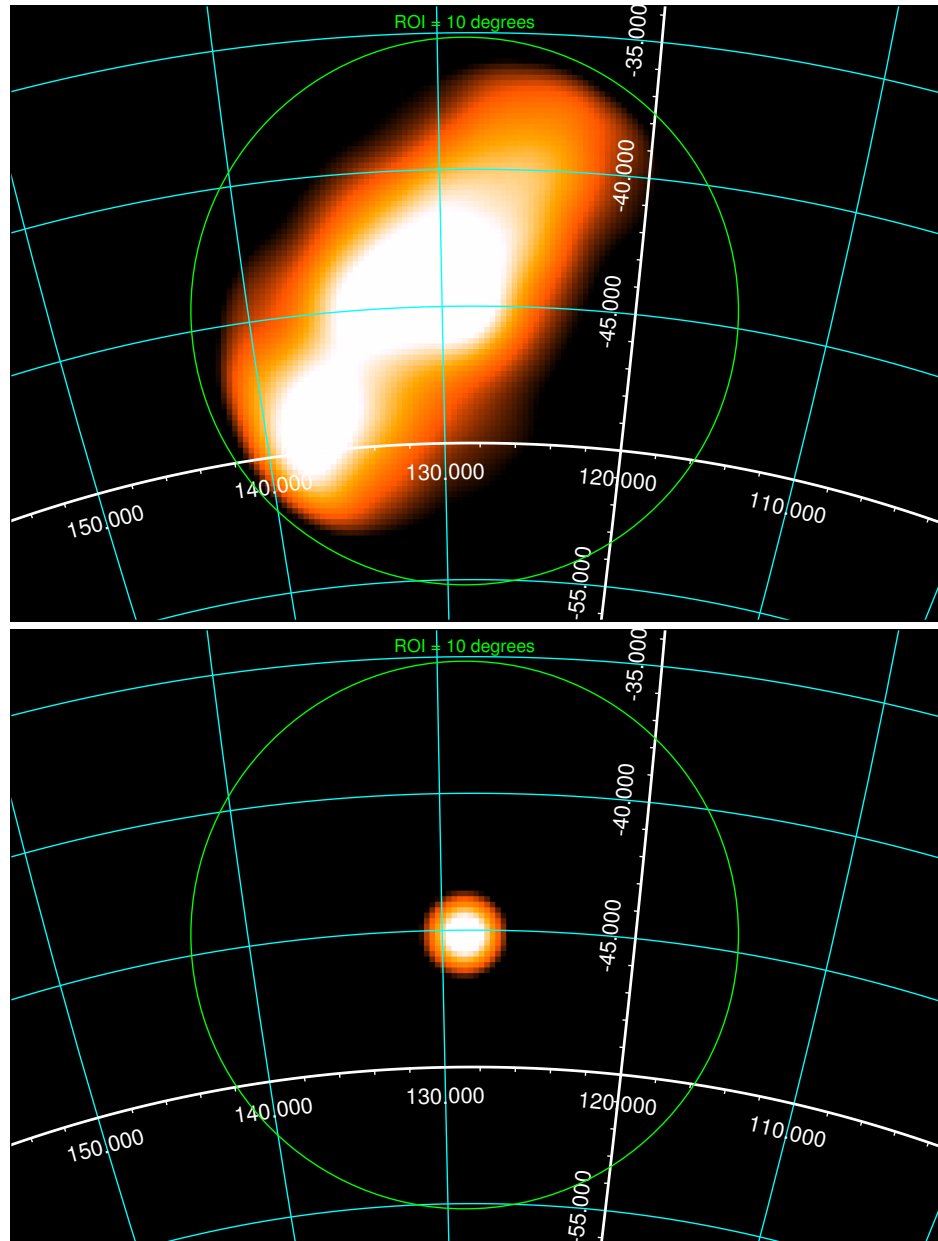
Figure 5.5: Smoothed count maps of gamma-ray events > 100 MeV from the Vela pulsar region observed with *Fermi* between 4th August 2008 (54682.6 MJD) and 2nd July 2009 (55014 MJD). The top panel illustrates the events arriving in the OFF pulse phase and the bottom panel the ON pulse phase. The top panel highlights the extended gamma-ray emission from Vela X. The grid shows right ascension (RA) on the horizontal axis and declination (DEC) on the vertical axis in units of degrees (J2000 catalogue). Both images are centred on the Vela pulsar (RA $= 128.836°$, DEC $= -45.1764°$). Images created using SAOImage DS9 developed by Smithsonian Astrophysical Observatory [80].

Using the *gtltcube* tool a live-time cube was generated for the observations of the Crab and Vela pulsars in order to determine the exposure time spent on the region of interest. This was done using an angular step size of cos(theta) = 0.025 and a pixel size of 1 degree. A binned exposure map was then generated using the *gtexpcube2* tool to account for the exposure at each position on the sky. In order to account for nearby sources a 400 x 400 pixel exposure map was generated using 0.2 degrees per pixel.

Source maps were computed using the *gtsrcmaps* tool in order to provide model counts for the binned likelihood analysis. The source models used were those obtained from the *2nd year Fermi Catalogue* [94]. Briefly, the source maps are generated by taking the source model spectra, multiplying this with the exposure at each of the source positions and convolving this with the effective point spread function. Hence, to account for nearby sources, a larger area is chosen for the binned exposure map.

The final step in the analysis was to use the *gtlike* tool in order to obtain a likelihood probability of the observed data given an input model. Full details of the likelihood fit can be found in the *Cicerone* [5]. The result of using the likelihood approach is a best fit model, which includes uncertainties, to describe the observed data. A test statistic (TS) is computed providing a measure of probability that the observed events cannot be obtained from background fluctuations alone. Thus it is a measure of the source's significance such that $\sigma = \sqrt{TS}$. Figure 5.6 shows the significance obtained for observations of the Crab and Vela pulsars analysed using the *Fermi* binned likelihood method.

5.3 Energy spectra results of the Crab and Vela pulsars

The energy spectra for both the Crab and Vela pulsars were derived using the reduced data, outlined above, recorded with the *Fermi* gamma-ray space telescope. The observed fluxes were converted into differential fluxes by dividing by the respective energy bin widths.
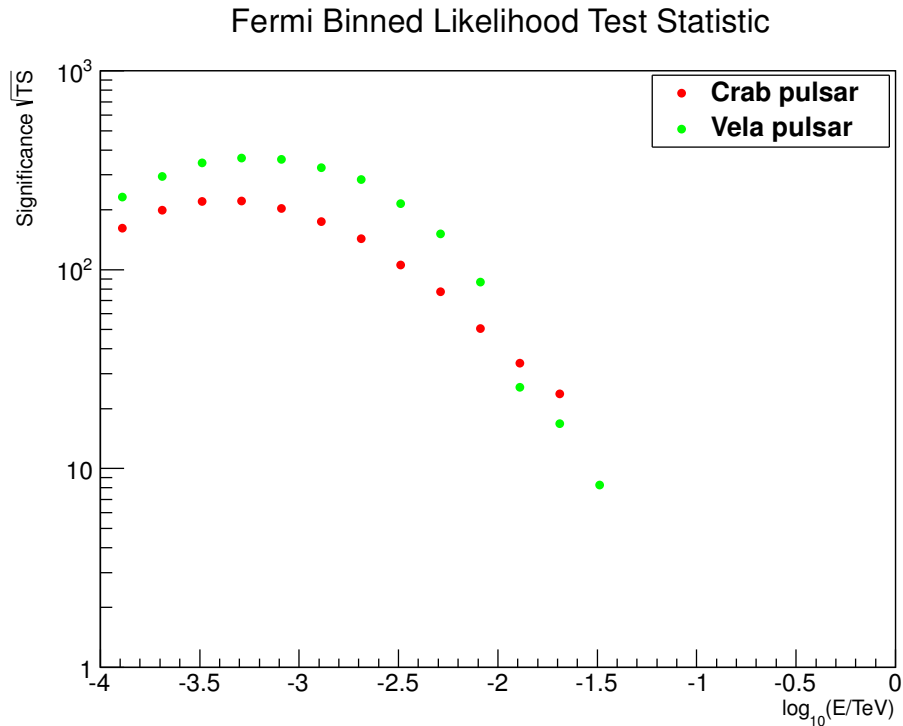
Figure 5.6: The binned likelihood method test-statistic providing a measure of how well the source models of the Crab and Vela pulsars fit the observed data points. Details of the *Fermi* binned likelihood method including a comprehensive description of the test-statistic can be found in the *Fermi Cicerone* [5].

Figure 5.7 illustrates the observed differential energy spectra for the Crab (red squares) and Vela (green squares) pulsars respectively.

Also shown in Figure 5.7 are the differential sensitivity performance curves (derived in this research) for CTA Subarray-E (solid black line), CTA Subarray-B (solid gold line) and the 3-year sensitivity performance of *Fermi* (solid blue line) [101]. The best-fit parametric functions reported by *Fermi* are shown for their observations of the Vela pulsar (dashed green line) [18] and the Crab pulsar (dashed red line) [19]. For both pulsars analysed in this work, the observed data appear to follow the spectra reported by the *Fermi* team. The error bars shown for these data points are purely statistical and no systematic errors are shown.

In October 2011, the VERITAS collaboration published the results of their observations of the Crab pulsar at energies above 100 GeV illustrated here with their best-fit broken-power-law parametric function (yellow dashed line) [30]. This was an exciting discovery
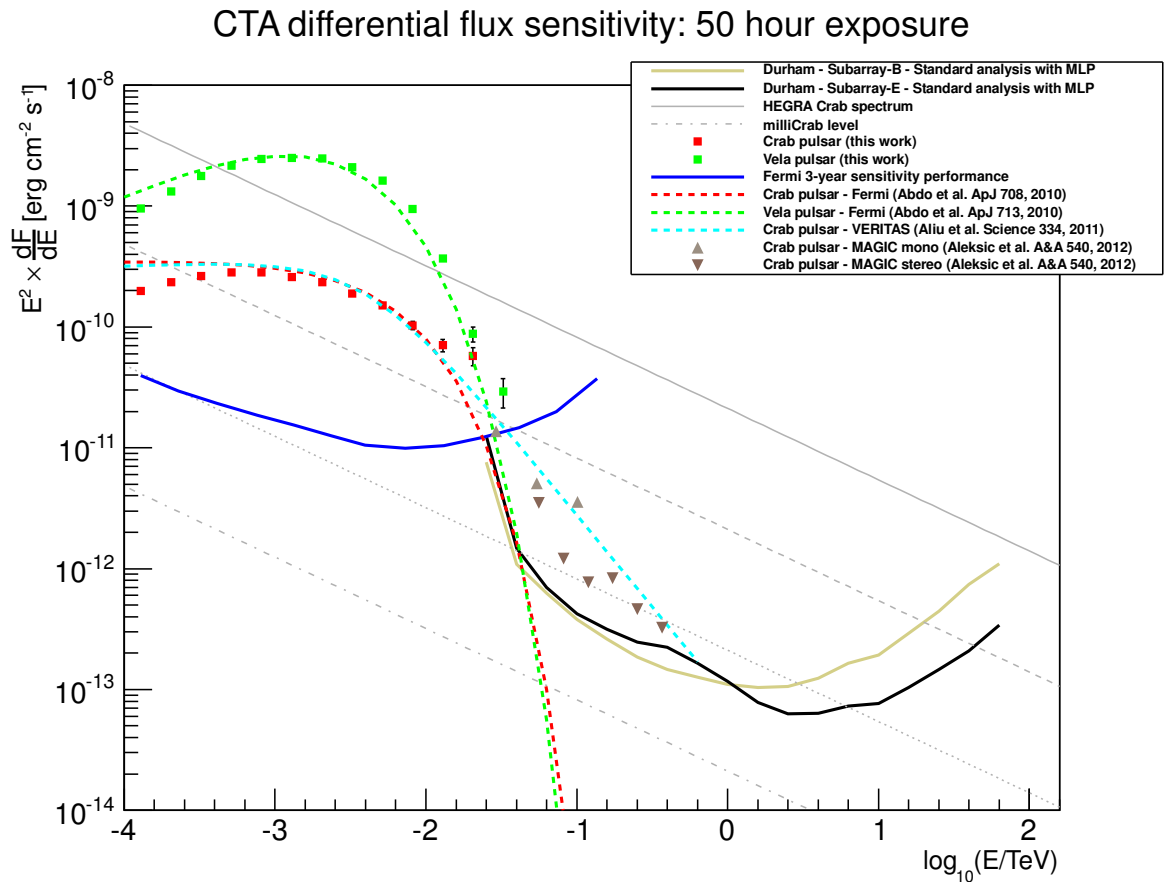
Figure 5.7: The phase-averaged differential energy spectrum of the Crab (red dots) and Vela (green dots) pulsars as a function of energy. These energy spectra were derived using the observations highlighted in this work. Also shown is the differential sensitivity performance of CTA Subarray-B (gold line), CTA Subarray-E (black line) and the 3-year differential sensitivity performance of *Fermi* (blue line) [101]. Recent ground-based detection of the Crab pulsar above 100 GeV by VERITAS [30] are illustrated by their best-fit broken-power-law parametric function (yellow dashed line) and above 25 GeV by MAGIC [29] using a single telescope (filled up triangles) and stereoscopic (filled down triangles). The best-fit parametric functions reported by *Fermi* for the Crab pulsar [19] (red dashed line) and the Vela pulsar [19] (green dashed line) are also highlighted. The error bars on the Crab and Vela observation data points are purely statistical and no systematic errors are shown. The CTA sensitivity curves shown here were derived for non-pulsed gamma-ray signal events.

from an existing ground-based Cherenkov system because it was generally accepted that pulsars should not produce pulsed emission at such high energies. The MAGIC collaboration have subsequently confirmed the VERITAS observations, as they too have detected pulsed gamma-ray emission from the Crab pulsar up to energies of approximately 400 GeV. These are shown for single-telescope observations (filled up triangles) and stereo observations (filled down triangles) [29]. It is clear that the sensitivity performance of the two CTA subarrays shown here, are well capable of detecting pulsed gamma-ray emission from the Crab pulsar. However, as a reminder, these two CTA performance curves were derived for a point-source at 20 degree zenith angle. In addition these performance curves are for the large southern-site CTA telescope array. Unfortunately when observing from the Southern hemisphere, the Crab pulsar is a relatively large zenith angle source thus there will be a loss in system sensitivity performance when viewing at low altitudes. For example, at large zenith angles the effective area performance scales roughly as $1/\cos^2\theta_{\mathrm{Zenith}}$ [62]. This is a factor 4 increase in effective area as well as array threshold, meaning CTA can expect a similar loss in sensitivity performance at the lowest energies below $\sim$100 GeV for large zenith angle observations. However despite this, and based on this work, it appears that CTA's prospects of being able to detect pulsed gamma-ray emission from the Crab pulsar are quite promising, although more work needs to be done to determine the sensitivity performance as a function of zenith angle.

One of the brightest small zenith angle pulsars observed with the H.E.S.S. telescopes in the Southern hemisphere is the Vela pulsar. However H.E.S.S. has never detected any pulsed gamma-ray emission from this or any other Galactic pulsars [26]. Nonetheless, Vela is a good candidate for detecting pulsed gamma-ray emission based upon the generally accepted criterion of high $\dot{\mathrm{E}}/d^2$ (see Section 1.5), and due to its high-energy flux of 879.4×10^{-11} [erg cm^{-2} s^{-1}] at energies 100 MeV $\lesssim$ E $\lesssim$ 100 GeV [56]. In comparison, the measured energy flux of the Crab is 130.6×10^{-11} [erg cm^{-2} s^{-1}] [56]. The analysis of the Vela observations conducted in this work suggests that the southern-site CTA telescope array should have sufficient sensitivity performance at and above approximately 25

GeV to detect pulsed gamma-ray emission from the Vela pulsar assuming it follows a power law with super-exponential cut off (green dashed line). This is very promising especially as no consideration has been given to the hardware optimisation of the telescope array for detecting pulsed emission, nor the ongoing research into overall system performance and sensitivity improvement at these energies such as using the 3D-analysis reconstruction method.

The ground-based detection of pulsed gamma-ray emission from the Crab pulsar at energies above 100 GeV, provide a strong suggestion that a simple power law with a super-exponential cut-off is not the best parametric function to describe the radiation mechanisms. From the VERITAS detection of pulsed gamma-ray emission from the Crab pulsar, Aliu et al. [30] suggest that their findings strongly favour a broken power law model of the form $A(E/E_0)^{\text{alpha}}/[1 + (E/E_0)^{\alpha - \beta}]$ (yellow dashed line). The authors conclude that for observed energies above 100 GeV, this strongly favours an inverse-Compton component as opposed to curvature radiation being the dominant radiation mechanism. Therefore the question is still open as to whether the Crab pulsar is truly a unique pulsar, or whether there are additional radiation mechanisms which primarily due to instrument sensitivity within the energy regime of interest have not been detected until now. From the sensitivity performance work conducted in this thesis and ongoing research by the CTA collaboration, CTA appears to be well placed to provide answers regarding this still poorly understood astrophysical problem.

5.4   Future work

As mentioned above, further research needs to be conducted into the large zenith angle sensitivity performance of CTA in order to appreciate fully the prospects of the large southern-site telescope array of being able to detect pulsed gamma-ray emission from the Crab pulsar. This includes looking into the gain in sensitivity performance when operating the telescope array at a trigger threshold optimised for pulsed-signals and low-energy trig-

gers. With respect to the Monte Carlo work package, further simulation work needs to be done in order to test whether any of the analysis procedures discussed in this thesis have any impact on determining pulsed gamma-ray signals. Preliminary work on this subject has already begun in the form of a CTA pulsar simulation. The aim of the pulsar simulation is to generate gamma-ray events following a typical 2 pulse phase-resolved light-curve that can be analysed with the post-reconstruction procedures. It is also possible to extend this simulation to include the reconstruction analysis stage as well.

Furthermore, it was highlighted in Abdo et al. [17] that the Crab pulsar is a notable exception with respect to its x-ray luminosity L_X, which is roughly 10 times its high-energy gamma luminosity L_γ. Although at this stage rather speculative, perhaps this provides CTA with an additional metric for determining suitable pulsar candidates. Thus it will be helpful to build a list of pulsars, particularly young fast rotators, with their measured L_X and L_γ to see if any other pulsars have an x-ray luminosity component that is larger than their gamma-ray component and whether this perhaps is an indicator of the potential for up-scattering photons via inverse-Compton to energies of a few hundred GeV.

Summary and future work

The research work conducted for this thesis focused on the performance studies for the Cherenkov Telescope Array (CTA). Chapter 1 provided a brief introduction to gamma-rays and their astrophysical origin within the known Universe. This included discussion of cosmic-rays, gamma-rays and the different interactions that lead to the production of gamma-rays. Examples and illustrations were given to highlight the models and physical concepts describing gamma-ray production mechanisms. Attention was given toward pulsars, how they might produce gamma-rays and why they are interesting astrophysical objects. Furthermore, some of the principal interactions that lead to gamma-ray absorption and attenuation are also discussed, as these interactions provide us with an opportunity for observing gamma-rays. Chapter 2 provided a brief introduction to gamma-ray astronomy, using space-based and ground-based telescopes. This included discussion of Extensive Air Showers (EAS) as well as the resulting Cherenkov light produced within the Earth's atmosphere. Furthermore, how Cherenkov light is detected using the imaging Atmospheric Cherenkov technique was highlighted. This included discussion of stereoscopic techniques, the Hillas parameters as well as background rejection.

Chapter 3 introduced the Cherenkov Telescope Array (CTA) including the motivations for constructing such an array, the specifications and the possible observatory layouts. Results of the extensive Monte Carlo simulation work were presented including calculation of various performance metrics such as energy resolution, angular resolution, effective area and flux sensitivity. This included deriving the performance for five different production-run 1 CTA layouts. Their performances were compared against each other as well as against

independently calculated performances. The performances derived in this research used a combination of standard reconstruction methods with a multi-layer perceptron neural network for background separation. The construction of the neural network architecture, including the training parameters, was discussed. Five different methods for determining the neural network response cut parameter were presented. It appears that the *energy-scaled significance cut method* is the best and most stably performing method. The final differential flux sensitivity results derived for the baseline Subarray-E are amongst the best within CTA. This work demonstrates that CTA will be capable of achieving milli-Crab integral sensitivity at 1 TeV for a 50 hours observation at the 5σ significance level.

Chapter 4 presented three short, focused studies undertaken for the CTA Monte Carlo working group (MCWG). The first study analysed the effect of site altitude on the overall array sensitivity. It was concluded that there is a gain in sensitivity performance below energies of approximately 100 GeV if the telescope array is constructed at a higher altitude site. However, this is only true when compared against sensitivity results calculated using standard shower reconstruction methods and not for those using the 3D-analysis method. The second and third studies addressed two specific questions relating to the dynamic range of the pixels to be used in the cameras. The first study concentrated on the upper dynamic range to investigate the amplitude to which the camera pixels can be saturated before adversely affecting subarray performance. This preliminary study only considered the large-sized telescopes (LSTs) and it is concluded that energy and angular resolution are not adversely affected when the cameras are saturated at an amplitude of approximately 1500 photo-electrons (p.e.). This is well below the CTA goal of 5000 p.e., but further work still needs to be conducted before a definite conclusion can be reached. In particular mono-energetic shower simulations need to be conducted for all three telescope sizes. The second study investigated the effect on subarray performance when the photo-electron to digital counts ratio was changed within the current analysis framework. It is concluded that reducing the assumed DC/PE ratio for all telescope types does not adversely affect the derived energy and angular resolution performance. This suggests that resolving the single

photo-electron may not be necessary. However, this study needs to be extended to include background shower simulations to allow a full background rejection analysis including the production of sensitivity curves. It is also recommended that a greater number of events should be simulated.

Chapter 5 presented the analysis results of data from the Crab and Vela pulsars recorded with the *Fermi* Large Area Telescope (LAT). This included discussion of the data reduction, timing analysis and use of the recommended binned likelihood method to derive differential energy spectra for the Crab and Vela pulsars. The spectra were compared with *Fermi's* published results as well as the latest results from both MAGIC and VERITAS. In addition the spectra were compared with the CTA sensitivity performances derived in this research. It can be concluded that CTA's prospects of detecting pulsed gamma-ray emission from pulsars are quite good. It is also concluded that should other pulsars like Vela exhibit similar properties to that seen from the Crab pulsar, the derived sensitivity performances suggest CTA is well placed to investigate the energy range from a few tens of GeV to a few hundred GeV. It is suggested that further Monte Carlo analysis work be conducted to see whether the current analysis procedure has any effect on the analysis of events from a periodic source like pulsars. In addition, it is recommended that a list of young pulsar candidates be drawn up, particularly southern hemisphere objects, with a high spin-down luminosity and particularly those with an x-ray luminosity component larger than their gamma-ray luminosity component. It is suggested that CTA could use such criteria for observations of pulsars to test whether the candidates emit pulsed gamma-rays up to energies near 100 GeV via inverse Compton processes.

Appendix A

The moments technique and the Hillas parameter definitions

A.1 Moments parameters

A geometrical representation of the shower in the camera is given by the moments (defined below Fegan [61]) of a body comprised of i pixel elements relative to the centre of the camera, with density ρ_i the count of each pixel and coordinates (x_i, y_i). These provide statistical parameters such as the mean. The n-th moment for an image consisting a total of N elements is then:

$$\frac{1}{N} \sum_i x_i^n \tag{A.1}$$

In ground-based gamma-ray astronomy moments are constructed to the second order and the following moments are used:

$$\Omega = \sum_i \rho_i \tag{A.2}$$

$$< x >= \frac{\sum_i \rho_i x_i}{\Omega} \tag{A.3}$$

$$< y >= \frac{\sum_i \rho_i y_i}{\Omega} \tag{A.4}$$

$$< x^2 >= \frac{\sum_i \rho_i x_i^2}{\Omega} \tag{A.5}$$

$$< y^2 >= \frac{\sum_i \rho_i y_i^2}{\Omega} \tag{A.6}$$

$$< xy >= \frac{\sum_i \rho_i x_i y_i}{\Omega} \tag{A.7}$$

the variances are then calculated as follows:

$$\sigma_{x^2} =< x^2 > - < x >^2 \tag{A.8}$$

$$\sigma_{y^2} =< y^2 > - < y >^2 \tag{A.9}$$

$$\sigma_{xy} =< xy > - < x >< y > \tag{A.10}$$

where the point (<x>,<y>) is the centroid of the ellipse i.e. the centre of the elliptical image in the camera. Reconstructions methods such as the 3D-analysis method use third order moments successfully.

A.2   Hillas parameters

The Hillas parameters are then functions of the moments defined above.

$$\text{Distance} = \sqrt{<x>^2 + <y>^2} \tag{A.11}$$

$$\text{Length} = \sqrt{\frac{\sigma_{x^2} + \sigma_{y^2} + z}{2}} \tag{A.12}$$

$$\text{Width} = \sqrt{\frac{\sigma_{x^2} + \sigma_{y^2} - z}{2}} \tag{A.13}$$

$$\text{Miss} = \sqrt{\frac{1}{3}(u<x>^2 + v<y>^2) - \left(\frac{2\sigma_{xy}<x><y>}{z}\right)} \tag{A.14}$$

$$\text{Alpha} = \arcsin\left(\frac{\text{Miss}}{\text{Distance}}\right) \tag{A.15}$$

where the following are the auxiliary functions:

$$d = \sigma_{x^2} - \sigma_{y^2} \tag{A.16}$$

$$z = \sqrt{d^2 + 4\sigma_{xy}^2} \tag{A.17}$$

$$u = 1 + \frac{d}{z} \tag{A.18}$$

$$v = 2 - u \tag{A.19}$$

Appendix B

Comparison of performance results for additional CTA subarrays analysed

B.1 CTA Subarray-B results

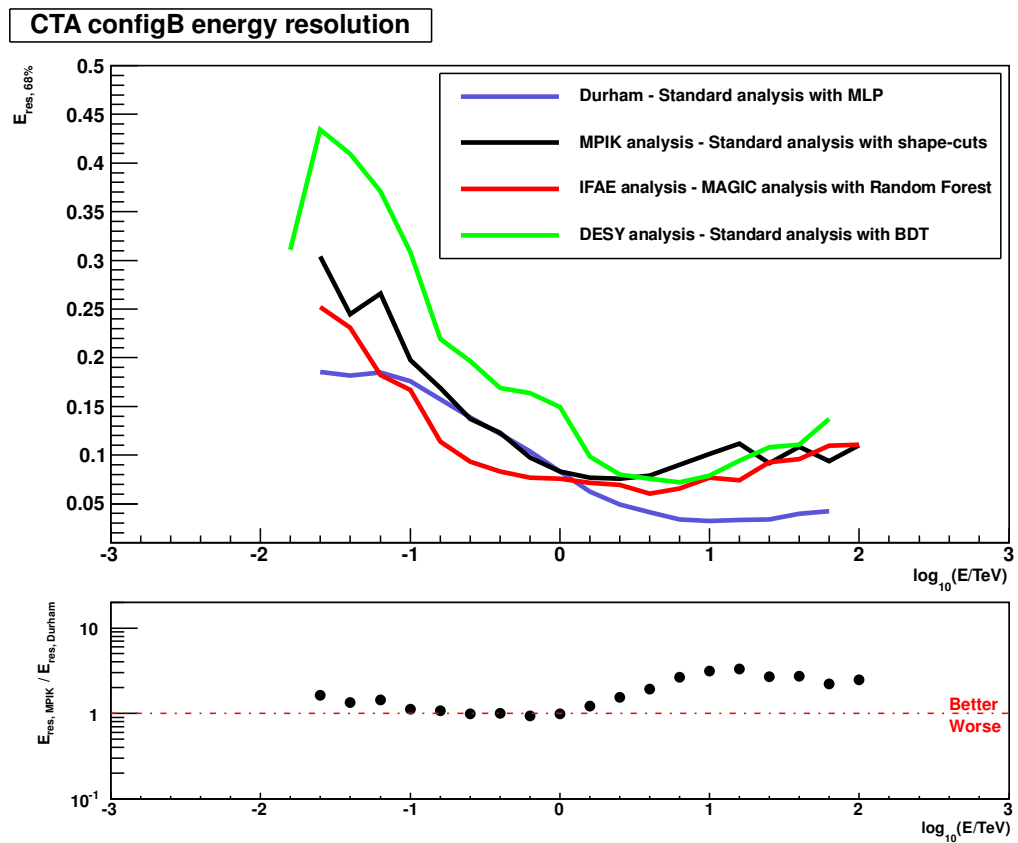## B.1.1 CTA Subarray-B energy resolution results

Figure B.1: Comparison of independently calculated energy resolution performances as a function of energy for CTA Subarray-B.
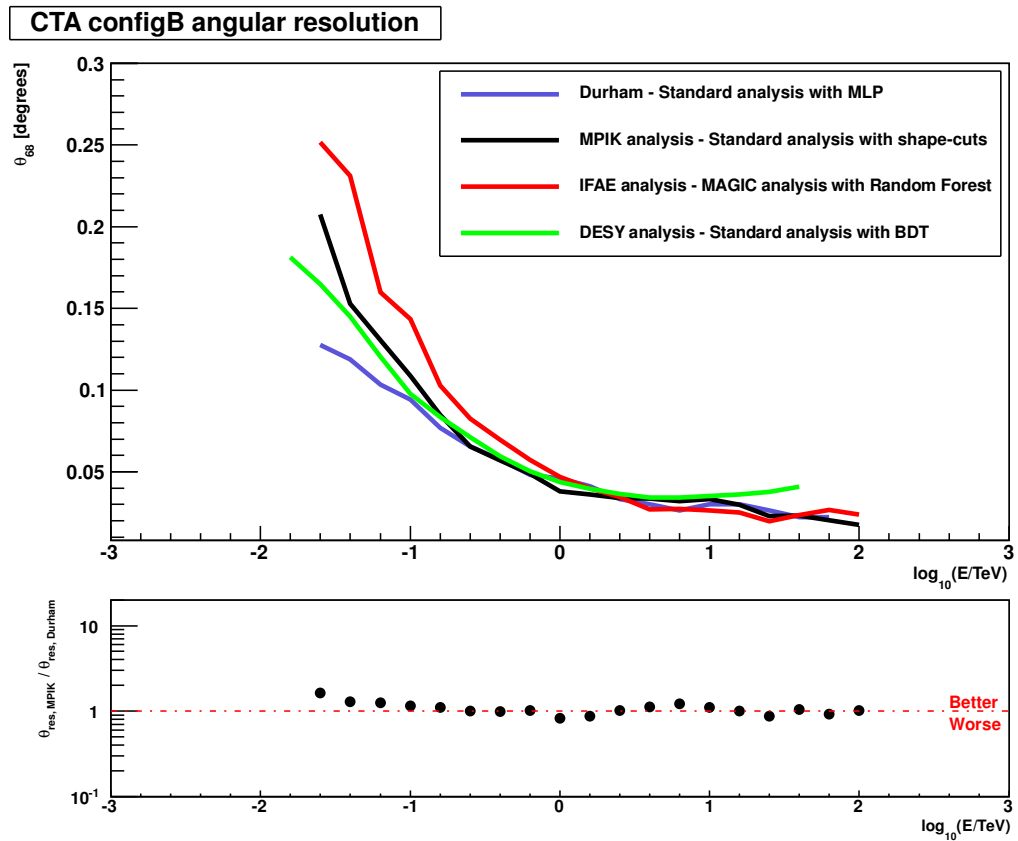
B.1.2 CTA Subarray-B angular resolution results

Figure B.2: Comparison of independently calculated angular resolution performances as a function of energy for CTA Subarray-B.

B.1.3 CTA Subarray-B effective area results

Figure B.3: Comparison of independently calculated effective area performances as a function of energy for CTA Subarray-B.

B.1.4 CTA Subarray-B differential sensitivity results

Figure B.4: Comparison of independently calculated differential sensitivity performances as a function of energy for CTA Subarray-B.

B.2   CTA Subarray-I results

B.2.1   CTA Subarray-I energy resolution results

Figure B.5: Comparison of independently calculated energy resolution performances as a function of energy for CTA Subarray-I.

B.2.2 CTA Subarray-I angular resolution results

Figure B.6: Comparison of independently calculated angular resolution performances as a function of energy for CTA Subarray-I.

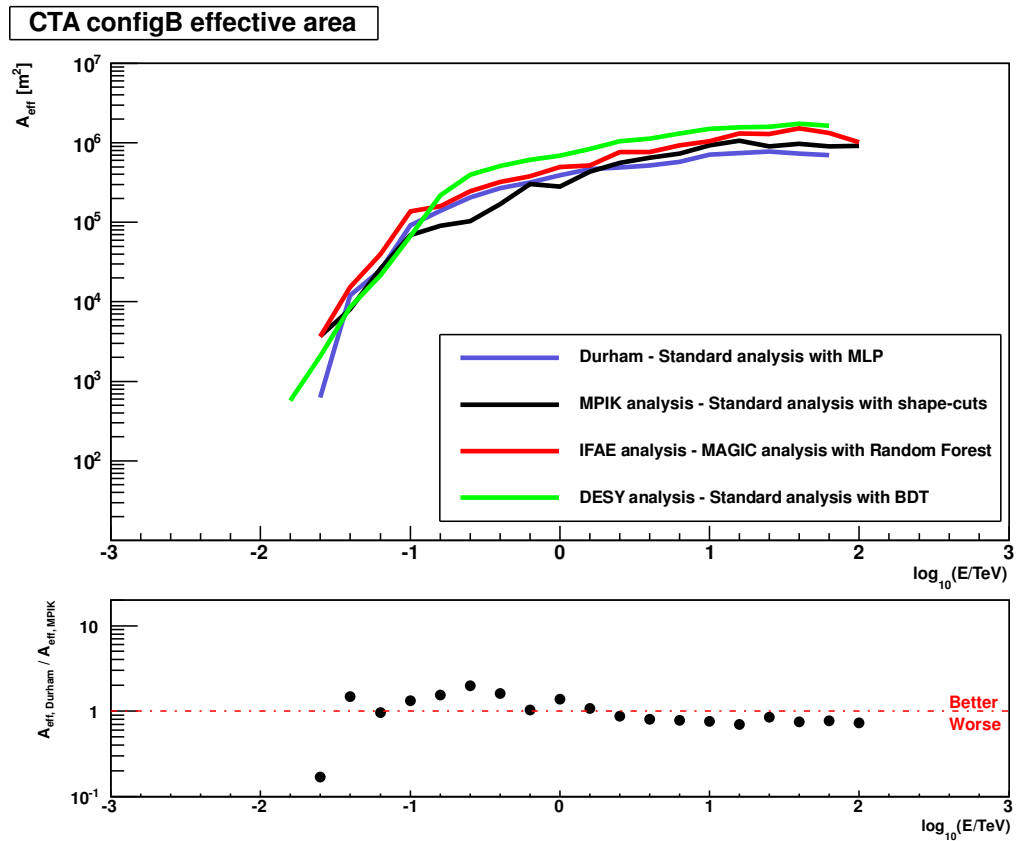### B.2.3 CTA Subarray-I effective area results

Figure B.7: Comparison of independently calculated effective area performances as a function of energy for CTA Subarray-I.

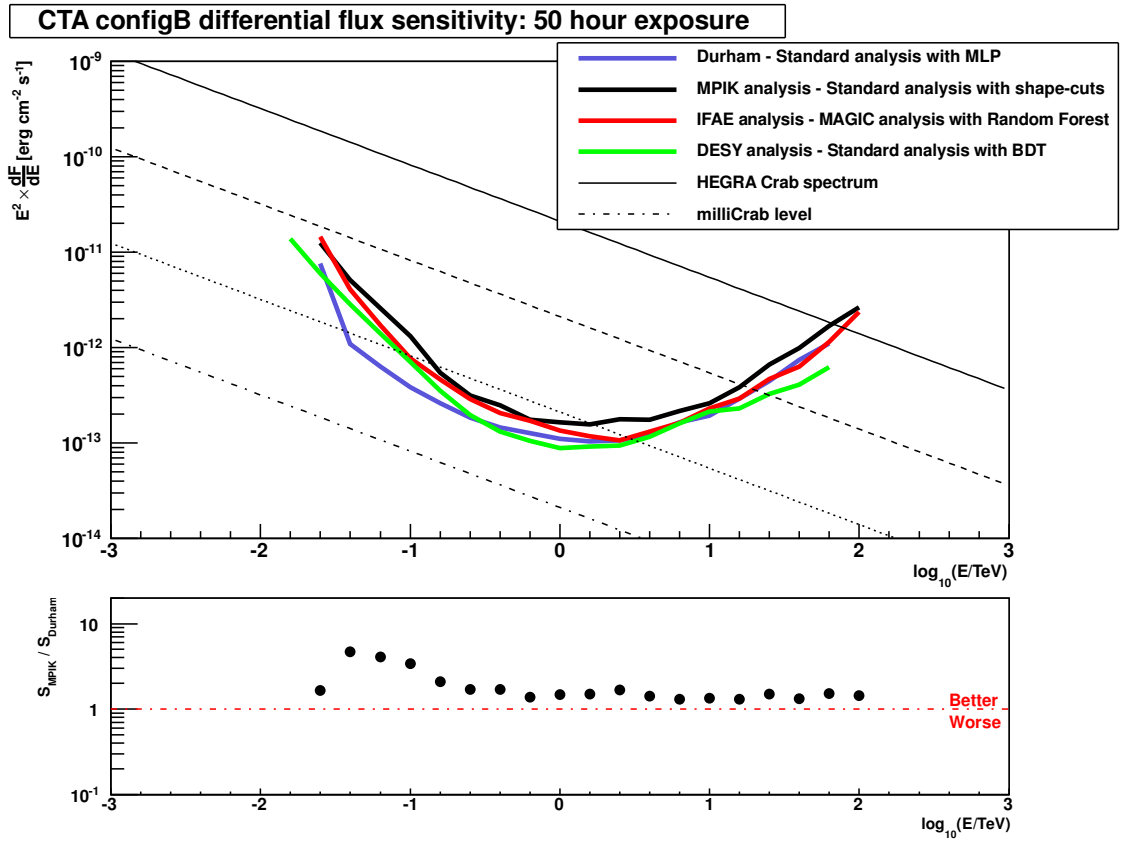## B.2.4   CTA Subarray-I differential sensitivity results

Figure B.8: Comparison of independently calculated differential sensitivity performances as a function of energy for CTA Subarray-I.

B.3   CTA Subarray-J results

B.3.1   CTA Subarray-J energy resolution results
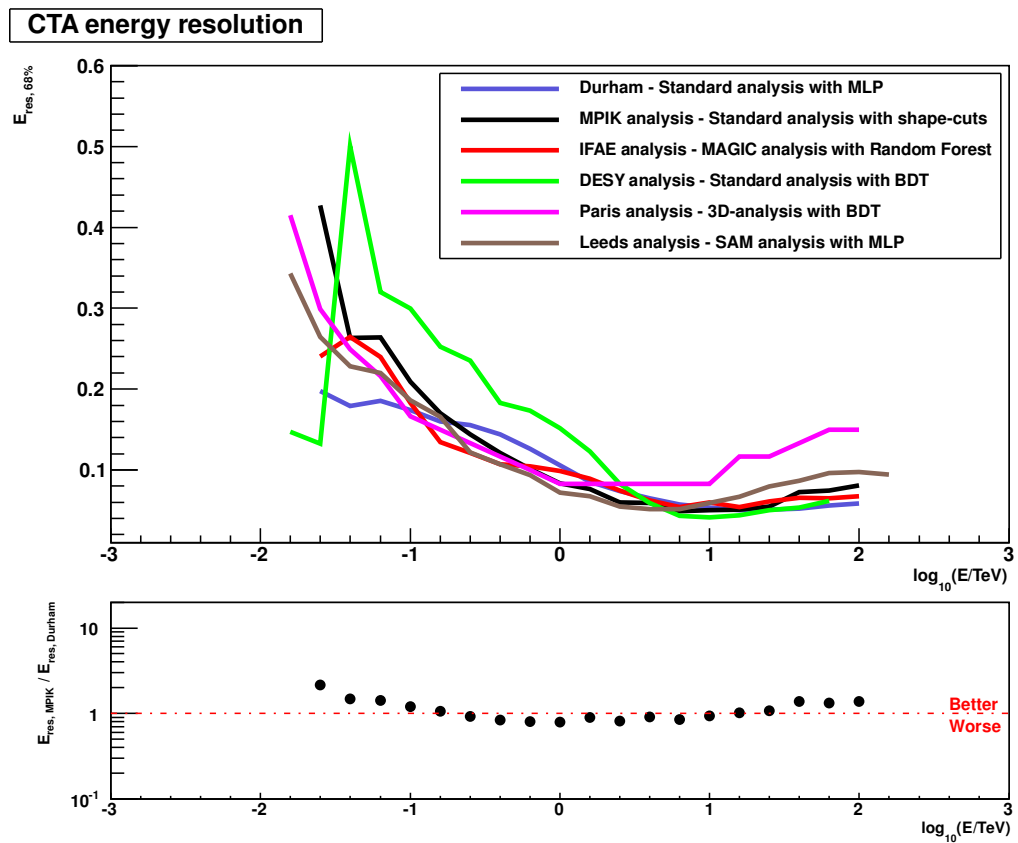

Figure B.9: Comparison of independently calculated energy resolution performances as a function of energy for CTA Subarray-J.
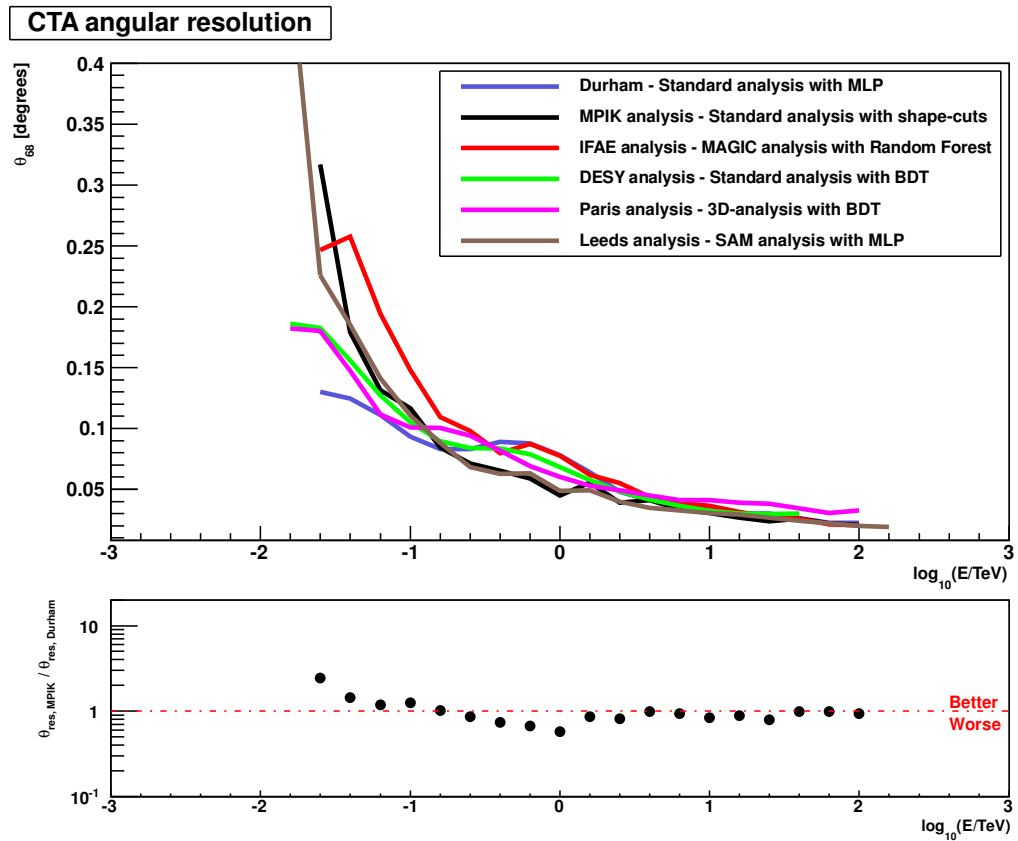
B.3.2 CTA Subarray-J angular resolution results

Figure B.10: Comparison of independently calculated angular resolution performances as a function of energy for CTA Subarray-J.
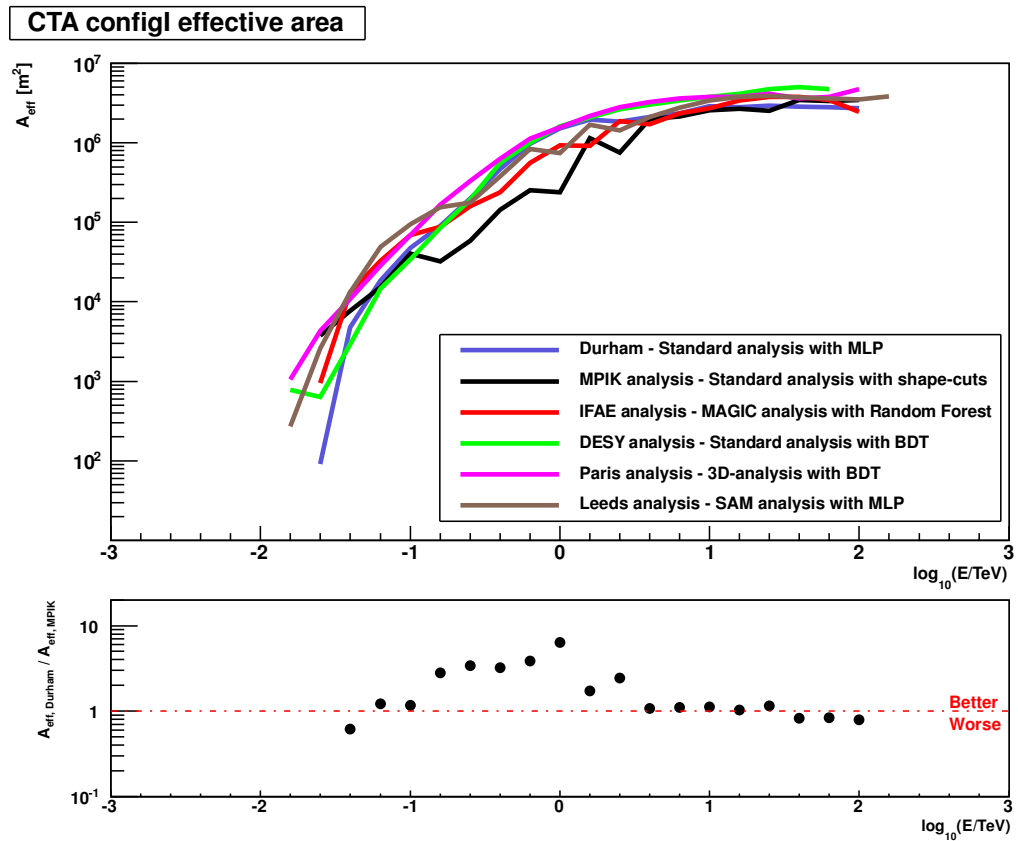
B.3.3   CTA Subarray-J effective area results

Figure B.11: Comparison of independently calculated effective area performances as a function of energy for CTA Subarray-J.

B.3.4   CTA Subarray-J differential sensitivity results

Figure B.12: Comparison of independently calculated differential sensitivity performances as a function of energy for CTA Subarray-J.

B.4 CTA Subarray-K results

B.4.1 CTA Subarray-K energy resolution results

Figure B.13: Comparison of independently calculated energy resolution performances as a function of energy for CTA Subarray-K.

B.4.2 CTA Subarray-K angular resolution results
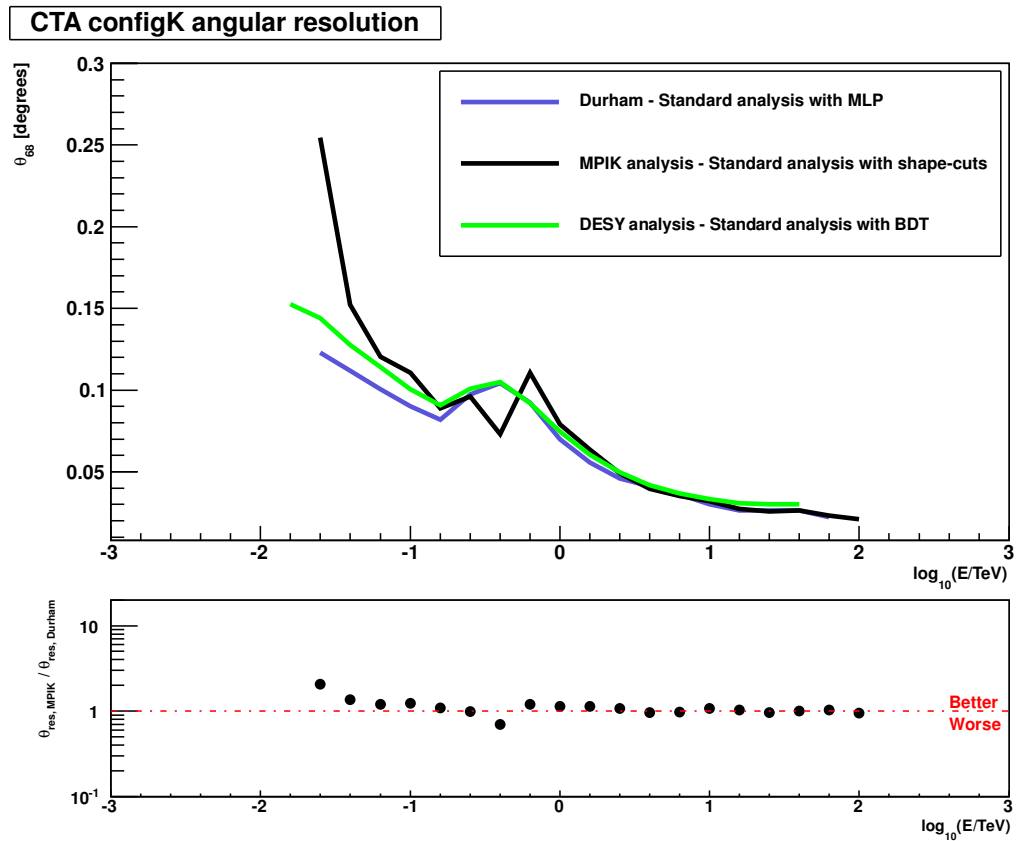
Figure B.14: Comparison of independently calculated angular resolution performances as a function of energy for CTA Subarray-K.

B.4.3   CTA Subarray-K effective area results
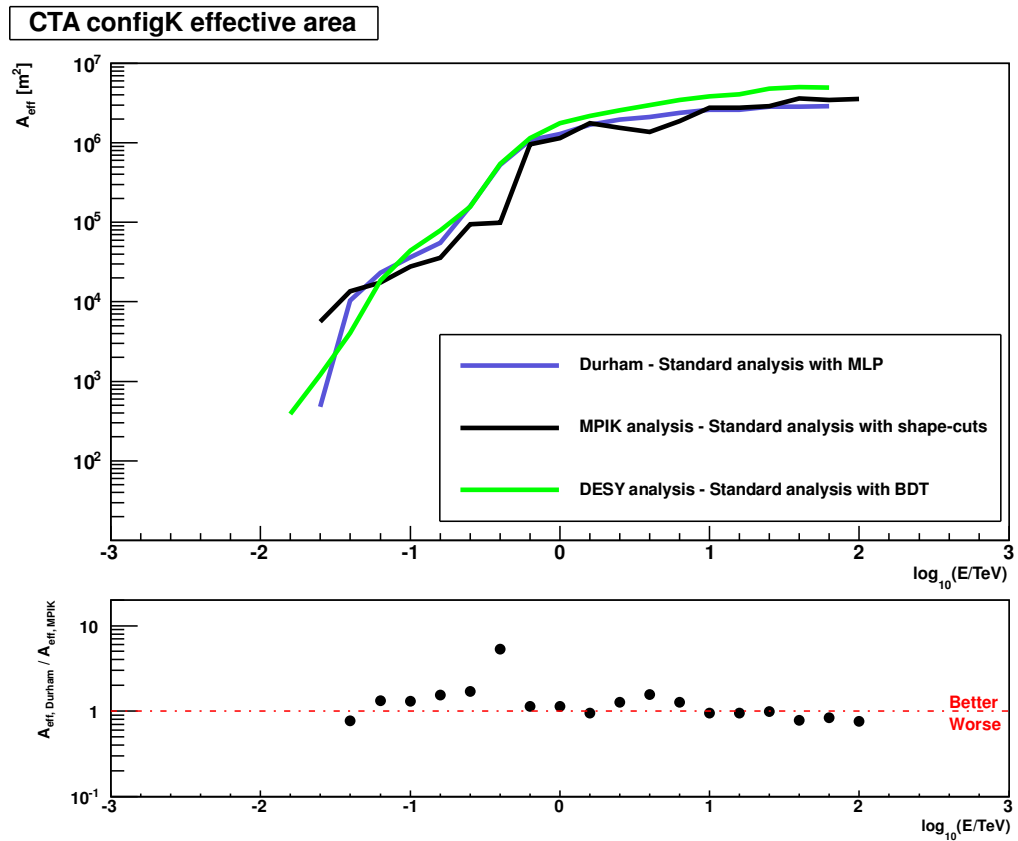
Figure B.15: Comparison of independently calculated effective area performances as a function of energy for CTA Subarray-K.

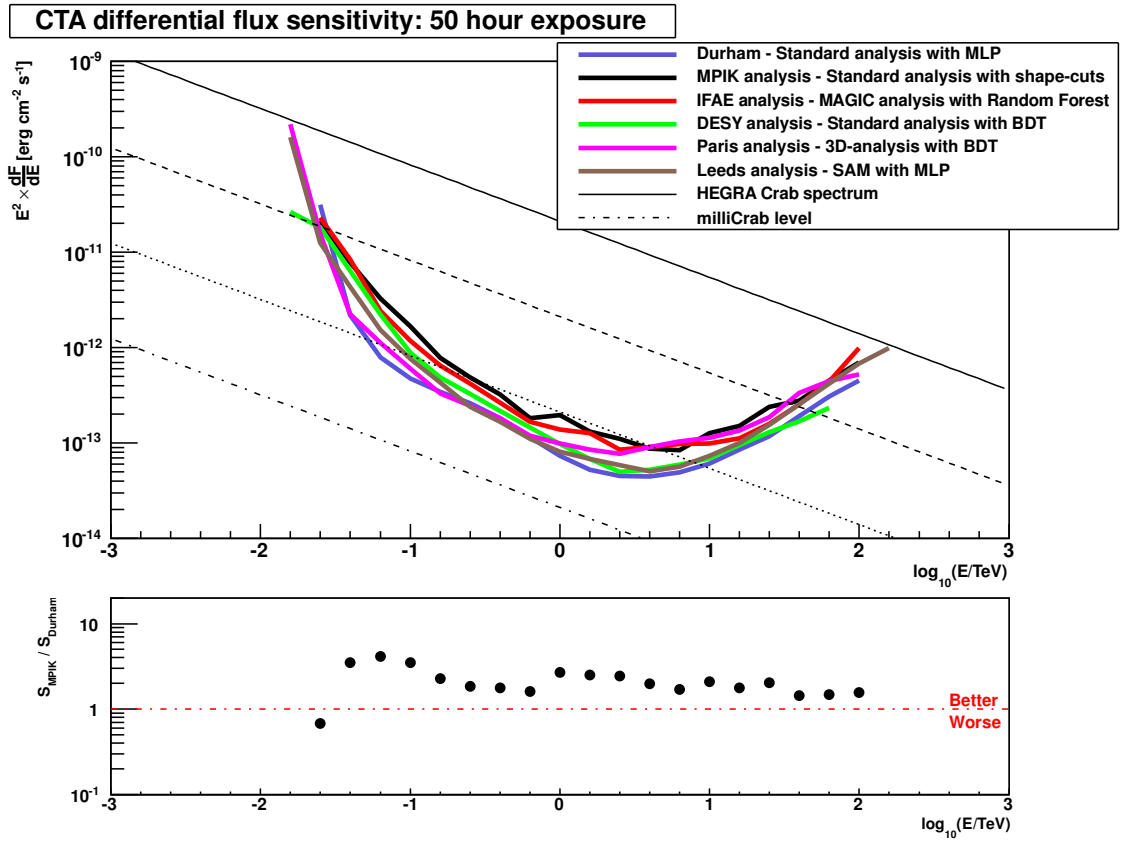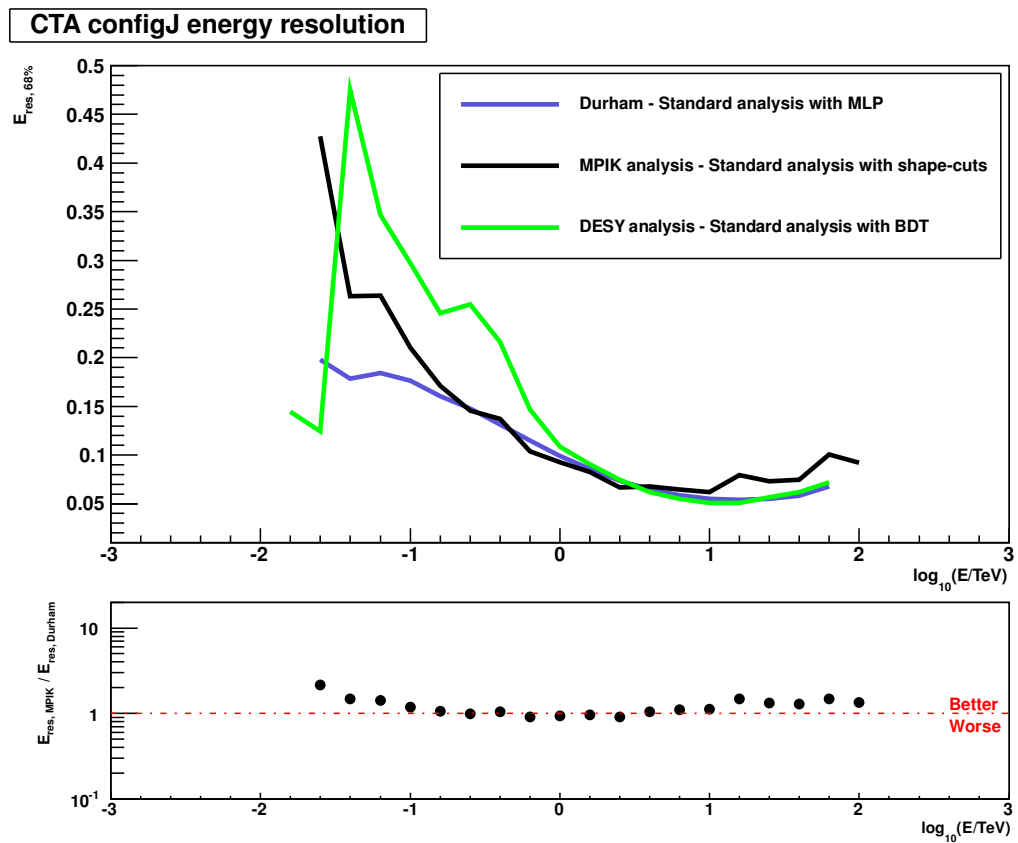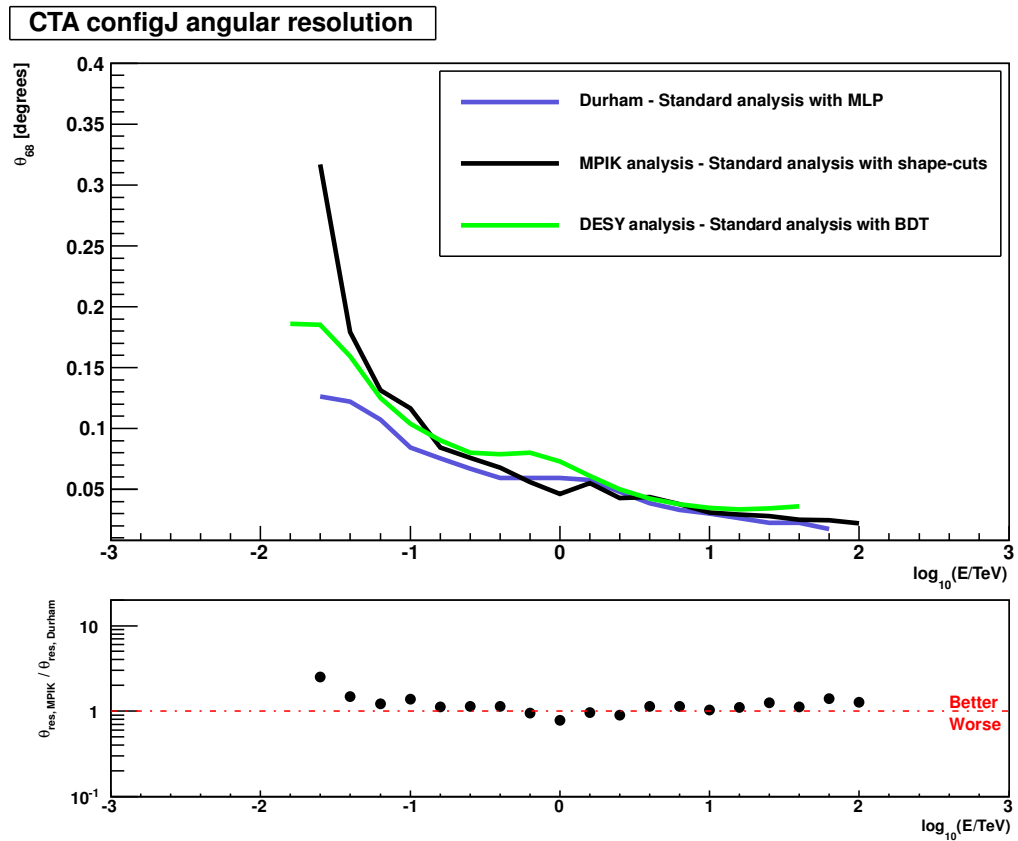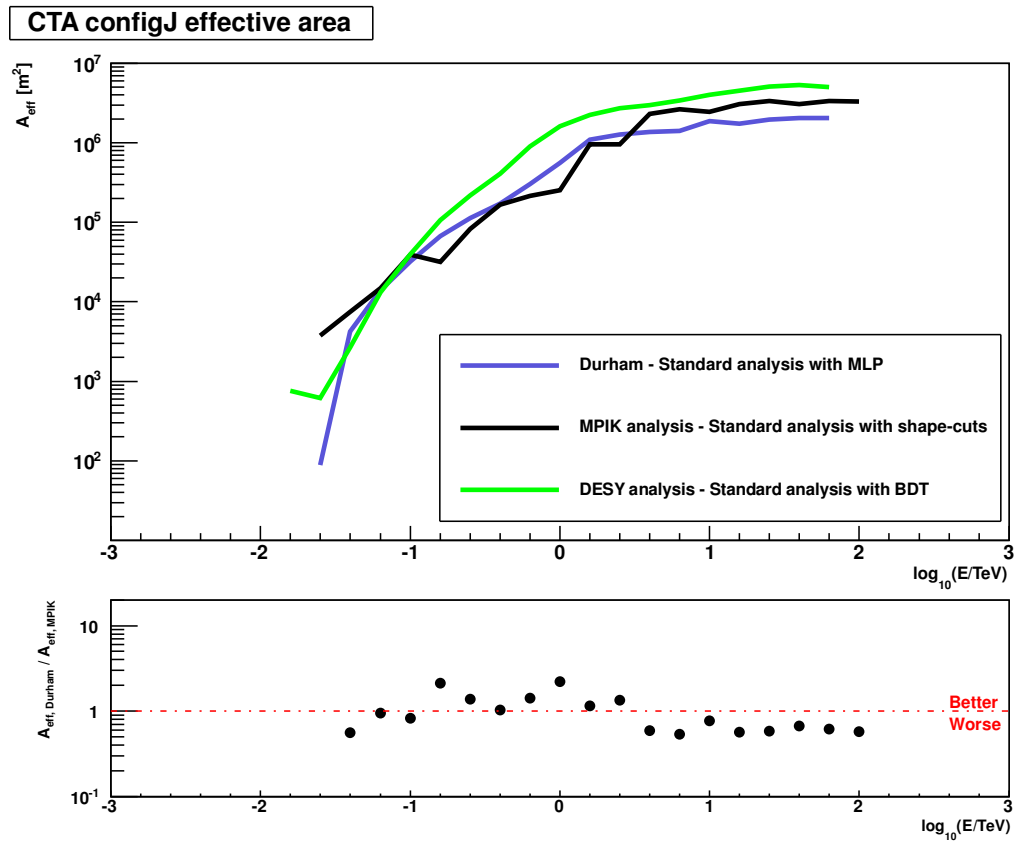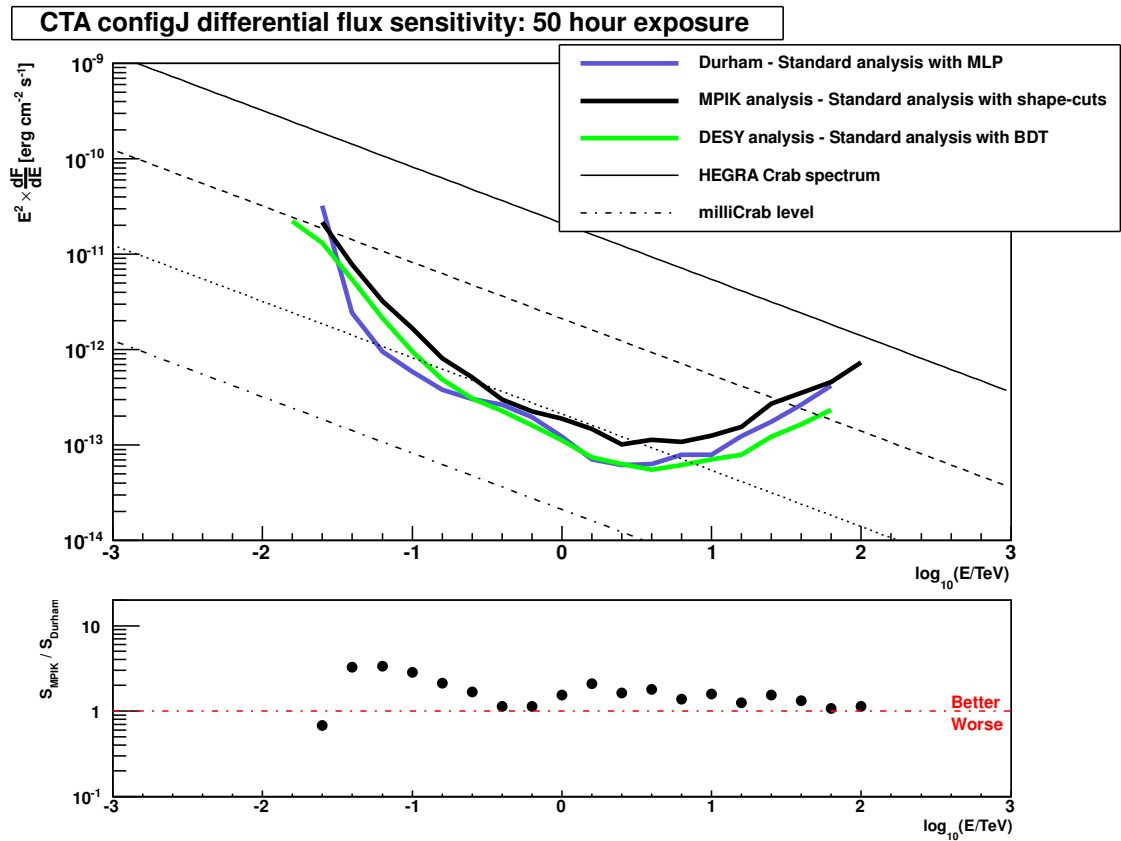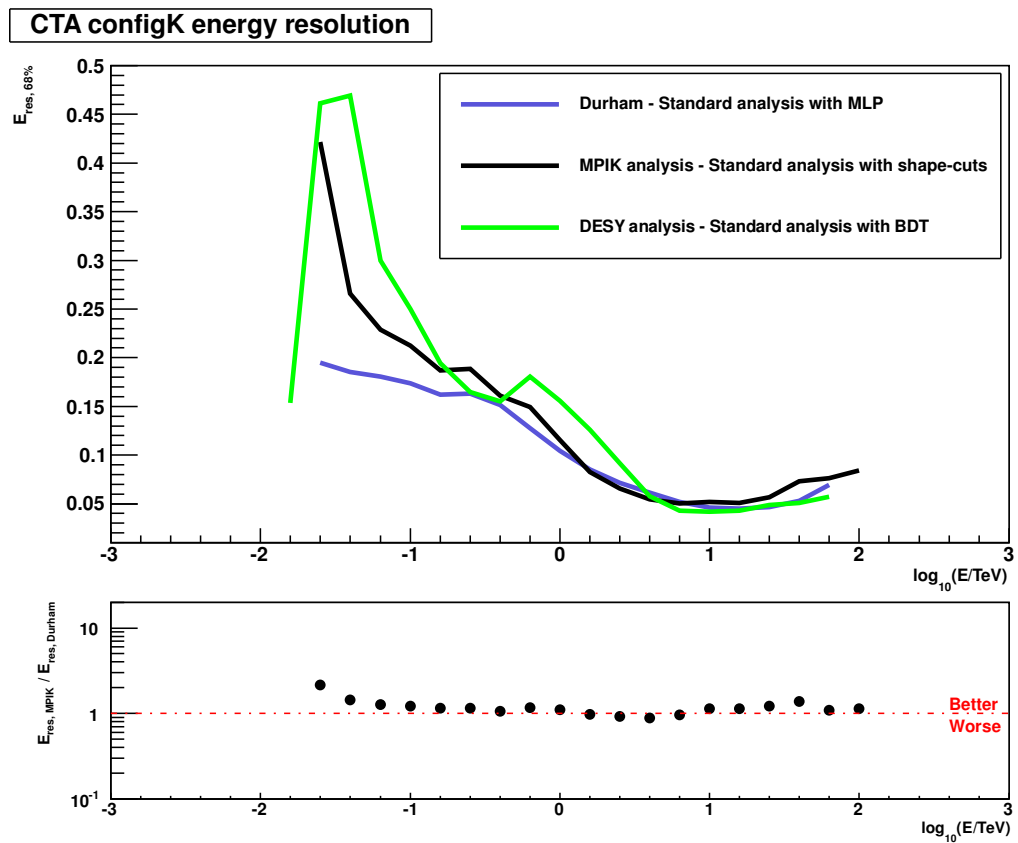## B.4.4   CTA Subarray-K differential sensitivity results
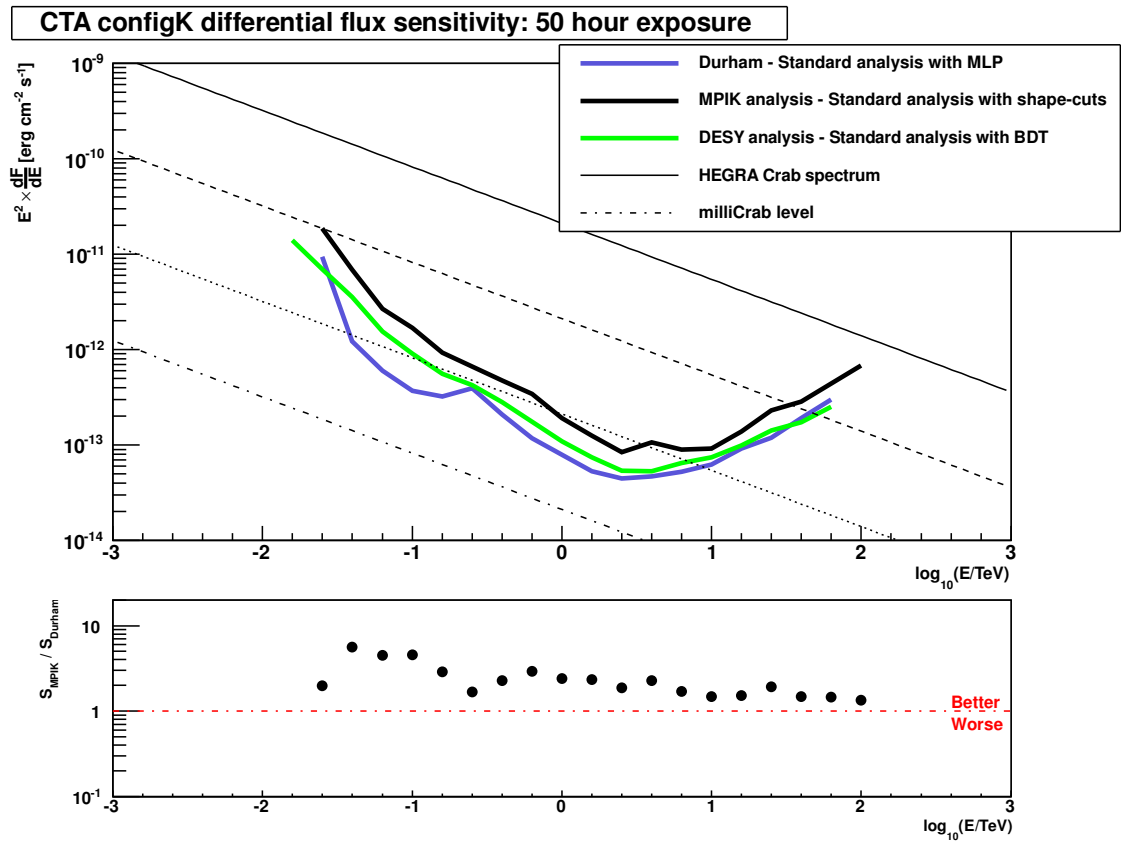
Figure B.16: Comparison of independently calculated differential sensitivity performances as a function of energy for CTA Subarray-K.

Appendix C

Event details for the upper dynamic range study

The following table details the number of events used in the upper dynamic range study for the large-sized telescopes (LSTs).

Method	Details	Amplitude (p.e.)											
		75	100	250	500	750	1000	1250	1500	1750	2000	3000	5000
Ignore	Total (E > 1 TeV)	16564	16634	16729	16735	16718	16716	16718	16717	16716	16717	16715	16709
	$E_{bin} \approx 6$ TeV	605	650	681	690	693	703	692	682	688	693	687	688
Throw	Total (E > 1 TeV)	6986	9009	12993	14679	15550	15946	16159	16306	16405	16466	16588	16681
	$E_{bin} \approx 6$ TeV	0	0	212	463	531	568	582	582	597	606	624	690

Table C.1: Table of event numbers passing cuts: upper dynamic study (LSTs only)

Bibliography

[1] http://cerncourier.com/cws/article/cern/39160. Fermi measures the spectrum of cosmic-ray electrons and positrons. *Last accessed: 1st April 2012*.

[2] http://hawc.umd.edu/. HAWC: the High-Altitude Water Cherenkov observatory. *Last accessed: 5th January 2011*.

[3] http://www.w3schools.com/tags/ref_ascii.asp. ASCII Definition. *Last accessed: 20th February 2011*.

[4] http://www.EGI.eu/. European Grid Infrastructure. *Last accessed: 9th January 2012*.

[5] http://fermi.gsfc.nasa.gov/ssc/data/analysis/documentation/ Cicerone/. The Fermi Cicerone. *Last accessed: 29th March 2012*.

[6] http://www.parkes.atnf.csiro.au/. The Parkes Radio Telescope. *Last accessed: 29th March 2012*.

[7] http://fermi.gsfc.nasa.gov/ssc/data/analysis/scitools/binned\ _likelihood_tutorial.html. Fermi Binned Likelihood Analysis. *Last accessed: 29th March 2012*.

[8] http://www.cplusplus.com/reference/clibrary/cmath/floor/. C++ floor function. *Last accessed: 1st April 2012*.

[9] http://www.mpi\-hd.mpg.de/hfm/HESS/. The High Energy Stereoscopic System. *Last accessed: 1st April 2012*.

[10] http://www.laserfocusworld.com/articles/print/volume\-37/issue\ -5/features/photomultiplier\-tubes/multiple\-anode\-pmt\-behaves\ -like\-many\-detectors\-in\-one.html. Multi-Anode Photomultiplier Tubes (MAPMTs). *Last accessed: 15th April 2012*.

[11] http://fermi.gsfc.nasa.gov/ssc/observations/. Fermi SSC Observations. *Last accessed: 1st April 2012*.

[12] http://wwwmagic.mppmu.mpg.de/. M.A.G.I.C. (Major Atmospheric Gamma-ray Imaging Cherenkov). *Last accessed: 21st May 2012*.

[13] http://veritas.sao.arizona.edu/. V.E.R.I.T.A.S. (Very Energetic Radiation Imaging Telescope Array System). *Last accessed: 21st May 2012*.

[14] ABDO, A., ET AL. Fermi large area telescope observations of the Vela pulsar. *Astrophys. J.* 696 (2009), pages 1084–1093.

[15] ABDO, A., ET AL. Fermi Large Area Telescope Bright Gamma-ray Source List. *arXiv:0902.1340v2* (2009).

[16] ABDO, A., ET AL. Measurement of the Cosmic Ray $e^+ + e^-$ Spectrum from 20 GeV to 1 TeV with the Fermi Large Area Telescope. *Phys. Rev. Lett. 102*, 181101 (2009), page 6.

[17] ABDO, A., ET AL. The First Fermi Large Area Telescope Catalog of Gamma-Ray Pulsars. *Astrophys. J.* 187 (2010), pages 460–494.

[18] ABDO, A., ET AL. The Vela Pulsar: Results from the first year of Fermi LAT observations. *Astrophys. J.* 713 (2010), pages 154–165.

[19] ABDO, A., ET AL. Fermi large area telescope observations of the Crab pulsar and nebula. *Astrophys. J.* 708 (2010), pages 1254–1267.

[20] ACKERMANN, M., ET AL. Fermi-LAT search for pulsar wind nebulae around gamma-ray pulsars. *Astrophys. J. 726*, 35 (2011), page 17.

[21] ACTIS, M., AGNETTA, F., AHARONIAN, F., ET AL. Design concepts for the Cherenkov Telescope Array CTA: an advanced facility for ground-based high-energy gamma-ray astronomy. *Exp. Astron. 32*, 3 (2011), pages 193–316.

[22] AHARONIAN, F., AND KONOPELKO, A. Stereo Imaging of VHE Gamma-Ray Sources. *arXiv:9712044v1* (1997).

[23] AHARONIAN, F., ET AL. The energy spectrum of TeV gamma rays from the Crab nebula as measured by the HEGRA system of imaging air Cerenkov telescops. *Astrophys. J.* 539 (2000), pages 317–324.

[24] AHARONIAN, F., ET AL. Calibration of cameras of the H.E.S.S. detector. *Astropart. Phys.* 22 (2004), pages 109–125.

[25] AHARONIAN, F., ET AL. Observations of the Crab nebula with HESS. *Astron. Astrophys. 457*, 3 (2006), pages 899–915.

[26] AHARONIAN, F., ET AL. Search for pulsed VHE gamma-ray emission from young pulsars with H.E.S.S. *Astron. Astrophys.* 466 (2007), pages 543–554.

[27] AHARONIAN, F., ET AL. High energy astrophysics with ground-based gamma ray detectors. *Rep. Prog. Phys.* 71 (2008), pages 1–56.

[28] ALBERT, J., ET AL. Implementation of the Random Forest method for the Imaging Atmospheric Cherenkov Telescope MAGIC. *Nucl. Instrum. Meth. A* 588 (2008), pages 424–432.

[29] ALEKSIC, ET AL. Phase-resolved energy spectra of the Crab pulsar in the range of 50-400 GeV measured with the MAGIC telescopes. *Astron. Astrophys. 540*, A69 (2012), pages 1–6.

[30] ALIU, E., ET AL. Detection of Pulsed Gamma Rays Above 100GeV from the Crab Pulsar. *Science* 334 (2011), pages 69–72.

[31] ARONS, J. Pair Creation Above Pulsar Polar Caps: Geometrical Structure And Energetics of Slot Gaps. *Astrophys. J.* 266 (1983), pages 215–241.

[32] ATWOOD, W., ET AL. Design and initial tests of the Tracker-converter of the Gamma-ray Large Area Space Telescope. *Astropart. Phys.* 28 (2007), pages 422–434.

[33] BADRAN.H.M, AND HORAN.D. `http://www.cfa.harvard.edu/news/archive/gamma.html`. Gamma-Ray Astronomers Detect "Extreme" Galaxies. Press Release. *Last accessed: 21st May 2012*.

[34] BECHERINI, Y., DJANNATI-ATAÏ, A., MARANDON, V., PUNCH, M., AND PITA, S. A new analysis strategy for detection of faint γ-ray sources with Imaging Atmospheric Cherenkov Telescopes. *Astropart. Phys.* 34 (2011), pages 858 – 870.

[35] BENBOW, W., ET AL. The H.E.S.S. Standard Analysis Technique. Technical report, for the H.E.S.S. collaboration, Max Plank Institut für Kernphysik, Postfach 103980, D-69029, Germany, 2005.

[36] BERGE, D., FUNK, S., AND HINTON, J. Background Modelling in Very-High-Energy γ-ray Astronomy. *arXiv:061095v1* (2008).

[37] BERNLÖHR, K. Shower simulations (Konrad.Bernloehr@mpi-hd.mpg.de). Private communication.

[38] BERNLÖHR, K. The read_hess analysis programme. Private Communication (Konrad.Bernloehr@mpi-hd.mpg.de).

[39] BERNLÖHR, K. CTA simulations with CORSIKA/sim_telarray. In *American Institute of Physics Conference Series* (2008), F. Aharonian, W. Hofmann, and F. Rieger, Eds., volume 1085 of *American Institute of Physics Conference Series*, pages 874–877, 2008.

[40] BERNLÖHR, K. Simulation of imaging atmospheric Cherenkov telescopes with CORSIKA and sim_telarray. *Astropart. Phys.* 30 (2008), pages 149–158.

[41] BERNLÖHR, K. *CORSIKA and sim_hessarray - Simulation of the imaging atmospheric Cherenkov technique for the H.E.S.S. experiment.* H.E.S.S., 2009.

[42] BERNLÖHR, K., CARMONA, E., AND SCHWEIZER, T. MC Simulation and Layout Studies for a future Cherenkov Telescope Array. In *International Cosmic Ray Conference* (2008), volume 3, pages 1469–1472, 2008.

[43] BERNLÖHR.K. Impact of atmospheric parameters on the atmospheric Cherenkov technique. *Astropart. Phys.* 12 (2000), pages 255–268.

[44] BLACKWOOD.J.D, ET AL. `http://www.nasa.gov/mission\_pages/GLAST/news/index.html`. Exploring the Extreme Universe: Science Writers Guide. *Last accessed: 21st May 2012*.

[45] BLÜMER, J., ENGEL, R., AND HÖRENDAL, J. Cosmic Rays from the Knee to the Highest Energies. *arXiv:0904.0725v1* (2009).

[46] BRUN, R., ET AL. `http://root.cern.ch/drupal/`. The ROOT analysis framework. *Last accessed: 1st April 2012.*

[47] BUZHAN, P., ET AL. The advanced study of silicon photomultiplier. In *Advanced Technology & Particle Physics* (2001), M. Barone et al., Eds., Proceedings of the 7th International Conference on ICATPP-7, pages 717–728, 2001.

[48] CARROLL, B., AND OSTLIE, D. *An Introduction to Modern Astrophysics*, 2nd edition. Addison-Wesley, San Francisco, U.S.A., 2007. ISBN: 0-321-44284-9.

[49] CHARLES, P., AND SEWARD.F.D. *Exploring the X-ray universe*. Cambridge University Press, Cambridge, U.K., 1995. ISBN: 0-521-43712-1.

[50] CORNILS, R., ET AL. The optical system of the H.E.S.S. imaging atmospheric Cherenkov telescopes Part II: mirror alignment and point spread function. *arXiv:0308247v1* (2003).

[51] COUDER, A. *Compt. Rend. Acad. Sci.*, 1276 (1926), page 183.

[52] DAUM, A., ET AL. First results on the performance of the HEGRA IACT array. *Astropart. Phys.* 8 (1997), pages 1–11.

[53] DAVIES, J., AND COTTON, E. Design of the quartermaster solar furnace. *Sol. Energy 1*, 2-3 (1957), pages 16–22.

[54] DE JAGER, O., SWANEPOEL, J., AND RAUBENHEIMER, B. A powerful test for weak periodic signals with unknown light curve shape in sparse data. *Astron. Astrophys.* 221 (1989), pages 180–190.

[55] DICKINSON, H. *Very High Energy Gamma-Rays from Binary Systems*. PhD thesis, Durham University, Department of Physics, South Road, Durham, DH1 3LE, 2009.

[56] DJANNATI-ATAÏ, A., ET AL. Search for pulsed VHE emission from PSR B1706-44 with H.E.S.S. H.E.S.S. internal note, 2011.

[57] DUNCAN.R.C., AND THOMPSON.C. Formation of very strongly magnetized neutron stars: implications for gamma-ray bursts. *Astrophys. J.* 392 (1992), pages 9–13.

[58] DYKS, J., AND RUDAK, B. Two-Pole Caustic Model for High-Energy Lightcurves of Pulsars. *arXiv:0303006v2* (2003).

[59] EDWARDS, R., HOBBS, G., AND MANCHESTER, R. TEMPO2, a new pulsar-timing package - I. The timing model and precision estimates. *Mon. Not. R. Astron. Soc.* 372 (2006), pages 1549–1574.

[60] FARNIER, C., AND LENAIN, J.-P. CTA-WP-MC Internal note: Performance studies on the CTA array for an altitude of 3700m and 2000m with Moon light background. Technical report, ISDC Data Centre for Astrophysics, University of Geneva, Versoix, Switzerland, 2011.

[61] FEGAN, D. γ/hadron separation at TeV energies. *J. Phys. G: Nucl. Part. Phys.* 23 (1997), pages 1013–1060.

[62] FIRPO, R. Study of MAGIC Telescope sensitivity for Large Zenith Angle observations. Master's thesis, Institut de Física d'Altes Energies, Universitat Autónoma de Barcelona, 2006.

[63] FRANK, I., AND TAMM, I. Coherent visible radiation of fast electrons passing through matter. *Dokl. Akad. Nauk SSSR* 14 (1937), page 109.

[64] FUNK, S., ET AL. The Trigger System of the H.E.S.S. Telescope Array. *arXiv:0408375v1* (2004), page 20.

[65] GAISSER.T.K. *Cosmic Rays and Particle Physics*. Cambridge University Press, Cambridge, U.K., 1990. ISBN: 0-521-33931-6.

[66] GHISELLINI, G., ET AL. Low power BL Lacertae objects and the blazar sequence. *Astron. Astrophys.* 386 (2002), pages 833–842.

[67] GOLD, T. Rotating Neutron Stars as the Origin of the Pulsating Radio Sources. *Nature* 218 (1968), pages 731–732.

[68] GRIEDER.P. *Cosmic rays at Earth: researcher's reference manual and data book*, first edition. Elsevier Science B.V., P.O. Box 211, 1000 AE, Amsterdam, The Netherlands, 2001. ISBN: 0-444-50710-8.

[69] GRUPEN.C. *Astroparticle Physics*. Springer-Verlag, Berlin Heidelberg, Germany, 2005. ISBN: 3-540-25312-2.

[70] HANLON, W. *The Energy Spectrum of Ultra High Energy Cosmic Rays Measured by the High Resolution Fly's Eye Observatory in Sereoscopic Mode*. PhD thesis, The University of Utah, Department of Physics & Astronomy, 115 south 1400 east, Salt Lake City, UT, USA, 2008.

[71] HARDING, A. High-Energy Emission From Millisecond Pulsars. *Astrophys. J.* 622 (2005), pages 531–543.

[72] HECK, D., KNAPP, J., AND PIEROG, T. `http://www\-ik.fzk.de/corsika/Welcome.html`. COsmic Ray SImulations for KAscade (CORSIKA). *Last accessed: 9th January 2012*.

[73] HESS, M., ET AL. The time structure of Cherenkov images generated by TeV $\gamma-$rays and by cosmic rays. *Astropart. Phys.* 11 (1999), pages 363–377.

[74] HILLAS, A. Cherenkov light images of EAS produced by primary gamma rays and by nuclei. In *In NASA. Goddard Space Flight Center 19th Intern. Cosmic Ray Conf.* (1985), volume 3 of *SEE N85-34862 23-93*, pages 445–448, 1985.

[75] HOBBS, G., AND EDWARDS, R. *Tempo2 User Manual*. Australia Telescope National Facility, CSIRO, PO Box 76, Epping, NSW 1710, Australia, v2.0 edition.

[76] Hobbs, G., Edwards, R., and Manchester, R. TEMPO2, a new pulsar-timing package - I. An overview. *Mon. Not. R. Astron. Soc.* 369 (2006), pages 655–672.

[77] Höcker, A., et al. TMVA - Toolkit for Multivariate Data Analysis. *arXiv:physics/0703039v4* (2007).

[78] Hofmann, W., et al. Comparison of techniques to reconstruct VHE gamma-ray showers from multiple stereoscopic Cherenkov images. *Astropart. Phys.* 12 (1999), pages 135–143.

[79] Johnson, W., et al. A CsI(Tl) Hodoscopic Calorimeter for the GLAST Mission. In *Nuclear Science Symposium* (Washington, DC, 1997), IEEE, pages 27–31, Washington, DC, 1997. Naval Res. Lab.

[80] Joye, W., and Mandel, E. New Features of SAOImage DS9. In *Astronomical Data Analysis Software and Systems XII* (2003), H. Payne, R. Jedrzejewski, and R. Hook, Eds., volume 295 of *ASP Conference Series*, pages 489–492. Smithsonian Astrophysical Observatory, Astonomical Society of the Pacific, 2003.

[81] Kaspi, V., Taylor, J., and Ryba, M. High-Precision Timing of Millisecond Pulsars. III. Long-Term Monitoring of PSRs B1885+09 and B1937+21. *Astrophys. J.* 428 (1994), pages 713–728.

[82] Kaspi, V., Roberts, M., and Harding, A. Isolated Neutron Stars. *arXiv:0402136v2* (2004).

[83] Konopelko, A. Stereo imaging of the VHE γ-rays with HEGRA & H.E.S.S. *arXiv:0011214v1* (2000).

[84] Konopelko, A., et al. Effectiveness of TeV $\gamma-$ray observations at large zenith angles with a stereoscopic system of imaging Cherenkov telescopes. *J. Phys. G: Nucl. Phys.* 25 (1999), pages 1989–2000.

[85] Lemoine-Goumard, M., Degrange, B., and Tluczykont, M. Selection and 3D-reconstruction of gamma-ray-induced air showers with a stereoscopic system of atmospheric Cherenkov telescopes. *Astropart. Phys.* 25 (2006), pages 195–211.

[86] Li, T., and Ma, Y. Analysis methods for results in gamma-ray astronomy. *Astrophys. J.* 272 (1983), pages 317–324.

[87] Lichti, G., et al. Measurements of Gamma-ray bursts with GLAST. *Balt. Astron.* 13 (2004).

[88] Longair, M. *High Energy Astrophysics*, Second edition. Cambridge University Press, Cambridge, U.K., 1992. ISBN: 0-521-38773-6.

[89] Longair, M. *High Energy Astrophysics*, 3rd edition. Cambridge University Press, Cambridge, U.K., 2011. ISBN: 978-0-521-75618-1.

[90] Maier, G. A short decription of an *evndisplay*-based CTA analysis. Internal note, DESY, gernot.maier@desy.de, 2011.

[91] MANCHESTER, R., HOBBS, G., TEOH, A., AND HOBBS, M. The ATNF pulsar catalogue. *arXiv:0412541* 129 (2005), pages 1993 – 2006.

[92] MELIA, F. *High-Energy Astrophysics*. Princeton University Press, Princeton, U.S.A., 2009. ISBN: 0-691-13543-6.

[93] MOISEEV, A., ET AL. The anti-coincidence detector for the GLAST large area telescope. *Astropart. Phys.* 27 (2007), pages 339–358.

[94] NOLAN, P., ET AL. Fermi large area telescope second source catalogue. *arXiv:1108.1435v2* (2012).

[95] NOLAN, S. J., PÜHLHOFER, G., AND RULTEN, C. B. Detailed studies of atmospheric calibration in imaging Cherenkov astronomy. *Astropart. Phys.* 34 (2010), pages 304–313.

[96] NOLAN, S. *Simulation Studies of the Imaging Atmospheric Cherenkov Technique using the Durham Mark 6 and H.E.S.S. Stand-Alone Telescopes*. PhD. thesis, University of Durham, Department of Physics, South Road, Durham, DH1 3LE, 2002.

[97] NOLAN.S.J, AND RULTEN.C. Studies of Lidar Calibration for the Next Generation of Imaging Atmospheric Cherenkov Telescopes. In *Proceedings of 31st International Cosmic Ray Conference* (2009), 2009.

[98] OHM, S., VAN ELDIK, C., AND EGBERTS, K. γ/hadron separation in very-high-energy γ-ray astronomy using a multivariate analysis method. *Astropart. Phys.* 31 (2009), pages 383–391.

[99] PONTIKIS, A. http://www.nobelprize.org/nobel_prizes/physics/laureates/1936/index.html. Nobel Prize in Physics. *Last accessed: 21st May 2012*.

[100] PÜHLHOFER, G. Background estimation, excess counts and significance determination when using a relative acceptance region. Internal note, H.E.S.S. Collaboration, 2004.

[101] RANDO, R., CHARLES, E., DIGEL, S., AND BALDINI, L. http://www.slac.stanford.edu/exp/glast/groups/canda/lat_Performance.htm. Fermi LAT Performance. *Last accessed: 7th March 2012*.

[102] RAY, P., ET AL. Precise γ-ray timing and radio observations of 17 Fermi γ-ray pulsars. *Astrophys. J. 194*, 17 (2011), page 28.

[103] ROMANI, R. Gamma-Ray Pulsars: Radiation Processes In The Outer Magnetosphere. *Astrophys. J.* 470 (1996), pages 469–478.

[104] ROULET, E. Latest results from the Pierre Auger Observatory. *arXiv:1101.1825v1* (2011).

[105] ROWELL, G. A new template background estimate for source searching in TeV gamma-ray astronomy. *Astron. Astrophys.* 410 (2003), pages 389–396.

[106] RULTEN, C. Atmospheric Monitoring For The H.E.S.S. Experiment Using A Single Scattering Lidar. Master's thesis, University of Durham, Physics Department, Rochester Building, South Road, Durham, DH1 3LE, United Kingdom, 2009.

[107] SANUKI, T., ET AL. Precise Measurement of Cosmic-Ray Proton and Helium Spectra with the BESS spectrometer. *Astrophys. J. 545*, 1135 (2000), page 12.

[108] SCHWARZSCHILD, K. Untersuchungen zur geometrischen Optik II. *Astronomische Mittheilungen der Königlichen Sternwarte zu Göttingen* 10 (1905), page 1.

[109] SHAPIRO, S., AND TEUKOLSKY, S. *Black holes, white dwarfs and neutron stars.* John Wiley & Sons, New York, U.S.A., 1983. ISBN: 0-471-87316-0.

[110] SWORDY.S. The Energy Spectra and Anisotropies of Cosmic Rays. *Space Sci. Rev. 99*, 1-4 (2001), pages 85–94.

[111] THE PIERRE AUGER COLLABORATION. http://www.auger.org/. Pierre Auger Observatory. *Last accessed: 1st April 2012.*

[112] WAKELY.S, AND HORAN.D. http://tevcat.uchicago.edu/. TeVCat. *Last accessed: 21st May 2012.*

[113] WEEKES, T. Observation of TeV gamma rays from the Crab Nebula using the atmospheric Cherenkov imaging technique. *Astrophys. J.* 342 (1989), page 379.

[114] WEEKES.T.C. *Very High Energy Gamma Astronomy.* IOP Publishing Ltd, Bristol, U.K., 2003. ISBN: 0-7503-0658-0.

[115] WHITE, R., HINTON, J., KHÉLIFI, B., HERMANN, G., AND BERNLÖHR, K. Energy Ranges and dynamic ranges for the CTA telescopes. Technical report, for the CTA collaboration, 2011.

[116] ZEILIK, M., AND GREGORY, S. *Introductory Astronomy & Astrophysics*, Fourth edition. Saunders College Pub., Forth Worth, U.S.A., 1998. ISBN: 0-030-06228-4.